

PUBLISHER :



Address of Publisher & Editor's Office :

GDAŃSK UNIVERSITY
OF TECHNOLOGY

Faculty
of Ocean Engineering
& Ship Technology

ul. Narutowicza 11/12
80-952 Gdańsk, POLAND
tel.: +48 58 347 13 66
fax : +48 58 341 13 66
e-mail : office.pmr@pg.gda.pl

Account number :
BANK ZACHODNI WBK S.A.
I Oddział w Gdańsku
41 1090 1098 0000 0000 0901 5569

Editorial Staff :

Tadeusz Borzęcki Editor in Chief
e-mail : tadbtor@pg.gda.pl

Przemysław Wierzchowski Scientific Editor
e-mail : e.wierzchowski@chello.pl

Jan Michalski Editor for review matters
e-mail : janmi@pg.gda.pl

Aleksander Kniat Editor for international relations
e-mail : olek@pg.gda.pl

Kazimierz Kempa Technical Editor
e-mail : kkempa@pg.gda.pl

Piotr Bzura Managing Editor
e-mail : pbzura@pg.gda.pl

Cezary Spigarski Computer Design
e-mail : biuro@oficynamorska.pl

Domestic price :
single issue : 20 zł

Prices for abroad :
single issue :
- in Europe EURO 15
- overseas US\$ 20

ISSN 1233-2585



POLISH MARITIME RESEARCH

in internet

www.bg.pg.gda.pl/pmr/pmr.php



POLISH MARITIME RESEARCH

No 4(76) 2012 Vol 19

CONTENTS

- 3 **EUGENIUSZ KOZACZKA, GRAŻYNA GRELOWSKA, SŁAWOMIR KOZACZKA, WOJCIECH SZYMCZAK**
Processing data on sea bottom structure obtained by means of the parametric sounding
- 11 **ZHENYU JIANG, MIN XIANG, MINGDONG LIN, WEIHUA ZHANG, SHUAI ZHANG**
Research on hydrodynamic properties of annular cavitator with water injection
- 16 **HAMID ZERAATGAR, ALI BAKHSHANDEH ROSTAMI, ABOLFAZL NAZARI**
A study on performance of planing-wing hybrid craft
- 23 **BOGDAN LIGAJ, GRZEGORZ SZALA**
Comparative analysis of fatigue life calculation methods of C45 steel in conditions of variable amplitude loads in the low- and high-cycle fatigue ranges
- 31 **HAO WANG, FEI ZHAO, YUAN-SHENG CHENG, JUN LIU, YUAN TIAN**
Dynamic response analysis of light weight pyramidal Sandwich plates subjected to water impact
- 44 **GRZEGORZ SKOREK**
Graphical interpretation of the power of energy losses and power developed in the hydrostatic drive and control system elements
- 54 **WOJCIECH LITWIN, ARTUR OLSZEWSKI**
Assessment of possible application of water-lubricated sintered brass slide bearing for marine propeller shaft
- 62 **LESZEK MATUSZEWSKI**
Multi-stage magnetic-fluid seals for operating in water – life test procedure, test stand and research results. Part I Life test procedure, test stand and instrumentation
- 71 **WOJCIECH HOMIK**
The effect of liquid temperature and viscosity on the amplitude-frequency characteristics of a viscotic torsion damper
- 78 **PIOTR BORKOWSKI**
Data fusion in a navigational decision support system on a sea-going vessel

Editorial

POLISH MARITIME RESEARCH is a scientific journal of worldwide circulation. The journal appears as a quarterly four times a year. The first issue of it was published in September 1994. Its main aim is to present original, innovative scientific ideas and Research & Development achievements in the field of :

Engineering, Computing & Technology, Mechanical Engineering,

which could find applications in the broad domain of maritime economy. Hence there are published papers which concern methods of the designing, manufacturing and operating processes of such technical objects and devices as : ships, port equipment, ocean engineering units, underwater vehicles and equipment as well as harbour facilities, with accounting for marine environment protection.

The Editors of POLISH MARITIME RESEARCH make also efforts to present problems dealing with education of engineers and scientific and teaching personnel. As a rule, the basic papers are supplemented by information on conferences , important scientific events as well as cooperation in carrying out international scientific research projects.

Scientific Board

Chairman : Prof. **JERZY GIRTLEK** - Gdańsk University of Technology, Poland

Vice-chairman : Prof. **ANTONI JANKOWSKI** - Institute of Aeronautics, Poland

Vice-chairman : Prof. **MIROSLAW L. WYSZYŃSKI** - University of Birmingham, United Kingdom

Dr **POUL ANDERSEN**
Technical University
of Denmark
Denmark

Prof. **STANISŁAW GUCMA**
Maritime University of Szczecin
Poland

Dr **YOSHIO SATO**
National Traffic Safety
and Environment Laboratory
Japan

Dr **MEHMET ATLAR**
University of Newcastle
United Kingdom

Prof. **ANTONI ISKRA**
Poznań University
of Technology
Poland

Prof. **KLAUS SCHIER**
University of Applied Sciences
Germany

Prof. **GÖRAN BARK**
Chalmers University
of Technology
Sweden

Prof. **JAN KICIŃSKI**
Institute of Fluid-Flow Machinery
of PASci
Poland

Prof. **FREDERICK STERN**
University of Iowa,
IA, USA

Prof. **SERGEY BARSUKOV**
Army Institute of Odessa
Ukraine

Prof. **ZYGMUNT KITOWSKI**
Naval University
Poland

Prof. **JÓZEF SZALA**
Bydgoszcz University
of Technology and Agriculture
Poland

Prof. **MUSTAFA BAYHAN**
Süleyman Demirel University
Turkey

Prof. **JAN KULCZYK**
Wrocław University of Technology
Poland

Prof. **TADEUSZ SZELANGIEWICZ**
Technical University
of Szczecin
Poland

Prof. **MAREK DZIDA**
Gdańsk University
of Technology
Poland

Prof. **NICOS LADOMMATOS**
University College London
United Kingdom

Prof. **WITALIJ SZCZAGIN**
State Technical University
of Kaliningrad
Russia

Prof. **ODD M. FALTINSEN**
Norwegian University
of Science and Technology
Norway

Prof. **JÓZEF LISOWSKI**
Gdynia Maritime University
Poland

Prof. **BORIS TIKHOMIROV**
State Marine University
of St. Petersburg
Russia

Prof. **PATRICK V. FARRELL**
University of Wisconsin
Madison, WI
USA

Prof. **JERZY MATUSIAK**
Helsinki University
of Technology
Finland

Prof. **DRACOS VASSALOS**
University of Glasgow
and Strathclyde
United Kingdom

Prof. **WOLFGANG FRICKE**
Technical University
Hamburg-Harburg
Germany

Prof. **EUGEN NEGRUS**
University of Bucharest
Romania

Prof. **YASUHIKO OHTA**
Nagoya Institute of Technology
Japan

Processing data on sea bottom structure obtained by means of the parametric sounding

Eugeniusz Kozaczka^{1,2)}, Prof.

Grażyna Grelowska¹⁾, Prof.

Sławomir Kozaczka¹⁾, M.Sc.

Wojciech Szymczak¹⁾, M.Sc.

¹⁾ Polish Naval Academy, Poland

²⁾ Gdansk University of Technology, Poland

ABSTRACT

The aim of the paper is to analyze data obtained during sounding the Gdansk Bay sea bed by means of the parametric echo-sounder. The accuracy of the sea bottom structure investigation needs correct configuration of research equipment and proper calibration of peripheral devices (GPS, heading sensor, MRU-Z motion sensor and navigation instruments which provide necessary data to bathymetrical measurement system, enabling its work with full capability. The parametric sub-bottom profiler delivers two types of data which include different information: envelope and pure echo signal sampled without processing. The first is used to present echograms in real time and the second one is stored during sounding and the obtained data can be analyzed by using post-processing software. Differences in the results are presented and discussed. And, are described also criteria taken into account during determination of the measurement areas and selection of different configurations of the software according to the information to be obtained from trials. Complementary information can be achieved from processing the data by means of the procedures offered by Matlab software, which allows for a clear 3D presentation of the results. The consideration are illustrated by echograms taken in the natural conditions.

Keywords: sea bottom acoustic; sub-bottom profiler; sea bed structure

INTRODUCTION

A bathymetrical measurement system fitted with SES-2000 sub-bottom profiler was installed on a small survey vessel of 10.5 m in length. Parametric echo-sounder antenna was installed on starboard and EM3002 multibeam transducer - on port, 100 cm below water surface on special mounting arms. Additional navigation devices were tested in different localizations and finally mounted in the places best suited to their functions. GPS was installed in the vessel's centre line, close to deck to minimize speed and position errors. MRU-Z motion sensor was fitted near the vessel's gravity centre. Application of the SES-2000 Standard - parametric sub-bottom profiler makes it possible to observe structure of the upper layers of seabed. Parametric sources used in studying the seabed allow - as a result of the minimum impact of two acoustic beams radiated into the water in the same area - to generate low frequency waves (of a few kHz only) of the geometric properties similar to the characteristics of the so-called primary waves. This allows for observation of stratification of the seabed with relatively high accuracy. In addition, the use of the equipment intended for the so-called electronic stabilization, in this particular case the MRU-Z system, allows to eliminate the sounding beam

movement associated with the movement of the antenna. After mounting the sounding devices, measurements were done to define lever arms and compensation parameters for each of the bathymetrical units. Signals from GPS and heading and motion sensor are distributed through multiplying modules to different devices. Trials on Gdansk Bay with calibrated instruments on small measurement vessel were made and interesting solutions connected with processing and sounding were quoted. At the beginning of this article, is presented and discussed information obtained during trials on the water tank 30 m long, 3 m wide and 1.5 m deep, owned by Gdansk University of Technology.

METHOD OF DATA PROCESSING

The analysis of data obtained during trials is preceded by information on characteristic parameters of antenna (directivity, sounding pulses) and methods of data processing prior to echogram visualization. Sounding pulse (of 4kHz frequency and two-pulse length) measured at 4 m distance from transducer (the near measurement point II marked in Fig. 2), is plotted in Fig. 1. The calculated depth resolution of such configuration amounts to 37.5 cm.

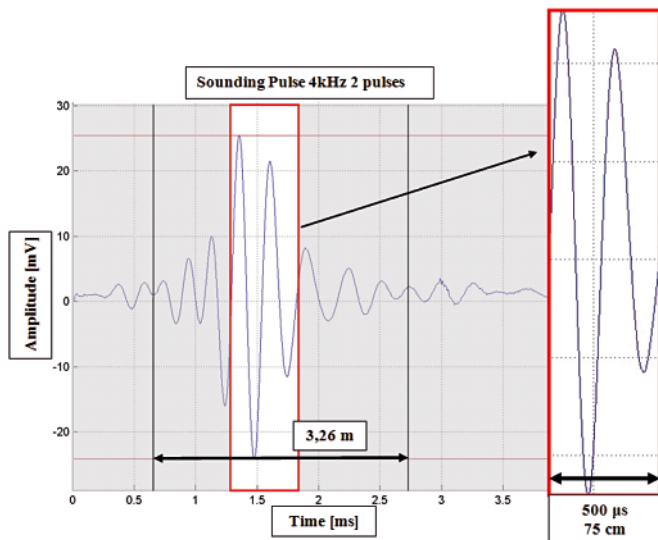


Fig. 1. Sounding pulse measured at 4 m distance from transducer

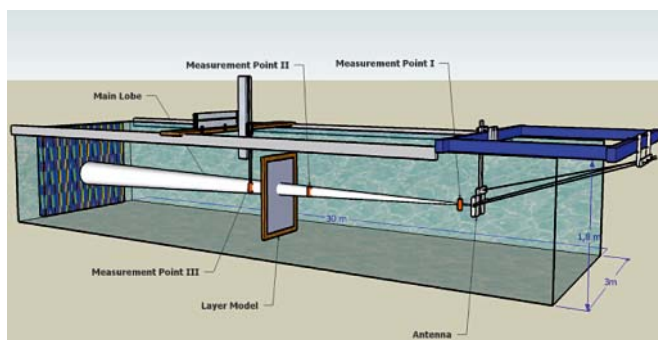


Fig. 2. Schematic view of the water tank

The data visualization method are presented on the example of sounding the concrete wall. Plots shown in the figures below were recorded with the use of Tektronix oscilloscope connected to analogue output of the echo-sounder, which provides a filtered and amplified signal just before sending it to analogue-digital converter (such signal is shown in Fig. 3). Fig. 4 illustrates the envelope calculated from pure echo signal.

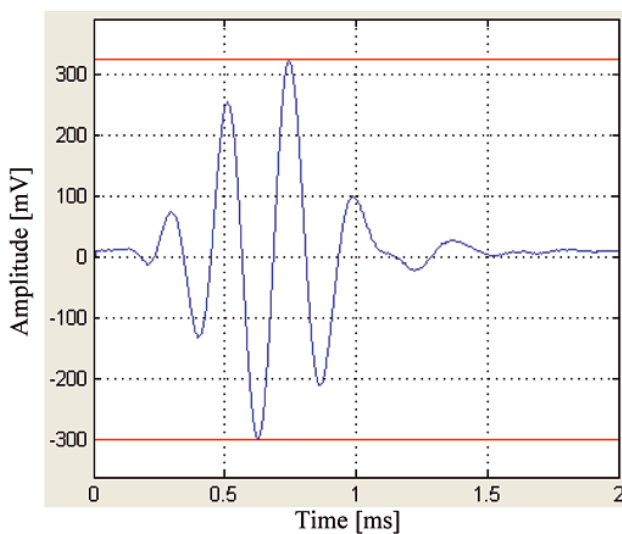


Fig. 3. Echo of sounding pulse

The measured signal length is 1.5 m, but not all its fragments should take part in visualization, that is shown in Fig. 5 where the gray flat area is the threshold, i.e. LF Min Level for small echoes and noise. Changing this value can strongly

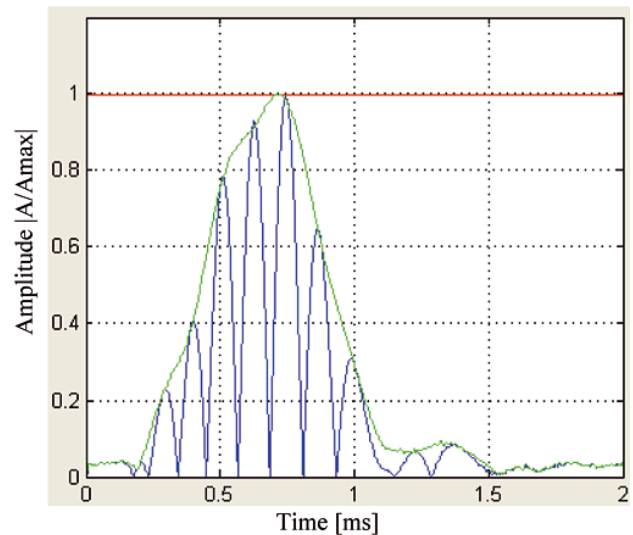


Fig. 4. Envelope of received pulse

influence visualization model and help examination of received information. The typical echogram which describes result of the sounding with all cut-off filters set to minimum values, is shown in Fig. 6.

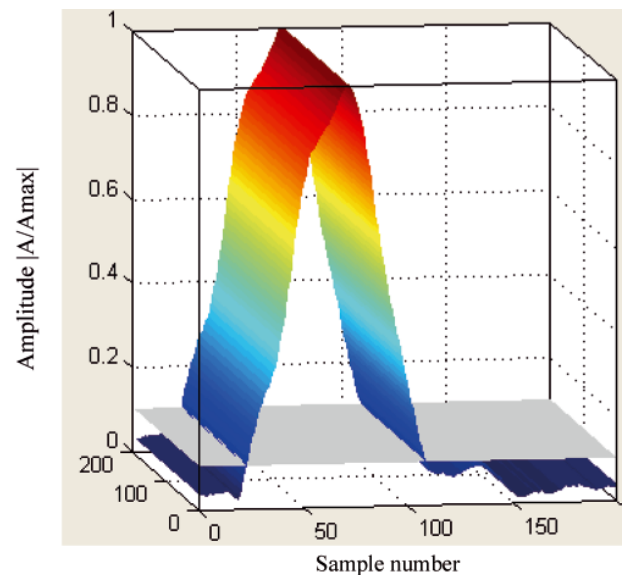


Fig. 5. 3D visualization performed by using the Matlab software

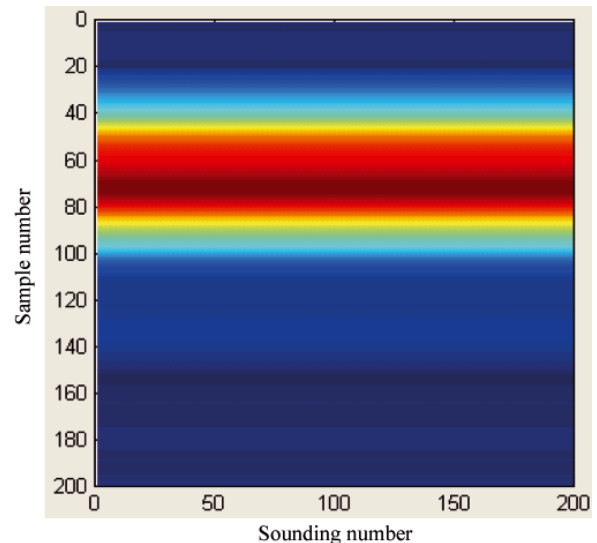


Fig. 6. 2D echogram received from the Matlab software

The data received from the stationary measurements in 30 m water tank, were used during analyzing the results from the trials at Gdansk Bay. It was important to set depth resolution for different sounding pulses depending on their frequency (4, 6, 8, 10, 12 - 15 kHz) and number of pulses which represent number of cycles. Increasing number of pulses increases energy of transmitted signal (better signal to noise ratio) but decreases the depth resolution:

$$\text{Depth_resolution} = t \cdot c / 2$$

Where:

- t – time,
- c – sound velocity in water



Fig. 7. Measurement layers with SES data file possible to be processed after recording

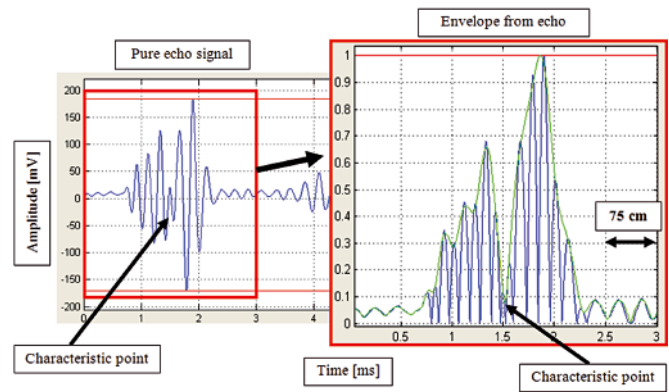


Fig. 8. Echo and envelope of received signal

The result obtained from sounding two artificial sediment layers is shown in Fig. 8. The two artificial sediment layers were arranged in the configuration shown in Fig. 7, where their mutual distance was 35 cm. Looking at the result, one can notice a characteristic point in which a jump in the envelope (shown on echogram as free space) is formed during calculating the envelope. The free space length depends on threshold level and type of visualization method, but the length is correlated with free space between frames.

DATA RECEIVED FROM SOUNDING

Comparison of pure signal and lower resolution envelope

Data from the sounding at Gdansk Bay where penetration depth of sediments reached 40 meters (the starting point is set at 50 m below sea surface) are presented in Fig. 9. 4 kHz frequency and 2 pulses length signal is used. The two following charts describe comparison of the data:

- SES data – contain 480 samples used to draw echograms in real time.
- RAW data – contain 5120 samples which are stored in parallel.

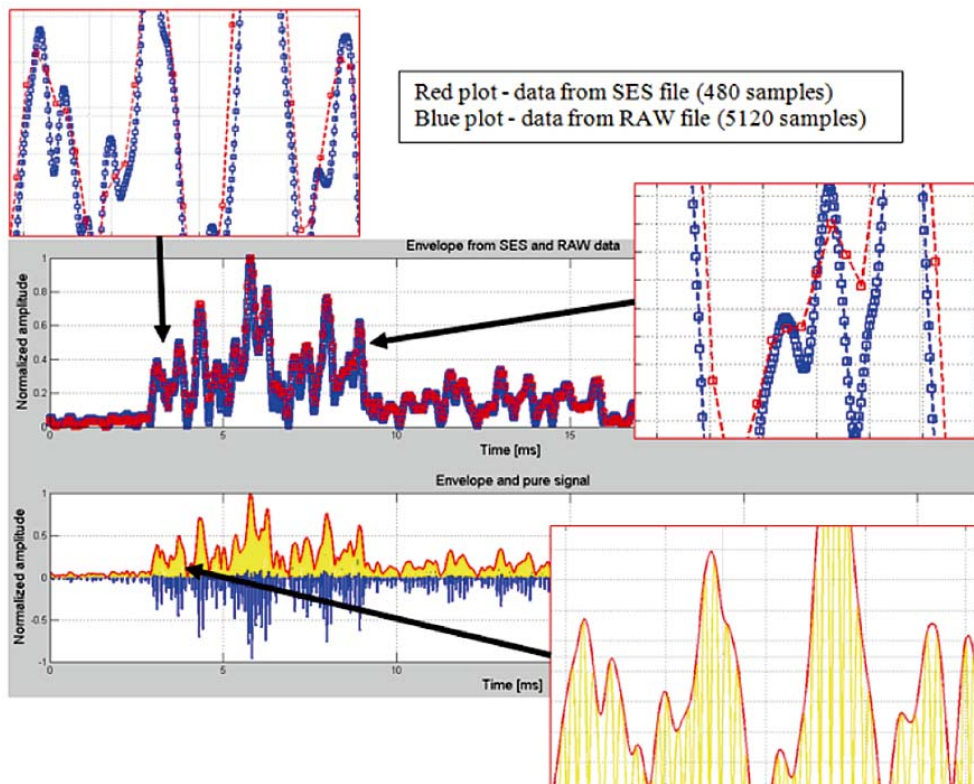


Fig. 9. Comparison of *.SES and *.RAW data

The interesting comparison of the data was expanded in the upper part of Fig. 9. Difference in their quality can be observed, which clearly shows that the slow sampling brings errors connected with resolution, causes losing information about e.g. rapid drops in envelope, that can be very important for searching the objects buried not deeply. The envelope calculated from the recorded pure echo signal is shown in the lower part of Fig. 9 – its expanded part shows all details without losing information. After using proper post-processing tools and *.raw data files small changes in signals can be observed during analyzing full echo runs.

Filtering pure signal and data presentation on echogram

The below described results are obtained from Matlab software where appropriate algorithms for data analyzing are implemented. Additionally, interesting results of sounding were selected to show rapid change in sediment properties. The first 370 m recorded on echogram show the sea bottom located in depth of 54 m and sediment layers up to 85 m. After sounding 380 m distance we can observe fast change of penetration depth which decreases to 2.5 m. Looking forward the nearest 1000 m of the visualized echogram one can observe a stronger echo reflected from the bottom and no information from the sub-bottom zone.

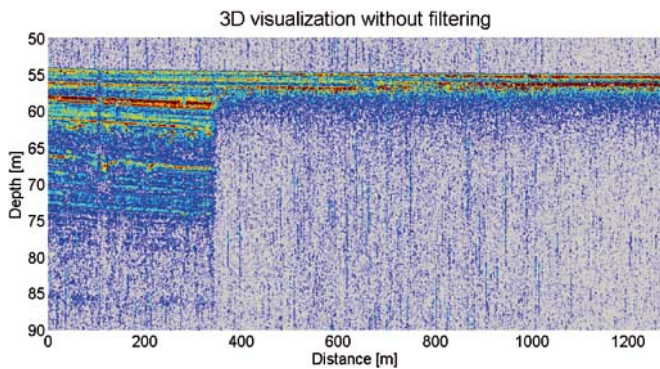


Fig. 10. Raw data displayed in the form of echogram - pure signal

Having known the sounding pulse and sampling frequency it was possible to filter signals by using the band-pass filter. The result of the filtering is shown in Fig. 11, where is possible to observe the clear echogram with more differentiated echo levels in the three marked zones.

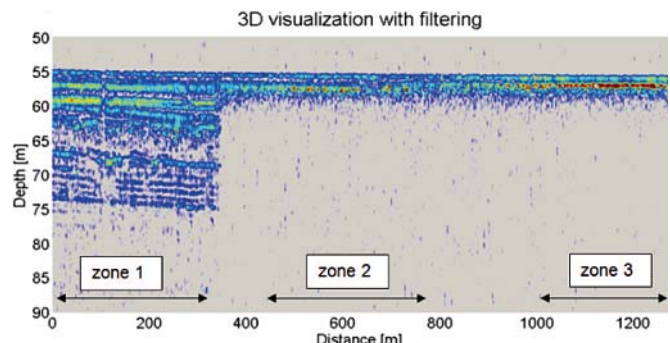


Fig. 11. Raw data displayed in the form of echogram - signal passed through band-pass filter

The time series of the reflected pulses received after transmitting sounding pulse were plotted on three charts (Fig. 12). The first one visualizes results from the sounding zone I. The analyzing of the signal did not give clear classification of echo reflected from layers - signals are continuous, but after forming the envelope characteristic hooks (which arise during impact of two overlapping reflected sounding pulses) allow to plot echograms with visible boundary between layers. The signal from the middle part of bottom sounding (zone II) exhibits echo from the first layer located on a higher level than in the zone I, that can be interpreted for instance as another type of bottom material imposed on a muddy bottom.

Looking at the third time series one can observe that in this case the first and second echo show much higher level than in the two first zones. To get proper interpretation of sounding results (especially in the third case - possible simulation of such layer arrangement) a correlation with the data received from trials on the 30 m water tank is necessary where differential sounding pulses were a.o. measured and the sounding of two

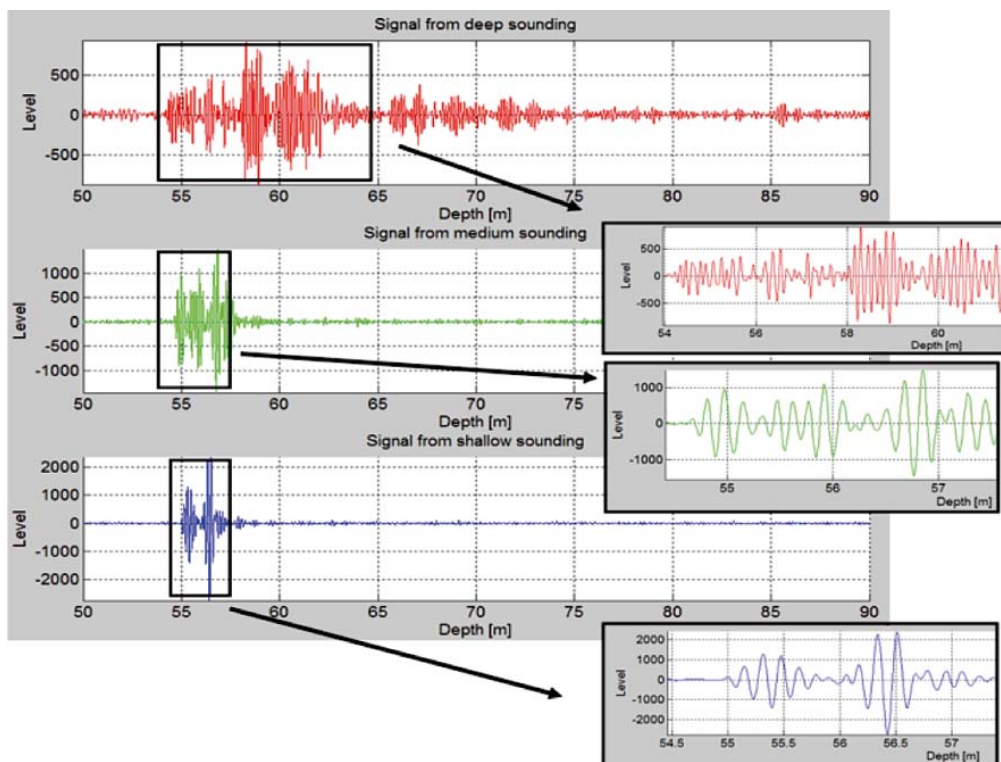


Fig. 12. Time series of raw signals

layers side by side with different types of bottom sediments placed in special frames, was performed.

4 kHz sounding pulse is shown in Fig. 13. The sounding pulse is nearly the same as the reflected signal from zone III, that can be checked during analyzing Fig. 12. The first echo is a little fuzzy, that can be interpreted as reflection from a muddy/clay material but the second one corresponds directly to the transmitted signal.

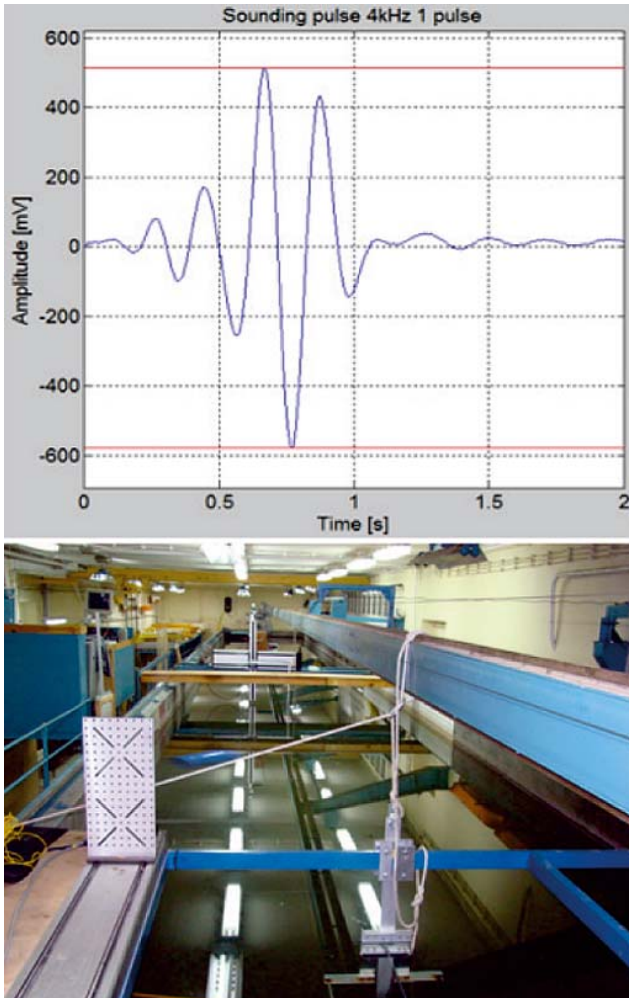


Fig. 13. Low-frequency pulse of 4kHz (upper figure) measured during the trials in the water tank (lower figure)

To compare echo power level, respective soundings from each zone, after filtration, were averaged and displayed in Fig. 14 in the form of artificial echogram.

3D visualization after processing - with filter

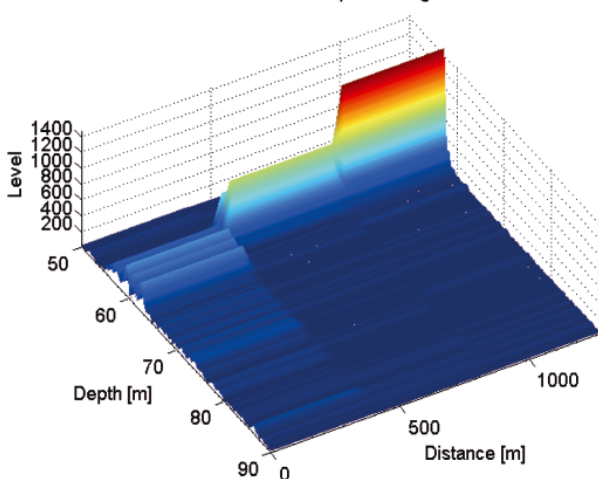


Fig. 14. Comparison of echo strength

The echogram confirms that the deepest bottom penetration has lower echo level along whole path. Strength of the signal reflected from the area near zone I is greater but not as great as the signal coming from zone III. During sea trials several points rapid change of sediment penetration depth were localized, that gives opportunity to mark the points on map and apportionment border on bay (red colour line) whose shape is regular and can confirm real natural properties of the sediments in this area.

The deepest penetration zone is marked yellow and the red area corresponds to place where investigation of sediments is reduced to that of the high power echo reflected from the first layer (the sediment samples, taken not from the whole coastal zone, were analyzed during water tank laboratory measurements, where they were placed in the frames to be sounded with low frequency pulses emitted by the same unit as during sea bottom trials).

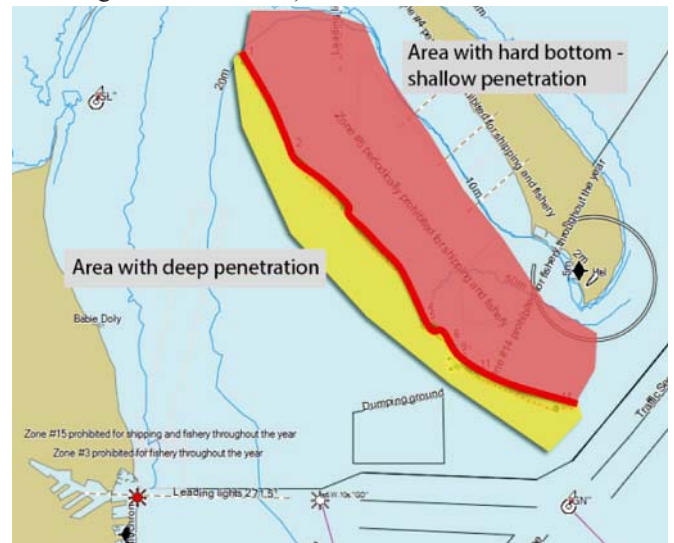


Fig. 15. Red line - border of penetration

After expanding an interesting fragment of the echogram (Fig. 16) it is possible to calculate a distance from which the penetration depth decreases from 20 to 5 m. The distance is near 13 m which corresponds to a fast change in bottom properties. However such geological case can also appear under natural conditions and this change does not result from one sounding ping to another so it is not due to a change in sounding parameters, like e.g. frequency.

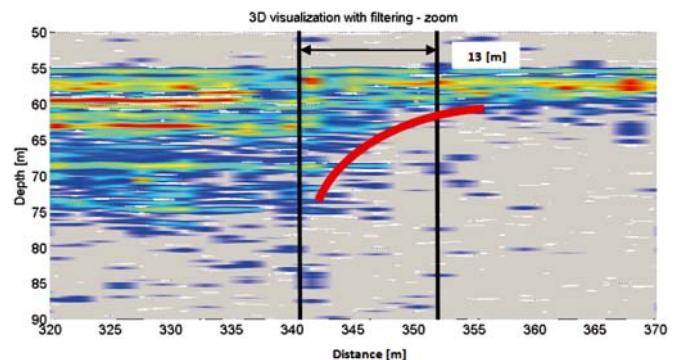


Fig. 16. Expansion of rapid change of penetration depth

The sounding results which show rapid change of penetration depth are correlated with results obtained by another researchers and published on relevant websites. The results obtained by these authors are equivalent to echograms produced by different echo-sounders, like e.g. the TOPAS 40 - results titled "Results from shallow gas area outside Namibia", published on Kongsberg website.

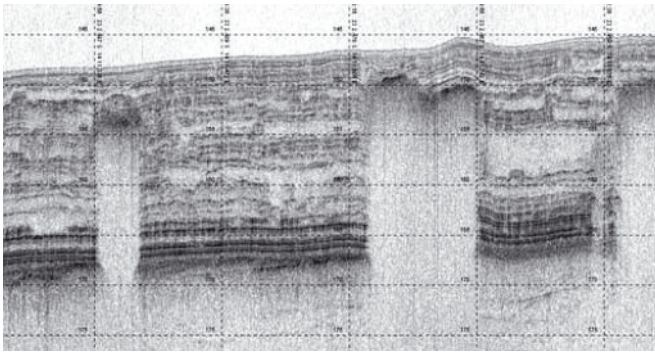


Fig. 17. Kongsberg's TOPAS 40 echogram

It is necessary to point out that during measurements a compensation of roll (beam stabilization) and heave motions was realized with the use of the MRU-Z device. But it is important to remember of influence of not compensated pitch motion, which depends on sea state and can be considerable. It is easy to confirm the influence during analyzing the echogram shown in Fig. 18 where bottom sediments are the same but pitch motion makes sounding pulses hitting bottom at different angles, that changes echo amplitude. These results were taken during high surge motion in order to get an example of such data. The typical sounding operation was realized during calm weather.

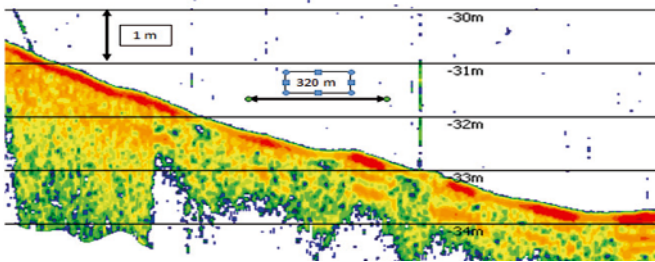


Fig. 18. Example of different levels of echo reflected from the same sediment

METHODS OF POST-PROCESSING VISUALIZATION

During searching for difference between sediment properties or checking a mud or silt layer covering sandy bottom it is important to set, in a proper way, threshold for minimum values to be visualized on echogram, in order to make substantial differences visible. Additionally, the algorithm which defines distribution of colours should be set to logarithmic or linear mode. By using the Matlab as programming software to visualize data, two examples taken during sounding two areas close to each other, are shown below.

Each echogram contains two parts – on the left side are visualized sounding results where penetration depth was up to 3 m, and on the right side - echoes reflected from the layers located 15 m under the bottom. The colour scale was set to linear mode. In Fig. 19 the threshold was set to minimum to make all details visible, but usually it is difficult (especially in logarithmic colour scale mode) to distinguish a mud layer placed on hard bottom. The threshold level was set to the value which cuts off envelope picks resulting from low power echoes, shown in Fig. 20. It can be observed that the three thick layers which were first the bottom layer, now are covered with 3 m thick sediment. The same comparison can be seen in 3D view of envelopes, as shown in Fig. 21. The envelope used in the comparison is averaged from sounding records, that makes its peaks smooth. Additionally, when data include much noise it is possible to use a stacking algorithm (adding consecutive echo signals and receiving new, processed data) and smoothing function which decreases influence of noise on the results.

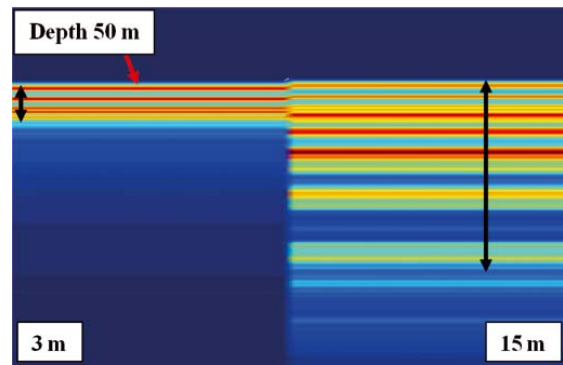


Fig. 19. Echogram with minimum threshold value

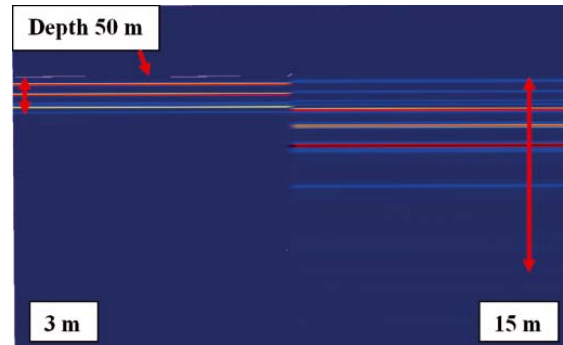


Fig. 20. Echogram with high threshold value

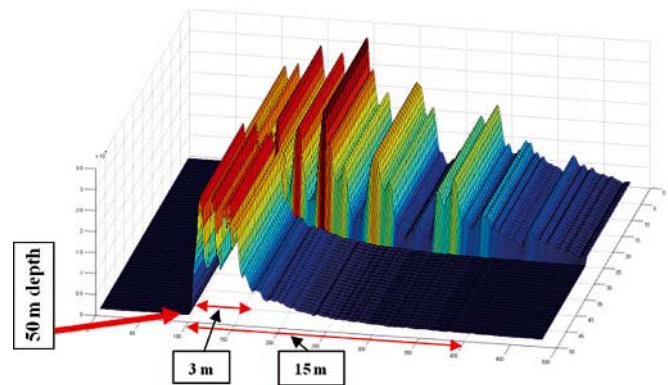


Fig. 21. 3D presentation of data by using Matlab software

Operator should select proper configuration of the software intended for co-operating with parametric echo-sounder, depending on the type of research to be performed, namely:

- examination of sediments layers,
- searching for a buried object.

Having known that the envelope contains constant number of samples, not depending on range, when searching for a small buried object located at constant depth on flat bottom, the start sampling range can be set $1 \div 2$ m above the bottom and 5 m in its value, i.e. the smallest one. It will give the highest resolution which provides the sampling step of 0.01 m, that makes it possible to observe small changes in reflected sounding pulse. When the main aim is to investigate the sediment layers up to 30 m below the bottom surface, operator should set up the start sampling range to be $4 \div 5$ m above the bottom surface and the sounding range should be set to $35 \div 40$ m. The resulting resolution is not very high but satisfactory in the case in question.

If something interesting is noticed in the seabed structure, for example at 10 m depth below the bottom surface, the sounding should be repeated with the sampling window set up in the way described in the searching for buried object but with the start sampling range value adjusted to actual situation (it could be set below bottom surface).

The sounding results obtained from the software intended for imaging data in real time are presented in Fig. 22 and 23, and the results post-processed with the use of the software dedicated to this type of data – in Fig. 24 and 25. In the considered case the bottom is located $46 \div 48$ m below sea surface and the penetration range reaches 27 m in the maximum point.

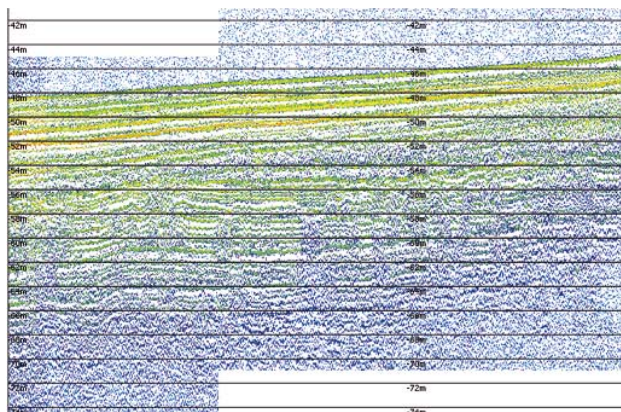


Fig. 22. Envelope from 480 samples - 6 kHz 2p (from SES data - differential view)

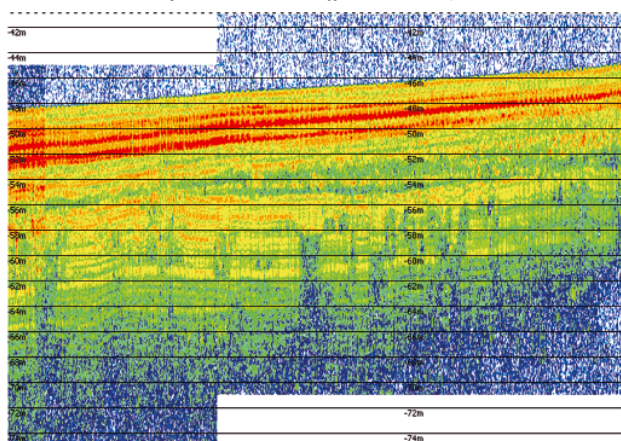


Fig. 23. Envelope from 480 samples - 6 kHz 2p (from SES data - full envelope view)

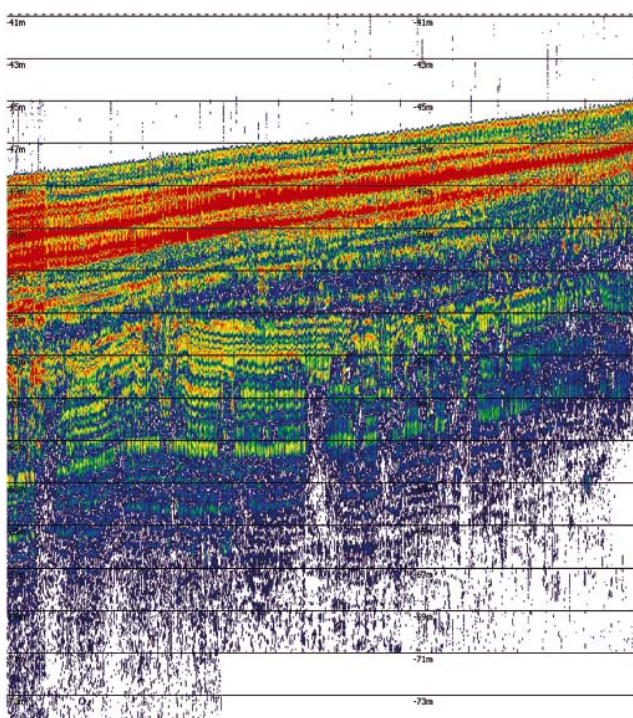


Fig. 24. Envelope from 5120 samples - 6 kHz 2p (RAW data - envelope with 15 colours)

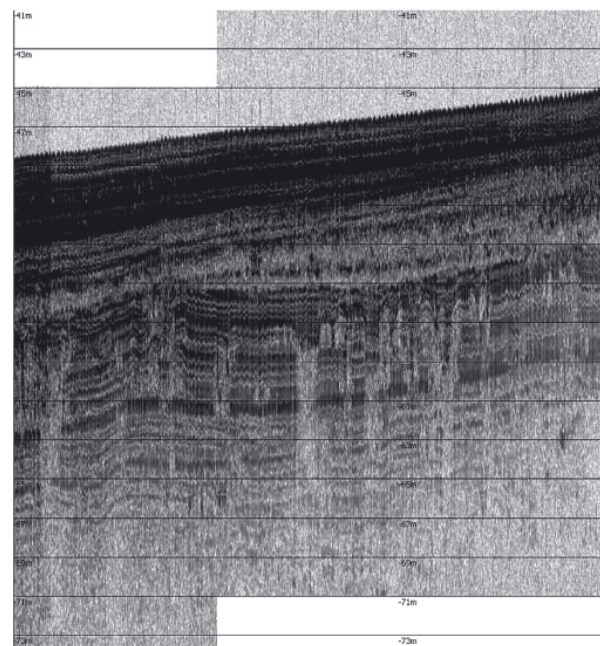


Fig. 25. Envelope from 5120 samples - 6 kHz 2p (RAW data - envelope with 30 gray-scale colours)

The software dedicated to the sub-bottom profiler offers various configurations. Most important is to set up frequencies of differential sounding pulses, which can be chosen in the range of 4 kHz \div 15 kHz. The primary frequencies are set up near 100 kHz, depending on a differential sounding pulse. During work with geological aspects where it is important to investigate structure of sediments, the lowest frequency is required, that can be checked on the below presented echograms (where high differences were used for visualization of the same sounded bottom). When a new research area is examined it is useful to apply multi-frequency option. It allows to sound with the use of three different sounding pulses one by one. An example of such research is illustrated in Fig. 12, 13 and 14. The results are elaborated in the logarithmic scale of colours and the TVG software set to 0.6 dB/m.

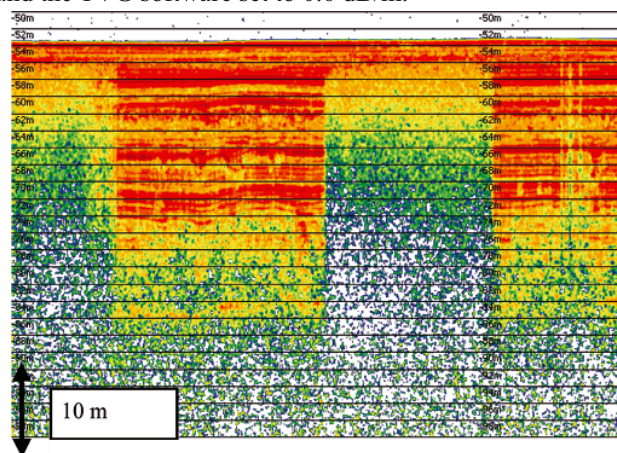


Fig. 26. 5 kHz frequency of echosounder sounding pulse

By using data processing algorithms and Matlab software to compare and analyze data which contain information about buried objects, is possible. There are many possibilities to illustrate processed data in 2D, 3D, horizontal and vertical view. Having geographical position linked with sounding data it is possible to visualize different models of searched objects. Below an example of visualization and measurement of three buried targets is shown. Additionally, application of scale of colours, where user can define step, threshold, maximum and minimum values, provides a wide range of visualization capabilities.

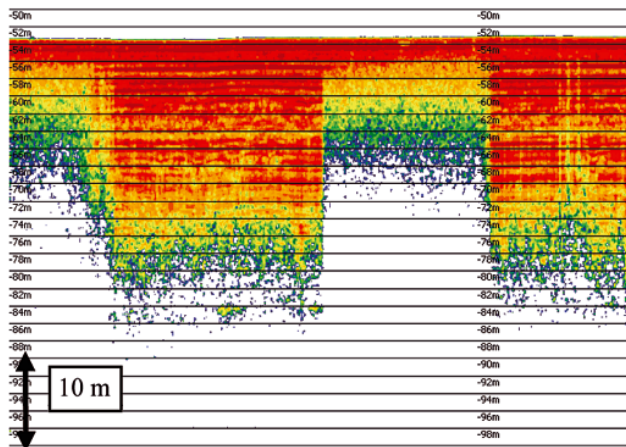


Fig. 27. 8 kHz Frequency of echosounder sounding pulse

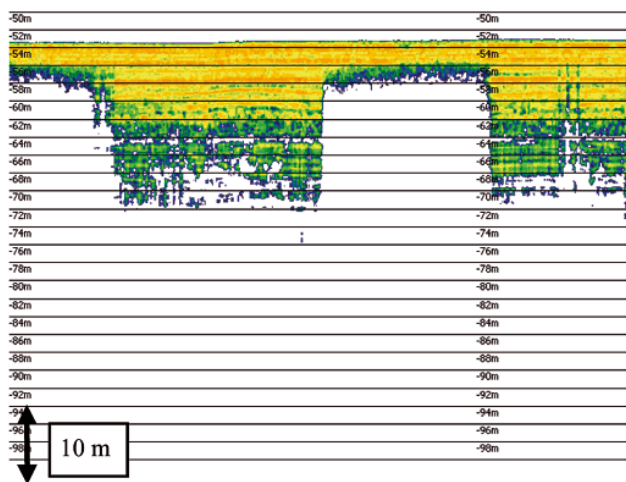


Fig. 28. 12 kHz Frequency of echosounder sounding pulse

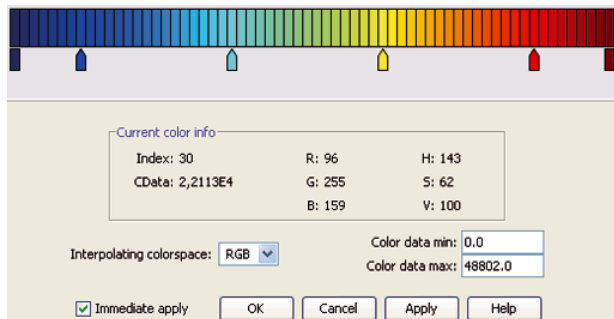


Fig. 29. Scale of colours of echosounder sounding pulse



Fig. 30. Set of default colours used in the Matlab

SUMMARY

During the post-processing of data different algorithms should be applied depending on a type of research (examination of sediment layers or searching for buried objects). The data

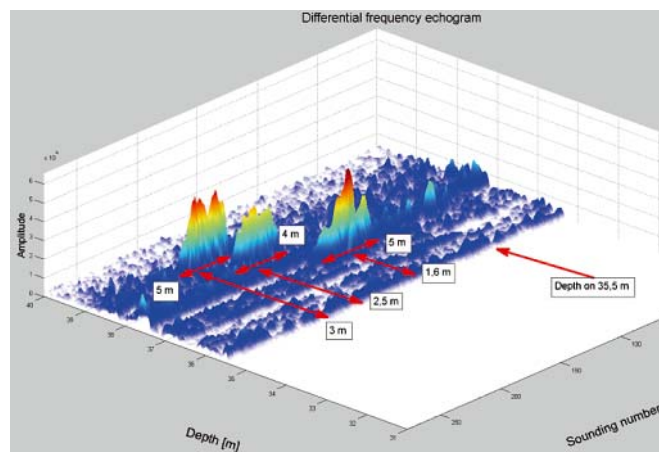


Fig. 31. Three buried objects - imaged by using the Matlab

analyzing should additionally improve operator's knowledge useful for new trials, as to the describing of proper configuration of a software intended for cooperating with parametric echosounder, frequency and length (number of cycles) of pulses to be set depending on currently received results. Methods of data processing in real time and raw data post-processing provide many possibilities. It is necessary to have at one's disposal an algorithm which describes a proper way of effective work with the data, even during trials.

Acknowledgments

The research presented in this paper has been partly conducted in the framework of the projects No. O ROB 0007 01.

BIBLIOGRAPHY

1. G. Grelowska, E. Kozaczka: *Nonlinear properties of water* (in Polish), AMW, Gdynia, 1996
2. K. Naugolnykh, L. Ostrovsky: *Nonlinear Wave Processes in Acoustics*, Cambridge University, Cambridge, 1998
3. P. Blondel, A. Caiti: *Buried Waste in the Seabed Acoustic Imaging and Bio-Toxicity*, University of Bath, UK, 2007
4. Innomar Technologie GmbH: *SES-2000 Narrow-beam parametric sub-bottom profiler*, Innomar Technologie, Rostock, 2008
5. E. Kozaczka, G. Grelowska, S. Kozaczka: *Images of the seabed of the Gulf of Gdansk obtain by means of the parametric sonar*, Acta Physica Polonica A, Vol. 118, No 1, 91-94, 2010.
6. G. Grelowska, E. Kozaczka: *Sounding of layered marine bottom - modelling investigations*, Acta Physica Polonica A, Vol. 118, No 1, 66-70, 2010.
7. G. Grelowska, E. Kozaczka, S. Kozaczka, W. Szymczak: *Sea bottom structure investigation by means of acoustic methods*, Polish Journal of Environmental Studies, Vol. 19, No 4A, 35-38, 2010.
8. G. Grelowska, E. Kozaczka, S. Kozaczka, W. Szymczak: *Post processing and selecting data obtain with parametric sub-bottom profiler SES-2000 Standard during sounding the Gulf of Gdansk*, 11th European Conference on Underwater Acoustics 2012 - ECUA 2012, Volume 34 Pt. 3, p. 1446-1453, Edinburgh United Kingdom, 2-6 July 2012.
9. Results from shallow gas area outside Namibia: <http://www.km.kongsberg.com/ks/web/nokbg0240.nsf/AllWeb/56E492C388344357C1256F800045E141?OpenDocument>

CONTACT WITH THE AUTHORS

Eugeniusz Kozaczka, Prof., kozaczka@pg.gda.pl
 Grażyna Grelowska, Prof., ggrel@wp.pl
 Sławomir Kozaczka, M.Sc., milites@vp.pl
 Wojciech Szymczak, M.Sc., ws2@o2.pl
 Polish Naval Academy
 Śmidowicza 69
 81-103 Gdynia POLAND

Research on hydrodynamic properties of annular cavitator with water injection

Zhenyu Jiang, Associate Research Fellow,
Min Xiang, Lecturer,
Mingdong Lin, Ph.D.,
Weihua Zhang, Professor,
Shuai Zhang, M.Sc.,
National University of Defense Technology Changsha, P.R. CHINA

ABSTRACT

Annular cavitator with water injection is one of the key parts of the long-range supercavitating vehicle powered by water ramjet. In this paper, hydrodynamic properties of annular cavitator are studied numerically. The standard $k \sim \varepsilon$ turbulence model is coupled with the Reynolds Averaged Navier-Stokes (RANS) equations to model the natural supercavitation process. The multiphase flow is considered as a mixture of varying density and modeled by the mass exchange equations. To fully understand this process, numerical simulations were performed for different annular cavitators. Computational Fluid Dynamics (CFD) results, including the pressure distribution and forces acting on the cavitator surface, mass flow and pressure loss of water injection, various supercavity sizes, were obtained and analyzed. The pressure distribution on the cavitator surface was significantly changed which resulted in 4 ~ 6% increase of the total drag of the vehicle. The results show that the mass flow and velocity of the injection water is mainly dependent on the tube size, while the total pressure loss of the water injection is mostly related to the outlet pressure. Supercavity generated by annular cavitator is smaller than that of the discal one. Based on the correlation analysis of the supercavity size and other factors, it could be concluded that the contraction of the cavity size is mainly caused by the diffluent mass flow of the water injection.

Key words: supercavitation; computation fluid dynamics (CFD); annular cavitator; water injection

INTRODUCTION

Cavitation, which happens when a vehicle travels fast enough underwater, brings extra noise, surface erosion, and other problems. To avoid cavitation, traditional underwater vehicles could hardly travel faster than 70 kn. Supercavitation, in contrast, which could reduce the drag by more than 90%, has been proved to be a revolutionary way to achieve ultrahigh speed underwater [1]. Due to the successful applications of the Russian torpedo 'Shkval' and the US supercavitating projectile 'RAMICS', supercavitating vehicles have received increasing research interests in recent years [2-4].

With stunt shape and sharp edge, cavitator generates and sustains a supercavity to envelope the whole vehicle during high speed motion. Both theoretical and numerical studies have been carried out to enhance the understanding of various properties of cavitators and the supercavitating flow.

By applying the theorem of the independence of cavity section expansion proposed by Logvinovich [5, 6], pioneering studies have been conducted by Russian and Ukrainian researchers such that they have been widely used for the predicting of the cavity shape [7, 8]. L.Sedov studied the jet cavitator which ejects water stream into the flow. In this case the body will suffer only half drag when the cavitation number is near zero [9]. Using computationally supercavitating flow,

Owis *et al* considered the compressibility of supercavitating flow and improved a numerical method for both single and multi-phase flows [10-12]. Drag force for NACA66 foil and a flat plate was investigated by Seif and the CFD model was successfully tested [13]. Carried out by Kuklinski, experimental studies of hydrodynamic properties of different cavitators provided test data for the dynamic modeling of cavitators [14]. Studied by Ahn, Shafaghat, and Lin, optimal designs of conical or spherical cavitators proved that a proper shape could improve performance of the cavitator [15-17]. To achieve long-range supercavitating motion, the water ramjet is the best propulsion device for supercavitating vehicles. In this case, water injection from the cavitator is required, which makes conducting research on annular cavitators necessary.

In this paper hydrodynamic properties of the annular cavitator are studied in detail. Based on the Reynolds Averaged Navier-Stokes (RANS) equations which is coupled with the standard $k \sim \varepsilon$ turbulence model, the supercavitating flow is considered as a varying-density single-phase flow. The water injection processes with assumed different tube size and outlet pressures are studied. Based on the simulation of different water injection conditions, total drag of the annular cavitators are obtained. The mass flow and the pressure loss of the water injection are studied. Related factors which affect the supercavity size are investigated by using the correlation

analysis. Experimental results shown in this paper can be utilized for the designing of supercavitating vehicles propelled by water ramjet.

MODELING AND COMPUTATIONAL APPROACHES

Governing equations

Based on three dimensional Reynolds Averaged Navier-Stokes equations, the supercavitating flow consisted of water and vapour is considered as a single phase of the same pressure and velocity field and is modelled by the mass exchange equations. The steady supercavitation flow is considered isothermal, therefore the energy equation is not considered.

The continuity and momentum equations of the mixture phase are given below:

$$\frac{\partial(\rho_m)}{\partial t} + \nabla g(\rho_m \mathbf{u}) = 0 \quad (1)$$

$$\begin{aligned} \frac{\partial(\rho_m \mathbf{u})}{\partial t} + \nabla g(\rho_m \mathbf{u} \times \mathbf{u}^T) = \\ = -\nabla p + \nabla g[\mu_m(\nabla \mathbf{u} + \nabla \mathbf{u}^T)] + \rho_m \mathbf{g} \end{aligned} \quad (2)$$

The continuity equation of the vapour phase is shown as follows:

$$\frac{\partial(\rho_v \alpha_v)}{\partial t} + \nabla g(\rho_v \alpha_v \mathbf{u}) = \dot{m}^+ - \dot{m}^- \quad (3)$$

where \mathbf{u} is the velocity vector of the mixture, \mathbf{g} is the gravity vector, ρ , α and μ represent density, volume fraction, and viscosity, respectively, subscript l, v and m represent liquid phase, vapour phase, and mixture phase separately, \dot{m}^+ , \dot{m}^- are the source terms caused by vaporization and condensation.

The mixture property, ϕ_m , can be obtained by:

$$\phi_m = \phi_l \alpha_l + \phi_v \alpha_v \quad (4)$$

where ϕ stands for density, viscosity, and so on.

At last, volume fraction-conservation equation is as follows:

$$\alpha_l + \alpha_v = 1 \quad (5)$$

Natural cavitation model

The Rayleigh-Plesset equation which provides the basis for the rate equation controlling vaporization and condensation, is given as follows:

$$R_B \frac{d^2 R_B}{dt^2} + \frac{3}{2} \left(\frac{dR_B}{dt} \right)^2 = \frac{p_v - p}{\rho_l} - \frac{2\sigma}{\rho_v R_B} \quad (6)$$

where:

- R_B – represents the gas bubble radius,
- p_v – saturated vapour pressure,
- p – the pressure in the liquid surrounding the bubble,
- ρ_l – the liquid density,
- σ – the coefficient of surface tension between the liquid and vapour.

By disregarding the second-order terms and surface tension, the rate of vaporization and condensation are shown below:

$$\dot{m}^+ = C_e \frac{3\alpha_{nuc} \alpha_l \rho_v}{R_B} \sqrt{\frac{2}{3} \frac{p_v - p}{\rho_l}}, \quad p < p_v \quad (7)$$

$$\dot{m}^- = C_c \frac{3\alpha_v \rho_v}{R_B} \sqrt{\frac{2}{3} \frac{p - p_v}{\rho_l}}, \quad p > p_v \quad (8)$$

where:

- α_{nuc} – the volume fraction of the nucleation sites,
- C_e, C_c – empirical factors which may be different for the rate of vaporization and condensation; usually: $C_e = 50$, $C_c = 0.01$.

Turbulence model

The standard $k \sim \epsilon$ turbulence model is used in this study. The turbulence kinetic energy, k , and its dissipation rate, ϵ , are obtained from the following transport equations:

$$\frac{\partial}{\partial t} (\rho_m k) + \nabla g(\rho_m v k) = \nabla g \left[\left(\mu + \frac{\mu_t}{\sigma_k} \right) \nabla k \right] + G_k - \rho_m \epsilon \quad (9)$$

$$\begin{aligned} \frac{\partial}{\partial t} (\rho_m k) + \nabla g(\rho_m v \epsilon) = \\ = \nabla g \left[\left(\mu + \frac{\mu_t}{\sigma_\epsilon} \right) \nabla \epsilon \right] + \frac{\epsilon}{k} (C_{1\epsilon} G_k - C_{2\epsilon} \rho_m \epsilon) \end{aligned} \quad (10)$$

where:

- $\mu_t = \rho C_\mu k^2 / \epsilon$ – the viscosity of turbulence,
- $G_k = 2\mu_t \nabla v$ – the kinetic energy of turbulence,
- $\sigma_k, \sigma_\epsilon$ – the Prandtl number of k and ϵ , respectively. Again, $\sigma_{1\epsilon} = 1.44$, $\sigma_{2\epsilon} = 1.92$, $C_\mu = 0.09$, $\sigma_k = 1.0$, $\sigma_\epsilon = 1.3$.

Settings for simulation

The vehicle model is illustrated in Fig. 1. The length of the vehicle is 2 m, while the diameter of the body is 0.2 m. The set diameter of the cavitator is 10 cm. To avoid the unstable region of the injection hole on the cavitator, the length of the tube is set to 1 m. The bottom of the tube is assumed to be the outlet surface. The incoming flow velocity is 100 m/s and the environmental pressure is 0.2 MPa.

The generic CFX code was used to investigate the liquid flow around the supercavity. Numerical calculations were performed over a 180° radial sector of the field with symmetrical boundary conditions. The computational mesh corresponding to the schematic geometry is shown in Fig. 2. In summary, over 500,000 hexahedral elements were formed and non-uniformly distributed within the entire computational domain. The transport equations were discretized by the finite volume approach. The convection terms were approximated by a high-order resolution scheme while the diffusion terms - by the second-order central difference scheme. Convergence was achieved within 2500 iterations when the RMS (root mean square) residual dropped below 10^{-6} .



Fig. 1. Schematic geometry of vehicle model

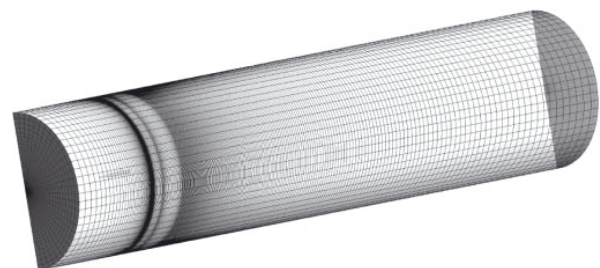


Fig. 2. Computational mesh of the annular cavitator

To consider the effect of the outflow pressure and tube diameter, different simulation cases were performed accordingly (Tab. 1). The same condition is assumed for case 3 and 7. The disk cavitator with the same diameter is selected to be the case 0 for comparison purpose.

Tab. 1. Values of tube diameter and outlet pressure for different CFD cases

Case	P_{out} [MPa]	D_{tube} [cm]	Case	P_{out} [MPa]	D_{tube} [cm]
1	4.0	2.0	5	3.0	4.0
2	4.0	3.0	6	3.5	4.0
3	4.0	4.0	7	4.0	4.0
4	4.0	5.0	8	4.5	4.0

RESULTS AND DISCUSSION

Pressure distributions and drag forces

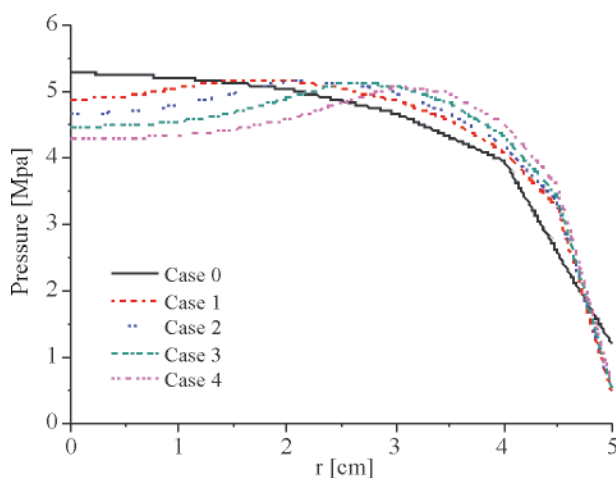


Fig. 3. Pressure distributions on the cavitator surface for case 1 through 4

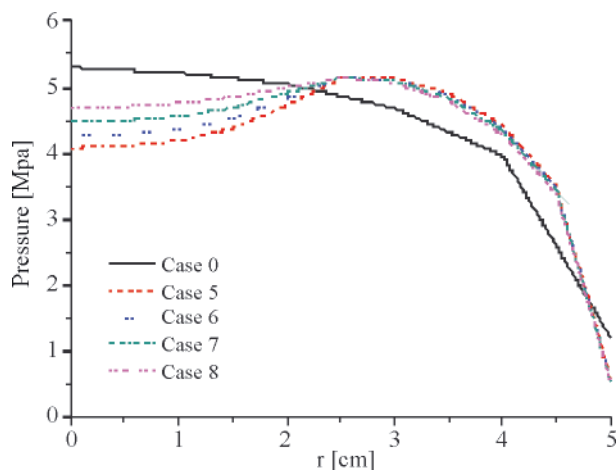


Fig. 4. Pressure distributions on the cavitator surface for case 5 through 8

Based on the assumption that the static pressure of the bottom of the tube to be 4 MPa, the pressure distributions on annular cavitators (case 1 through 4), are presented in Fig. 3. In the radial direction, the pressure increases on the tube section and then decreases on the cavitator. As the diameter of the injection tube increases, the stagnation ring of the cavitator surface moves outward along the radial direction. The pressure in the centre is larger than the outlet pressure, which means that certain pressure loss happened during the water injection. As shown in Fig. 4, although the outlet pressures are different, the position of the maximum pressure is almost the same. It means

that position of stagnation ring is hardly related to the outlet pressure, which only depends on the size of the injection tube. Furthermore, the pressure distribution on the ring part of the cavitator surface is independent on the pressure distribution in the tube section.

Tab. 2. Forces acting on region of cavitator with different tube diameter

Case	F_{cav} [N]	F_{tube} [N]	F_{total} [N]	Increment [%]
0	30608	0	30608	0
1	30260	1565.4	31825.4	3.98
2	28720	3408	32128	4.97
3	26480	5870	32350	5.69
4	23480	8886	32366	5.74
5	26740	5488	32228	5.29
6	26640	5676	32316	5.58
7	26480	5870	32350	5.69
8	26260	6076	32336	5.65

By integrating the pressure in the radial direction the forces acting on the cavitator surface are obtained (Tab. 2). As the tube diameter increases (case 1 through 4), the cavitator force decreases significantly due to contraction of the cavitator surface. Meanwhile, the forces acting on the tube section increase faster. As a result, the total forces acting on the vehicle increase by about 4 ~ 6%. Furthermore, the larger the tube diameter the greater increase of the total force. Total forces in the case 5 through 8 are still larger than the ones in the case 0, but they change slightly as the outlet pressure of the tube varies. Such variety means that the contribution of pressure in the central tube section results in a relatively small contribution to the total force. Outlet pressure of the tube shows a lower significance to the total force acting onto the supercavitating body.

Mass flow and pressure loss

The water injection mass flows and velocities versus tube diameters are illustrated in Fig. 5. The results show that the mass flow is almost proportional to the tube section area and that the velocity of the injecting flow is less sensitive to the tube size. As shown in Fig. 6, both the mass flow and water injection velocity decrease as the outlet pressure of the tube increases. Compared with the results in Fig. 5, the mass flow is rather more dependent on the tube size than on the outlet pressure.

Due to the sudden contraction of the tube section and the friction on the tube wall, pressure loss is unavoidable during water injection. Since the water is incompressible and the tube diameter is constant along the pipe, the total pressure loss is equal to the static pressure decrease of the water. The pipe static pressure distribution is illustrated in Fig. 7. In all the cases significant pressure drop and turbulence can be observed near the inlet to the pipe. It means that the pressure distribution near the inlet is highly unstable. In case 1, for the smallest tube diameter, pressure loss along the pipe is the fastest in comparison with the ones for other tube diameters, while case 4 shows the opposite result. Total pressure loss is larger when the injection tube diameter is relatively smaller. In case 1, the total loss is about 1 MPa. Regarding the cases 5 through 8, it can be concluded that the pressure loss is proportional to the pressure difference between the total pressure of flow field and the outlet pressure. The smaller outlet pressure the larger pressure loss. In case 5, the total pressure loss achieves 1.38 MPa while in case 8 the loss amounts only to 0.34 MPa. In summary, by applying larger tube size and higher outlet pressure, the total pressure loss could be reduced dramatically.

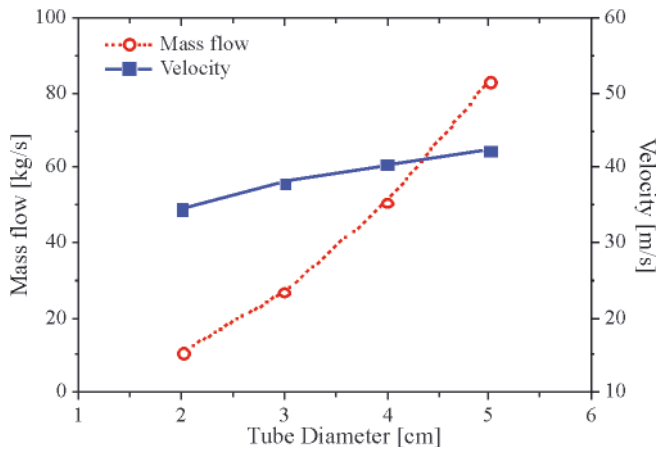


Fig. 5. Mass flow and velocity vs. tube diameter

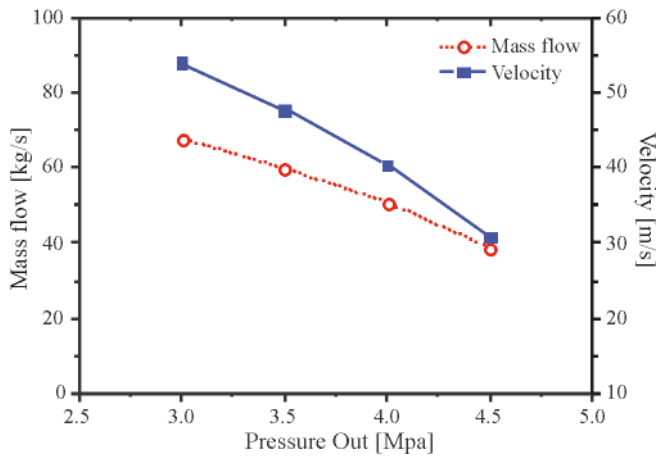


Fig. 6. Mass flow and velocity vs. outlet pressure

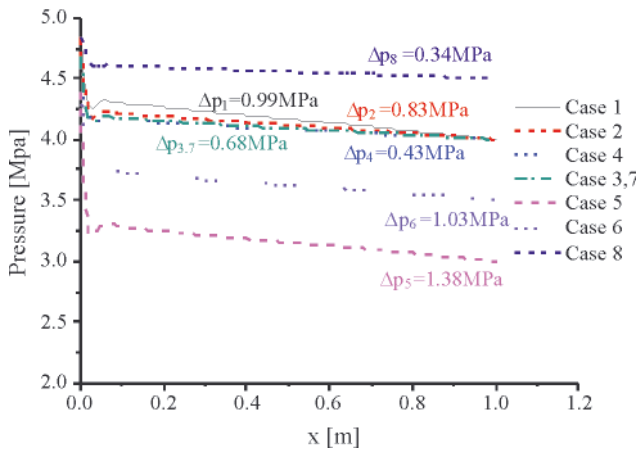


Fig. 7. Pressure loss of the water injection versus tube length

Dimension of supercavities in different cases

According to the CFD algorithm the multi-phase supercavitating flow is treated as a mixture of varying density. Thus the supercavity boundary is considered as the position where the density of flow is $\rho_m = 0.5$. The supercavities generated by different cavitators are presented in Fig. 8. Clear reentrant jet flow can be observed in the tail of supercavities. Despite the total force increase on cavitator surface, supercavities generated by the annular cavitator are smaller than those generated by the disc in case 0. We can conclude that the cavity size is dependent not only on the drag force. When passing from case 1 to case 4, as the tube diameter increases, the cavity size becomes smaller. However, when passing from case 5 to case 8, the cavity size grows due to the outlet pressure increase.

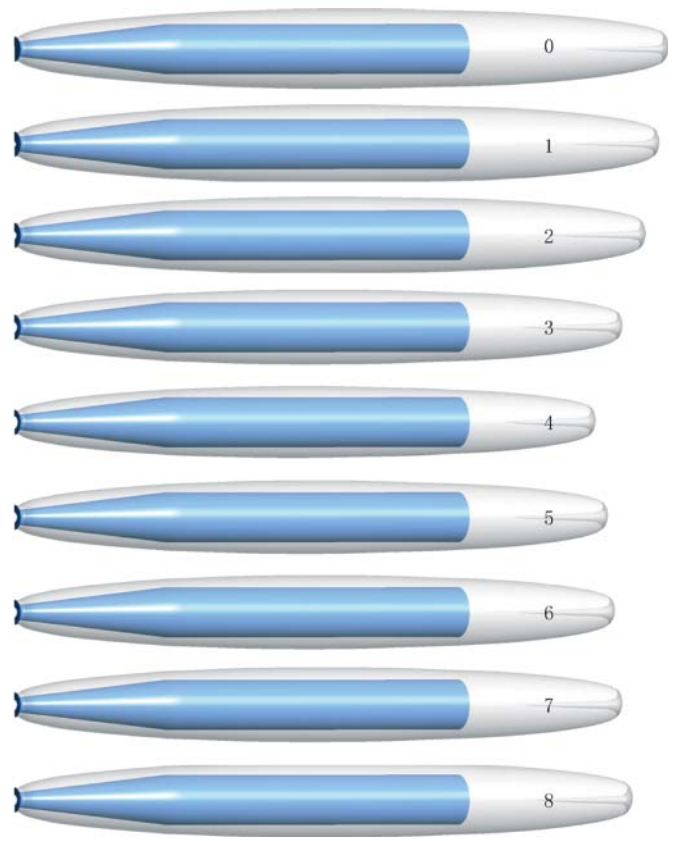


Fig. 8. Supercavities generated by different cavitators

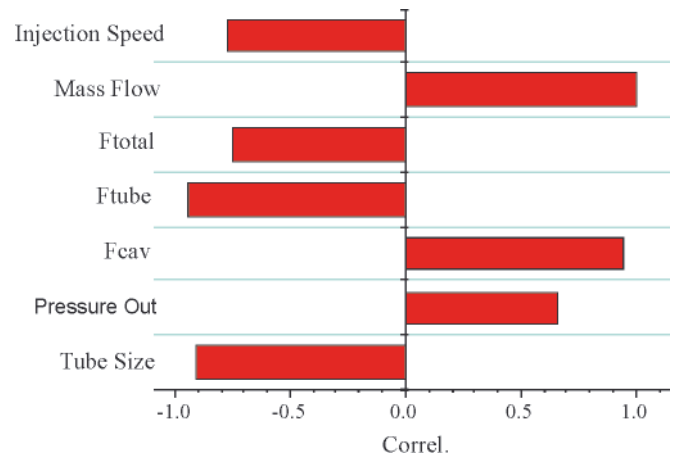


Fig. 9. Coefficients of correlation between cavity size and other possible factors

To underlie the reason of cavity contraction, a correlation analysis was performed. The correlation coefficients between cavity size and other possible factors are presented in Fig. 9. The result shows that the cavity size is positively correlated with the cavitator force and mass flow through the tube. The force acting on tube section and the tube size is correlated negatively. The correlation coefficient between the cavity size and water injection mass flow is equal to 0.999, which indicates that the supercavity contraction is caused by the water injection diffidence in the flow field.

CONCLUSIONS

In this paper a numerical research on the natural supercavitation problem is performed with the use of a high-speed annular cavitator. To model the supercavitating flow, the liquid and vapour phase of the flow field is considered as

a mixture of varying density. The RANS equations coupled with the standard $k \sim \epsilon$ turbulence model are applied to CFD simulation. Properties of the flow field are obtained for given different injection tube size and outlet pressure conditions.

Pressure distributions, forces acting on the cavitator surface and injection water flow properties are analyzed. The obtained results show that the stagnation region on annular cavitator moves outward along the radial direction, which results in about 4 ~ 6% increase of the total drag. The tube diameter affects the drag increase more than the pipe outlet pressure. The injection water mass flow mainly depends on the tube diameter. Both the mass flow and injection velocity increase with the tube diameter and decrease with the outlet pressure. The design of the water injection system will affect not only the amount of injected water but also the total pressure loss. The pressure loss is inversely proportional to the tube diameter.

The annular cavitators form smaller supercavities than the discal one of the same diameter. According to the correlation analysis it is caused by diffuence of the water injection.

To better understand the performance of a water-ramjet-propelled supercavitating vehicle, it is essential to take it into account the drag increase and the cavity size contraction caused by the annular cavitator. In such case, motion dynamics of a supercavitating vehicle may need some modification. Furthermore, in terms of mass flow and pressure loss, the obtained results would be very helpful in optimal designing the water injection system.

BIBLIOGRAPHY

1. Savchenko Y.N.: *Supercavitation – problems and perspectives*. In: CAV2001.; 2002.
2. Ashley S.: *Warp Drive Underwater*. Scientific American Special Online Issue, 2002.
3. Stinebring D.R., Cook R.B., Dzielski J.E., Kunz R.F.: *High-Speed Supercavitating Vehicles*. In: AIAA Guidance, Navigation, and Control Conference and Exhibit. Keystone, Colorado, USA; 2006.
4. Kam W.N.: *Overview of the ONR Supercavitating High-Speed Bodies Program*. In: AIAA Guidance, Navigation, and Control Conference and Exhibit. Keystone, Colorado, USA; 2006.
5. Garabedian P.R.: *The principle of independence of the cavity section expansion(Logvinovich's principle) as the basis for investigation on cavitation flows*. In: RTO/NATO Lecture Series 005 Supercavitating Flows. France; 2002.
6. Logvinovich G.V.: *Hydrodynamics of flows with free boundaries*: Halsted Press; 1973.
7. Savchenko Y.N.: *Experimental investigation of supercavitating motion of bodies*. In: RTO/NATO Lecture Series 005 Supercavitating Flows. France; 2002.
8. Semenenko V.N.: *Artificial supercavitation. physics and calculation*. In: RTO/NATO Lecture Series 005 Supercavitating Flows. France; 2002.
9. Sedov L.I.: *Mechanics of Continuum*. Moscow: Nauka Publishing House; 1976.
10. Owis F.M., Nayfeh A.H.: *A compressible multi-phase flow solver for the computation of the supercavitation over high-speed torpedo*. In: 40th AIAA Aerospace Sciences Meeting & Exhibit. Reno, NV, US; 2002.
11. Owis F.M., Nayfeh A.H.: *Numerical simulation of super- and partially-cavitating flows over an axisymmetric projectile*. In: 39th AIAA Aerospace Sciences Meeting & Exhibit. Reno, NV, US; 2001.
12. Kinzel M.P., Lindau J.W., Kunz R.F.: *Free-surface proximity effects in developed and super-cavitation*. In: DoD HPCMP Users Group Conference, 2008.
13. Seif M.S., Asnaghi A., Jahanbakhsh E.: *Drag force on a flat plate in cavitating flows*. Polish Maritime Research, 2009.
14. Kuklinski R., Fredette A., Henoch C., Castano J.: *Experimental Studies in the Control of Cavitating Bodies*. In: Guidance, Navigation, and Control Conference and Exhibit. Keystone, Colorado, USA: AIAA; 2006.
15. Choi J.H., Penmetsa R.C., Grandhi R.V.: *Shape Optimization of the Cavitator for a Supercavitating Torpedo*. Struct Multidisc Optim, 2005.
16. Shafaghat R., Hosseinalipour S.M.: *Shape Optimization of Two-Dimensional Cavitators in Supercavitating Flows, Using NSGA II Algorithm*. Appl. Ocean Res., 2008.
17. Lin M., Hu F., Zhang W.: *Optimal Design of Conical Cavitator of Supercavitating Vehicles*. Journal of National University of Defense Technology, 2010.
18. Savchenko Y.N.: *Supercavitating object propulsion*. In: RTO/NATO Lecture Series 005 Supercavitating Flows. France; 2002.
19. Miller T.F., Herr J.D.: *Green Rocket Propulsion by Reaction of Al and Mg Powders and Water*. In: 40th AIAA/ASME/SAE/ASEE Joint Propulsion Conference and Exhibit. Fort Lauderdale, Florida; 2004.

CONTACT WITH THE AUTHORS

Zhenyu Jiang, Associate Research Fellow,
Min Xiang, Lecturer,
Mingdong Lin^{*)}, Ph.D.,
Weihua Zhang, Professor,
Shuai Zhang, M.Sc.,

Team 6, College of Aerospace Science and Technology
National University of Defense Technology
Changsha, P.R. China, 410073

^{*)} Corresponding author. e-mail: lmd231@yahoo.com.cn

A study on performance of planing-wing hybrid craft

Hamid Zeraatgar, Assistant Professor
Ali Bakhshandeh Rostami, MSc. in Naval Architecture
Abolfazl Nazari, MSc. in Naval Architecture
Amirkabir University of Technology, Tehran, Iran

ABSTRACT

A hybrid craft is defined as a combination of different lifting surfaces. The lift force can be of aerodynamic or hydrodynamic character. This research deals with the conditions of using planing mono-hulls equipped with a couple of wings, called planing-wing hybrid craft. A parametric study is conducted by using Vortex Lattice Method to determine feasibility of using an aerodynamic wing mounted to planing craft. It has been determined that the wing area should be more than twice as much as the wetted surface of the craft, to get an effective wing for planing craft. Furthermore, the wing should be so designed as to obtain its high aspect ratio. Maximum lift force contribution resulting from different wing configurations considered in this study is less than 35 percent of the total hydrodynamic lift force at an arbitrary condition. On this basis it may be concluded that the wing may be effectively used only in special conditions, hence this is not recommended for general application.

Key words: hydrodynamics; ground effect; wing; planing; aerodynamics; VLM

INTRODUCTION

People are always looking for increasing productivity and improving performance of transportation. Serious limitations on increasing speed and gradual development of existing marine crafts led to a new generation of craft, known as hybrid crafts. The objective of this paper is to examine performance of one kind of such crafts, namely the planing-wing hybrid craft in which hydrodynamic and aerodynamic lift forces mainly supports the craft's weight at service speed.

Due to higher density and viscosity of water than air, large speed of a body in water causes its frictional and wave-making resistance greater than in case of moving in air. One solution to reduce this type of resistance is reducing the wetted surface of craft. Although lifting surfaces produce a higher lift force and reduce craft's draught but they may cause also some detrimental effects such as cavitation of hydrofoils, degradation of craft's performance in waves, reduction of its stability etc. The restrictions may put obstacles on increasing the craft speed.

WIG crafts (Wing- In- Ground- effect crafts) are the crafts which make use of aerodynamic forces at service speed. Undoubtedly, the use of aerodynamic forces can be considered as a worthy contribution to reaching higher speeds in marine transportation. The reason is that a significant lift force can act onto a craft moving near water surface, by which WIG crafts are able to achieve very high speeds. However, the WIG crafts are facing some problems such as structural and dynamic complexities, construction cost and safety [1] as well as low efficiency of air propulsion system. Another disadvantage of WIG craft is inability to perform even very simple manoeuvres in planing mode.

Some types of high speed crafts, so called the hybrid crafts, may use hydrodynamic lift of planing hull, hydrodynamic lift of hydrofoils and aerodynamic lift of aerofoils. It means that in the hybrid craft the capability of various lifting surfaces are used to gain more efficiency and performance quality.

This study is intended for examining usage of aerodynamic forces including ground effect and hydrodynamic forces simultaneously to increase the efficiency and performance quality. A high lift-to-drag ratio of the aerodynamic foils can make a fundamental change in power consumption of propulsion system and allow reaching higher speeds.

The main question is what should be the wing dimensions so that a significant part of the craft weight to be supported by air lift? Is there any advantage from using air lift instead of hydrodynamic lift?

In this context a literature review shows that there are some products which use a combination of different kinds of lift force, and that none of them have been theoretically discussed. In some cases only patent registration was done. In 1976, Shipps [2] introduced a type of hybrid craft, known as "tunnel hull", used as a race boat. This design in which two planing hulls were applied at the end of a ram wing and considered as end plates, could promptly demonstrate its better performance than planing mono-hulls; and thus a major step was made in designing the race crafts. One of the benefits of this design was the use of aerodynamic lift force for bearing craft weight. In 1978, Ward [3] presented some results of testing the vessel KUDU II (a modified form of the vessel KUDU I designed in 1976), which could sail at speed up to 78 knot. In 1996, Privalov and Kirillovikh [4] designed a hybrid craft called TAP (Transport Amphibious Platform) which consisted of

two catamaran-like bodies, an aircraft fuselage, aerodynamic wing and tail. Its motion in close proximity to water surface or ground resulted in forming an air cushion between the hulls. Among other merits it allows to develop a very high speed (250 km/h). In 1997, an ekranocat vessel was presented by Doctor [5] during WIG's97 Conference, in which an aerodynamic superstructure was arranged on catamaran body, resulting in drag reduction by 50 percent, according to the calculations and measurements.

Furthermore, several patents for the use of aerodynamic elements in high speed crafts have been registered in the US [6], and in all of them utilization of ground effect has been indicated as the reason for using the wings. In 2005, a research program was started at Cranfield University, UK, whose goal was the use of aerodynamic forces for high speed craft [7].

Balancing the different forces which act on hybrid crafts has been a target of some research projects in recent years. Collu *et al.* [8] and [9] has considered longitudinal stability of hybrid crafts in both static and dynamic states.

The motivation for this study is based on the attractive parameters of a boat called Seaphantom, claimed by its manufacturer [10]. The Seaphantom is an innovative hybrid craft whose original idea formed in 2000 was registered as a US patent [6]. In 2004 was built its prototype on which a set of tests and trials was performed. The second unit was built in 2007 and tested in January 2008. The craft's designer and manufacturer tried to use different lifting elements to achieve the maximum possible speed by minimum power. According to the manufacturer's claim, the 300-hp Seaphantom is able to move with the speed of 70 knot which is considered an excellent feature of the boat. Its wings have a low breadth compared to hull breadth, which is other key point to be mentioned about the craft. Tab. 1 shows the Seaphantom specification.

Tab. 1. Seaphantom specification [10]

Item	Quantity	Unit
Length overall	9.27	m
Breadth overall	3.818	m
Speed(max)	70	kn
Power	224	kW
Engine type	Mercury race	
Engine configuration	Outboard	
Engine speed	9000	rpm

The purpose of this study is to examine hydrodynamic advantages of a hybrid craft which uses both the hydrodynamic lift force of a planing body and the aerodynamic lift force resulting from air wings which are placed close to the water level to benefit from aerodynamic lift due to ground effect.

To achieve the above mentioned objective, a model planing-wing hybrid craft on which different air wings are assembled, is selected. A schematic image of the hybrid craft is shown in Fig. 1. The lift and drag forces produced by main body, wings and ground effect are calculated with the use of Vortex-lattice method. Comparison between the lift-to-drag ratio of wings and planing body is done. The total lift force of the aerodynamic wings with respect to craft weight is determined. Finally, the idea of using the planing-wing hybrid craft is discussed and the conditions in which aerodynamic

lift force of wing is beneficial for planing mono-hull crafts are formulated.

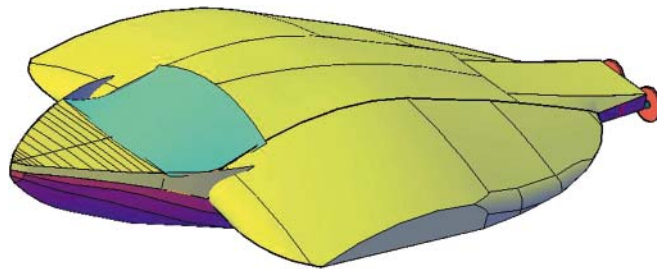


Fig. 1. A schematic image of the model planing-wing hybrid craft

THE PROBLEM STATEMENT

This research, based on considering the issue of hybrid craft as a combination of aerodynamic and hydrodynamic forces and taking into account the Seaphantom as a model, is aimed at examination of usefulness of this kind of craft. The problem is defined as follows: a planing craft equipped with two wings is designed as a hybrid craft moving in water with the speed in the range of planing mode. The air is blown under the wings due to craft's speed thus the aerodynamic lift is generated. A small gap between wings and water surface results a higher aerodynamic lift due to ground effect. Some further assumptions are as follows:

- The craft has to remain in contact with water.
- Size and geometry of the main hull follow the principles of planing body.
- Dimensions and size of aerodynamic wings are in consistency with general arrangement of a planing craft
- Trim angle of planing body and angle of attack of wing are selected rationally.
- It should be noted that around wings water spray occurs that is not considered here.
- In this study craft steady motion at constant speed in calm water is considered.
- The Vortex-lattice method is used as a tool for both hydrodynamic and aerodynamic force calculations.
- Friction forces are calculated by a regression formula and added to Vortex-lattice method calculation results.
- Gap between water surface and the lowest point of wing is related to wing chord at root section, and marked H/C, where H is gap height and C is chord length of wing root section.

THE GOVERNING EQUATION AND COMPUTER SOFTWARE

Governing equation

The Vortex-lattice methods are based on solutions of Laplace's equation. They were first formulated in the late 30s and first called "Vortex Lattice" by Faulkner in 1943. The velocity potential should satisfy Laplace's equation as follows:

$$\nabla^2\Phi = 0 \quad (1)$$

where: Φ is total velocity potential and, for a steady flow, written as follows:

$$\Phi = Ux + \phi \quad (2)$$

where: U is the uniform stream velocity and ϕ is the perturbation potential. Both Φ and ϕ satisfy Laplace's equation.

Computer software

To perform aerodynamic calculations of a ground-effect craft a computer software called Autowing based on the boundary element method (called VLM), has been developed by Korneev [11]. In the computer program the main hull and wings are meshed by square panels on which singularities are distributed. This software has been developed specially to design wings for ground-effect crafts. The Autowing is capable of calculating hydrodynamic and aerodynamic lift and drag. The frictional drag could not be calculated by means of the Vortex-lattice method, hence it is computed by using an empirical formula inserted in the Autowing.[11].

THE PROCESS OF RESEARCH

A planing body whose geometric characteristics are presented in Tab. 2, is selected as a hull. Its dead-rise angle varies from 10 degrees aft to 15 degrees amid-ship. The body lines of the craft and its 3D image are shown in Fig. 2 and 3, respectively. White area in Fig. 3 distinguishes the underwater part of the hull on even keel condition.

Tab. 2. Main particulars of the hybrid craft

Particulars	Quantity	Unit
LOA	18.2	m
LBP	17	m
B(max)	5.6	m
Draught	1.36	m
Height	2.9	m
Displacement	66.57	t
LCG from aft	7.957	m

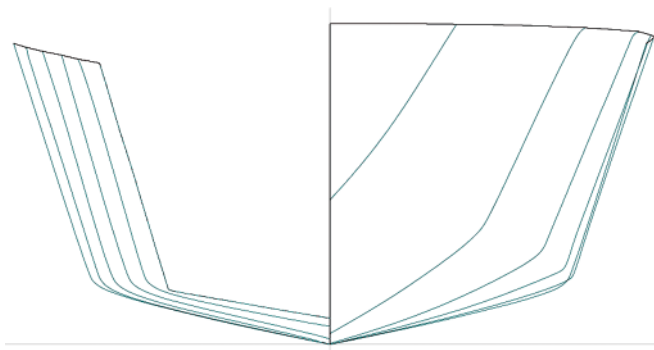


Fig. 2. Body lines of the hybrid craft

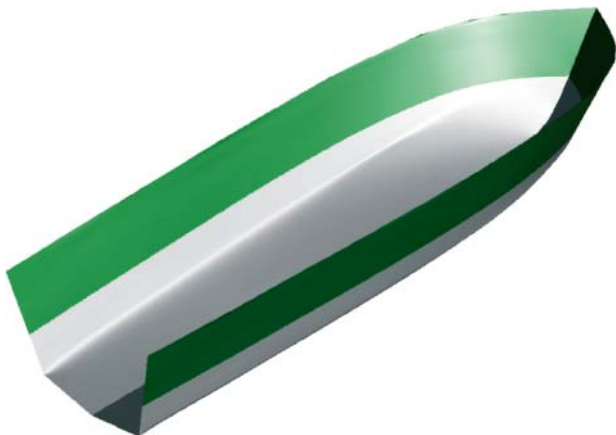


Fig. 3. 3D image of the hybrid craft

The 3D model was used to perform hydrostatic calculations and consequently to obtain centre of buoyancy and displacement of the craft. Furthermore, its wetted surface was calculated at different trim angles and draughts. To determine hydrodynamic lift force the vessel was modelled by using the Autowing, as shown in Fig. 4. The calculations were done for four draughts and five trim angles at six different speeds as given in Tab. 3.

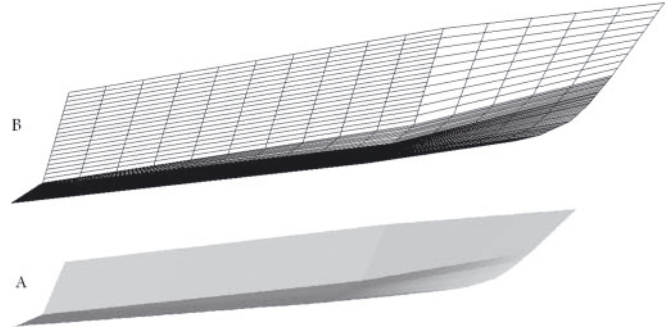


Fig. 4. A model of the planing hull part used as input to the Autowing software

Tab. 3. Input parameters of example calculations

Item	Quantity	Unit
Draught	0.5, 0.65, 0.8, 0.95	m
Trim	2, 3, 4, 5, 6	deg
Speed	25, 40, 55, 70, 85, 100	kn

According to the research on the ground effect [12], the pressure side of wing surface, which has been carefully examined in the case study, should be flat. The wing shape is like an inverse delta, known as Lippisch type, whose important advantage is providing the craft with a better stability [13].

The aerodynamic calculations were also done by using the Autowing. The wing geometry is shown in Fig. 5. In Fig. 6 a typical airfoil section of the wing is shown. The dimensions of the wings are selected proportionally to the dimensions of the craft. Tab. 4 shows the ratios of wing dimensions in respect with the craft, where C and S are the chord length and span of the wing, respectively. Furthermore, H is gap height, and L and B are the craft length and beam, respectively (see Fig. 7).

Tab. 4. Wing main dimensions

Item	Quantity
C/L	0.5, 0.75, 0.9
S/B	0.5, 1, 1.5
H/C	0.05, 0.059, 0.088
C (m)	8.5, 12.75, 15.3

For aerodynamic analysis the gap of 75 cm measured from water level to the end point of the wing, is considered because, the maximum ground effect happens at a height of less than 10 percent to the wing chord length [14]. To obtain better performance and achieve higher lift force the wings with the initial angle of attack of 7 degrees, are assumed. It means that if the craft is on even keel in water, its wing will have the angle of attack of 7 degrees.



Fig. 5. Wing geometry modelled by the Autowing

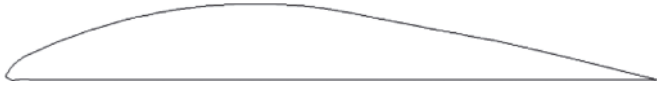


Fig. 6. Typical airfoil section used for wing

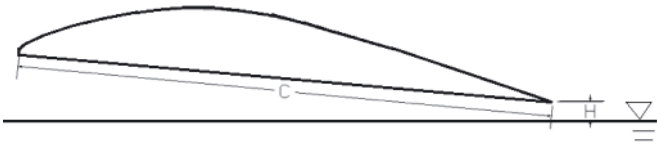


Fig. 7. Parameters defined for ground effect

RESULTS OF PARAMETRIC STUDIES

A set of calculations was done for several configurations of the hybrid craft, in which its draught, trim, wing size and speed were systematically changed. Their results are below presented and discussed.

Comparison of the hydrodynamic and aerodynamic lift-to-drag ratios

Since two elements support craft's weight by dynamic lift, the lift-to-drag ratio is a good measure of merit for comparing different lifting surfaces. Obviously, the higher lift-to-drag ratio the better performance of a lifting surface.

In Fig. 8 through 10, the lift-to-drag ratios are presented in function of angle of attack and wing area for three different speeds. The speeds of 25, 55 and 100 knot were selected to cover the ranges of low, intermediate and very high speeds. It is observed that the lift-to-drag ratio of wing varies from 2.5 to 9.5 and decreases as the angle of attack increases. The ratio

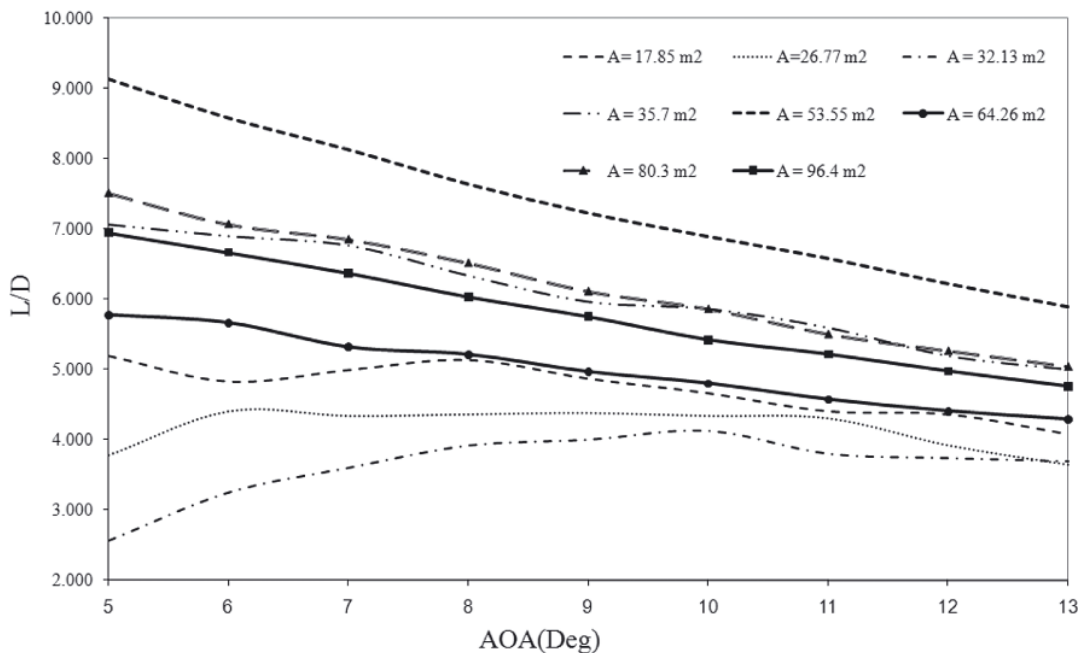


Fig. 8. The lift-to-drag ratio of air wing with respect to the angle of attack and wing area at speed of 25 knot

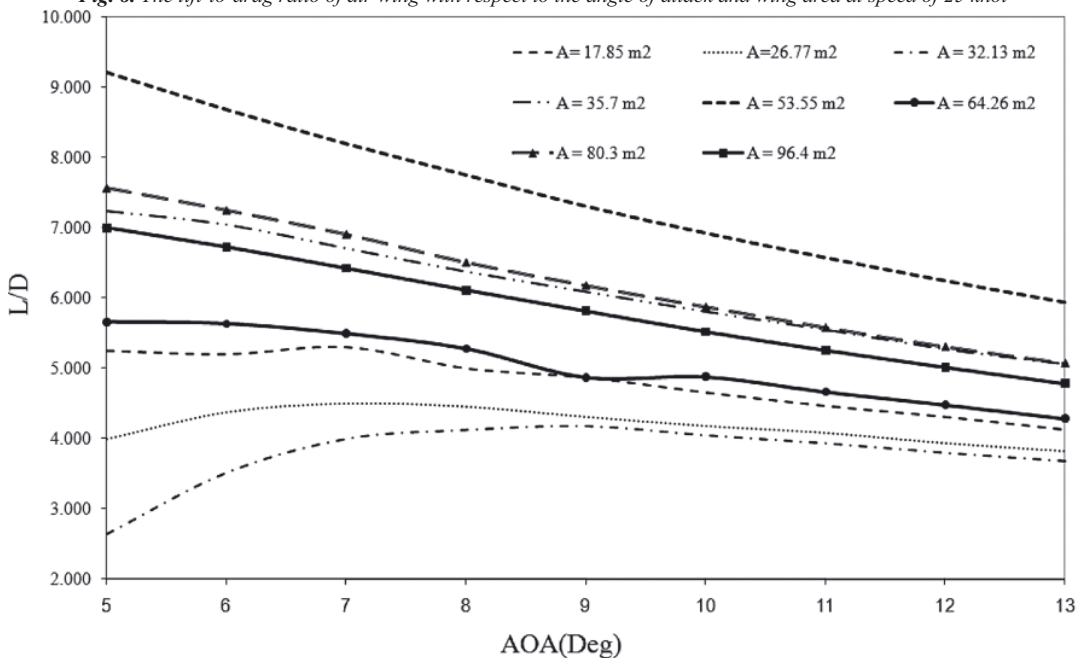


Fig. 9. The lift-to-drag ratio of air wing with respect to the angle of attack and wing area at speed of 55 knot

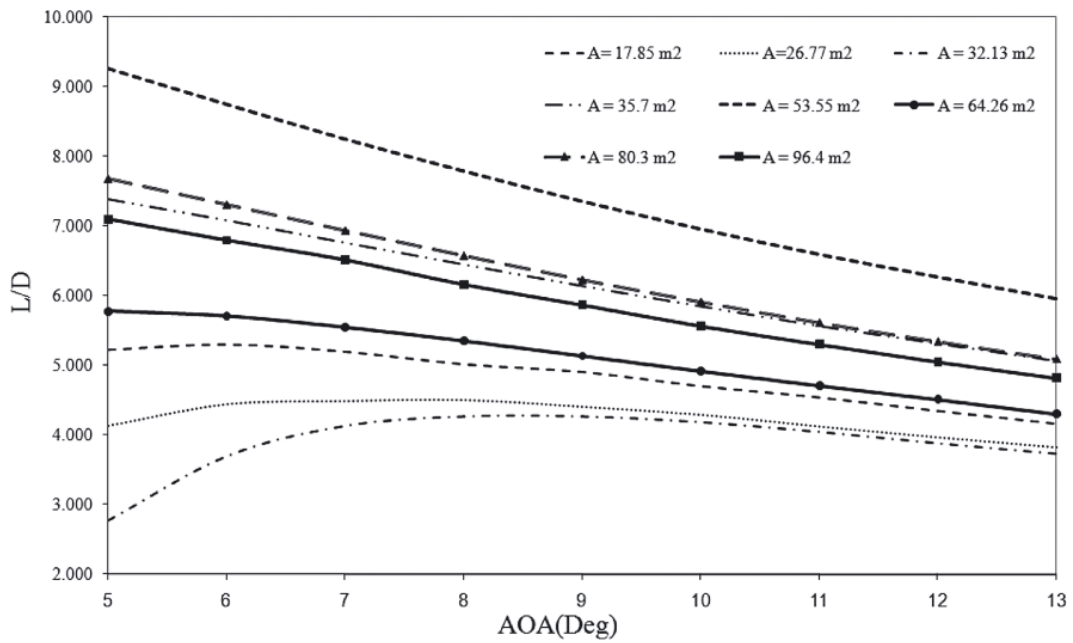


Fig. 10. The lift-to-drag ratio of air wing with respect to the angle of attack and wing area at speed of 100 knot

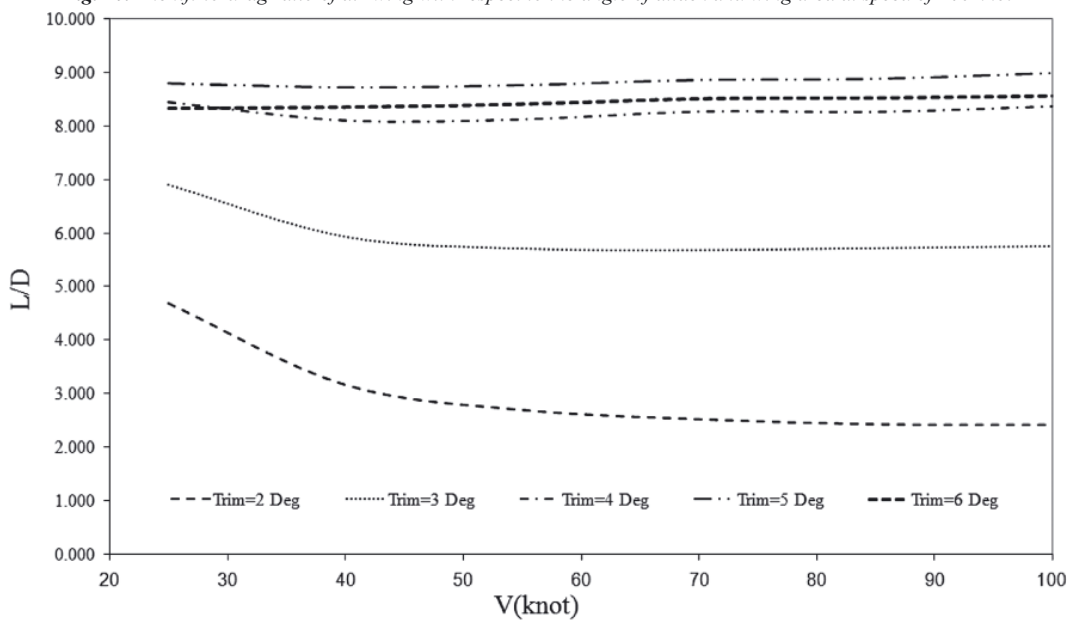


Fig. 11. The lift-to-drag ratio of a planing hull with respect to speed and trim at the draught of 0.5 m

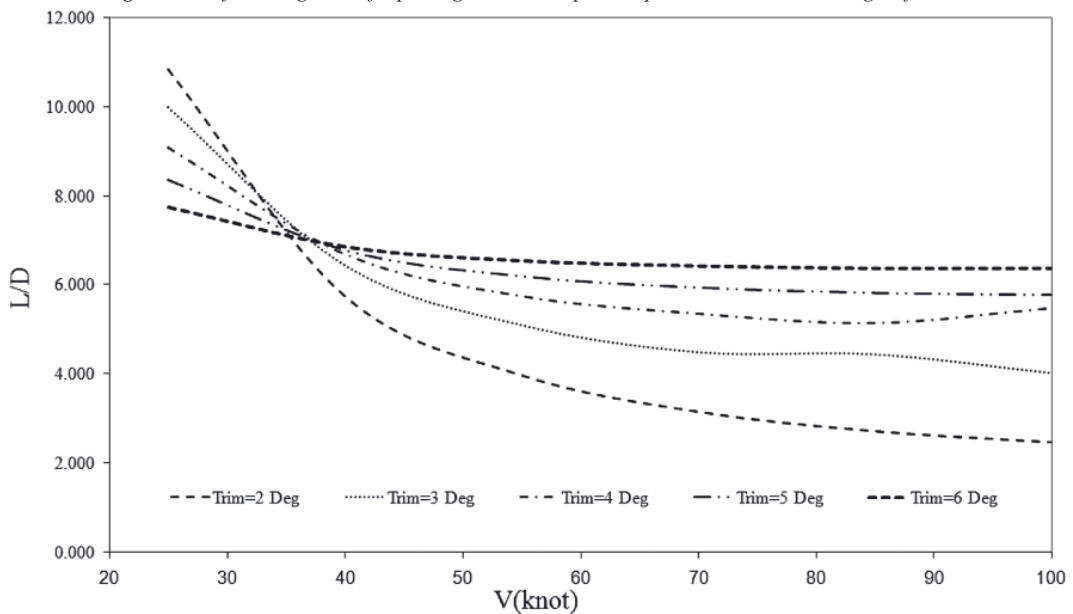


Fig. 12. The lift-to-drag ratio of a planing hull with respect to speed and trim at the draught of 0.95 m

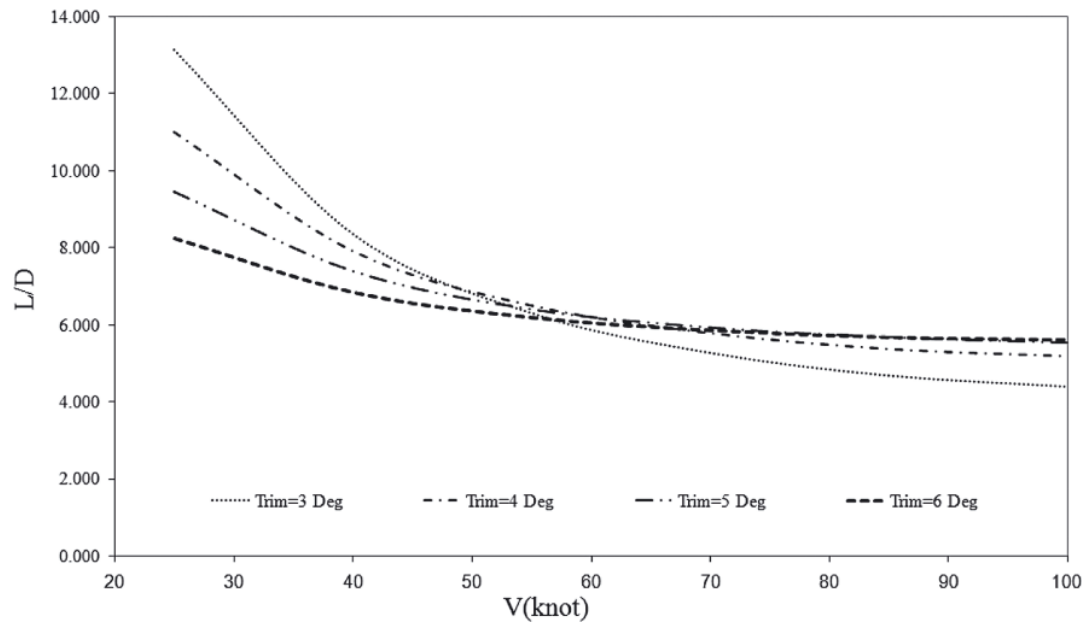


Fig. 13. The lift-to-drag ratio of a planning hull with respect to speed and trim at the draught of 1.36 m

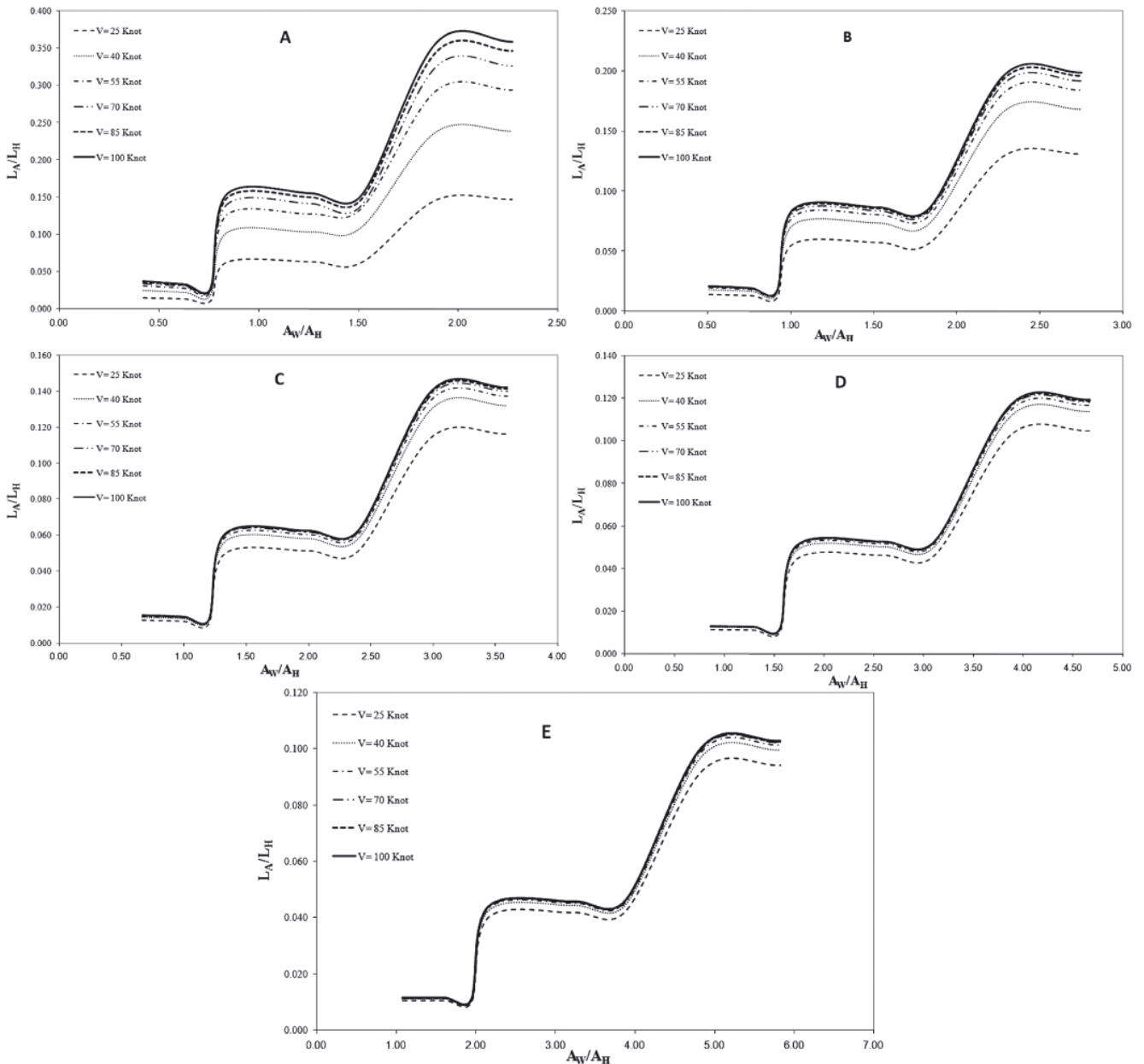


Fig. 14. The lift ratio versus the surface ratio for different speeds at the draught of 0.5 m

obtains its peak value in the case of the wing of 53m² area, whose chord length is the least (of 50 percent of craft length) and span is the largest (of 150 percent of craft breadth). On this basis, it is concluded that the wing should be so designed as to obtain the possible highest aspect ratio.

The lift-to-drag ratio of a typical planning hull is shown in Fig. 11 through 13, which varies from 2 to 12. It decreases as the draught and speed of the craft increases. Additionally, the greater trim the greater lift-to-drag ratio.

A comparison of the two groups of curves leads to an important conclusion that there is no certain advantage from using the wing aerodynamic force instead of the hydrodynamic lifting surface force.

Comparison of hydrodynamic lift with aerodynamic lift

The ratio of aerodynamic lift (of wings) and hydrodynamic lift (of planing hull), hereafter called the lift ratio, versus the ratio of wing area and planing wetted surface, hereafter called the surface ratio, is shown in Fig. 14.

As trim angle increases the lift ratio increases too. This is due to the positive angle of attack of 7 degree of the wings for the craft on even keel. That is why the maximum lift ratio occurs at the trim angle of 2 deg at the speed of 100 knot. However, it may not be greater than 40 percent.

As far as the surface ratio has been concerned, increasing the surface ratio leads to increasing the lift ratio. Furthermore, the lift ratio has three distinct zones not associated with different trim angles. In the case of a low surface ratio, less than 1.0, the hydrodynamic forces plays a dominant role in supporting the craft weight while the aerodynamic force is negligible. For the surface ratio of a moderate value from the range of 1.5 up to 2.0, the lift ratio is less than 10 percent. For the surface ratio of more than 2.0 the lift ratio may reach as much as 35 percent.

(A: trim angle of 2 deg, B: trim angle of 3 deg, C: trim angle of 4 deg, D: trim angle of 5 deg and E: trim angle of 6 deg)

CONCLUSIONS

A typical hybrid craft was analyzed to examine the conditions in which aerodynamic lift force of wing is beneficial for planing mono-hull. A typical planing body fitted with wings of different dimensions proportional to the main dimensions of the craft, was considered. The analysis showed that if a planing-wing hybrid craft has to be used, its surface ratio should be more than two in conjunction with a high aspect ratio of wing. The main conclusions of this study are as follows:

- In the planing-wing hybrid craft the hydrodynamic lift-to-drag ratio is usually slightly greater than the aerodynamic lift-to-drag ratio. Therefore, there is no comparative advantage from using air wing.
- The absolute lift force developed by the hybrid craft is a key element for supporting its weight. Generally, the maximum share of the lift force produced by the air wing is equal to about 20 percent of the hydrodynamic lift force in practical conditions.
- Some phenomena such as the hitting of spray to wings as well as impact of the wings against wave surface may produce some undesirable behaviour of a hybrid craft.

Finally, it should be mentioned that air wing may be used only in special circumstances, but not in general.

This conclusion is based on results of technical investigations only, but sometimes aesthetic view of a craft is more important than its efficiency. A planing-wing hybrid craft seems to be much more beautiful than a simple planing craft.

BIBLIOGRAPHY

1. Matveev K. I., Dubrovsky V. A.: *Aerodynamic Characteristics of a Hybrid Trimaran Model*. Ocean Engineering, 34(3-4),2007.
2. Shipps, P. R.: *Hybrid ram-wing/planning craft - today's raceboats, tomorrow's outlook*. AIAA/SNAME Advanced Marine Vehicles Conference, 1976
3. Ward, T. M., Goelzer, H. F., Cook, P. M.: *Design and performance of the ram wing planning craft - KUDU II*. AIAA/SNAME Advanced Marine Vehicles Conference, 1978
4. Privalov, E. I., Kirillovikh, V. N.: *Transport amphibious platforms: a new type of high-speed craft*. Proceedings of Ekranoplans & Very Fast Craft Workshop, 1996
5. Doctors, L. J.: *Analysis of the efficiency of an ekranocat: a very high speed catamaran with aerodynamic alleviation*. International Conference on Wing In Ground Effect Craft (WIGs '97), RINA, 1997
6. www.freepatentonline.com
7. Collu M., Patel M. H., Trarieux F.: *High speed marine vehicles with aerodynamic surfaces: development of a dynamic model for a novel configuration*. Cranfield Multi Strand Conference, 6-7 May 2008. Cranfield, Bedfordshire, UK
8. Collu M., Patel M. H., Trarieux F.: *A Unified Mathematical Model for High Speed Hybrid (Air and Waterborne) Vehicles.*, 2nd International Conference on Marine Research and Transportation, 2007
9. Collu M., Patel M. H., Trarieux F.: *A Mathematical Model to analyze the Static Stability of Hybrid (Aero hydrodynamically supported) vehicles*. 8th Symposium on High Speed Marine Vehicles 2008 (HSMV08), Naples, Italy, 2008
10. www.seaphantom.com
11. Korneev, N.V., Taranov, A.E., Treshkov, V.K.: *Efficient software for numerical calculation of ekranoplans (WIG craft) and hydrofoils*. Proc. Workshop WISE up to Ekranoplan GEMS, The University of New South Wales, Sydney, Australia, pp. 263-266, 1998.
12. Bakhshandehrostamai A. Ghasemi H.: *Design and Analysis of 2D Wing In Ground Effect Based on Maximum Lift-Drag Ratio.* MSc thesis, Amirkabir University of Technology, Tehran, Iran, 2008
13. Matjasic K. *et al.*: *WIG (Wing In Ground effect) craft in military and paramilitary applications*. NATO Conference, TO-AVT Symposium, April 7 -11, 2003
14. Park K. and Lee J.: *Influence of endplate on aerodynamic characteristics of low-aspect-ratio wing in ground effect*. Journal of Mechanical Science and Technology, Vol.22, 2008, pp. 2578-2589,
15. Husa B.: *WIG configuration development from component matrix*. Orion technology, Aerospace design and engineering, Internal report, 2000
16. Yun L. Bliault A., Doo J.: *WIG craft and Ekranoplan; Ground effect craft technology*. ISBN 978-1-4419-0041-8 e-ISBN 978-1-4419-0042-5, Springer, 2010

CONTACT WITH THE AUTHORS

Hamid Zeraatgar, Assistant Professor
 Ali Bakhshandeh Rostami, MSc.
 Abolfazl Nazari, MSc.
 Faculty of Marine Technology,
 Amirkabir University of Technology,
 Somayyeh Str., Hafez Ave.
 Tehran, Iran
 POBox: 5875-4413
 e-mail: hamidz@aut.ac.ir

Comparative analysis of fatigue life calculation methods of C45 steel in conditions of variable amplitude loads in the low- and high-cycle fatigue ranges

Bogdan Ligaj, Ph. D.

Grzegorz Szala, Ph. D.

University of Technology and Life Science, Bydgoszcz, Poland

ABSTRACT

In the paper [1] assumptions for fatigue life calculations in the low- and high- cycle fatigue ranges of metal alloys, have been formulated. Three calculation methods: that expressed in stresses, strains and a mixed (stress-strain) one, have been there presented. In this paper results of fatigue life calculations of C45 steel performed in line with the above mentioned methods have been described, and their comparative analysis has been made. The calculations have been carried out for two-level and multi-level load programs of the varying parameters: maximum load within a load program and different values of spectrum filling factor. The comparative analysis of the results of fatigue life calculations in compliance with the above mentioned methods makes it possible to assess differences in the results and dependence of the differences on values of load program parameters.

Keywords: fatigue life calculations; low- and high- cycle fatigue; C45 steel

INTRODUCTION

Operational loads of structural elements are generally random. Load spectra elaborated in accordance with relevant cycle-counting methods contain sets of sinusoidal cycles of different parameters, especially different values of the load amplitude S_a and mean value S_m [2]. In the case when the load $S_{max} = S_m + S_a \leq R_e$ fatigue life is calculated with the use of the method which applies Wöhler diagram (stress approach – the high-cycle fatigue range, HCF), whereas for $S_{max} > R_e$ the method using Manson-Coffin diagram is applied to fatigue calculations (strain approach – the low-cycle fatigue range, LCF) [3, 4].

Load spectrum usually contains cycles of different share of S_{max} values occurring both in the HCF and LCF range. Therefore in the authors' research project [5] has been introduced the theme of a hybrid calculation method in which fatigue damage due to cycles in the HCF range is calculated by means of the stress approach method whereas in the LCF range the strain approach method is used. Then the question appears whether applying either stress approach methods or strain approach ones for the entire range of loads (LCF + HCF) one obtains fatigue life results significantly different from those calculated by using the hybrid method. Significance of the so formulated problem, as shown in [6, 7], consists also in that criteria for qualifying the loads either to LCF or HCF range are ambiguous – blurred. This work is aimed at answering the above formulated question.

Assumptions for calculations of fatigue life of metal alloys in the conditions when loading occurs both in the LCF and HCF ranges, were presented in the paper [1]. In the calculation

method described in the paper three paths were distinguished: 1st – based on application of the full (complete) Wöhler diagram (i.e. acc. stress approach) 2nd – based on application of Manson-Coffin diagram (i.e. acc. strain approach), and 3rd – hybrid one.

Fatigue life calculations in the varying amplitude load conditions require to know a load spectrum or program, cyclic properties of material, usually in the form of the above mentioned fatigue diagrams, as well as to assume an appropriate hypothesis for fatigue damage summation [8]. Out of many known hypotheses, for the calculations described in this paper the Palmgren-Miner linear summation hypothesis, the best experimentally verified one, was selected.

In accordance with the hypothesis the sum of damages resulting from the number of cycles, n_0 , during realization of loading program, is calculated from the formula:

- for 1st path:

$$D_0 = \sum_{i=1}^k \frac{n_{oi}}{N_i} \quad (1)$$

- for 2nd path:

$$D_0 = \sum_{i=1}^k \frac{n_{oi}}{N_{fi}} \quad (2)$$

- for 3rd path:

$$D_0 = \sum_{i=1}^l \frac{n_{oi}}{N_{fi}} + \sum_{i=(l+1)}^k \frac{n_{oi}}{N_i} \quad (3)$$

Fatigue fracture will occur when the sum of damages $D = 1.0$. which leads to the number of program repetitions:

$$\lambda = 1.0/D_0 \quad (4)$$

and to the fatigue life expressed by number of cycles:

$$N_c = \lambda \cdot n_o \quad (5)$$

DATA FOR CALCULATIONS OF C45 STEEL FATIGUE LIFE

Load programs

The calculations were performed for load programs of two kinds: two-level one of variable parameters, and multi-level one (Fig. 1).

In the two-level program the following parameters were assumed:

- four values of the maximum stresses S_{max} within the program: 650 MPa, 570 MPa, 460 MPa and 340 MPa,
- three ratios of stress values, S_{a2}/S_{a1} : 0.75; 0.5; 0.25,
- four ratios of numbers of load cycles, n_{o1}/n_0 : 0.75; 0.5; 0.25; 0.1.

In the further part of this work the assumed values of S_{max} loads are marked as follows: I – 650 MPa, II – 570 MPa, III – 460 MPa i IV – 340 MPa.

Such selection of the parameters makes it possible to realize a wide research program comprising 64 different cases.

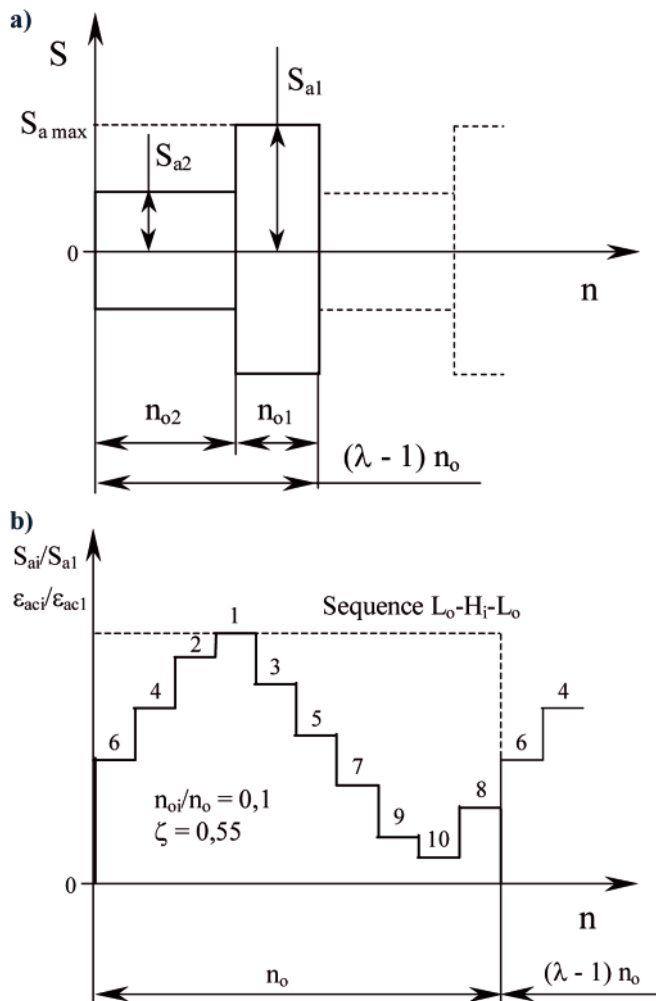


Fig. 1. Schematic diagrams of the load programs assumed for calculations: a) two-level program, b) multi-level program

In the tests according to 2nd path (i.e. strain approach) and 3rd path (i.e. hybrid one) values of the total strains ϵ_{ac} correspond to relevant values of the stresses S_a .

The parameter which characterizes load intensity is the spectrum filling factor described by the formula:

$$\zeta = \sum_{i=1}^k \frac{S_{ai}}{S_{a\max}} \cdot \frac{n_{oi}}{n_o} \quad (6)$$

which, on transformation, for the two-level program, takes the following form:

$$\zeta = \frac{n_{o1}}{n_o} + \frac{S_{a2}}{S_{a1}} \left(1 - \frac{n_{o1}}{n_o}\right) \quad (7)$$

Values of the spectrum filling factor for the assumed parameters are collected in Tab. 1.

Tab. 1. Values of the spectrum filling factor ζ

		S_{a2}/S_{a1}			
		0.25	0.50	0.75	1.0
n_{o1}/n_o	0.10	0.325	0.550	0.775	1.0
	0.25	0.437	0.625	0.812	1.0
	0.50	0.625	0.750	0.875	1.0
	0.75	0.812	0.875	0.937	1.0

The data contained in Tab. 1 indicate the wide range of loading conditions for fatigue calculations, starting from $\zeta = 0.325$ which corresponds to e.g. the loading of track system elements of road vehicles, up to $\zeta = 1.0$ which corresponds to sinusoidal load of constant amplitude.

The multi-level load program was elaborated on the basis of the load spectrum of the mean value of the spectrum filling factor ζ , calculated from the corresponding data given in Tab. 1. And, the graphical form of the program is shown in Fig. 2 in the system of relative quantities.

The program assumed for the tests in question has 10 load levels (S_{ai} or ϵ_{aci}) of the same cycle capacity $n_{oi}/n_o = 0.1$ and the same load span $S_{ai} - S_{ai+1} = 0.1 \cdot S_{a1}$. The spectrum filling factor $\zeta = 0.55$.

Moreover, for the fatigue life tests and calculations were assumed maximum stress levels complying with those taken for fatigue life analyses in the two-level loading conditions.

Static and cyclic properties of C45 steel

Mechanical properties of C45 steel were determined on the basis of specimens prepared in compliance with the Polish standards: static properties – acc. PN-EN ISO 6892-1:2010. cyclic properties – acc. PN-84/H-04334. The values of the determined parameters are: $R_m = 682$ MPa, $R_e = 458$ MPa, $E = 2.15 \cdot 10^5$ MPa. The Wöhler diagram experimentally determined for $R = -1.0$ is described by the formula:

$$\log S_a = -0.1020 \log N + 2.9611 \quad (8)$$

for which the fatigue limit at $N_0 = 10^6$ is equal to $S_{f(-1)} = 223.5$ MPa, and the exponent $m_{(-1)} = 9.8$.

The Manson-Coffin diagram experimentally determined is described by the formula:

$$\epsilon_{ac} = \frac{1204}{2.15 \cdot 10^5} (2N_f)^{-0.1033} + 0.2179 (2N_f)^{-0.475} \quad (9)$$

To transform the load program from that formulated in stress approach to strain approach one, was used the experimentally determined Ramberg-Osgood diagram of the following form:

$$\epsilon_{ac} = \frac{S_a}{2.15 \cdot 10^5} + \left(\frac{S_a}{1232}\right)^{5.06} \quad (10)$$

RESULTS OF CALCULATIONS FOR TWO-LEVEL LOADS

Results of calculations according the 1st path

The calculation results in the form of Gassner diagrams are shown in Fig. 2 on the Wöhler diagram background. As results from the data assumed for the calculations, the levels I, II and III correspond to the LCF condition, i.e. $S_{a1} > R_{e3}$, similarly the values S_{a2} for $S_{a2}/S_{a1} = 0.75$ are contained within the low-cycle fatigue (LCF). The remaining values, S_{a1} and S_{a2} are smaller than R_{e3} , hence in compliance with the assumed criterion they are rated to be in the high-cycle fatigue range (HCF).

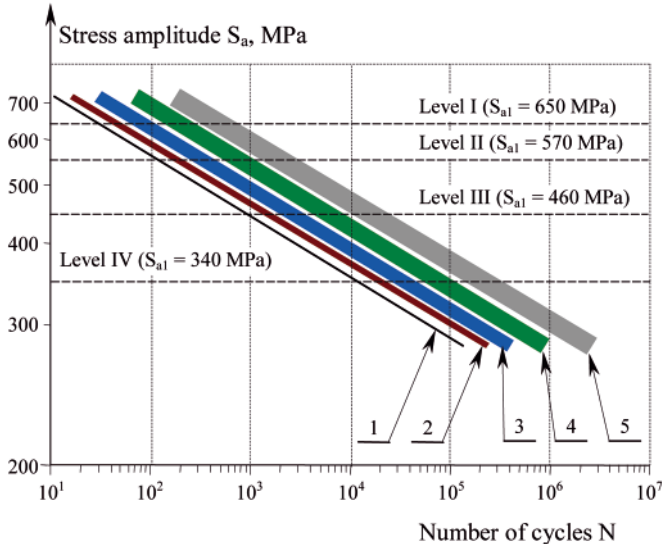


Fig. 2. Fatigue life diagrams for C45 steel determined by calculations according to 1st path in the two-level loading conditions: 1) Wöhler diagram for $n_{01}/n_0 = 1.0$; 2) Gassner diagram for $n_{01}/n_0 = 0.75$; 3) Gassner diagram for $n_{01}/n_0 = 0.5$; 4) Gassner diagram for $n_{01}/n_0 = 0.25$; 5) Gassner diagram for $n_{01}/n_0 = 0.1$

Results of calculations according to the 2nd path

In compliance with the description given in p. 1. in the 2nd path calculations the load ranges LCF and HCF have to be related to Manson-Coffin diagram. To this end, it is necessary, for description cyclic strain diagram, to transform loads expressed in stress units into those expressed in total strains by using the Ramberg-Osgood diagram (10). The total strain values corresponding to relevant stress values are given on the ordinate axis of the diagrams in Fig. 3. The number of $2N_f$ recurrence to fatigue fracture was calculated by using the Mason-Coffin formula (9). The calculation results are graphically presented in Fig. 3.

In Fig. 2 and 3 the diagrams are presented in the form of shadowed bands. Their left edges correspond to the ratio $S_{a2}/S_{a1} = 0.75$, right ones – the ratio $S_{a2}/S_{a1} = 0.25$, and the middle line of the band corresponds to the ratio $S_{a2}/S_{a1} = 0.5$.

Calculations in compliance with the hybrid method for two-level loading (the 3rd path)

According to the hybrid method (the 3rd path) complete damage corresponds to sum of the damage resulting from the loading within the low-cycle range (LCF), calculated by using Manson-Coffin fatigue diagram and the damage due to the loading within the high-cycle range (HCF) calculated by means of Wöhler fatigue diagram according to the formula (3).

The sums of damages calculated acc. (3) and the fatigue life calculated in compliance with the hybrid method, are presented in Tab. 2.

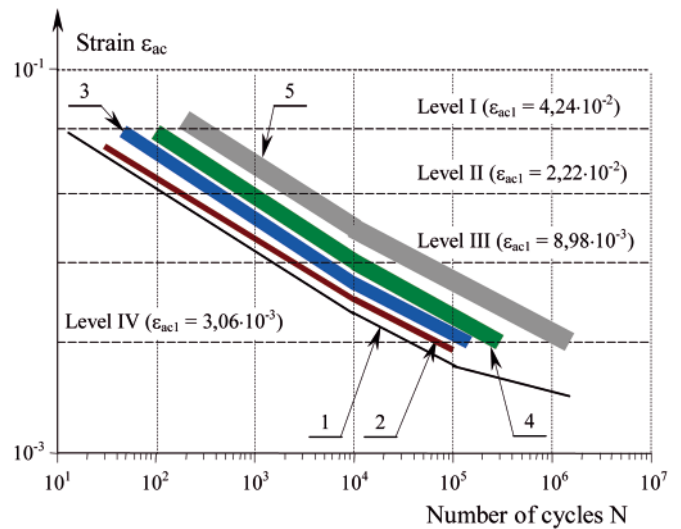


Fig. 3. Fatigue life diagrams for C45 steel determined by calculations according to 2nd path in the two-level loading conditions: 1) Manson-Coffin diagram; 2) Gassner diagrams for $n_{01}/n_0 = 0.75$; 3) Gassner diagrams for $n_{01}/n_0 = 0.5$; 4) Gassner diagrams for $n_{01}/n_0 = 0.25$; 5) Gassner diagrams for $n_{01}/n_0 = 0.1$

In line with expectations, for high load values (the level I) the results of fatigue life calculated by using the hybrid method (the 3rd path) are closer to the results of calculations according to the 2nd path, and for low load values (the level IV) the results of fatigue life calculations according to the 3rd path are closer to those calculated in compliance with the 1st path.

The above given statement shows that in the case of higher values of the ratio the higher level, i.e. the amplitude S_{a1} or ϵ_{ac1} , is significantly decisive of fatigue whereas influence of the lower level, i.e. S_{a2} or ϵ_{ac2} , is not significant. This is confirmed by the data given in Tab. 3 and 4. Tab. 3 contains the numerical data concerning the ratio of the fatigue life calculated by applying stress approach (the 1st path) and that calculated by using strain approach (the 2nd path).

As results from the data contained in Tab. 3, for high stress values and strains corresponding to them (the load levels I and II) the more conservative results are achieved from the strain approach calculations (the 2nd path), whereas for lower load values (the levels II and IV) the results of stress approach calculations (the 1st path) are more conservative. Fig. 4 illustrates the conclusion.

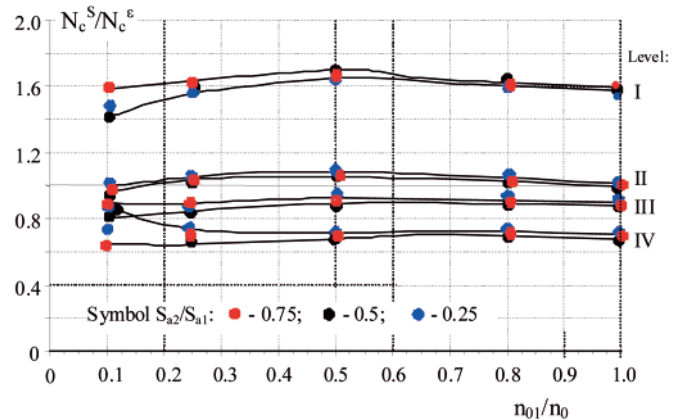


Fig. 4. Dependence of the ratio of the fatigue life calculated acc. the 1st path and that calculated acc. the 2nd path on load level and the test program form described by the ratios S_{a2}/S_{a1} and n_{01}/n_0

As results from the diagrams shown in Fig. 4, the influence of loading program form on difference in the calculation

Tab. 2. Values of damage parameter and fatigue life calculated in compliance with the hybrid method (the 3rd path)

No. of level	n_{01}/n_0							
	0.75		0.5		0.25		0.1	
	$D_0 = D_{01}+D_{02}$	N_cH						
1	2	3	4	5	6	7	8	9
$n_0 = 10$								
I								
a	0.433540	23.0	0.297120	33.6	0.144466	69.0	0.077200	129.0
b	0.428100	23.4	0.286198	35.0	0.143098	70.0	0.057557	173.7
c	0.428000	23.4	0.286002	35.0	0.142800	70.0	0.572004	175.0
II								
a	0.084850	117.9	0.058500	170.9	0.032260	309.9	0.016330	612.3
b	0.083423	120.0	0.055655	179.7	0.027882	358.7	0.011198	893.0
c	0.083400	120.0	0.055600	180.0	0.027800	360.0	0.011100	900.9
III								
a	0.085180	1173.9	0.059100	1692.0	0.032950	3034.9	0.011743	8515.7
b	0.083434	1198.6	0.055667	1796.4	0.027701	3609.9	0.011112	8999.1
c	0.083400	1200.0	0.055600	1800.0	0.027600	3623.2	0.011100	9009.0
IV								
a	$4.76 \cdot 10^{-5}$	21000	$3.315 \cdot 10^{-5}$	30166	$1.805 \cdot 10^{-5}$	55400	$6.281 \cdot 10^{-6}$	159200
b	$4.69 \cdot 10^{-5}$	21300	$3.134 \cdot 10^{-5}$	31912	$1.667 \cdot 10^{-5}$	60000	$6.250 \cdot 10^{-6}$	160000
c	$4.69 \cdot 10^{-5}$	21300	$3.134 \cdot 10^{-5}$	31912	$1.667 \cdot 10^{-5}$	60000	$6.250 \cdot 10^{-6}$	160000
Notation: a – $S_{a2}/S_{a1} = 0.75$; b – $S_{a2}/S_{a1} = 0.5$; c – $S_{a2}/S_{a1} = 0.25$								

Tab. 3. The ratio of the fatigue life calculated by applying stress approach (the 1st path) and that calculated by using strain approach (the 2nd path)

No. of level	S_{a1} MPa	ϵ_{ac1}	$S_{a2}/S_{a1}; \epsilon_{ac}/\epsilon_{ac1}$	n_{01}/n_0									
				1.0	0.75	0.50	0.25	0.1					
1	2	3	4	5	6	7	8	9					
I	650	$4.24 \cdot 10^{-2}$	1.0	1.6									
			0.75							1.59	1.65	1.62	1.41
			0.50							1.58	1.59	1.61	1.44
			0.25							1.58	1.60	1.61	1.60
II	570	$2.22 \cdot 10^{-2}$	1.0	1.13									
			0.75							1.14	1.14	1.07	0.99
			0.50							1.14	1.14	1.13	1.13
			0.25							1.14	1.14	1.13	1.13
III	460	$8.93 \cdot 10^{-3}$	1.0	0.93									
			0.75							0.93	0.93	0.89	0.83
			0.50							0.93	0.93	0.92	0.92
			0.25							0.93	0.93	0.92	0.92
IV	340	$3.06 \cdot 10^{-3}$	1.0	0.71									
			0.75							0.71	0.67	0.67	0.88
			0.50							0.71	0.71	0.72	0.75
			0.25							0.71	0.71	0.72	0.71

Tab. 4. The ratio of the fatigue life calculated acc. stress approach (the 1st path) and acc. strain approach (the 2nd path), respectively, and the fatigue life calculated by using the hybrid method

No. of level	S _{a1} MPa	ε _{ac1}	S _{a2} /S _{a1} ; ε _{ac} /ε _{ac1}	n ₀₁ /n ₀																	
				1.0		0.75		0.5		0.25		0.1									
				N _c ^S /N _c ^H	N _c ^Z /N _c ^H	N _c ^S /N _c ^H	N _c ^Z /N _c ^H	N _c ^S /N _c ^H	N _c ^Z /N _c ^H	N _c ^S /N _c ^H	N _c ^Z /N _c ^H	N _c ^S /N _c ^H	N _c ^Z /N _c ^H								
I	2	3	4	5	6	7	8	9	10	11	12	13	14								
I	650	4.24 · 10 ⁻²	1.0	1.6	1.0	1.56	1.00	1.65	1.00	1.60	1.00	1.42	1.00								
			0.75											1.56	1.00	1.60	1.00	1.60	1.00	1.43	1.00
			0.50											1.56	1.00	1.60	1.00	1.60	1.00	1.60	1.00
II	570	2.22 · 10 ⁻²	1.0	1.13	1.0	1.16	1.00	1.13	1.01	1.12	1.04	1.08	1.09								
			0.75											1.14	1.00	1.13	0.99	1.13	1.00	1.13	1.00
			0.50											1.14	1.00	1.13	0.99	1.13	1.00	1.13	1.00
III	460	8.98 · 10 ⁻³	1.0	0.93	1.0	0.93	1.00	0.93	1.00	0.93	1.05	0.63	0.76								
			0.75											0.92	0.99	0.92	0.99	0.92	0.99	0.91	0.99
			0.50											0.92	0.99	0.92	0.99	0.92	0.99	0.93	0.99
IV	340	3.06 · 10 ⁻³	1.0	1.0	0.71	1.0	1.41	1.0	1.49	1.0	1.50	1.0	1.13								
			0.75											1.0	1.40	1.0	1.41	1.0	1.38	1.0	1.33
			0.50											1.0	1.40	1.0	1.41	1.0	1.49	1.0	1.40

results according to the 1st path and 2nd path, expressed by the fatigue life ratio (N_c^S/N_c^ε), is not significant and observed only for the programs of n₀₁/n₀ = 0.1. However in accordance with expectations, the load level influence on the ratio (N_c^S/N_c^ε) is significant and amounts to: (N_c^S/N_c^ε) ≈ 1.6 for the level I, (N_c^S/N_c^ε) = 1.4 for the level II, (N_c^S/N_c^ε) = 0.92 for the level III and (N_c^S/N_c^ε) = 0.71 for the level IV.

On assumption that the reference point is the fatigue life value N_c^H, calculated in accordance with the hybrid method (the 3rd path), the fatigue life ratios N_c^S/N_c^H and N_c^ε/N_c^H were calculated. The data are collected in Tab. 4 and illustrated by the diagram shown in Fig. 5a and 5b.

Like in the case of the data shown in Fig. 4, load level shows significant influence on the conformity between the results of calculations according to the 1st, 2nd and 3rd path, and a lower influence is produced by load program form described by the ratios S_{a2}/S_{a1} and n₀₁/n₀, the latter - with the exception for n₀₁/n₀ = 0.1. Comparing the diagrams in Fig. 5a with the relevant diagrams in Fig. 5b one states that a greater conformity is shown by the calculation results according to the 1st and 3rd path for low load levels (obviously, full conformity is observed for the load levels III and IV) as well as the 2nd and 3rd path for high load levels (obviously, full conformity is observed for the load levels I, II and III).

The maximum difference between fatigue life calculated according to the 1st and 3rd path amounts to δ = 39%, whereas the relative difference between fatigue life calculated according to the 2nd and 3rd path amounts to δ = 33%.

CALCULATIONS FOR C45 STEEL IN MULTI-LEVEL LOAD CONDITIONS

Results of calculations according to the 1st path

The multi-level load program has been already described in p. 2.1. In Fig. 6 is presented Gassner diagram (2) on the background of Wöhler diagram (1), moreover for comparison, by means of the dotted line (3) is shown the Gassner diagram

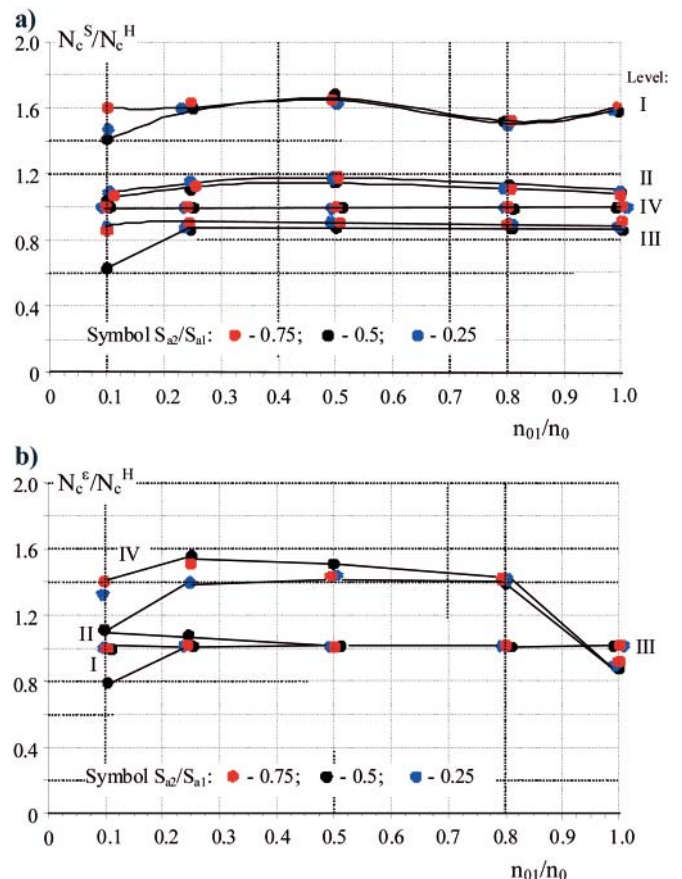


Fig. 5. Dependence of the ratio of the fatigue life: **a)** calculated acc. the 1st path and that calculated acc. the hybrid method (the 3rd path), **b)** calculated acc. the 2nd path and that calculated acc. the hybrid method (the 3rd path), on load level (I, II, III and IV, respectively) and the test program form described by the ratios S_{a2}/S_{a1} and n₀₁/n₀

for the same two-level loads and the same spectrum filling factor ζ.

As results from the comparison the fatigue life determined in the two-level load conditions differs from that determined in the multi-level load conditions within the entire variability range of S_{a1} .

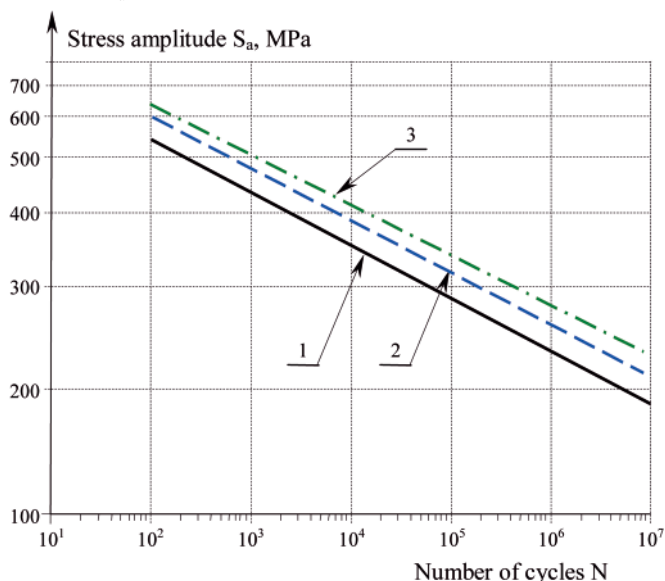


Fig. 6. Fatigue diagrams for C45 steel in stress approach: **1)** Wöhler diagram, **2)** fatigue life diagram (acc. Gassner) for the multi-level load program of the spectrum filling factor $\zeta = 0.55$, **3)** fatigue life diagram (acc. Gassner) for the two-level load program of the spectrum filling factor $\zeta = 0.55$

In accordance with the criterion of LCF assumed in the program for the load level I ($S_{a1} = 650$ MPa) four first levels of the program are situated within LCF range. Similarly, in the program for the load level II ($S_{a1} = 570$ MPa) three first levels of the program are situated within LCF range, whereas in the program for the load level III ($S_{a1} = 460$ MPa) only the first level is contained within LCF range. The remaining levels in all the programs are situated in HCF range.

Results of calculations according to the 2nd path

The Gassner fatigue life diagram (the line marked 2) on the background of the Manson-Coffin fatigue diagram (the line marked 1) is presented in Fig. 7. On the discussed diagram is presented for comparison the fatigue life diagram for two-level load program (the line marked 3). Both the two-level and multi-level program are of the same value of the spectrum filling factor ζ . The mutual location of the diagrams 2 and 3 shows small differences in fatigue life values calculated for multi-level and two-level program.

Like in the case of calculations according to the 1st path, some part of the programs is located in LCF range and the remaining in HCF range. Specification of the levels has been given in the description of the 1st path.

Results of calculations according to the 3rd path

The hybrid method (the 3rd path) consists in summing damages in LCF range in accordance with the method based on the concept of application of Manson-Coffin fatigue diagram (the 2nd path), and in HCF range in accordance of the method based on the concept of application of Wöhler diagram (the 1st path).

In Fig. 8 is presented the comparison of fatigue life diagrams for C45 steel, determined in the conditions of multi-level load program. The diagrams were elaborated in the system: the

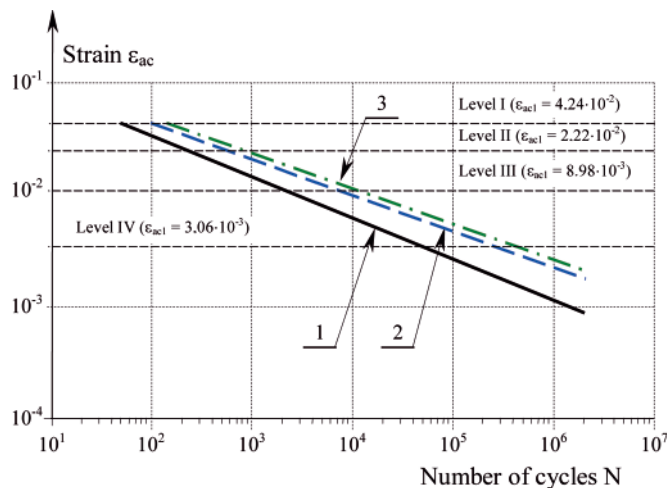


Fig. 7. The fatigue life diagram for C45 steel in the conditions of the multi-level load program (line 2) on the background of the Manson-Coffin fatigue diagram (line 1), as well as the diagram for the two-level load program (line 3)

load level S_a (I, II, III, IV) versus fatigue life expressed by the number of cycles N_c . As results from the comparison of the diagrams, the results of the stress approach calculations (the 1st path) are closest to the values of fatigue life determined by using the hybrid method (the 3rd path). Only for the level I (650 MPa) the results of the strain approach calculations (the 2nd path) show a higher conformity with those calculated by using the hybrid method (the 3rd path). The above given observation is in compliance with the conclusion formulated in the case of analysis of the data achieved from the calculations in the conditions of two-level load programs with the exception that in the case of multi-level load programs differences in calculation results are much smaller and amount, in extreme cases, to:

- for the level I ($S_{a1} = 650$ MPa), between the results acc. the 3rd and 1st path:

$$\delta_{H1}^I = \frac{N_c^{(H)} - N_c^{(1)}}{N_c^{(H)}} = -0.42$$

- for the level I ($S_{a1} = 650$ MPa), between the results acc. the 3rd and 2nd path:

$$\delta_{H2}^I = \frac{N_c^{(H)} - N_c^{(2)}}{N_c^{(H)}} = 0.008$$

- for the level IV ($S_{a1} = 340$ MPa), between the results acc. the 3rd and 1st path:

$$\delta_{H1}^{IV} = \frac{N_c^{(H)} - N_c^{(1)}}{N_c^{(H)}} = 0$$

- for the level IV ($S_{a1} = 340$ MPa), between the results acc. the 3rd and 2nd path:

$$\delta_{H2}^{IV} = \frac{N_c^{(H)} - N_c^{(2)}}{N_c^{(H)}} = -0.66$$

ANALYSIS OF RESULTS AND SUMMARY

The basic analysis of fatigue life calculation methods for C45 steel concerns programmed two-level loads whose parameters assumed in the program: S_{a1} ; S_{a2}/S_{a1} and n_{01}/n_0 made it possible to perform calculations for 64 cases. The so wide range of the

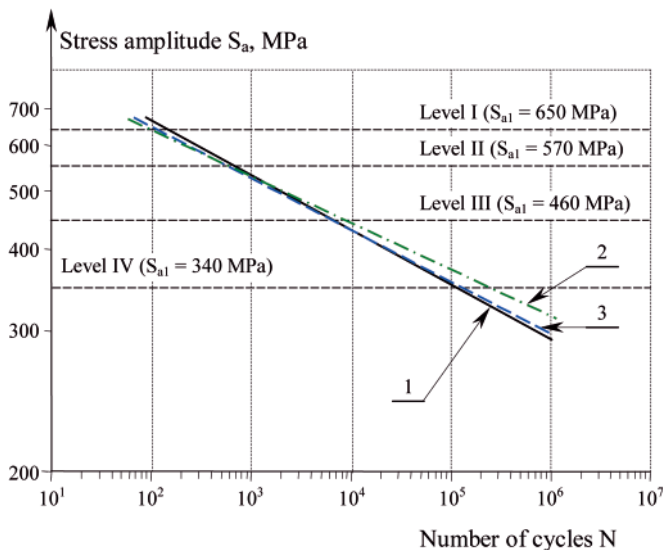


Fig. 8. Gassner fatigue life diagrams for C45 steel in the multi-level load conditions, determined with the use of the following calculation methods: 1) acc. stress approach (the 1st path) 2) acc. strain approach (the 2nd path), 3) hybrid one (the 3rd path)

two-level load cases makes it possible to quantitatively assess influence of program's parameters on fatigue life calculated in accordance with all the calculation paths.

As expected, results of the calculations demonstrate:

- prevailing influence of the load level: S_{a1} or ε_{ac1} .
- much lower influence of the program's form: S_{a2}/S_{a1} and n_{01}/n_0 , which decreases along with spectrum filling factor increasing.

Purposefulness of assuming, in the calculation program, the loads of high values of the spectrum filling factor ζ (Tab. 1) results from the necessity of stressing significant contribution of loads from LCF range. This is the case which corresponds to trends in the proposed calculation methods. The programs in question differ, as to the range of ζ -values, from the known programs elaborated on the basis of random operational loads of structural elements. For instance [9] for the track system elements of road vehicles the ζ factor takes values from the interval of $0.25 \div 0.35$.

As results from the data contained in Fig. 2 (the 1st path), Fig. 3 (the 2nd path) and Tab. 2 (the 3rd path), influence of fatigue damages due to cycles of the 2nd degree amplitude (S_{a2} ; ε_{ac2}) on fatigue life is insignificant, with the exception of the program of $n_{01}/n_0 = 0.1$.

As expected, is observed a high conformity of the calculation results according to the assumed paths on the load level $S_{a1} \approx R_o$ (Fig. 4 and 5) for which the fatigue life ratios N_c^S/N_c^E , N_c^S/N_c^H and N_c^E/N_c^H are close to 1.

The wide range of analysis of calculation results of fatigue life for the two-level load programs made it possible to elaborate an appropriate multi-level load program (of 10 levels). The selected ten-level load program (Fig. 1b) is characteristic of the same number of cycles on particular levels ($n_{0i} = n_0/10$) and the same load increase on particular levels ($\Delta S_a = S_{ai} - S_{a(i-1)} = S_{a1}/10$). It leads to the spectrum filling factor $\zeta = 0.55$, close, as for value, to the mean counted from Tab. 1 for two-level load programs. Moreover the same load levels S_{a1} and ε_{ac1} were maintained, that makes it possible to conduct comparative analysis of calculation results of fatigue life for multi-level programs and those for two-level programs.

As results from the data contained in Fig. 6, the low values of the stress amplitude S_{ai} corresponding to the program levels from $i = 6$ through $i = 10$, are of insignificant influence on the

summing of fatigue damages (less than $0.001 D_{01}$) and therefore may be neglected in fatigue life analyses. The above formulated statement is highly important for programmed fatigue tests since exclusion, from the program, of load levels which insignificantly affect fatigue life, shortens testing duration time considerably.

The similar conclusion results from the calculations according to the 2nd path (Fig. 7) and those according to the 3rd path (Fig. 8). From comparison of the fatigue life diagrams determined in accordance with the analyzed paths it results, like in the case of two-level load programs, that the results of the strain approach calculations (the 2nd path) for high load levels (the level I) are closest to those obtained from the hybrid method (the 3rd path) whereas for low load levels (the level IV) the results of the stress approach calculations (the 1st path) are closest to the results of the calculations according to the hybrid method (the 3rd path). For mean values of loads (the level II and III) the results of the fatigue life calculations according to the assumed paths (1st, 2nd and 3rd one) are close to each other. The relative maximum differences in calculation results amount, in extreme cases, to: between those acc. the 3rd and 1st path – the relative difference $\delta_{H1}^I = -0.42$; between those acc. the 3rd and 2nd path – the relative difference $\delta_{H2}^{IV} = -0.66$, and are significantly smaller than the corresponding differences observed in two-level programs.

In Fig. 6 are collected fatigue life diagrams determined by means of calculations in accordance with the 1st path for the multi-level load program (the line 2) and two-level program (the line 3) of similar values of the spectrum filling factor ζ . From their comparison rather low relative difference in calculated fatigue life values, amounting to 0.40 in the extreme case (for the load level IV), results. In the case of the calculations according to the 2nd path relative difference in calculated fatigue life values (for the load level IV), amounts to 0.26. The above formulated statements indicate that to simplify load program form by reducing number of program levels is possible, that is very important for programmed experimental tests.

The problems described in this work find application to fatigue calculations of ship structures and significantly widen the calculation methods described in the subject-matter literature [10, 11 and 12] to cover the load range common for both low-cycle and high-cycle fatigue. The above mentioned load case - a sum of regularly changeable loads and high overloads imposed on them - is that commonly occurring in ship structures.

Acknowledgement

This research work has been financially supported by Polish Ministry of Science and Higher Education in the frame of the research project No. 2221/B/T02/2010/39.

NOMENCLATURE OF MAJOR NOTATIONS

- D_0 – fatigue damage due to realization of n_0 cycles of loading,
- N – number of cycles to fatigue damage – general notation (fatigue life),
- N_c – fatigue life expressed by number of cycles, determined in conditions of programmed loading,
- N_{fi} – number of cycles to fatigue fracture read from Manson-Coffin fatigue diagram for the total strain ε_{aci} ,
- N_i – number of cycles to fatigue fracture read from Wöhler diagram for the stress amplitude S_{ai} ,
- N_0 – basic number of cycles corresponding to fatigue limit,
- S – general notation of stress, [MPa],
- S_{max} – maximum stress value in sinusoidal cycle, [MPa],
- S_{min} – minimum stress value in sinusoidal cycle, [MPa],

- S_a – stress amplitude in sinusoidal cycle, ($S_a = 0.5(S_{max} - S_{min})$), [MPa],
 S_m – mean stress value in sinusoidal cycle, ($S_a = 0.5(S_{max} - S_{min})$), [MPa],
 R – stress ratio ($R = S_{min}/S_{max}$),
 R_c – yield point [MPa],
 R_m – tensile strength of a material [MPa],
 k – number of load levels in a loading program,
 l – number of load levels in a loading program of LCF range,
 n_0 – number of cycles in a loading program,
 n_{01} – number of cycles on 1st level of a loading program,
 n_{0i} – number of cycles on i -th level of a loading program,
 $m_{(-1)}$ – exponent in Wöhler diagram formula,
 δ – relative difference between results of tests and calculations,
 ϵ_{ac} – total strain value,
 ζ – spectrum filling factor,
 λ – number of repetitions of a program to fatigue fracture,
 LCF – low-cycle fatigue,
 HCF – high-cycle fatigue.

BIBLIOGRAPHY

1. Szala J.: *Fatigue life load assumptions for low-cycle and high-cycle fatigue ranges of metal alloys* (in Polish), Materials of 24th Symposium on Fatigue and Fracture Mechanics, Bydgoszcz-Pieczyska, 2012.
2. Kocańda S., Szala J.: *Backgrounds of fatigue calculations* (in Polish), 3rd Edition, Polish Scientific Publishing House (Wydawnictwa Naukowe PWN), Warsaw, 1997.
3. *FITNET Fitness-for-Service Procedure – Final Draft MK7*, 2006.
4. Neimitz A., Dzioba I., Graba M., Okrajni J.: *Assessment of strength, life and operational safety of structural elements containing defects* (in Polish). Publishing House of Świętokrzyska Technical University (Wydawnictwo Politechniki Świętokrzyskiej), Kielce, 2008.
5. Szala J., et al.: *Hybrid method of fatigue life calculations and its experimental verification on the example of results of fatigue tests of Al-alloys and steels* (in Polish). Research project No. 2221/B/T02/2010/39, 2010.
6. Szala G., Ligaj B.: *Criteria for assessment of low-cycle and high-cycle fatigue in calculating fatigue life of structural elements* (in Polish). Logistyka, 6, 2009.
7. Mroziński S., Szala J.: *Problem of cyclic hardening or softening in metals under programmed loading*. Scientific Problems of Machines Operation and Maintenance, 4(164), vol. 45, Radom, 2010.
8. Szala J.: *Hypotheses of fatigue damage summation* (in Polish), Publishing House of Technical Agricultural Academy (Wydawnictwo Uczelniane Akademii Techniczno-Rolniczej), Bydgoszcz, 1998.
9. Ligaj B., Szala G.: *Analysis of loads in fatigue life tests and calculations of structural elements on the example of car operational loads* (in Polish), Logistyka, 6, 2009.
10. Fricke W., Petershagen H., Paetzold H.: *Fatigue Strength of Ship Structures, Part I: Basic Principles*. Germanischer Lloyd, Hamburg, 1997, pp. 34-36.
11. Fricke W., Petershagen H., Paetzold H.: *Fatigue Strength of Ship Structures, Part II: Examples*. Germanischer Lloyd, Hamburg, 1998, pp. 20-21.
12. Polski Rejestr Statków: *Fatigue strength analysis of ship's steel hull* (in Polish). Publication No. 45/P, Gdańsk, 1998, pp. 35-43.

CONTACT WITH THE AUTHORS

Bogdan Ligaj, Ph. D.,
 Grzegorz Szala, Ph. D.
 Faculty of Mechanical Engineering,
 University of Technology and Life Science,
 Prof. S. Kaliskiego 7
 85-763 Bydgoszcz, POLAND
 e-mail: bogdanj@utp.edu.pl

Dynamic response analysis of light weight pyramidal sandwich plates subjected to water impact

Hao Wang, Dr.,
Fei Zhao, Master Graduate Student,
Yuan-Sheng Cheng, Dr., Professor,
Jun Liu, Dr., Lecturer
Yuan Tian, Master Graduate Student,
School of Naval Architecture and Ocean Engineering,
Huazhong University of Science and Technology, Wuhan, P.R. CHINA

ABSTRACT

The fluid-solid interaction (FSI) dynamic responses for a Light Weight Pyramidal Sandwich Plate Structure (LWSPSPS) under different water-entry velocities (1m/s-6m/s) are investigated numerically and theoretically. The characteristics of impact pressure and structure deformation are obtained by using LS-DYNA code based on the proposed 3D multi-physics (air-water-solid) FEM model. Numerical results show that the average water impact pressure of LWSPSPS is much lower than that of the monolithic plate with same mass. Moreover, a phenomenon called "local air cushion" is observed for LWSPSPS which does not exist for a monolithic plate. Theoretical hydroelasticity analysis demonstrates that the FSI effect of LWSPSPS is weak when the ratio of water impact duration time to wet natural vibration period is greater than 4. In the study, an engineering estimation method to predict the maximum deformation of the LWSPSPS is proposed, in which the total deformation is divided into two parts, i.e. local field deformation and global field deformation, and they are both computed using analytical model. Good agreement between the numerical results and ones obtained from the proposed engineering estimation method is achieved. Furthermore, the geometric variation sensitiveness analysis is also conducted.

Keywords: light weight pyramidal sandwich plate structures (LWSPSPS); multi-physics numerical model; maximum deformation; quasi-static; local air cushion

INTRODUCTION

The water impact phenomenon exists in many practical engineering areas such as slamming of ship experienced boisterous weather and heavy sea, seaplane landing on water in an emergency situation et al. [1]. The significant local structural deformation may occur due to high peak water impact transient shock pressure in a very short duration [2]. Because of the severity and significance of slamming accident on naval vessels, many research efforts have been devoted during the past century. Since the late-1920s, the pioneer works of hull-water impacts have been investigated by analyzing a two-dimensional wedge impact on a calm water surface. Two of these early studies related to slamming problem of a rigid v-shaped wedge with small deadrise angle were carried out by Von Karman [3] and Wagner [4]. After then Chuang [5] performed the systematic tests with flat bottom panels in free fall against the free surface of the water in order to overcome the problem of the Von Karman asymptotic theory due to the lack of application for zero deadrise angles and to detect the effect of trapped air between the free surface and the plate on the dynamic response of the plate. He concluded that the effects

of air cushion cannot be neglected if the deadrise angle was less than 3 degree in his experiments.

The equivalent rigid/quasi-static method has been widely adopted in the design rule for water impact problem due to its convenience [2]. However, the hydroelastic interaction effects should not be neglected in the design of high-speed craft [6]. Thus the hydroelastic criterion and models have been developed from 90s in [7-10]. Generally, the hydroelastic effects of water impact event are typically characterized by a relation between the loading period and the natural vibration period of structure [7-10]. Most of the previous hydroelastic interaction investigations are limited to simple steel structures such as 2D transverse section with v-shaped section of a ship-hull.

In recent years, the mechanical behavior of composite materials and sandwich structure are widely concerned [11]. Kozak [12] presented a deep and extensive view on selected problems concerning application of steel sandwich plates in shipbuilding industry. To investigate the fluid-structure interaction (FSI) during the water impact process, Qin and Batra [13] developed a hydroelastic model based on a (3, 2)-order sandwich theory and 2D Wagner's water impact theory. The hydroelastic effect on hull's deflections and the unsteady water

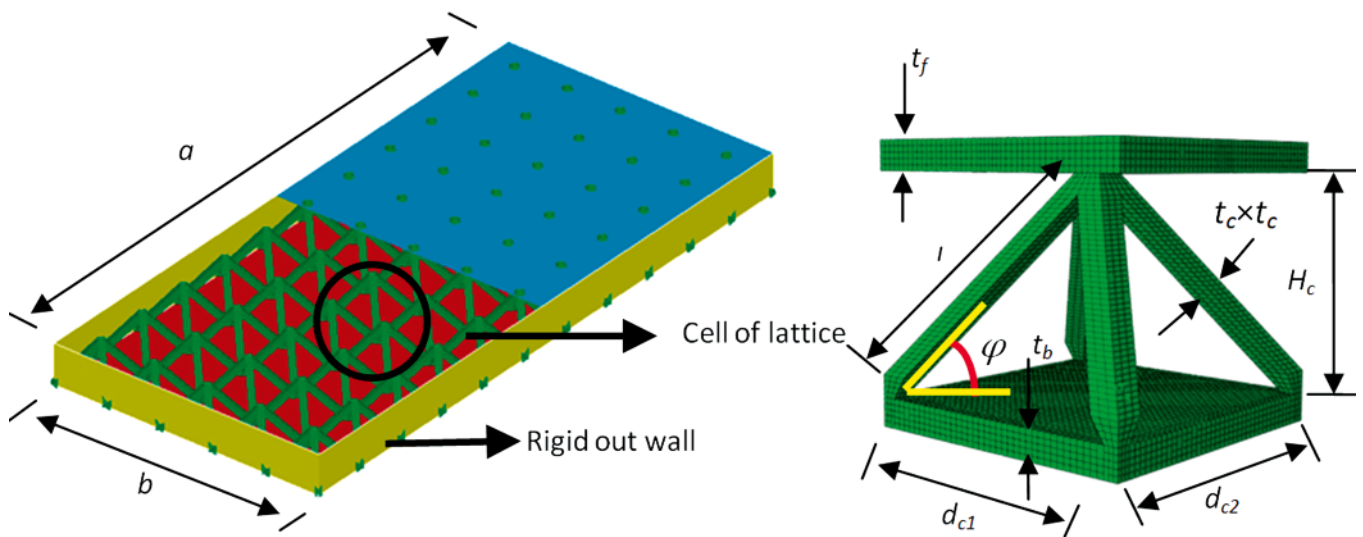


Fig. 1. Light weight sandwich plate structures with pyramidal lattice cores (LWSPSPS)

impact load has been delineated. Baral et al. [14] presented results from a test simulating the water impact (slamming) loading of sandwich boat structures. Test results suggested that a novel foam core reinforced in the thickness direction with pultruded carbon fiber pins would offer significant resistance to water impact load.

The lattice structures with various core topologies have now been recognized to be attractive candidates for multifunctional ultra-light structures due to their superior properties of light weight, high specific stiffness and excellent impulsive resistant performance et al. [15-18]. As the lattice structures are periodic micro-architected cellular solids in which the individual truss elements deform by stretching rather than by bending. Consequently, the dynamic behavior of sandwich plates with pyramidal lattice truss topology cores (LWSPSPS) is quite different from other traditional constructions, including those with honeycomb core or corrugated (prismatic) core et al. Most of the previous studies focused on the static mechanism and energy absorption behavior of LWSPSPS subjected to intense impact loading [15-18]. But the fluid-solid interaction (FSI) characteristics of LWSPSPS subjected to water impact load are neglected, which should also be considered due to the fact that LWSPSPS used in the construction of naval structures would be impacted in slamming conditions. Therefore, investigation should be undertaken on analyzing the hydroelastic pressure and deformation of LWSPSPS subjected to slamming load at present.

To this end, the present study first primarily concerns on the detailed dynamic characteristic and hydroelastic mechanism of sandwich plates with *pyramidal lattice truss topology cores* (LWSPSPS) subjected to water impact loading. The nonlinear explicit finite element (FE) software LS-DYNA is employed to build up the 3D multi-physics (air-water-solid) numerical model with the water modeled as an inviscid, compressible and non-irrotational fluid. In order to verify the FEM model, the central impact pressure values of circular solid plate are compared with experimental results. It is found that hydroelastic water impact pressure predicted by LS-DYNA agrees well with those experimental data. Furthermore, the detailed characteristics of hydroelastic water impact pressure and hull deformation of LWSPSPS are summarized and compared with those of the monolithic plates with equal mass. Then the hydroelastic effect of LWSPSPS is discussed theoretically by using the criteria of $2\tau_s/T$ (the ratio of water impact duration time $2\tau_s$ to the wet natural period T). Subsequent to calculate the maximum total elastic deformation of LWSPSPS, an engineering theoretical

estimation method is proposed, in which the total deformation is divided into two parts, i.e. local field deformation and global field deformation. Results from this proposed model agree well with those from the 3D FSI finite element analysis. Moreover, the individual effects of design parameters of LWSPSPS such as face sheet thickness, thickness of lattice core and relative density of core on the water impact pressure and structural deformation are also investigated in the study.

DESCRIPTION OF THE LWSPSPS GEOMETRY MODEL

To analyze the characteristic of LWSPSPS, the first step is to choose its different constituents. LWSPSPS consists of two thin face sheets attached to both sides of a light weight lattice core with an exposed area $595.1 \text{ mm} \times 270.5 \text{ mm}$ referred a practical monolithic flat panel of cruiser [19] (see Fig. 1). The mass of LWSPSPS (case 1 - case 6) is equal to the monolithic flat panel which the thickness of this mild steel monolithic flat panel is equal to 11.11 mm. The boundary condition of the panel can be taken as clamped [19]. Therefore, a sealed off round structure made by rigid materials (rigid out wall, see Fig. 1) is used to model clamped boundary condition (also see Fig. 1). The calculated parameters for all 22 cases are shown in Table 1.

NUMERICAL SIMULATION MODEL OF LWSPSPS

The hydroelastic performance of LWSPSPS subjected to water impact load is investigated using 3D multi-purpose, explicit and implicit finite element program LS-DYNA. Both Lagrangian and Eulerian solvers are available in LS-DYNA code to enable modeling of structures and fluids in a single model and to simulate the interaction between them. Interaction between the fluids and structures is achieved through arbitrary Lagrangian-Eulerian (ALE) description. In the fluid-structure coupling algorithm (typically, penalty coupling algorithm), two superimposed meshes are considered, a fixed Eulerian or ALE mesh for the fluid and a deformable Lagrangian mesh for the structure. Additionally, the ALE Multi-Material formulation is a method allowing the finite element mesh to move independently from the material flow and where each element in the mesh can contain a mixture of two or more different materials such as air and water. Therefore, ALE Multi-material formulation and penalty coupling algorithm [20-22] are adopted in the present 3D multi-physics numerical model

Tab. 1. Various computational cases considered

Case No.	a(cm)	b(cm)	$d_{c1} = d_{c2}$ (mm)	$\tan(\varphi)$	t_r (mm)	t_b (mm)	H_c (mm)	$t_c \times t_c$ (mm \times mm)	v (m/s)
C1	59.51	27.05	54.10	1.00	4.219	4.219	38.25	6.00 \times 6.00	5
C2	59.51	27.05	54.10	1.00	4.219	4.219	38.25	6.00 \times 6.00	1
C3	59.51	27.05	54.10	1.00	4.219	4.219	38.25	6.00 \times 6.00	2
C4	59.51	27.05	54.10	1.00	4.219	4.219	38.25	6.00 \times 6.00	3
C5	59.51	27.05	54.10	1.00	4.219	4.219	38.25	6.00 \times 6.00	4
C6	59.51	27.05	54.10	1.00	4.219	4.219	38.25	6.00 \times 6.00	6
C7	59.51	27.05	54.10	1.00	4.219	2.219	38.25	6.00 \times 6.00	5
C8	59.51	27.05	54.10	1.00	4.219	3.219	38.25	6.00 \times 6.00	5
C9	59.51	27.05	54.10	1.00	4.219	5.219	38.25	6.00 \times 6.00	5
C10	59.51	27.05	54.10	1.00	4.219	6.219	38.25	6.00 \times 6.00	5
C11	59.51	27.05	54.10	1.00	2.219	4.219	38.25	6.00 \times 6.00	5
C12	59.51	27.05	54.10	1.00	3.219	4.219	38.25	6.00 \times 6.00	5
C13	59.51	27.05	54.10	1.00	5.219	4.219	38.25	6.00 \times 6.00	5
C14	59.51	27.05	54.10	1.00	6.219	4.219	38.25	6.00 \times 6.00	5
C15	59.51	27.05	54.10	0.48	4.219	4.219	18.25	6.00 \times 6.00	5
C16	59.51	27.05	54.10	0.74	4.219	4.219	28.25	6.00 \times 6.00	5
C17	59.51	27.05	54.10	1.26	4.219	4.219	48.25	6.00 \times 6.00	5
C18	59.51	27.05	54.10	1.52	4.219	4.219	58.25	6.00 \times 6.00	5
C19	59.51	27.05	54.10	1.00	4.219	4.219	38.25	5.00 \times 5.00	5
C20	59.51	27.05	54.10	1.00	4.219	4.219	38.25	5.50 \times 5.50	5
C21	59.51	27.05	54.10	1.00	4.219	4.219	38.25	6.50 \times 6.50	5
C22	59.51	27.05	54.10	1.00	4.219	4.219	38.25	7.00 \times 7.00	5

to simulate water impact phenomenon. The detailed description of ALE formulation and penalty coupling algorithm is provided in References [20-21].

Constitutions of solid

The LWSPSPS is made of mild steel for marine industry [23]. For the constitutive law of this steel, the kinematic hardening rule and elastic-linear work-hardening model are adopted in the analysis. And the materials properties are described as follows [19]:

- Modulus of elasticity $E = 206.85$ GPa;
- Yielding strength $\sigma_Y = 206.85$ MPa;
- Density $\rho_s = 7850$ kg/m³;
- Poisson ratio $\nu = 0.3$;
- Tangential modulus $E_t = 250$ MPa.

Generally, the effect of strain rate is sufficiently important to analyze the dynamic responses of structures. The plastic kinematic hardening description is commonly used in these impact analyses, which is a strain rate dependent elastic-plastic

model. In the analysis, strain rate is taken into account by using the Cowper-Symonds model [23] which scales the yield stress by the strain rate dependent factor. According to Ref. [24], the strain-rate sensitivity model provides a reasonably good representation of test results up to strain rate of 1000 S⁻¹. Eq. (1) shows the relationship between the stress ratio and the plastic strain rate [23]. The dynamic yield stress σ_{YD} is a function of plastic strain rate and can be expressed as follow:

$$\frac{\sigma_{YD}(\dot{\epsilon}_{pl})}{\sigma_Y} = 1 + \left(\frac{\dot{\epsilon}_{pl}}{D_{cs}} \right)^{1/q} \quad (1)$$

where the Cowper-Symonds strain rate parameters D_{cs} and q have values of 40.4 S⁻¹ and 5 for mild steel in this study [23], and σ_Y is the initial static yield stress of the material.

Equation of state

In general, the equation of state (EOS) specified for water is a Gruneisen equation and it can be used to calculate the internal characteristics of seawater. It properly handles wave propagation

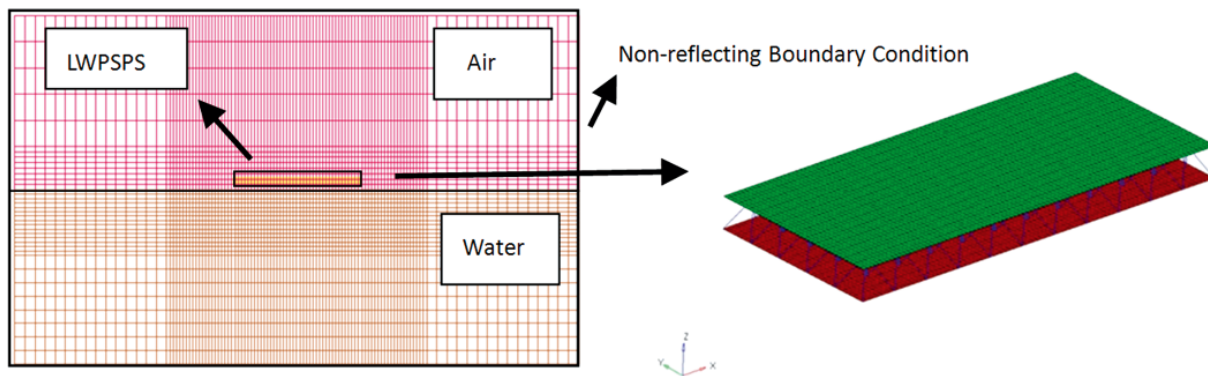


Fig. 2. 3D multi-physics finite element model of air, water and LWSPS

phenomenon in water impact events by incorporating a non-linear shock velocity-particle velocity relationship. And this equation addresses fluid under tension/compression which can capture cavitation phenomena in seawater. The Gruneisen EOS is defined as follow:

$$p_{\text{water}} = \frac{\rho_{w0} C \mu \left[1 + \left(1 - \frac{\gamma_0}{2} \right) \mu - \left(\frac{\eta}{2} \right) \mu^2 \right]}{\left[1 - (S_1 - 1) \mu - S_2 \frac{\mu^2}{(1 + \mu)} - S_3 \frac{\mu^3}{(1 + \mu)^2} \right]} + (\gamma_0 + \eta \mu) e \quad (2)$$

where e is the internal energy per unit volume, C is the intercept of the us-up curve, S_1 , S_2 , and S_3 are the coefficients of the slope of the us-up curve, γ_0 is the Gruneisen gamma, and η is the first-order volume correction to γ_0 . The constants C , S_1 , S_2 , S_3 , γ_0 , and η et al. are all input constant parameters [20]: reference sea water density $\rho_{w0} = 1025 \text{ kg/m}^3$; sea water temperature $T = 20^\circ\text{C}$; speed of sound in water $C_0 = 1480 \text{ m/s}$; dynamic viscosity coefficient $\nu_s = 1.13\text{E-}03 \text{ N}\cdot\text{s/m}^2$; intercept of us-up curve $C = 2417 \text{ m/s}$; Gruneisen coefficient $S_1 = 1.41$, $S_2 = 0$, $S_3 = 0$; Gruneisen gamma $\gamma_0 = 1.0$; first-order volume correction to gamma $\eta = 0$; internal energy of water per specific volume $e = 1.89 \text{ E} + 06 \text{ J/m}^3$; related volume at time 0 to reference specific volume is equal to 1.

And the compression of sea water is defined in terms of relative volume V as:

$$\mu = \frac{1}{V} - 1 = \frac{\rho_w}{\rho_{w0}} - 1 \quad (3)$$

where ρ_{w0} is the reference sea water density; ρ_w is the overall sea water density.

In LS-DYNA, the perfect gas law (gamma law) is used as the equation of state for air. This equation of state is given by [20]:

$$p_{\text{air}} = (\gamma - 1) \frac{\rho_{\text{air}}}{\rho_{\text{air}0}} e_0 \quad (4)$$

where ρ_{air} is the overall air density for perfect gas, e_0 is the internal energy of air per unit mass and γ is the adiabatic expansion coefficient. Here, $\gamma = 1.40$, $e_0 = 2.11 \text{ E} + 06 \text{ J/kg}$ and $\rho_{\text{air}0} = 1.239 \text{ kg/m}^3$ are conducted in the present study for perfect gas.

Finite element model and verification

Fig. 2 shows the 3D multi-physics finite element model adopted in the simulation. The face sheets of LWSPS are modeled as Lagrangian Belytschko-Tsay shell elements (see

Fig. 2), where the lightweight lattice cores are modeled as Hughes-Liu beam elements, seawater and air are modeled as Euler solid elements (see Fig. 2). The dimensions of the water region for the 3D finite element model are $2.6 \times 1.3 \times 0.8 \text{ m}^3$ while those of the air region are also $2.6 \times 1.3 \times 0.8 \text{ m}^3$.

In general, it is known that the results based on ALE algorithm are sensitive to the Euler mesh density. The Euler mesh needs to be fine enough to capture the highest gradients in the pressure fields, yet a coarser mesh is favorable in terms of computational cost. Furthermore, for the selection of the contact stiffness in penalty based contact algorithm, it is required that the maximum pressures are approximately known ahead. So the non-physical contact penetration can be controlled [20-22].

Hence, the Euler mesh density and parameters of contact penetration stiffness in simulation are firstly verified by water impact experimental results provided in literature [25]. With four different impact velocities, a circular monolithic plate (made by 6061-T6 aluminum alloy, thickness = 11.5 mm, diameter = 200.0 mm) free falls on to the water surface. The simulation model of this circular plate is similar to that of LWSPS, as shown in Fig. 2. The other detailed description of these water impact experiments can be found in reference [25]. The material constants for 6061-T6 aluminum alloy conducted in the numerical validation analysis of this circular plate model are: $E = 68.94 \text{ GPa}$, $E_t = 0.7 \text{ GPa}$, $\nu = 0.33$, $\rho_{\text{al}} = 2700 \text{ kg/m}^3$ and $\sigma_y = 352 \text{ MPa}$ [26].

Water impact velocities employed in these experiments are 1.40 m/s, 1.98 m/s, 2.43 m/s and 2.80 m/s respectively. When the Euler mesh size is about 1.0 cm, the high frequent oscillations in the pressure curve are not obvious, and the peak FSI pressure results are found acceptable compared with experimental results in Table 2.

Tab. 2. Tabulated central hydroelastic pressure results for aluminum alloy plates

Case	1.40 [m/s]	1.98 [m/s]	2.43 [m/s]	2.80 [m/s]	Average
Pressure-Experiment [KPa][25]	56.90	76.52	105.95	138.45	—
Pressure-Numerical [KPa]	62.07	76.66	114.40	151.02	—
Relative Error	9.08%	0.18%	7.97%	9.07%	6.58%

Water impact FSI pressure

The empirical expressions are commonly used to describe the hydrodynamic impact pressure. Yuzuru (1954) [25], Chuang

(1970) [5] and Jones (1973) [27] all proposed typical equations which are as follows:

1. Yuzuru (1954) [25]

$$p_{\max} = kv^{1.56} \quad (5a)$$

2. Chuang (1970) [5]

$$p_{\max} = A = Bv \quad (5b)$$

3. Jones (1973) [27]

$$p_{\max} = kv^2 \quad (5c)$$

Notations A, B and k in Eqs. (5) are constants based on the geometry dimensions and material properties of structure. It can be observed that the main difference of Eqs. (5) is the selection of the powers of velocity v. The unified expression of Eqs. (5) is below:

$$p_{\max} - p_{\infty} = kv^{\alpha} \quad (6a)$$

or:

$$\ln(p_{\max} - p_{\infty}) = \ln(k) + \alpha \ln(v) \quad (6b)$$

where p_{∞} is atmosphere pressure; α and k are also the parameters based the geometry dimensions and material properties of structure.

The water impact loading pressure of LWSPSPS in terms of $\ln(v)$ for six different free fall velocities (C1-C6) are shown in Fig. 3. For comparison, the numerical results of monolithic flat panels with the same mass are also given in Fig. 3. According to the simulation results plotted in Fig. 3, the following observations can be drawn:

- The performance of central water impact pressure for both monolithic plate and LWSPSPS follows a linear trend, as determined from a least square linear fit:

$$\ln(p_{\max} - p_{\infty}) = 3.75 + 1.64 \ln(v) \quad (7a)$$

$$\ln(p_{\max} - p_{\infty}) = 4.05 + 1.44 \ln(v) \quad (7b)$$

- By means of the least square linear fit, the average FSI pressure for monolithic plate and LWSPSPS is also determined:

$$\ln(p_{\max} - p_{\infty}) = 2.71 + 2.03 \ln(v) \quad (7c)$$

$$\ln(p_{\max} - p_{\infty}) = 2.63 + 1.69 \ln(v) \quad (7d)$$

- During the hull-water impact, the advantage of LWSPSPS decreasing peak pressure amplitude on entire FSI surface at high impact velocity ($>2\text{m/s}$) is observed. But the difference of water impact pressure characteristics between LWSPSPS and monolithic plate located in the central point is insignificant.

- The values of α and k are constants though the range of water impact pressure varies widely. This conclusion has been identified by previous experimental results of solid plate [5, 25, 27]. Furthermore, the value of α of average FSI pressures for LWSPSPS is close to 1.69, which is lower than the one of monolithic plate ($= 2.03$).

As a summary, the impulsive shapes are shown in Fig. 4. A more precise two parameters parabolic mathematical expression is defined as follows, which is different from the expressions conducted in the literature [27-29]:

$$p(t) = \begin{cases} K_1 t^2 + K_2 t, & 0 \leq t \leq 2\tau_s \\ 0, & 2\tau_s \leq t \end{cases} \quad (8a)$$

where:

$$K_1 = -\frac{p_{\max}}{\tau_s^2}, K_2 = \frac{2p_{\max}}{\tau_s}, p_{\max} = kv^{\alpha} \quad (8b)$$

where p_{\max} is the maximum value of water impact pressure impulse; $2\tau_s$ is the duration time of impulse.

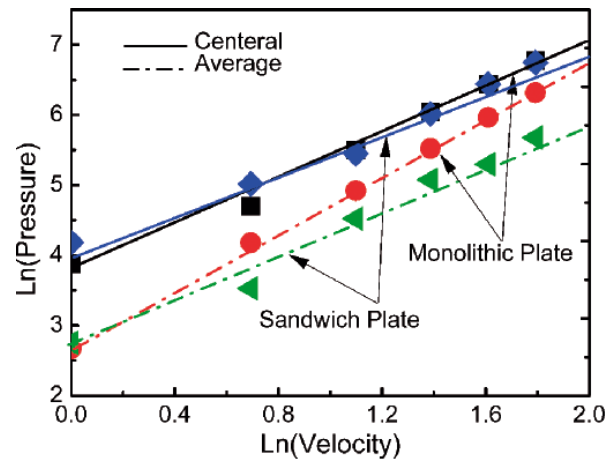
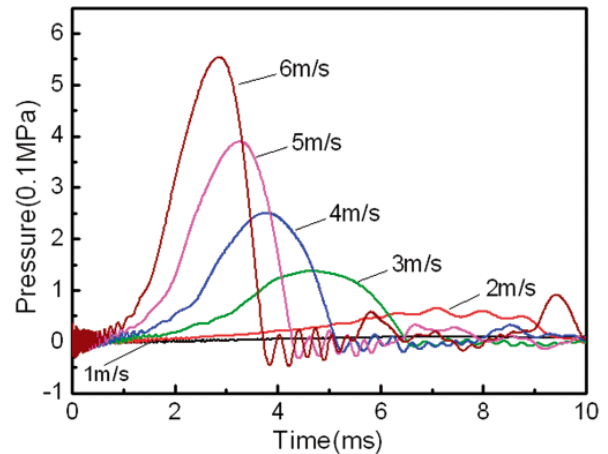
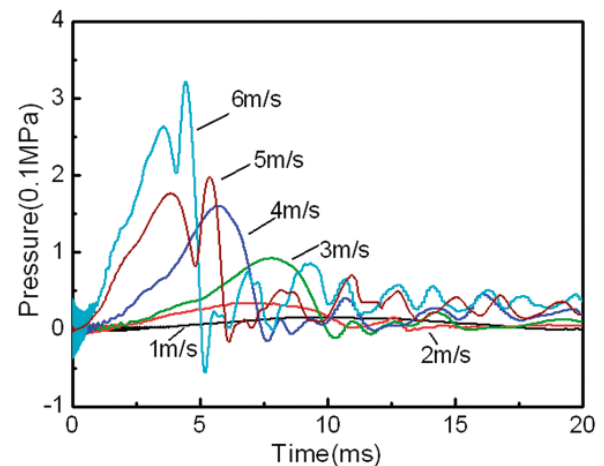


Fig. 3. Peak pressure of monolithic plate and LWSPSPS at different water impact velocity



a) Monolithic plate



b) LWSPSPS

Fig. 4. Pressure time history of water impact for monolithic plate and LWSPSPS (C1-C6)

If the peak impulsive pressure p_{\max} is observed in Eqs. (7), the objective now is to determine the duration time of impulsive $2\tau_s$. The pulse pressure loading time of circular plate has been suggested by Chuang [4] as following estimation:

$$2\tau_s \cong \frac{4r}{C_0} \quad (9a)$$

where r is the radius of circular plate; C_0 is the sound speed of air ($C_0 = 340$ m/s). For rectangular plates, the peak pulse pressure loading time can be modified as [4]:

$$2\tau_s \cong \frac{2\sqrt{a^2 + b^2}}{C_0} \quad (9b)$$

It is obtained that the $2\tau_s$ of monolithic panel in the present research is nearly 4.0 ms from Eq. (9b). This estimation is consisted with the numerical results in Fig. 4. Furthermore, the duration time of impulse $2\tau_s$ is less sensitive to the variation of water impact velocity. As shown in Fig. 4, the water impact loading time of LWSPSPS is longer than that of solid plate. Based on the numerical results, a modified estimation of $2\tau_s$ for LWSPSPS is given by:

$$2\tau_s \cong \frac{(2.1 \sim 2.6)\sqrt{a^2 + b^2}}{C_0} \quad (10)$$

It is observed that the impulsive duration time $2\tau_s$ for all cases of LWSPSPS is 4.50 ms-5.50 ms from Eq. (10).

Moreover, the results obtained from fluid materials volume distribution iso-surface in initial water entry period show that an interesting phenomenon - "local air cushion" exists during the initial water impact duration (see the dashed line in Fig. 5). But this interesting phenomenon does not exist in initial water impact period of monolithic plate. This local cushion is mainly caused by lattice cell local deformation which has significant effects on the water impact pressure and dynamic responses of LWSPSPS. Because of the existence of this *local air cushion*, which plays a role as a buffer device, the peak value of average FSI pressure of contacted-water wet face sheet of LWSPSPS is much lower than that of monolithic plate (see Fig. 3). Additionally, as shown in Fig. 4b, the high frequency components of hydroelastic pressure curve for LWSPSPS are excited by the local cell deformation.

THEORETICAL ANALYSIS: HYDROELASTICITY ASSESSMENT AND DEFORMATION CALCULATION

Basic vibration characteristics of monolithic plate and LWSPSPS

In order to evaluate the hydroelastic effects in section 4.2, the fundamental frequency f (f_s) of bending vibration mode for solid plate (LWSPSPS) with clamped supported

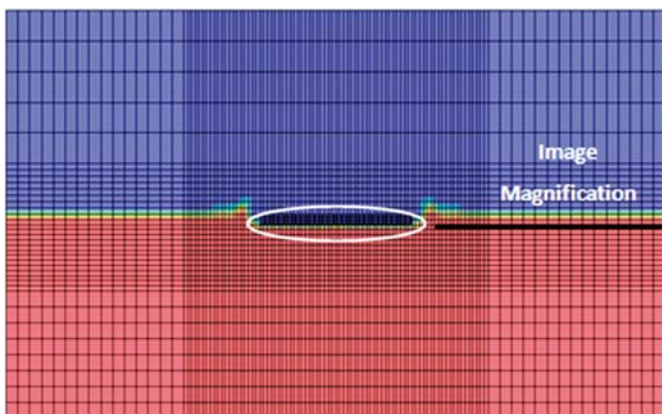


Fig. 5. Fluid volume distribution of initial entry period of LWSPSPS and free surface contour iso-surface

boundaries is calculated firstly. The fundamental frequency f of bending vibration modes of a clamped monolithic plate [30] is given by:

$$2\pi f = \omega = \sqrt{\frac{16\pi^4 D}{9 m_0} \left(\frac{3}{a^4} + \frac{3}{b^4} + \frac{2}{a^2 b^2} \right)} \quad (11)$$

where m_0 is the mass unit area, D is the bending stiffness of plate, a and b are the length and the width of plate. In the present analysis, the fundamental frequency f of this monolithic plate is 938 Hz and the analytical result is in good agreement with the FEM simulation result (922 Hz).

Because of the discrete characteristics of lattice truss core, the calculation of the natural frequency of LWSPSPS is much more complicated. Usually, the generalized equivalent model can be mostly used in the preliminary analysis stage of design process. It can be used to reduce the time spent for the analysis of LWSPSPS. The homogenization method also makes it possible to avoid the problems involved in heterogeneities. Here, a new equivalent method to calculate the fundamental bending vibration frequencies of LWSPSPS is proposed as follows (Fig. 6):

- Step 1: calculate the equivalent shear rigidity of LWSPSPS lattice core.

There are a few methods to calculate the equivalent shear constant of lattice materials. Liu [31] proposed a matrix displacement method of lattice truss based on the small displacement assumption. Therefore, this homogenization method is employed here to calculate the shear rigidity of LWSPSPS lattice core as follows:

$$\bar{\rho}_c = \rho_s \frac{2t_c^2}{l^2 \cos^2 \varphi \sin \varphi} \quad (12a)$$

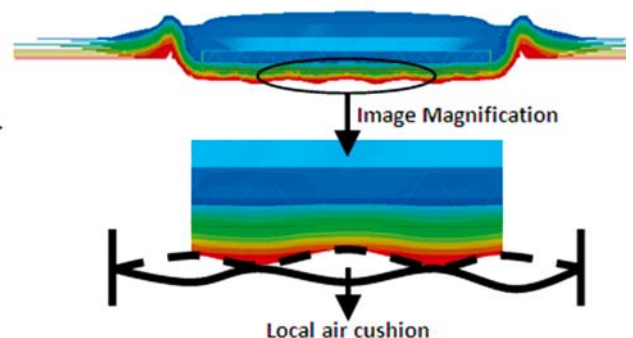
$$E_c = E \bar{\rho}_c \sin^4 \varphi \quad (12b)$$

$$C_G = \frac{[H_c + (t_f + t_b)/2]^2}{H_c} \begin{bmatrix} C_{55}^H & C_{54}^H \\ C_{45}^H & C_{44}^H \end{bmatrix} \quad (12c)$$

where $\bar{\rho}_c$ is the relative density of this lattice core [32], E_c is the normal modulus of LWSPSPS core [32], C_G is the transverse shear rigidity matrix of LWSPSPS core (the detailed expressions of the homogenized moduli of lattice core $C_{\alpha\beta}^H$, ($\alpha, \beta = 4, 5$) can be found in literature [31]), the definitions of l , φ and t_c can be seen in Fig. 1 and ρ_s is the material density of the cell structure.

- Step 2: calculate the bending rigidity of LWSPSPS.

For the thin face sheets of LWSPSPS, only bending deformation is considered (the bending stiffness D_f of face



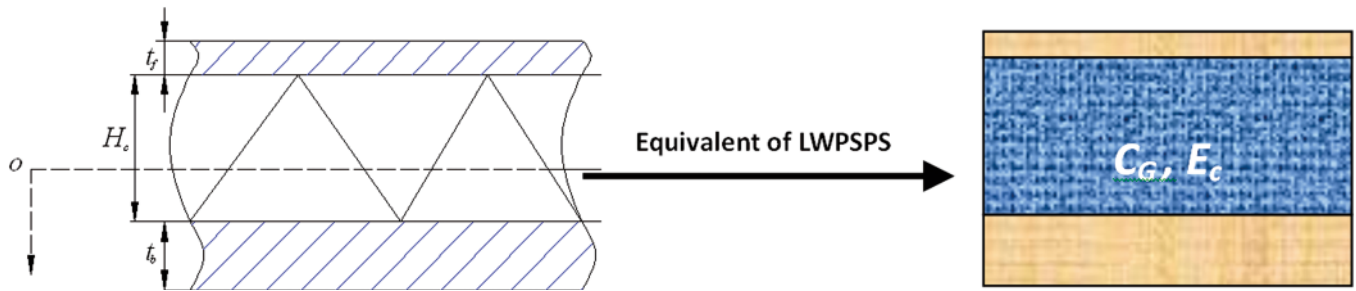


Fig. 6. Equivalent model of LWSPSPS

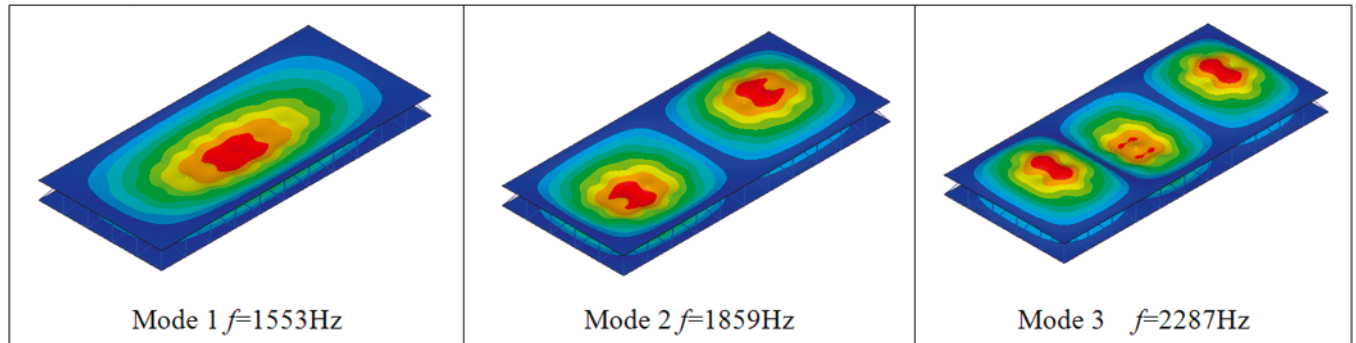


Fig. 7. The 1st - 3rd bending vibration modals of LWSPSPS (Case1)

sheets is included). The bending stiffness of sandwich panel (LWSPSPS) with face layers of non-equal thickness [33] is given by:

$$D_1 = \frac{E((H_c + t_f + t_b)^3 - H_c^3)}{12(1 - \nu^2)} \quad (13)$$

$$\cdot \left(1 - \frac{3(t_f - t_b)^2}{\left(1 + \frac{H_c}{(H_c + t_f + t_b)} + \frac{(H_c + t_f + t_b)}{H_c} \right) (t_f + t_b)^2} \right)$$

The meanings of all nomenclatures are given in Fig. 1 and Fig. 6.

- Step 3: calculate the natural frequency of LWSPSPS with clamped supported boundary conditions.

If the bending rigidity and shear rigidity of LWSPSPS are obtained in step 1 and step 2, the last step is to calculate the natural frequency with clamped supported boundary conditions. In this key step, an approximate method [34] is adopted to analyze the fundamental vibration frequency of the LWSPSPS. Due to the complexity of approximate mathematic equations, only the calculation results are given here. Detailed steps of solving approximate equations can be found in literature [34-35].

The first modal frequency f_s of LWSPSPS (Case 1) based on the equivalent-approximate method is 1698 Hz which is close to the FEM result (1553 Hz) in Fig. 7 (the error is 9.34 %). It must be pointed out that the equivalent-approximate method is more accurate in high frequencies [35]. Thus, the error between FEM numerical result and equivalent approximate result for the second (third) bending vibration frequency is less than 5 %.

Analysis of hydroelastic effect

As mentioned in the previous section, the transient response of a free fall structure subjected to hull-water impact loading is greatly complicated. The evaluation of hydroelastic (FSI) effect

is an important part of this investigation topic. In Ref. [8], the hydroelastic effect indicator is formulated by Bereznitski:

$$R_B = T_{LPB}/T_{NPB} \quad (14)$$

where T_{LPB} is the water impact loading time, and T_{NPB} is the first dry natural period of vibration. Compared Eq. (14) with the definition $2\tau_s f_s$ (or $2\tau_s f$), it is found that these two expressions have the same physical meaning. Bereznitski [8] concluded that the hydroelastic effects become important when a ratio R_B (or $2\tau_s f_s$) $< R_{Blim}$, where $R_{Blim} \approx 2.0$.

Jones also pointed out that the responses of structure can be seen as quasi-static if the duration of water impact loading time $2\tau_s$ is much longer than the first natural bending vibration period T ($2\tau_s \gg T$) [27]. In fact, for a single-degree spring-mass system (SDOF), the deformations calculated for the same load applied statically agree with the corresponding maximum dynamic deformations to within approximately 17 % when $2\tau_s/T > 1.75$ [36].

According to Eq. (11), the responses of this clamped plate can be seen as quasi-static ($2\tau_s f_s \approx 4.2 - 5.2 > 2.0$). For LWSPSPS, the multiplication $2\tau_s f_s$ ($2\tau_s = 4.50 - 5.50$ ms, $f_s = 1560$ Hz) is 6.8-8.3. Thus, the dynamic responses of LWSPSPS in the present case can also be seen as quasi-static. Normally, this criterion is absolutely true as a matter of fact that the slamming duration time is about 0.02 s - 0.1 s in practical case [19], which is much longer than that of the present investigation.

While the dynamic inertial effect cannot be ignored, the calculation of dynamic deflection in linear elastic range under uniform impact pressure is given by following equation [36]:

$$K(t) = \frac{w_d(t)}{w_s} = \frac{\omega}{p_{max}} \int_0^t p(\tau) \sin \omega(t - \tau) d\tau \quad (15)$$

where $K(t)$ is the dynamic inertial effect factor function, ω is the first circular frequency of structure, p_{max} is the peak pressure value of impact, $p(\tau)$ is the formula of impact loading, $w_d(t)$ is the load-deflection function and w_s is the static deflection of structure under uniform maximum pressure p_{max} . The maximum value of $K(t)$ at $t = t_0$ is commonly considered in the practical case, which satisfies the following conditions:

$$\frac{dK(t)}{dt} = 0 \Big|_{t=t_0}, \frac{d^2K(t)}{dt^2} < 0 \Big|_{t=t_0} \quad (16)$$

In this study, the maximum value of $K(t)$ (Here it is defined as η_{sd}) can be easily calculated for monolithic plate based on Eqs. (7)-(10) and Eqs. (15)-(16). The value of K is only associated with the fundamental circular frequency ω and the impact duration time $2\tau_s$ in Eq. (15). If the fundamental frequency is obtained in the previous section 4.1, the maximum value of $K(t)$ for LWSPSPS (Here it is defined as η_{sd}^s) can be calculated from Eqs. (15)-(16).

In the present investigation, η_{sd} (for monolithic plate) is equal to 1.20 - 1.25. For LWSPSPS, η_{sd}^s is equal to 1.05 - 1.10. Compared with computation results, the values for η_{sd} and η_{sd}^s are both verified reasonable. Therefore, the values of η_{sd} (1.20 ~ 1.25) and η_{sd}^s (1.05 ~ 1.10) indicate that the dynamic inertial effects is not remarkable during the water impact process in these cases.

Considering the added mass of the first vibration modal of structure for a v-shaped ship section, a similar definition given by Stenius et al. [6, 10, 37] is defined as follow:

$$R = T_{LP}/T_{NP} \quad (17)$$

where T_{LP} is the loading period based on the Wagner theory, and T_{NP} is the first wet natural period of vibration. It is concluded that the hydroelastic effects are negligible and the response can be set as quasi-static for $R > 4$ [6, 10, 37].

Obviously, the first wet natural period of vibration T_{NP} is longer than the first dry natural period of vibration T_{NPB} . Though a detailed hydroelastic analysis of two-dimensional v-shaped transverse section was conducted in [6, 10, 37], the hydroelastic problem of a flat panel with zero wedge deadrise angle are neglected in previous investigations.

The indicator of hydroelastic effect introduced by Berezniński [8] and the inertia effect indicator introduced by Jones [27] are both based on the dry natural period of vibration. However, the added water mass is not considered in their analysis. Pointed out by Stenius et al. [6, 10, 37], hydroelastic effects incorporate both dynamic inertial effect and added mass effect. Thus, the added water mass should be considered in the evaluation of hydroelastic effects.

For a rectangular clamped monolithic plate with one face contacted with water, the added water mass coefficient is defined as f_A/f according to Ref. [30]:

$$\frac{f_A}{f} \cong \frac{1}{\sqrt{1 + \zeta \frac{a}{\gamma_s t}}} \quad (18)$$

where f is the first dry natural frequency of vibration, f_A is the first wet natural frequency of vibration, t is the thickness of this rectangular monolithic panel, γ_s is the specific gravity of steel (here $\gamma_s = 7.85$), a is the length of this monolithic plate and ζ is the constant based on the length-width ratio of a/b . In the present case, the ratio of a/b is equal to 2.2 and the value f_A/f is equal to 1.34. According to this observation, the first wet natural frequency of vibration f_A is equal to 699 Hz which is consistent with the result (677 Hz) obtained by FSI vibration analysis in ANSYS by using acoustic fluid element Fluid30 [38].

As the FSI occurs, the calculation of wet natural frequencies of LWSPSPS (here it is defined as f_A^s) is greatly complicated. Up to now, no study analyzed the FSI vibration characteristic of LWSPSPS. Thus, the acoustic-solid coupling method in commercial code ANSYS is adopted to calculate the wet

natural frequencies of LWSPSPS. The fluid is also modeled as non-viscous acoustic fluid element Fluid30, and Lagrange elements (shell 63 and beam 181) are adopted for solid parts (face sheets and core trusses); where the sum of all elements is nearly 80,000. When the added water mass effect is taken into account, the first wet natural frequency of LWSPSPS is 1034 Hz for Case 1 - Case 6, which is about 2/3 of the first dry natural frequency (1553 Hz).

Once the first wet natural frequency of LWSPSPS is obtained, the hydroelastic indicator of R can be calculated. By applying Eq. (14), the value of hydroelastic indicator R for LWSPSPS (C1-C6) is 4.653 - 5.687 ($2\tau_s = 4.50 - 5.50$ ms). In Ref. [6, 10, 37], Stenius et al. concluded that the hydroelastic effects are negligible when $R > 4$. Thus, one could give a definitive conclusion that the hydroelastic effect of LWSPSPS is not significant based on this criteria.

This conclusion can be validated from 3D FEM FSI simulation results (3D-FEM-FSI), 3D FEM dynamics simulation results (the FSI effects are not considered, 3D-FEM-Dynamic) and 3D FEM quasi-static simulation results (3D-FEM-Static) in Fig. 8. The comparison of these analyses shows that the results of 3D-FEM-FSI and 3D-FEM-Dynamic are very close, which means the hydroelastic effect is not significant. As shown in Fig. 8, due to the neglect of inertial effect, the quasi-static results are slightly lower than the results of dynamic calculation.

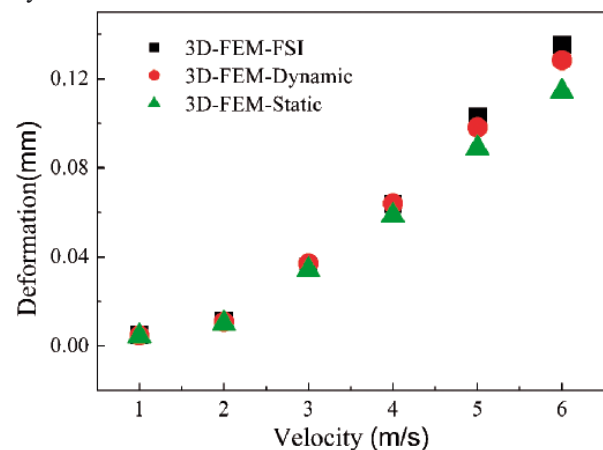


Fig. 8. Comparison of 3D-FEM-FSI, 3D-FEM-Dynamic and 3D-FEM-Static Results

4.3. Engineering approach of maximum deformation for LWSPSPS

Next, the analytical investigations are performed to study the deformation characteristics of LWSPSPS. As shown in Fig. 9, the inflection points exist at adjacent lattice core cells. The total deformation field of LWSPSPS can be divided into two components:

- 1) The global bending deformation field of LWSPSPS ($w_{max,T}$).
- 2) The local bending deformation field of each cell ($w_{max,L}$).

Based on this deformation field assumption, a mathematical model to describe the total maximum deformation field is presented as follow:

$$W_{max} = W_{max,T} + W_{max,L} \quad (19)$$

- Calculation of the global bending deformation $w_{max,T}$. The global linear elastic maximum deformation $w_{max,T}$ of sandwich plate with clamped boundary condition under static uniform pressure is given by [35]:

$$w_{\max,T} = \frac{4 p_{\max} a^4}{\pi^4 D_1} \sum_{m=1,3,\dots}^{\infty} \frac{(-1)^{\frac{(m-1)}{2}}}{m^5} \cdot \left[\left(1 - \frac{\alpha_m \operatorname{th}(\alpha_m) + 2}{2 \operatorname{ch}(\alpha_m)} \right) - \delta_m \left(1 - \frac{1}{\operatorname{ch}(\alpha_m)} \right) \right] + \sum_{m=1,3,\dots}^{\infty} (-1)^{\frac{(m-1)}{2}} \left(\frac{\alpha_m \operatorname{th}(\alpha_m)}{2 m^2 \pi^2 \operatorname{ch}(\alpha_m)} \frac{a^2}{D_1} H_m \right) + \sum_{n=1,3,\dots}^{\infty} (-1)^{\frac{(n-1)}{2}} \left(\frac{\alpha_n \operatorname{th}(\alpha_n)}{2 n^2 \pi^2 \operatorname{ch}(\alpha_n)} \frac{a^2}{\alpha^2 D_1} G_n \right)$$

$$\alpha_m - (\alpha_m \operatorname{th}(\alpha_m) - 1) \operatorname{th}(\alpha_m) +$$

$$+ 2 \delta_m \left(\operatorname{th}(\alpha_m) - \frac{m \pi}{\eta_m} \operatorname{th}(\alpha_m) \right) H_m + \sum_{n=3}^{\infty} \frac{8 n m^2}{\alpha} \quad (20b)$$

$$\cdot \left[\frac{1}{\alpha^3 \pi \left(\frac{m^2}{\alpha^2} + n^2 \right)^2} - \frac{\delta_m}{m^2 \pi} \left(\frac{1/\alpha}{\frac{m^2}{\alpha^2} + n^2} - \frac{\pi^2}{\alpha \eta_n^2 + \frac{m^2 \pi^2}{\alpha}} \right) \right] G_n +$$

$$+ \frac{1}{m^3} \left[(\alpha_m \operatorname{th}(\alpha_m) + 1) \operatorname{th}(\alpha_m) - \alpha_m \right] p_{\max} = 0$$

$$\alpha_n - (\alpha_n \operatorname{th}(\alpha_n) - 1) \operatorname{th}(\alpha_n) +$$

$$+ 2 \delta_n \left(\operatorname{th}(\alpha_n) - \frac{n \pi}{\eta_n} \operatorname{th}(\alpha_n) \right) G_n + \sum_{n=3}^{\infty} \frac{8 m n^2}{\alpha} \quad (20c)$$

$$\cdot \left[\frac{1}{\pi \left(\frac{m^2}{\alpha^2} + n^2 \right)^2} - \frac{\delta_m}{n^2 \pi} \left(\frac{1/\alpha}{\frac{m^2}{\alpha^2} + n^2} - \frac{\pi^2}{\frac{\eta_m^2}{\alpha^2} + n^2 \pi^2} \right) \right] H_m +$$

$$+ \frac{1}{\alpha^2 n^3} \left[(\alpha_n \operatorname{th}(\alpha_n) + 1) \operatorname{th}(\alpha_n) - \alpha_n \right] p_{\max} = 0$$

$$\alpha_m = \frac{m \pi b}{2a}, \quad \eta_m = \left[m^2 \pi^2 + \frac{2}{\delta_a (1-\nu)} \right]^{1/2}, \quad (20d)$$

$$\delta_a = \frac{D_1}{C_G a^2}, \quad \delta_m = m^2 \pi^2 \delta_a$$

$$\alpha_n = \frac{n \pi a}{2b}, \quad \eta_n = \left[n^2 \pi^2 + \frac{2}{\delta_b (1-\nu)} \right]^{1/2}, \quad (20e)$$

$$\delta_b = \frac{D_1}{C_G b^2}, \quad \delta_n = n^2 \pi^2 \delta_b$$

where C_G is the equivalent shear stiffness of lattice core and p_{\max} is the maximum value of average FSI pressure, the other nomenclatures have the same meanings as mentioned in the

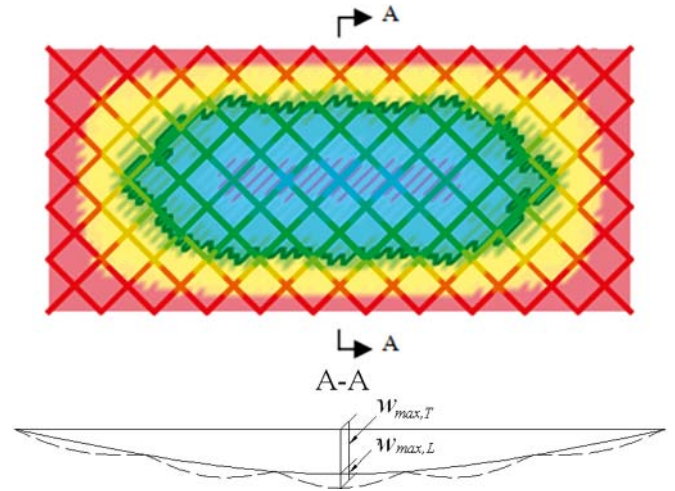


Fig. 9. The out-plane deflection counters plot of LWSPS

previous section. Firstly, the bending and shear stiffness of lattice core D_1 and C_G are calculated from Eqs. (12) - (13). Then the coefficient H_m and G_n are obtained from Eq. (20b) and Eq. (20c). If all the parameters in Eqs. (20b) - (20e) are observed, the maximum static deformation can be easily solved from Eq. (20a).

- Calculation of the local bending deformation field of each cell $w_{\max,L}$.

The confirmation of boundary condition is a key step to analyze the local deformation field of each cell. Here, three boundary condition assumptions of lattice cell are compared as follows:

1. Cylindrical bending with built-in edges (Analytical-C, see Fig. 10a)[39]

$$w_{\max,L} = \frac{p_{\max} d_c^4}{384 D_1} \quad (21a)$$

2. Cylindrical bending with simply supported edges (Analytical-S, see Fig. 10b) [39]

$$w_{\max,L} = \frac{5 p_{\max} d_c^4}{384 D_1} \quad (21b)$$

3. Bending of each lattice cell supported by rows of equidistant trusses (Analytical-T, see Fig. 10c) [39]

$$w_{\max,L} = 0.005507 \frac{p_{\max} d_c^4}{D_1} \quad (21c)$$

Where $w_{\max,L}$ is the local maximum deformation, p_{\max} is the maximum value of water impact pressure loading on central cells, d_c is the width of cell (see Fig. 1) and D_1 is the flexural rigidity of cell face sheet defined as:

$$D_1 = \frac{E t_b^3}{12 (1-\nu^2)} \quad (22)$$

If the inertial effect during water impact loading process is significant ($2\tau_s f_s \sim 1.0$), the total static deformation $w_{\max,T}$ of LWSPS must be multiplied the dynamic load inertial coefficient η_{sd} . The value of η_{sd} is equal to 1.05 - 1.10 for case 1 - case 6 from Eq. (16) and Eq. (17). Here, the value 1.10 of η_{sd} is adopted in the following investigation.

Compared with the 3D-FEM FSI simulation, the maximum deformations w_{\max} of LWSPS under different water impact velocity for the three assumptions (Analytical-C, Analytical-S and Analytical-T) are illustrated in Fig. 11. It is clear that the analytical deflections match well with computed results by

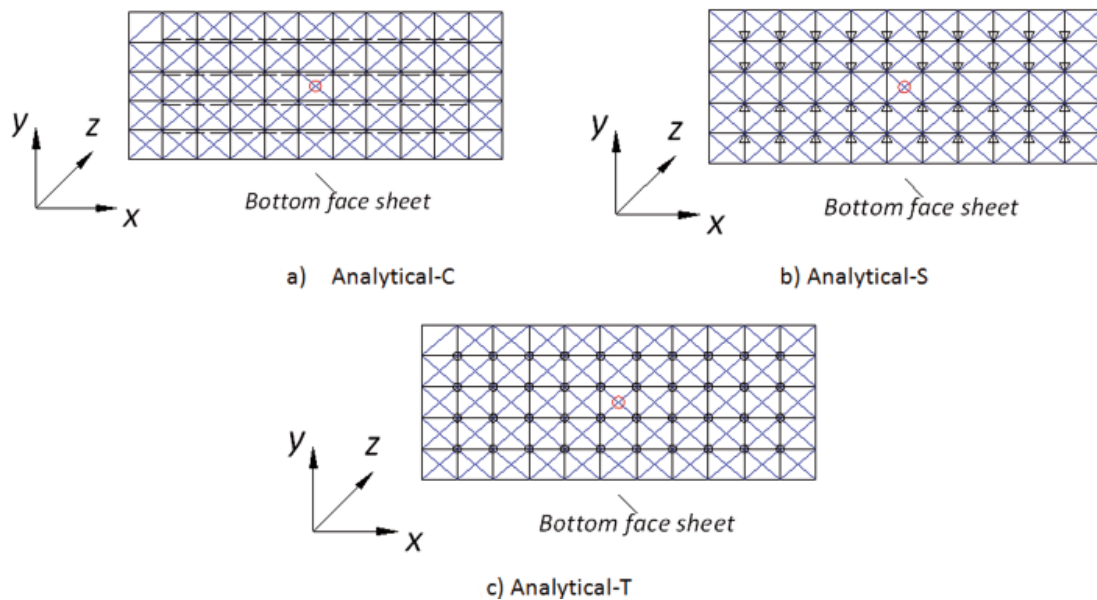


Fig. 10. Three local cell deformation field assumptions of LWSPSPS

adopting the Analytical-S assumption. The results show that the maximum percentage difference ($100\% \times (W^{sim} - W^{ani}) / W^{sim}$) between this engineering approach (W^{ani}) and the FSI simulation results (W^{sim}) is less than 9 % (impact velocity $v = 3 - 6$ m/s). Furthermore, the results based on Analytical-T assumption can give a better estimation in the low velocity range (impact velocity $v = 1 - 2$ m/s). The maximum difference between the simulation and the approximate method is less than 3 %. As shown in Fig. 11, the results based on Analytical-C assumption for LWSPSPS are unacceptable.

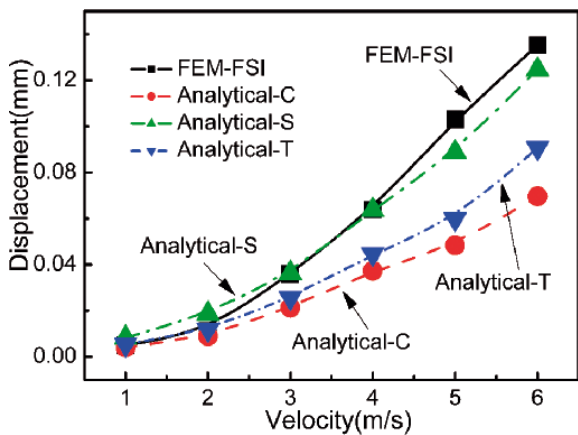


Fig. 11. Comparison of the maximum deformation of LWSPSPS by using approximate method and FSI simulation

PARAMETRIC STUDY

In this section, the effects of design parameters of t_b , t_t , H_c , $t_c \times t_c$ on water impact pressure and maximum deflection of LWSPSPS are examined by numerical simulation and engineering prediction.

Effects of thickness of face sheets t_b and t_t (C7-C14)

To investigate the effects of thickness of face sheet on water impact loading pressure, LWSPSPS with four different bottom face sheet thicknesses (C7 - C10) and four different top face sheet thicknesses (C11 - C14) are considered. The material properties, plate geometry, water impact velocity and boundary

conditions are the same as those that adopted in the previous study for C1 - C6.

With respect to the fundamental case C1, the variation in thickness of bottom face sheet t_b leads to the significant shifts of water impact loading pressure and maximum deflection, as shown in Fig. 12 and Fig. 13. However, the influence of variation in thickness of top faces t_t is insignificant. With the increase in thickness of t_b (the contact water face sheet “hardens”), the FSI peak pressure of central point increases, as illustrated in Fig. 12. On the contrary, the average FSI peak pressure of contacted water face sheet has a minimum when t_b is nearly equal to 4.5 mm.

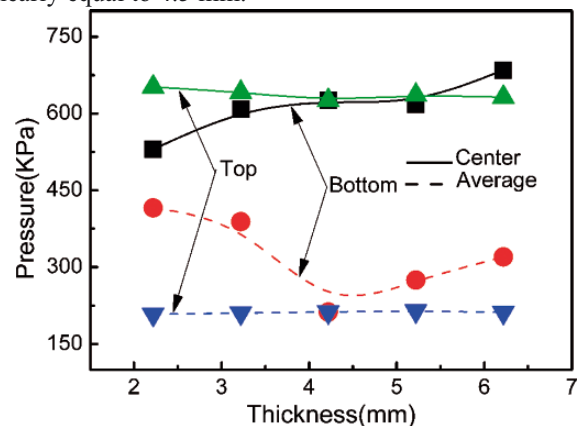


Fig. 12. Peak water impact pressure magnitudes at central point and average FSI area with different face sheet thickness: top and bottom

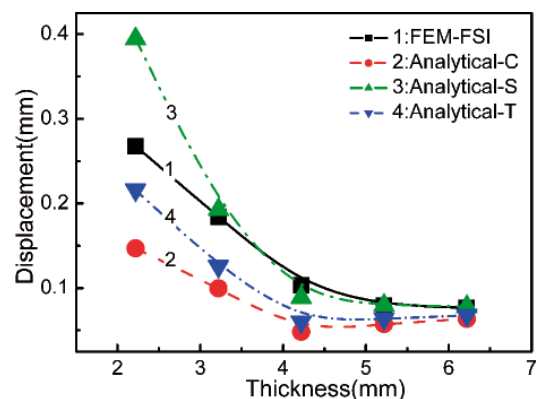


Fig. 13. Maximum deformations of LWSPSPS with different bottom face sheet thickness predicted by analytical method and FEM

It can be seen clearly from Fig. 13 that, with the thickness of bottom face sheet increases, the deformation curves demonstrate a progressive decrease when $t_b < 4.5$ mm. Contrarily, when $t_b > 4.5$ mm, a slowly increasing trend of deformation curve is observed. In an interpreting way, when $t_b > 4.5$ mm, though the flexural rigidity of LWSPS increase slowly, both the central pressure and the average pressure increase faster, as shown in Fig. 12.

With no remarkable change of water impact pressure, the maximum deformation magnitude of LWSPS is smaller when t_f becomes thicker (Fig. 14). The approximate method also gives good estimations here under the Analytical-S assumption, and the error is less than 10% in most of the cases. With very few exceptions (t_f or $t_b = 2.219$ mm), the precision of this analytical prediction is high enough. As a possible factor, the Analytical-S assumption cannot reflect the true boundary condition of local lattice cell when the face sheet is relatively thin.

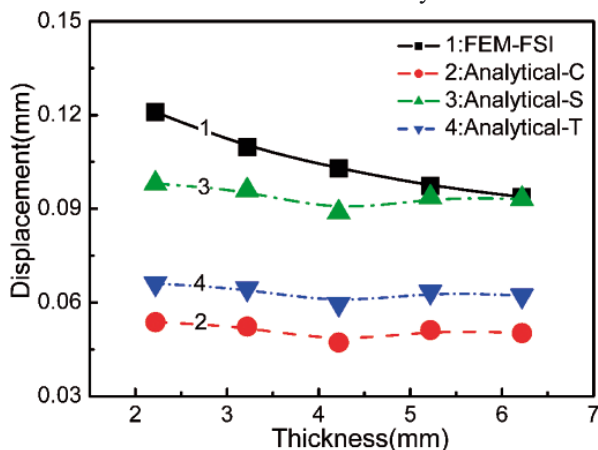


Fig. 14. Maximum deformations of LWSPS with different top face sheet thickness predicted by analytical method and FEM

Effects of core thickness of LWSPS H_c (C15-C18)

Next, the influence of core thickness on the water impact pressure and maximum deflection of LWSPS is considered (C15 - C18, see Table 1). The peak pressure magnitude versus core thickness for C15 - C18 under the same water impact velocity 5m/s are demonstrated in Fig. 15. Along with the increasing thickness of core, the peak pressure value moves to a lower magnitude. As illustrated in Fig. 15, the slope of decreasing curve changes slowly for central pressure when H_c is in the range of 1.825 - 2.825 cm. But the slope of central pressure curve drops dramatically in the range of $H_c = 2.825 - 5.825$ cm. Moreover, a slight decrease of average FSI peak pressure magnitude with a thicker core is observed.

To quantify the effects of core thickness of LWSPS on the structural response, the predicted deflections versus core thickness are plotted for these four cases with three different local boundary condition assumptions, as shown in Fig. 16. As the thickness of core increases, it is shown that the deformation of LWSPS decreases rapidly in the range of $H_c = 1.825 - 4.825$ cm. This is because of the decrease of FSI pressure and the increase of bending rigidity of LWSPS with thicker core. The best prediction of maximum deformation of LWSPS is also obtained under the Analytical-S assumption. When $H_c > 2.5$ cm, the engineering approach results are consistent well with those obtained from numerical calculation. Also with very few exceptions (when $H_c < 2.5$ cm), the discrepancy between the numerical results and the analytical solutions displays in

Fig. 16. Compared with FEM result, the error of the prediction is about 25 %.

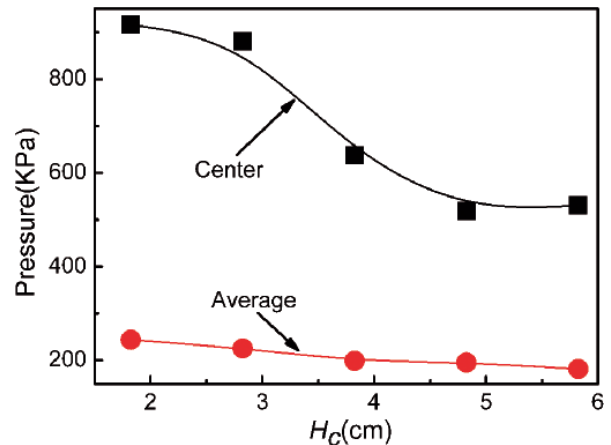


Fig. 15. Peak water impact pressure magnitudes at central point and average FSI area with different core thicknesses

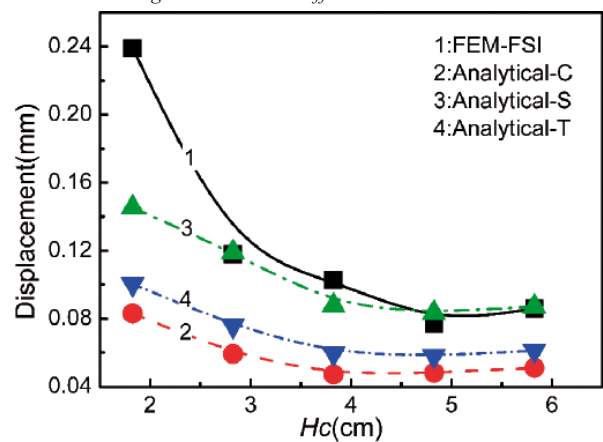


Fig. 16. Maximum deformations of LWSPS with different core thicknesses predicted by analytical method and FEM

Effects of cross section area $t_c \times t_c$ (C19 - C22)

Finally, the influence of the section area of lattice column as an indicator of relative density is discussed. According to the calculation results, nearly 2 times increasing of relative density of lattice core (from 4.83 to 9.47 %) results in 10 % decrement of FSI pressure located in the central point and 10 % increment of the average FSI pressure.

As demonstrated previously, the contacted water face sheet and core thickness both have significant effects on the dynamic response behavior of LWSPS. But it is shown that the change of relative density has a slight effect on the dynamic response behavior. In contrast, in the evaluation of the energy absorption characteristic of LWSPS under intense impact loading such as UNDEX (underwater explosion) or AIREX (air explosion), the relatively density of lattice core plays a pivotal role on the dynamic mechanical properties of lattice materials [17-18]. However, unlike with the plastic collapse under these intense impact loads (UNDEX or AIREX), the serious failure modes (like the plastic dynamic buckling) would not occur under the practical water impact loading (here, impact velocity $v = 5$ m/s) only if the relative density is extremely low.

The maximum deformations of C19 - C22 are also predicted by numerical simulation and analytical method. With no remarkable change of the water impact pressure, the corresponding results demonstrate that the maximum deformation decreases slowly (about 20 %).

CONCLUSIONS

The hydroelastic characteristics for light weight pyramidal sandwich plate structures (LWSPSPS) under water impact by using 3D simulation are studied. A theoretical hydroelasticity assessment model for LWSPSPS and a new engineering approach method to predict the maximum deformation of LWSPSPS under water impact load are developed.

In numerical analysis, an arbitrary Lagrangian and Eulerian algorithm (ALE) in the nonlinear finite element code LS-DYNA is used to simulate the fluid-solid interaction phenomenon between structure hull and fluid medium. The equivalent core model and the approximation method are adopted to calculate the fundamental bending vibration frequencies of LWSPSPS. Furthermore, based on the first fundamental modal frequency, the hydroelastic characteristic is discussed in detail by introducing a non-dimensional criterion $2\tau_s f_s$. By dividing the real displacement field of LWSPSPS into global displacement field and local displacement field, the real maximum deformation solutions are obtained. Compared with 3D FEM results, the results of the engineering calculation method presented in this analysis are obtained with good accuracy. At last, the influences of key design parameters of LWSPSPS on dynamic behavior are quantified, including the face sheet thickness, the thickness of lattice core and the relative density of LWSPSPS core.

The following conclusions from the viewpoint of hydroelastic characteristics of LWSPSPS can be drawn:

- 1) In the form of water impact velocity, the performance of water impact pressure for LWSPSPS is close to two parameters parabolic mathematical expression. Compared with the monolithic plate, in medium-high water impact velocity range (2m/s-6m/s), the advantage of decreasing water impact pressure peak for LWSPSPS is significant. A notable phenomenon called "local air cushion" exists during the initial water impact process of LWSPSPS caused by the cell local deformation, which has significant effects on the dynamic characteristic of LWSPSPS.
- 2) The hydroelastic effect of LWSPSPS is not significant in the present study because the non-dimensional criteria $2\tau_s f_s > 4$, which means the duration time of water impact pressure loading is much longer than the first wet natural period of vibration.
- 3) Results from the proposed engineering analytical model are in good agreement with those from finite element predictions for LWSPSPS. All the geometric parameters are included and the local structural displacement is captured in this model. The predictions based on this method show that, compared with the other two local deformation field assumptions (cylindrical bending with simply supported edges and cylindrical bending with built-in edges), the local cylindrical bending assumption with simply supported edges each row lattice core is more realistic to reflect the true boundary condition in most cases.
- 4) In the parametric study of LWSPSPS, it is found that the thinning of contacted water face sheet reduces the central water impact loading pressure, while the average FSI water impact loading pressure has a local minimum value at a certain thickness. Additionally, along with the increasing of core thickness, the peak pressure moves to a lower magnitude. Another key design parameter-the relative density of lattice core, has no significant effect on the FSI pressure and maximum deflection when the relative density of core is doubled.

Acknowledgements

The authors are pleased to acknowledge the support of the National Natural Science Foundation of P.R. China (Contract No. 51079058) and the Research Award Program for Outstanding Doctor Thesis of Huazhong University of Science and Technology (Contract No. 0109140921).

BIBLIOGRAPHY

1. Faltinsen O.M.: *Hydrodynamics of High-Speed Marine Vehicles*. Cambridge, UK: Cambridge University Press, 2005.
2. DNV: *Rules for Classification of High Speed, Light Craft and Naval Surface Craft*. 2012.
3. Karman V.T.: *The impact on sea plane floats during loading*. NACA-TN-321, 1929.
4. Wagner H.: *Loading of seaplane*. NACA-TN-622, 1932.
5. Chuang S.L.: *Investigation of impact of rigid and elastic bodies with water*. NSRDC-TR-3248, 1970.
6. Stenius I., Rosen A., Battley M., et al.: *Hydroelastic Effects in Slamming Loaded Panels*. In: 11th. International Conference on Fast Sea Transportation (FAST 2011), Honolulu, Hawaii, USA, 26-29 September 2011. p. 644-652.
7. Faltinsen O.M.: *Hydroelastic slamming*. Journal of Marine Science and Technology 2000; 5(2):49-65.
8. Berezinski A.: *Slamming: the role of hydroelasticity*. International Shipbuilding Progress 2001;48(4):333-351.
9. Hirdaris S.E., Temarel P.: *Hydroelasticity of ships: Recent advances and future trends*. Proceedings of the Institution of Mechanical Engineers, Part M: Journal of Engineering for the Maritime Environment 2009;223(3):305-330.
10. Stenius I., Rosen A., Kuttenukeuler J.: *Hydroelastic interaction in panel-water impacts of high-speed craft*. Ocean Engineering 2011;38(2-3):371-381.
11. Metschkow B.: *Sandwich panels in shipbuilding*. Polish Maritime Research 2006 special issue 1:5-8.
12. Kozak J.: *Selected problems on application of steel sandwich panels to marine structures*. Polish Maritime Research 2009;16(4):9-15.
13. Qin Z., Batra R.C.: *Local slamming impact of sandwich composite hulls*. International Journal of Solid and Structures 2009;46(10):2011-2035.
14. Baral N., Cartie D.R., Partridge I.K., et al.: *Improved impact performance of marine sandwich panels using through-thickness reinforcement: experimental results*. Composite Part B: Engineering 2010;41(2):117-123.
15. Panciroli R., Abrate S., Minaka G., et al.: *Hydroelasticity in water-entry problems: Comparison between experimental and SPH results*. Composite Structures 2012;94(2): 532-539.
16. Vasiliev V.V., Barynin V.A.: *Anisogrid composite lattice structures-Development and aerospace applications*. Composite Structures 2012;94(3):1117-1127.
17. McShane G.J., Deshpande V.S. and Fleck N.A.: *The underwater blast resistance of metallic sandwich beams with prismatic lattice cores*. Journal of Applied Mechanics 2007;74(2): 352-364.
18. Zhu F., Lu G.X., Ruan D., et al.: *Plastic Deformation, Failure and Energy Absorption of Sandwich Structures with Metallic Cellular Cores*. International Journal of Protective Structures 2010;1(4):507-541.
19. Greenspon J.E.: *Sea tests of the U.S.C.G.C. Unimak (Part3)*. DTMB-TR-978,1956.
20. Olovsson L., Souli M.: *LS-DYNA Advanced Course in ALE and Fluid-Structure Coupling*. Class Notes, Livermore Software Technology Corporation, Livermore, CA, 2000.
21. Aquelet N., Souli M., Olovsson L.: *Euler-Lagrange coupling with damping effects-Application to slamming problems*. Computer Methods in Applied Mechanics and Engineering 2006; 195(1-3):110-132.

22. Stenius I., Rosen A., Kuttenukeuler J.: *Explicit FE-modeling of fluid-structure interaction in hull-water impacts*. International Shipbuilding Progress 2006;53(2):103-121.
23. Jones N.: *Structural Impact*. Cambridge, UK: Cambridge University Press, 1989.
24. Symonds P.S.: *Survey of methods of analysis for plastic deformation of structures under dynamic loading*. Brown University, Division of Engineering Report, 1967.
25. Yuzuru F.: *On the impulsive of circular plate falling upon water surface*. Journal of Zosen Kiokai 1954;94:105-110. (In Japanese)
26. McKirgan J.: *Characterization of aluminum 6061-T6 tube for high-rate loading applications*. Naval Surface Warfare Center (NSWC) Carderock Division Technical Report, 2004.
27. Jones N.: *Slamming damage*. Journal of Ship Research 1973;17(2):80-86.
28. Wierzbicki T., Chrysostomidis C., Wiernicki C.: *Rupture analysis of ship plating due to hydrodynamic wave impact*. Ship Structure Symposium '84, Arlington, VA, 15-16 October 1984. p.237-256.
29. Nagai T.: *Elastic response of high tensile steel plates developed by impact on water surface*. Bulletin of Society of Japan Naval Architecture and Ocean Engineering 1966; 120:175-184. (In Japanese)
30. Szymanski Y.A.: *Ship Structural Mechanics Guide* (Volume II). Moscow, RUS: National Technology Press, 1959. (Шиманский Ю А. Корабль структурных руководства механика (том II). Москва, Россия: Национальный технологии Пресс, 1959.). (In Russian)
31. Liu T., Deng Z.C., Lu T.J.: *Design optimization of truss-cored sandwich with homogenization*. International Journal of Solid and Structures 2006;43(25-26):7891-7918.
32. Wadley H.N.G.: *Multifunctional periodic cellular metals*. Philosophical Transactions of the Royal Society A 2006;364(1838): 31-68.
33. Edward W.K.: *Flexure of structural sandwich construction*. Forest Productions Laboratory Report NO.1829, 1951.
34. Bolotin B.B.: *Calculation of strength*. 1960, 6(6), Mashgiz. (Болотин В В. Расчёт на прочность, вы(6), Машгиз, 1960). (In Russian)
35. Institute of Mechanics, Chinese Academy of Sciences. *Bending, Vibration and Stability of Sandwich Plates and Shells*. Beijing, CHN: Science Press, 1977. (In Chinese)
36. Biggs J.B.: *Introduction to Structural Dynamics*. New York, US: McGraw-Hill, 1964.
37. Stenius I., Rosen A., Kuttenukeuler J.: *Explicit FE-modeling of hydroelasticity in panel-water impacts*. International Shipbuilding Progress 2007;53(2-3):111-127.
38. ANSYS Inc. *ANSYS Theory Manual* (Version 5.0). 2002.
39. Timoshenko S., Woinowsky-Krieger S.: *Theory of plates and shells*. New York, US: McGraw-Hill, 1959.

CONTACT WITH THE AUTHORS

Hao Wang, Dr.,
 Fei Zhao, master graduate student,
 Yuan-Sheng Cheng^{*)}, Dr., Professor,
 Jun Liu, Dr., Lecturer
 Yuan Tian, master graduate student,
 School of Naval Architecture and Ocean Engineering,
 Huazhong University of Science and Technology,
 Wuhan 430074, P.R. China

^{*)} Corresponding author. e-mail: lucascheng62@gmail.com

Graphical interpretation of the power of energy losses and power developed in the hydrostatic drive and control system elements

Grzegorz Skorek, Ph.D.
Gdynia Maritime University, Poland

ABSTRACT



This publication presents, analyses and compares the areas of the power fields of energy losses occurring in the elements of two hydraulic systems with different structures of the hydraulic linear motor speed control.

Keywords: hydraulic motor; energy balance; energy losses; energy efficiency; capacity pump; hydraulic servo mechanism; hydrostatic drive system

INTRODUCTION

The paper presents graphical interpretation of the power of energy losses and power developed in the elements of two different systems with the throttling series control of the hydraulic linear motor speed. The analysis was carried out by comparing, at selected hydraulic linear motor operating parameters, the areas of the power fields of energy losses occurring in the elements of those structures.

The investigations involved two systems with proportional directional valve, fed by a constant capacity pump (Fig. 1):

- with the use of an overflow valve - a constant pressure structure,
- with the use of a hydraulic cylinder supply conduit pressure controlled overflow valve - a variable pressure structure.

The investigated structures operated at the same hydraulic linear motor operating parameters, i.e. its load F_M and speed v_M .

The analysis allows to compare the values of power ΔP of losses ensuing from the used structure of control of the hydraulic linear motor speed as well as the value of power P_{pc} absorbed (consumed) by the pump from its driving electric motor, power necessary for providing the required stable value of useful power $P_{Mu} = F_M v_M$ of the hydraulic linear motor driven by the pump.

Graphical presentation, by fields of specified areas, of the power of energy losses in the hydrostatic drive and control system elements as well as power developed in the hydraulic displacement machines used in the system, becomes a tool facilitating comparing the values of particular losses [1].

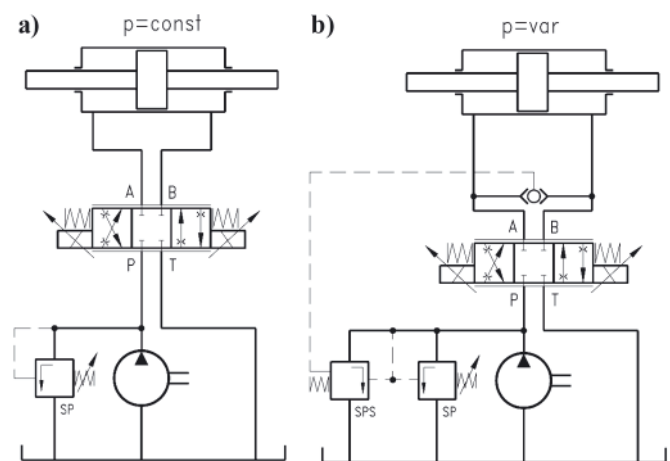


Fig. 1. System with proportional directional valve fed by a constant capacity pump [3]: **a)** with the use of an overflow valve – $p = \text{const}$ structure, **b)** with the use of a hydraulic cylinder supply conduit pressure controlled overflow valve – $p = \text{var}$ structure

Presentation of the fields of power of energy losses allows to make conclusions regarding e.g. elimination of the power of structural volumetric and pressure losses in the motor speed throttling control elements, in the proportional control systems and in the hydraulic servo-mechanism systems. Graphical interpretation by the field areas of the power of energy losses in the hydrostatic drive system elements and of the power developed by the system elements allows to compare those losses and powers with the area of the reference power field defined by the product $Q_{pt} p_n$ of the theoretical pump capacity and the system nominal pressure [1].

HYDRAULIC SYSTEM WITH PROPORTIONAL CONTROL OF THE CYLINDER FED BY A CONSTANT CAPACITY PUMP IN THE CONSTANT (P = CONST) AND VARIABLE (P = VAR) PRESSURE SYSTEM

Proportional control of a cylinder consists in throttling the liquid stream both at its inlet and outlet [3].

The basic proportional control system is a system fed by the constant capacity pump. The overflow valve SP (Fig. 1a) determines the system nominal pressure. The pressure decrease in the cylinder compensates the load on the cylinder. The proportional directional valve generates two pressure drops at the cylinder inlet and outlet. The pump in the $p = \text{const}$ system must generate, before the overflow valve, pressure not lower than pressure required by the cylinder. Therefore, the hydraulic cylinder or the system working cylinder may require pressure, depending on the load, in the range from zero to the nominal value. When the load approaches the nominal value, pressure decrease in the directional valve throttling slots tends to zero. It may be said that the pump-overflow valve assembly in the $p = \text{const}$ system is ready to feed the system with the maximum pressure and maximum capacity, but most often it is not used to that extent as the working element is loaded with a force that requires pressure drop smaller than the

nominal value [3]. A constant pressure system achieves a high energy efficiency, equal to the efficiency of a system without throttling control, only at the point of maximum values of the controlled hydraulic linear motor load coefficient \bar{M}_M and speed coefficient $\bar{\omega}_M$. The system efficiency η decreases rapidly with decreasing motor load and particularly with simultaneous decreasing motor speed [2].

The variable pressure ($p = \text{var}$) structure is represented by a system with constant capacity pump cooperating with an overflow valve controlled by the cylinder inlet pressure (Fig. 1b). This is an advantageous solution from the viewpoint of the cylinder energy efficiency as well as of the pump and the whole control system efficiency. The variable pressure ($p = \text{var}$) structure with the overflow valve SPS controlled by the current directional valve outflow to cylinder pressure allows to adjust the pump discharge conduit pressure to the current cylinder load, which limits the pressure loss in the working liquid outflow slot from the directional valve to the tank. Additionally, the system maintains constant piston speed irrespective of the load. This is an effect of maintaining practically constant pressure drop Δp_{DE1} in the proportional directional valve throttling slot [3].

Fig. 2 presents graphical interpretation of the power of energy losses in elements of an individual system with proportional control of a hydraulic cylinder, fed by a constant capacity pump cooperating with an overflow valve in a constant

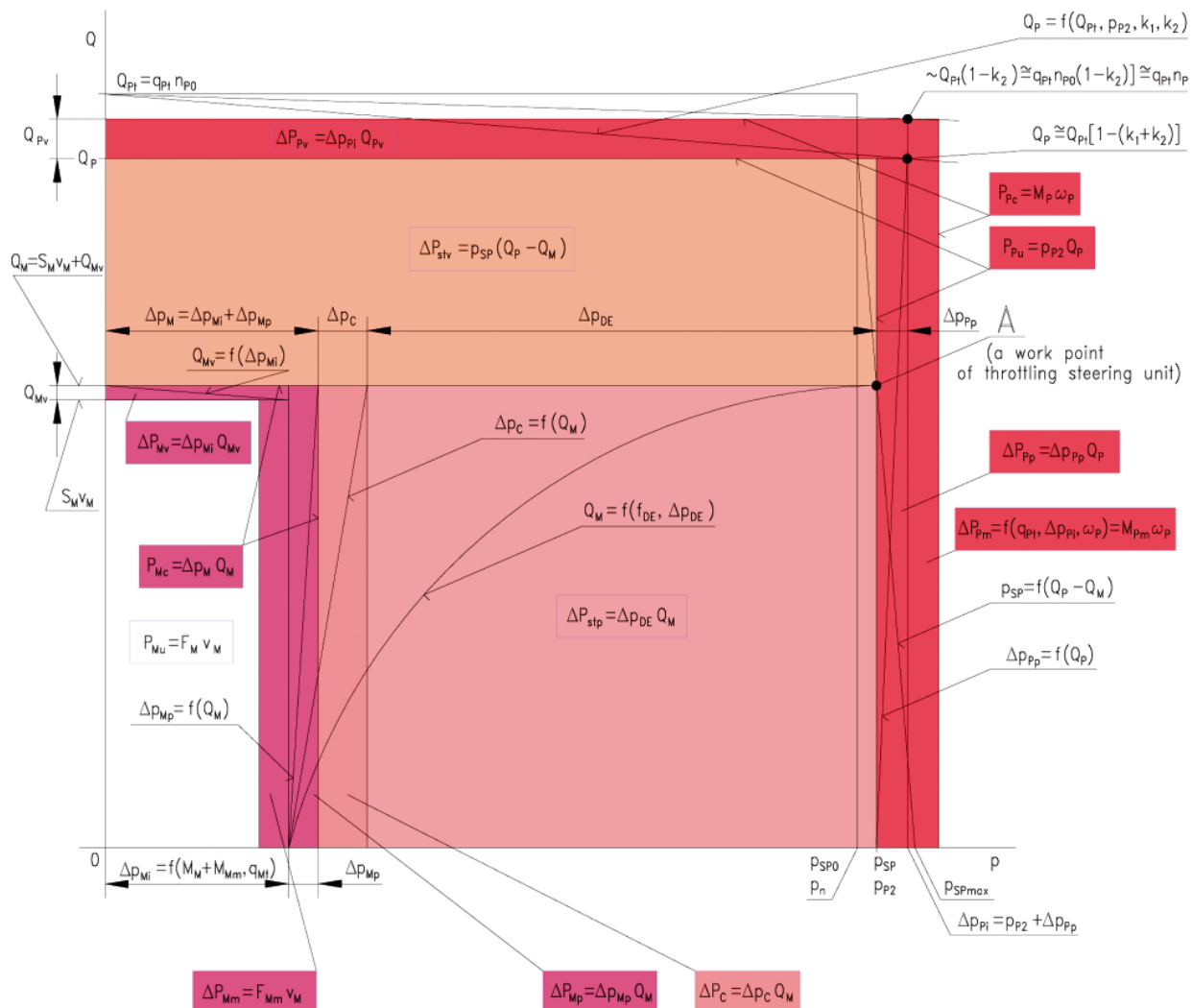


Fig. 2. Graphical interpretation of the power of losses in the hydrostatic drive and control system elements. An individual system with series throttling control of the hydraulic linear motor speed, fed by a constant capacity pump cooperating with the overflow valve in a constant pressure system – $p = \text{const}$; the series throttling control assembly in the form of [3]:
 - adjustable throttling valve; - adjustable two-way flow regulator; - servovalve; - proportional directional valve

pressure system ($p = \text{const}$), and Fig. 3 – with an overflow valve controlled in a variable pressure system ($p = \text{var}$).

The pump operation nominal pressure p_n is determined by the need to ensure the hydraulic linear motor a maximum pressure drop $\Delta p_{M_{\text{max}}}$ to cope with the maximum force $F_{M_{\text{max}}}$ on the cylinder piston rod that may occur from time to time as an effect of the cylinder load.

The current cylinder useful power $P_{Mu} = F_M v_M$ is a product of the cylinder piston rod force F_M and the piston rod speed. The hydraulic linear motor useful power P_{Mu} depends on the current load and is independent of the control structure and of the losses in the elements of a hydrostatic drive system with a specific structure [1].

In figure 2, the hydraulic linear motor current useful power $P_{Mu} = F_M v_M$ is presented as the area of the white rectangle, to which the following fields are “added”:

- field $\Delta P_{Mm} = F_{Mm} v_{Mm}$ of the power of mechanical losses in the cylinder,
- field $\Delta P_{Mv} = \Delta p_{Mi} Q_{Mv}$ of the power of volumetric losses in the cylinder,
- field $\Delta P_{Mp} = \Delta p_{Mp} Q_M$ of the power of pressure losses in the cylinder,
- field $\Delta P_C = \Delta p_C Q_M$ of the power of pressure losses in the system conduits,
- field $\Delta P_{stp} = \Delta p_{DE} Q_M$ of the power of structural pressure losses in the throttling control assembly (in the proportional directional valve),
- field $\Delta P_{stv} = p_{SP} (Q_p - Q_M)$ of the power of structural volumetric losses in the throttling control assembly (in the overflow valve),
- field $\Delta P_{Pp} = \Delta p_{Pp} Q_M$ of the power of pressure losses in the pump,
- field $\Delta P_{Pv} = \Delta p_{Pvi} Q_{Pv}$ of the power of volumetric losses in the pump,
- field $\Delta P_{Pm} = M_{Pm} \omega_p$ of the power of mechanical losses in the pump.

The sum of areas of the cylinder current useful power P_{Mu} rectangle and the ΔP rectangles representing the values of power of particular losses occurring at a given instant in the hydrostatic drive and control system elements, makes up the area of rectangle corresponding to the current power P_{pc} absorbed (consumed) by the pump from its driving electric motor and equal to the product of the current torque M_p and current pump shaft angular speed – $P_{pc} = M_p \omega_p$ [1].

The power P_{pc} absorbed by the pump from the driving motor may be greater than the reference power $p_n Q_{pt}$ – a product of the nominal pressure p_n and pump theoretical capacity Q_{pt} [1].

In figures 2 and 3 the pump capacity is represented by two descending lines originating at point Q_{pt} . The higher line illustrates the pump capacity in the situation when the pump volumetric loss coefficient k_1 has a zero value ($k_1 = 0$). The line below represents the pump capacity at $k_1 > 0$. The volumetric losses occur in the latter situation [3].

The Q_M curve presents the proportional directional valve characteristic with a given pressure drop Δp_{DE} in the directional valve and with a given throttling slot area f_{DE} (Fig. 2 and 3). At point “A” it crosses the overflow valve (SP) characteristic $p_{SP} = f(Q_p - Q_M)$. In effect, the intensity Q_M of flow through the throttling slot to the cylinder is obtained, and with a given piston and piston rod area – the speed v_M . The working point A is a result of the overflow valve SP and of the proportional directional valve characteristics [3].

The cylinder useful power P_{Mu} is a product of its speed v_M and load F_M . In other words, it is power developed by the cylinder on the piston rod. The cylinder useful power P_{Mu} field

is marked white to distinguish it from the power of losses in the system.

Power ΔP_{Mv} of volumetric losses is a function of the pressure drop Δp_{Mi} in the cylinder.

Power ΔP_{Mm} of mechanical losses is a function of the load force F_M .

Power ΔP_C of losses in the system conduits is a product of the sum of resistance of flow Δp_C and flow intensity Q_M towards the cylinder.

Power ΔP_{stp} of structural pressure losses is a product of the sum of pressure losses Δp_{DE} in the directional valve throttling slots and of the flow intensity Q_M corresponding to the cylinder speed v_M . It can be reduced almost to zero during cylinder operation at the $F_{M_{\text{max}}}$ load.

Power ΔP_{stv} of structural volumetric losses is a product of pressure p_{SP} in the pump discharge conduit and of the flow intensity Q_0 directed, through the overflow valve SP or the controlled overflow valve SPS, to the tank [3]. It decreases almost to zero when the cylinder operates with maximum speed $v_{M_{\text{max}}}$.

There are three types of losses in the pump.

Power ΔP_{Pm} of mechanical losses in the pump occurs between the pump working chamber and the shaft. It is proportional to the pump capacity per one revolution q_p and to the pressure increase Δp_{pi} in its working chambers. The Δp_{pi} value is influenced by the resistance of flow Δp_{pp} in the pump channels [3]. Fig. 2 presents the power of pump mechanical losses in the $p = \text{const}$ system as a field whose width is determined by the torque M_{pm} of mechanical losses and height corresponds to the pump shaft angular speed ω_p .

In the $p = \text{var}$ system (Fig. 1b and 3), the pump working pressure p_{p2} , controlled by the controlled overflow valve SPS, is set at a level higher by the value:

$$\Delta p_{SPS} = \Delta p_{DE1|f_{DE1_{\text{max}}, Q_{Pt}}} + \Delta p_{C1_{\text{max}}} = \text{cte}$$

than the current pressure p_2 in the throttling directional valve outlet conduit to the hydraulic linear motor. The value Δp_{SPS} of the pressure difference $\Delta p_{SPS} = p_{p2} - p_2$ must ensure obtaining, with the throttling directional valve slot DE1 controlling the flow intensity Q_M feeding the hydraulic linear motor, the flow intensity Q_M equal to the theoretical pump capacity Q_{pt} , i.e. $Q_M = Q_{pt}$. The slot cross-section area DE1 reaches then its maximum value $f_{DE1_{\text{max}}}$, with a possibility of obtaining the $\Delta p_{DE1|f_{DE1_{\text{max}}, Q_{Pt}}}$ drop required by the throttling directional valve structure and at the same time the capability of overcoming the maximum resistance of flow $\Delta p_{C1_{\text{max}}}$ that may appear between the pump and the directional valve. The pressure value p_1 before the throttling directional valve slot DE1 is equal to $p_1 = p_{p2} - \Delta p_{C1}$ [1].

The current value of the pump discharge pressure p_{p2} , higher by Δp_{SPS} than the current p_2 value at the throttling directional valve outlet to the hydraulic linear motor, results from the pressure value p_{M1} required by the hydraulic cylinder at its inlet. The maximum limit pressure value $p_{p2_{\text{max}}}$ in the pump discharge conduit is determined by the overflow valve SP, whose opening pressure p_{SP0} is equal to the system nominal pressure p_n [1].

In the $p = \text{var}$ system (Fig. 3), the width of the field of power ΔP_{Pm} of mechanical losses in the pump is proportional to the pressure and is smaller as the pressure in the pump working chambers is lower. In effect, it requires a smaller torque on the pump driving motor shaft [3].

The field ΔP_{Pp} of the power of pressure losses in the $p = \text{var}$ system pump is greater than the $p = \text{const}$ system ΔP_{Pp} .

The power ΔP_{Pv} of volumetric losses in a $p = \text{var}$ system pump is distinctly smaller than the power ΔP_{Pv} of those losses in a $p = \text{const}$ system pump.

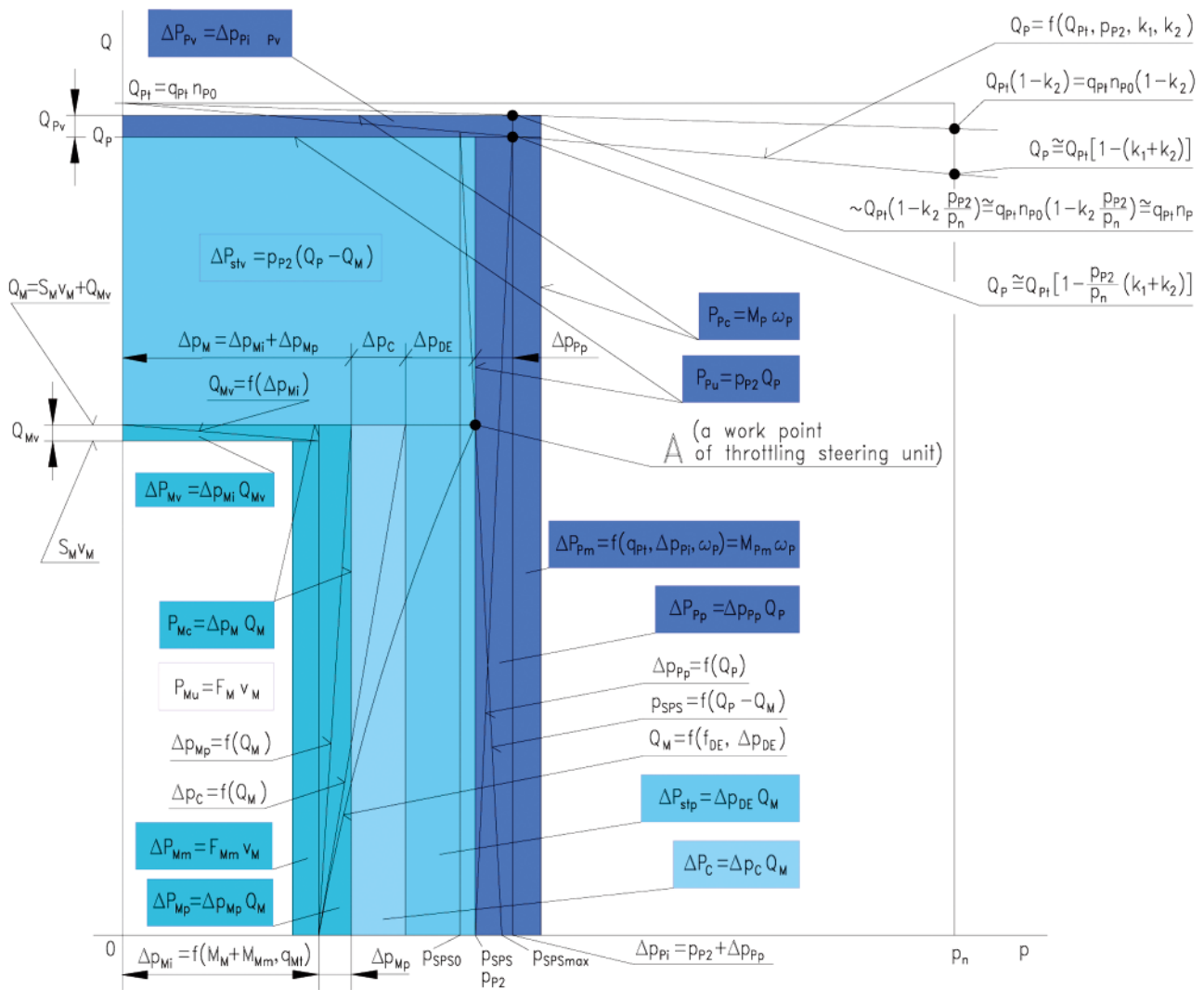


Fig. 3. Graphical interpretation of the power of losses in the hydrostatic drive and control system elements. An individual system with series throttling control of the hydraulic linear motor speed, fed by a constant capacity pump cooperating with the overflow valve in a variable pressure system – $p = \text{var}$; the series throttling control assembly in the form of [3]:
 - adjustable throttling valve (together with a controlled overflow valve, creating a three-way flow regulator); - servovalve; - proportional directional valve

The intensity Q_M of flow towards the hydraulic cylinder results from the pressure drop Δp_{DE1} and Δp_{DE2} in the proportional directional valve slots. On the other hand, those pressure drops change when the pressure drop Δp_M required by the hydraulic cylinder changes [3].

COMPARISON OF THE AREAS OF FIELDS OF THE POWER OF ENERGY LOSSES IN THE ELEMENTS OF TWO STRUCTURES – $P = \text{CONST}$ AND $P = \text{VAR}$

Figures 4 to 9 present graphical interpretation of the power of losses in the hydrostatic drive and control system elements, investigated in a constant pressure ($p = \text{const}$) and variable pressure ($p = \text{var}$) system, with the hydraulic cylinder load values $F_M = 10 \text{ kN}$, 25 kN and speed values $v_M = 0.05 \text{ m/s}$, 0.20 m/s and 0.35 m/s . The fields of power of losses ΔP in the constant pressure system are shaded red and fields of power of losses in the variable pressure system - shaded blue.

At the cylinder zero load $F_M = 0$ there is no field of the cylinder useful power P_{Mu} and only losses occur in the $p = \text{const}$ and $p = \text{var}$ system.

In Fig. 4, at the cylinder load $F_M = 10 \text{ kN}$ and speed $v_M = 0.05 \text{ m/s}$, great structural volumetric losses ΔP_{stv} are visible in the SP overflow valve, as with small cylinder speed

the flow intensity Q_M towards the cylinder is small. Most part of the flow intensity Q_P generated by the pump is directed to the tank as the Q_0 intensity.

Fig. 5 illustrating a variable pressure ($p = \text{var}$) structure shows structural volumetric losses ΔP_{stv} , occurring in the controlled overflow valve SPS, the greatest among the losses as with small cylinder speed the flow intensity Q_M towards the cylinder is small. Most part of the flow intensity Q_P generated by the pump is directed to the tank in the form of a Q_0 intensity. At the same time, power ΔP_{stv} of volumetric losses is much smaller here than ΔP_{stv} in the $p = \text{const}$ system (Fig. 4), as the pump working pressure p_{p2} , set with the controlled overflow valve, is much lower.

Comparing the energy balance of the $p = \text{var}$ system shown in Fig. 5 with the $p = \text{const}$ system balance shown in Fig. 4, with the same cylinder load and speed coefficients, one can notice much smaller structural losses ΔP_{st} in the proportional directional valve and in the controlled overflow valve as well as the pump volumetric losses ΔP_{pv} in the $p = \text{var}$ system. This is connected with adjusting the p_{p2} pressure in the pump discharge conduit to the current cylinder load, i.e. to the p_2 pressure. As Fig. 5 illustrates the energy balance of a $p = \text{var}$ system under a small load, losses in the system are smaller.

Losses in the conduits are the smallest in this case, as the power of losses in the conduits ΔP_C is a product of the sum

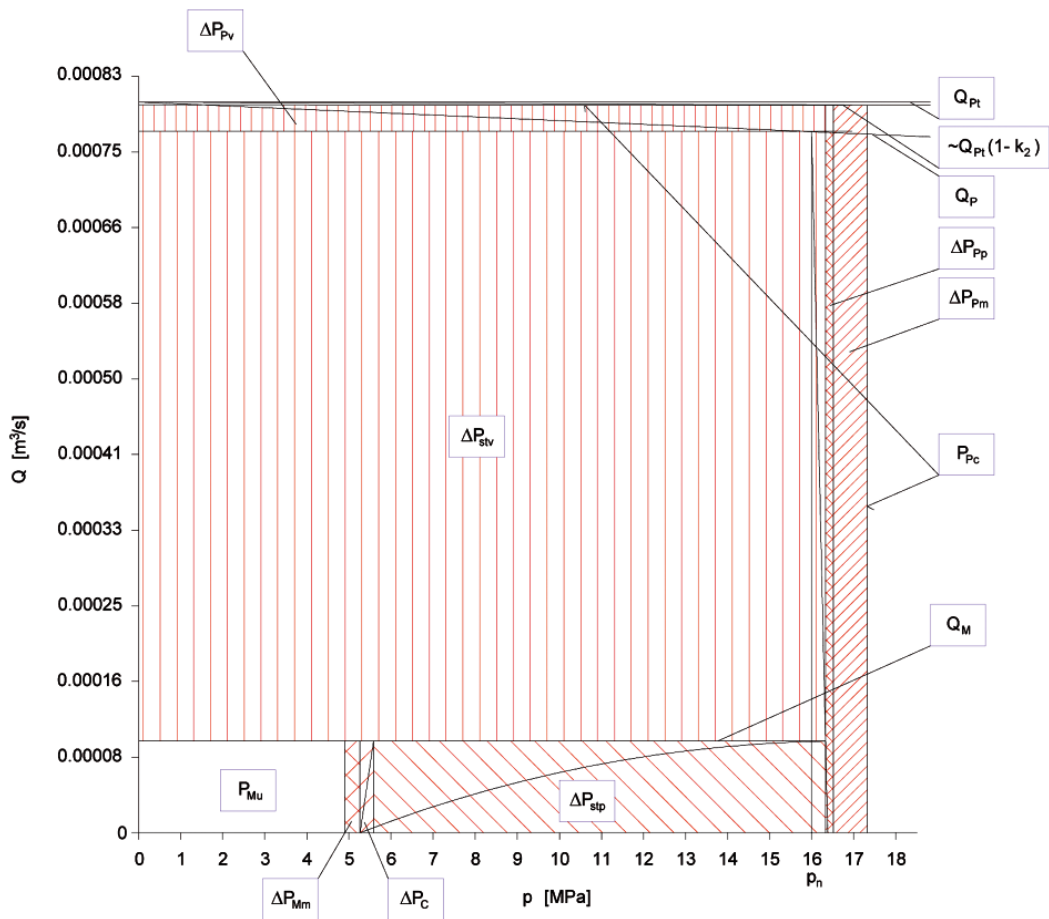


Fig. 4. Energy balance of a constant pressure ($p = \text{const}$) system investigated at the cylinder load $FM = 10\text{kN}$ and speed $v_M = 0.05\text{m/s}$

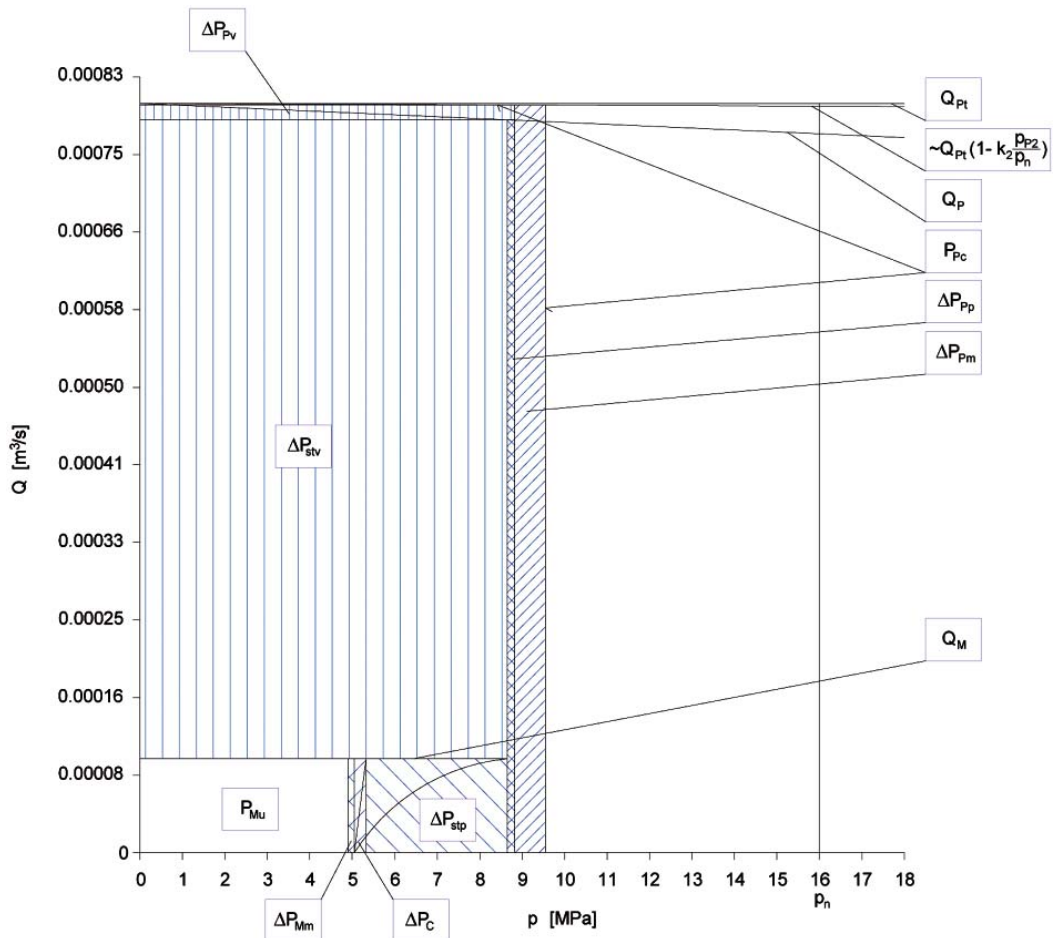


Fig. 5. Energy balance of a variable pressure ($p = \text{var}$) system investigated at the cylinder load $FM = 10\text{kN}$ and speed $v_M = 0.05\text{m/s}$

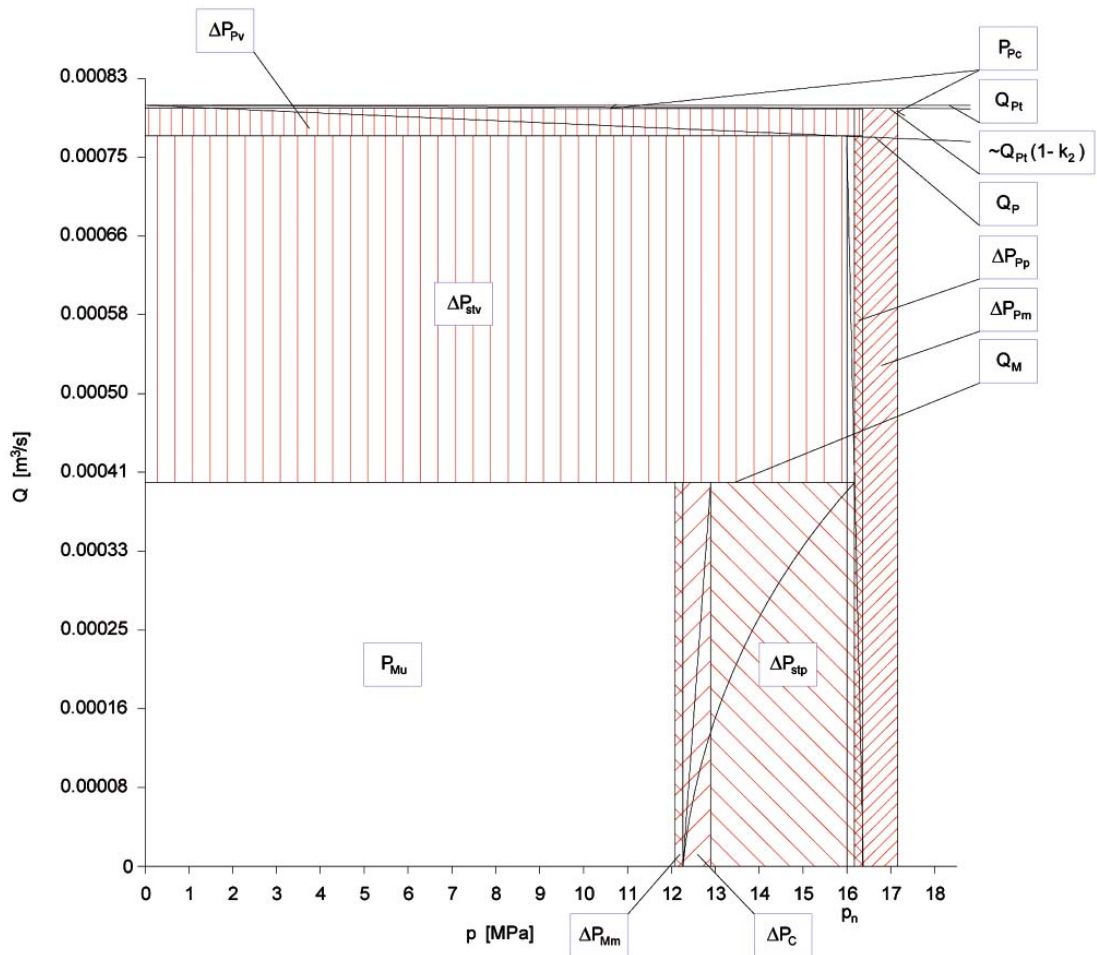


Fig. 6. Energy balance of a constant pressure ($p = \text{const}$) system investigated at the cylinder load $FM = 25\text{kN}$ and speed $vM = 0.20\text{m/s}$

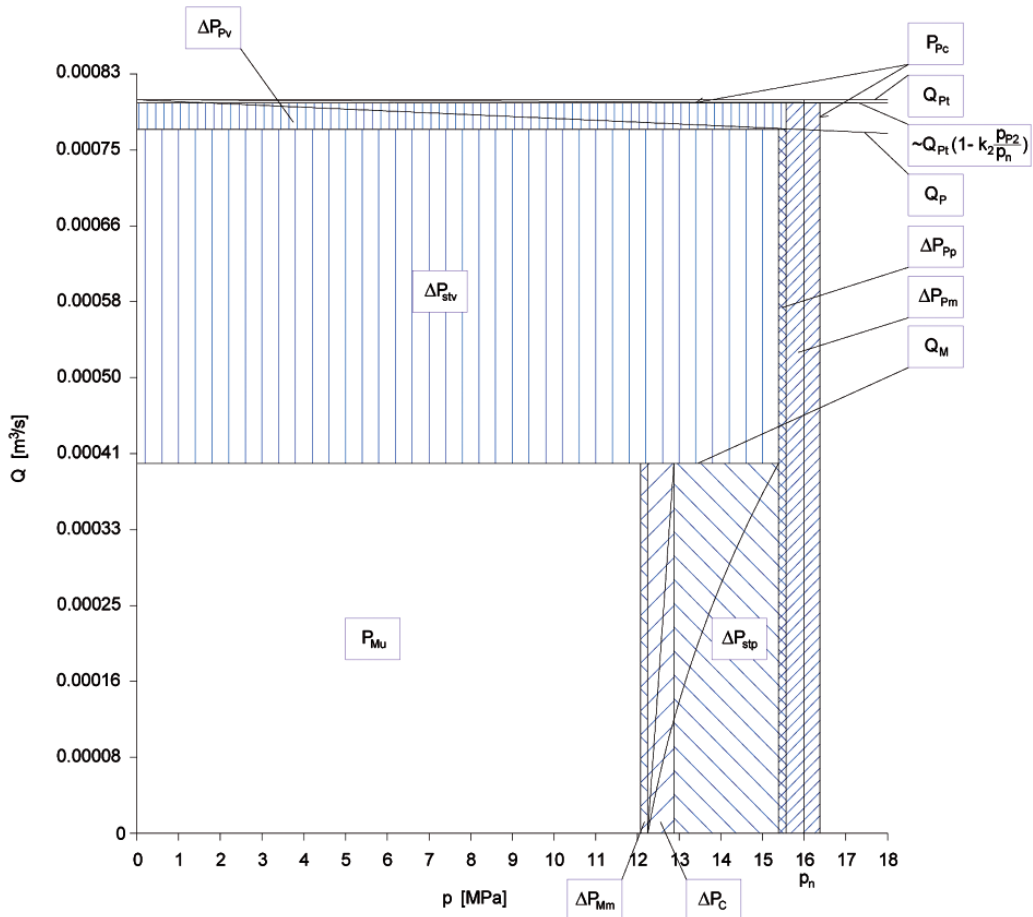


Fig. 7. Energy balance of a variable pressure ($p = \text{var}$) system investigated at the cylinder load $FM = 25\text{kN}$ and speed $vM = 0.20\text{m/s}$

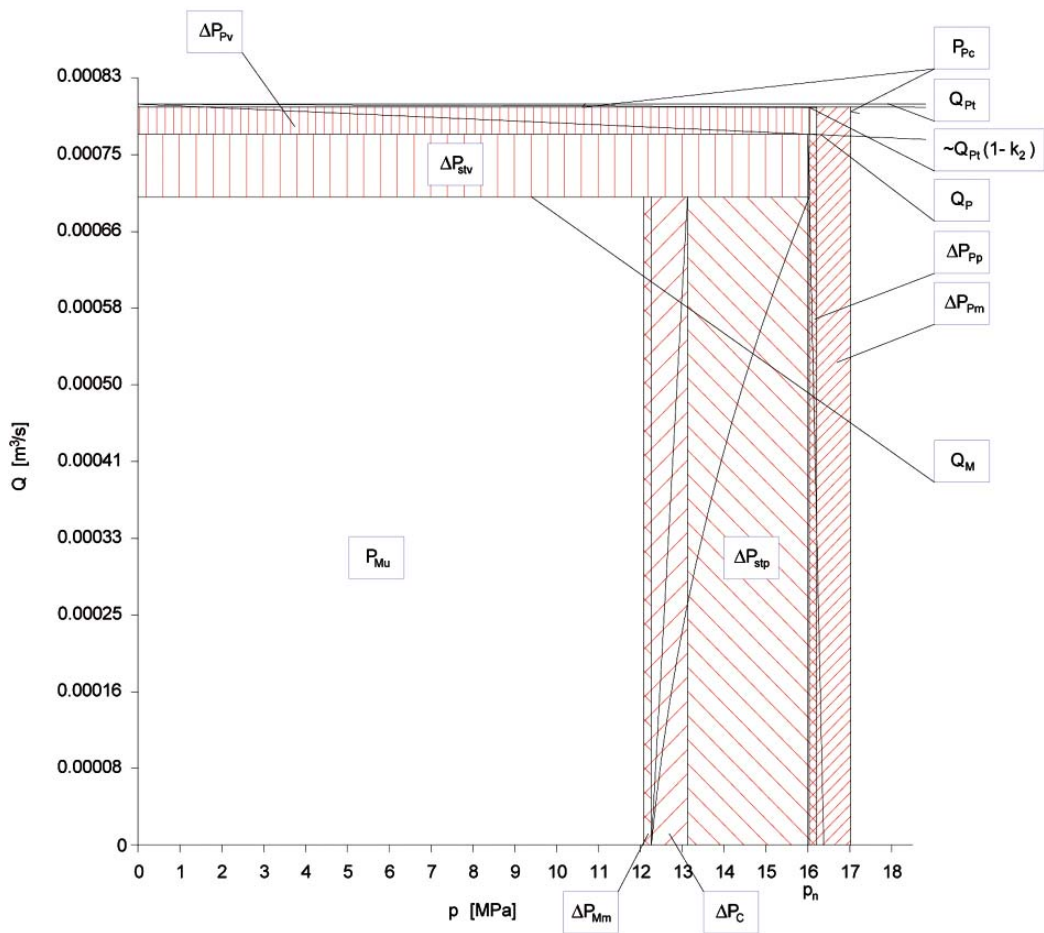


Fig. 8. Energy balance of a constant pressure ($p = \text{const}$) system investigated at the cylinder load $FM = 25\text{kN}$ and speed $vM = 0.35\text{m/s}$

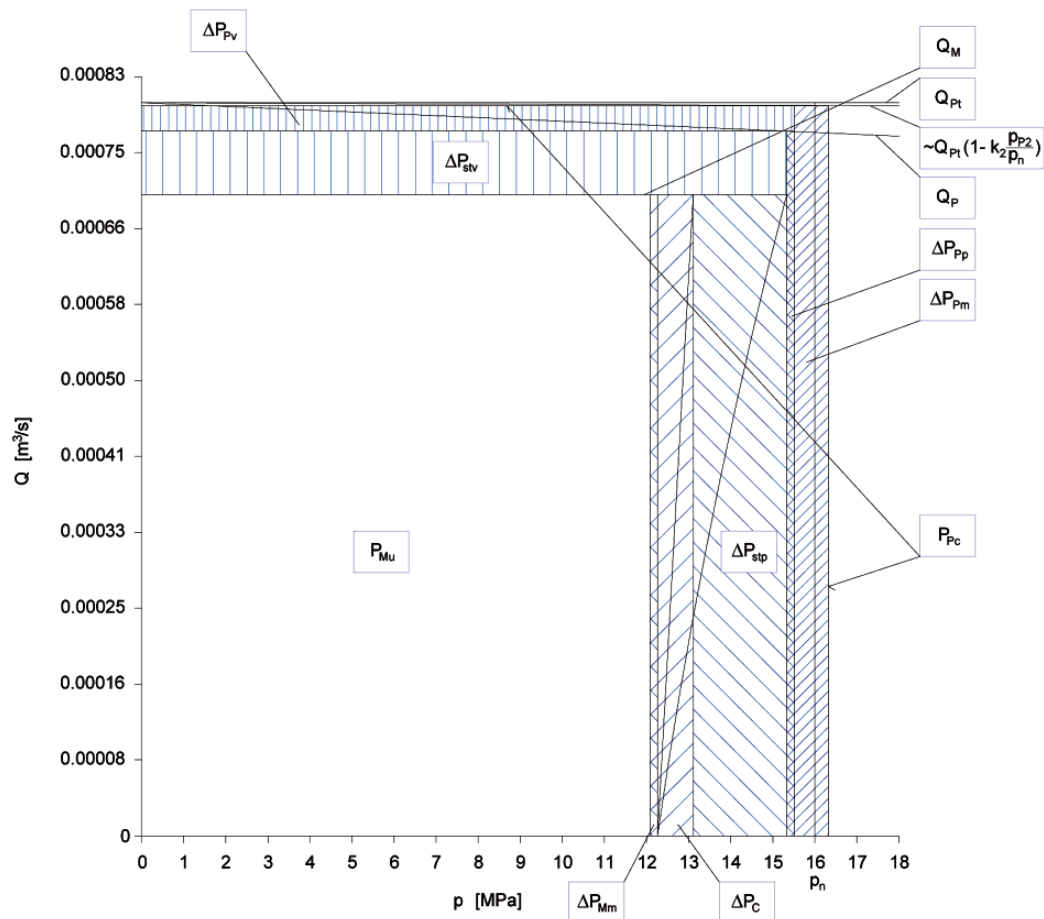


Fig. 9. Energy balance of a variable pressure ($p = \text{var}$) system investigated at the cylinder load $FM = 25\text{kN}$ and speed $vM = 0.35\text{m/s}$

of resistance of flow Δp_c and flow intensity Q_M towards the hydraulic cylinder, and that intensity is small due to small cylinder speed $v_M = 0.05$ m/s.

Figures 6 and 7 present the field P_{Mu} of the hydraulic cylinder useful power (white field) and the fields of the power ΔP of losses that occur in the $p = \text{const}$ system (Fig. 6) and $p = \text{var}$ system (Fig. 7) at the cylinder speed $v_M = 0.20$ m/s and cylinder load $F_M = 25$ kN. The fields of power ΔP of losses are shaded red.

The share of structural volumetric losses ΔP_{stv} and pressure losses ΔP_{stp} in the total energy balance of a constant pressure system is relatively great compared with other losses in the elements. The pressure energy accumulated in the liquid pressed by the pump is only partially used effectively in the cylinder. The remaining power, presented in the form of losses ΔP , is a loss of power. The greatest share in the losses have the ΔP_{stv} losses connected with the SP overflow valve. The pressure drop in the directional proportional valve is integrally connected with the system operation, as it decides the flow intensity and hydraulic cylinder speed. As the cylinder speed is assumed equal to $v_M = 0.20$ m/s and the load equal to $F_M = 25$ kN, the ΔP_{stp} losses are the second greatest losses in the system. Noteworthy is here much greater field P_{Mu} of the cylinder useful power compared with that field presented in Fig. 4. This is also connected with higher cylinder speed.

Also noteworthy in the presented figures are losses connected with the pump. Although they make a small part of the total losses, they are next in size to the structural losses ΔP_{st} in the system. Mechanical losses ΔP_{pm} are in the first place. The field of pump volumetric losses ΔP_{pv} is smaller and the field of pump pressure losses is smaller than that of the volumetric losses.

In figures 6 and 7 the field of cylinder useful power P_{Mu} is a smaller part of the field P_{pc} of power absorbed by the pump. This is connected with the hydraulic cylinder small load and small speed. As the power of mechanical losses ΔP_{Mm} in the cylinder is a function of the loading force F_M , the field of power of those losses is also small compared with other losses in the system.

Comparing the energy balance of a $p = \text{var}$ system presented in Fig. 7 with the balance of a $p = \text{const}$ system shown in Fig. 6 with the same cylinder speed and load coefficients, it can be noted that the structural losses ΔP_{st} in the proportional directional valve and in the controlled overflow valve as well as the pump volumetric losses ΔP_{pv} in a $p = \text{var}$ system are smaller due to the smaller pump discharge pressure p_{p2} .

Also smaller is power ΔP_{pm} of the pump mechanical losses.

Figures 8 and 9 present the energy balance of an investigated constant pressure ($p = \text{const}$) and variable pressure ($p = \text{var}$) system with the hydraulic cylinder $F_M = 25$ kN load and $v_M = 0.35$ m/s speed. It can be seen that structural losses are much smaller than in the case of limited or partial use of the cylinder speed and load, which is presented in figures 4 to 7. The pressure losses ΔP_c in the conduits increased due to higher cylinder speed.

Comparing the energy balance of the $p = \text{var}$ system shown in Fig. 9 with the balance of the $p = \text{const}$ system in Fig. 8, with the same cylinder speed and load coefficients, it can be noted that the balances are similar in the sense of areas of the corresponding fields.

Structural losses are much smaller than in the case of limited or partial use of the cylinder speed and load. Mechanical losses ΔP_{Mm} in the cylinder and pressure losses ΔP_c in the conduits increased due to higher cylinder speed and load.

SUMMARY AND CONCLUSIONS

The hydrostatic drive energy efficiency is a product of the efficiencies of drive system components. Efficiency of the component elements is, in turn, a product of the mechanical, pressure and volumetric efficiency of those elements. While determining those efficiencies, the power of losses in the elements is not taken into account, but only torque or force of the mechanical losses, pressure losses in the conduits or intensity of the volumetric losses. It is acceptable in the case of rotational pumps and motors and double-piston rod cylinders. However, it is not sufficient in considering the energy efficiency of commonly used linear motors, single-piston rod cylinders and systems with those machines. Therefore, not always justified simplifying assumptions are applied [3].

Full picture of the energy losses in a hydrostatic drive system is a picture of the power of energy losses in the system elements. The system feeding pump shaft power is equal to the sum of the hydraulic motor shaft or piston rod power plus powers of losses occurring in the energy stream flowing through the component elements. Power delivered to the system on the pump shaft is also influenced by the interrelation between the pump driving motor speed $n_p = n_{Mm}$ and the pump shaft torque M_p . Powers of the energy losses in the system elements and also powers developed by the elements must be precisely defined. The picture of energy losses requires the range to be determined of the hydraulic motor useful power P_{Mu} , determined in turn by the range of torque M_M and angular speed ω_M of a rotational motor shaft, or force F_M and linear speed v_M of a linear motor. The picture of energy losses in a hydrostatic drive system should be built from the hydraulic rotational motor shaft or linear motor piston rod towards the system feeding pump shaft [4, 5].

CONCLUSIONS

1. The impact is presented of the P_{Mu} power on the P_{pc} power in the analysed systems and also the impact of power ΔP of losses in the elements on the P_{pc} power. The hydraulic cylinder instantaneous useful power P_{Mu} , defined as a product of force F_M and cylinder piston rod speed v_M , is independent of all the losses. The following powers should be added to the useful power P_{Mu} : power ΔP_{Mm} of mechanical losses in the cylinder, power ΔP_c of losses in conduits, power ΔP_{stv} of structural volumetric losses and power ΔP_{stp} of structural pressure losses connected with the throttling control, as well as powers of the pump losses: pressure losses ΔP_{pp} , volumetric losses ΔP_{pv} and mechanical losses ΔP_{pm} . The sum of the useful power P_{Mu} and the ΔP power of all the system losses determines the instantaneous value of the P_{pc} power that the pump requires of its driving motor.
2. The analysis of the power of losses has been performed; for instance, in the $p = \text{const}$ system (Fig. 4), power ΔP_{Mm} of mechanical losses in the cylinder is smaller than power ΔP_{pm} of mechanical losses in the pump. In the $p = \text{var}$ system (Fig. 5), powers of losses ΔP_{Mm} and ΔP_{pm} are smaller; also here the ΔP_{Mm} is smaller than the ΔP_{pm} power.
3. It has been shown that with cylinder unchanged load F_M and its increased speed v_M , the power of structural pressure losses ΔP_{stp} increases, because the intensity of flow through the proportional directional valve is increased (Figures 6 to 9).
4. The change of structure from $p = \text{const}$ to $p = \text{var}$, with the same system useful power P_{Mu} , brings in effect a serious decrease of the power ΔP_{st} of structural losses (Figures 8 and 9). Simultaneously, at the same cylinder speed v_M , in

- the $p = \text{var}$ structure, the power ΔP_{pv} of volumetric losses in the pump and power ΔP_{pm} of mechanical losses in the pump decrease, but power ΔP_{pp} of pressure losses in the pump slightly increases.
5. Comparing the energy balance of the $p = \text{var}$ system with the $p = \text{const}$ system balance, with the same greatest values of the hydraulic cylinder speed coefficient $\bar{\omega}_M$ and load coefficient \bar{M}_M it can be noticed that those energy balances are close to each other in the sense of size of the field of power of losses (Fig. 8 and 9).
 6. Considerable decrease of the power of pump structural losses ΔP_{st} and power of volumetric losses ΔP_{pv} in the $p = \text{var}$ system in relation to the $p = \text{const}$ system can be seen with smaller hydraulic cylinder loads. This is connected with lower p_{p2} pressure in the $p = \text{var}$ system, because a system with the overflow valve controlled by the current pressure p_2 of outflow from the directional valve to the cylinder inlet chamber allows to adjust the p_{p2} pressure in the pump discharge conduit to the current cylinder load, i.e. the p_2 pressure, in such a way that pressure loss Δp_{DE1} in the directional valve slot f_{DE1} and pressure loss Δp_{DE2} in the directional valve slot f_{DE2} are limited. The Δp_{DE1} pressure drop in the directional valve is smaller than the Δp_{DE1} drop in the $p = \text{const}$ system. In connection with lower p_{p2} pressure, the power P_{pc} absorbed by the pump is significantly lower (Fig. 4 and 5).
 7. With small hydraulic cylinder speed v_M and small load F_M it can be noticed, that in spite of using a constant capacity pump, the power of structural pressure losses ΔP_{stp} and also power of structural volumetric losses ΔP_{stv} is considerably smaller in the $p = \text{var}$ system compared with the $p = \text{const}$ system. Although the intensity of flow Q_0 through the overflow valve to the tank with the same cylinder speed v_M is in the compared systems practically the same, the product of smaller pump discharge pressure p_{p2} and the flow intensity Q_0 (the $Q_p - Q_M$ difference) results in a smaller value of the power ΔP_{stv} of structural volumetric losses in the $p = \text{var}$ system (Fig. 4 and 5).
 8. Power ΔP_C of losses in the conduits is great at a great value of flow intensity Q_M towards the hydraulic cylinder (Fig. 8 and 9) compared with the power ΔP_{pp} of pressure losses in the pump. In the investigated $p = \text{const}$ and $p = \text{var}$ systems, in the individual conduit sections many elements are installed (filters, conduit connections, cut-off valves in fully opened position, temperature sensors), which change the direction or speed of flow in the conduits. Therefore, even greater pump capacity Q_p causes smaller flow resistance in the pump channels (which in the drawing corresponds to smaller width of the field of power ΔP_{pp} of losses) than the flow resistance in the conduits (which in the drawing corresponds to the width of the field of power ΔP_C of losses).
 9. Power ΔP_{Mm} of mechanical losses in the hydraulic cylinder changes with the change of pressure in its chambers. In a variable pressure system power ΔP_{Mm} of mechanical losses is smaller than in the $p = \text{const}$ system, as the F_{Mm} force of friction losses in the cylinder is smaller (Fig. 4 and 5).
 10. With increasing the hydraulic cylinder speed v_M and load F_M to the maximum values v_{Mmax} and F_{Mmax} respectively, the power ΔP_{stv} of structural volumetric losses and power ΔP_{stp} of structural pressure losses, connected with the throttling control assembly, is minimized.
 11. When the hydraulic cylinder does not displace (when its speed is equal to zero - $v_M = 0$) and the pump operates, the cylinder useful power P_{Mu} is equal to zero; the following powers of losses occur in the system: power ΔP_{stv} of structural volumetric losses and powers of losses in the pump: pressure losses ΔP_{pp} , volumetric losses ΔP_{pv} and mechanical losses ΔP_{pm} . The sum of those powers is equal to the power P_{pc} absorbed by the pump. With smaller loads F_M of the stopped cylinder, power P_{pc} absorbed by the pump in the $p = \text{var}$ system is smaller than power P_{pc} in the $p = \text{const}$ system
 12. The presented energy balances indicate that power P_{pc} absorbed by the pump (with the same cylinder useful power P_{Mu}) is different in two investigated systems. Pump operating in the $p = \text{const}$ system with constant capacity and nominal pressure p_n absorbs all the time much greater power P_{pc} than in the $p = \text{var}$ system. Apart from the wasted power, elements of the constant pressure system get worn out faster and hydraulic oil as the working medium is also used faster.
 13. Presentation of the energy balance of investigated systems by means of graphical interpretation as fields of power of energy losses shows in a legible and simple way the powers in the system and powers of losses in the elements, dependent on the hydraulic cylinder speed v_M and load F_M , on the speed v_M throttling control structure and on the quality of the system component elements. This is the first example of the changes of fields of power ΔP of losses in the elements and of power P_{pc} absorbed by the pump, as a function of the hydraulic cylinder useful power P_{Mu} .
 14. The variable pressure system has clearly smaller, compared with the constant pressure system, power of structural pressure losses in the throttling control assembly during a decreasing external load on the hydraulic linear motor. Also power of structural volumetric losses in the controlled overflow valve decreases, although the intensity of flow of the volumetric losses in that valve slightly increases compared with the constant pressure system due to greater pump capacity. In the pump operating in a variable pressure system, slight increase occurs of the power of pressure losses, decrease of the power of volumetric losses and also decrease of the power of mechanical losses. In effect, during a small load on the hydraulic linear motor, a decrease is noticed of the power absorbed by the pump from its driving electric motor, which, with unchanged useful power of the hydraulic linear motor, significantly increases the energy efficiency of the whole system compared with the constant pressure system efficiency.
 15. The two compared systems may achieve, during operating with maximum load and maximum speed, the same maximum overall efficiency. The variable pressure system becomes then a constant pressure system and the working conditions of both systems are the same.

BIBLIOGRAPHY

1. Paszota Z.: *Graphical presentation of the power of energy losses and power developed in the hydrostatic drive and control system elements. Part I – Systems with the series throttling control of the hydraulic rotational motor speed.* Chapter in the monograph: "Research, design, manufacturing and operation of hydraulic systems". Adam Klich, Edward Palczak and Andrzej Meder editors, "Cylinder" Library (in Polish), Centrum Mechanizacji Górnictwa „Komag”, Gliwice 2008, p. 121-139, figures: 12, bibliographic positions: 10.
2. Paszota Z.: *Model of losses and energy efficiency of a hydraulic system with proportional control of the cylinder fed by a constant capacity pump in a variable pressure system.* Chapter in the monograph: "Research, design, manufacturing and operation of hydraulic systems". Edward Palczak editor, "Cylinder" Library (in Polish). Centrum Mechanizacji

- Górnictwa „Komag”, Gliwice 2005, p. 145-162, figures: 6, bibliographic positions: 8.
3. Skorek G.: *Energy characteristics of a hydraulic system with proportional control of the cylinder fed by a constant capacity pump in a constant and variable pressure system*. Doctor dissertation (in Polish), Gdansk University of Technology, Faculty of Ocean Engineering and Ship Technology, Chair of Ship and Ocean Engineering Equipment, Gdansk 2008, 253 pages, 141 figures, 62 bibliographic positions.
 4. Paszota Z.: *Power of energy losses in the hydrostatic drive system elements – definitions, relations, change ranges, energy efficiencies. Part I – Hydraulic motor*. Chapter in the monograph: "Research, design, manufacturing and operation of hydraulic systems". Andrzej Meder and Adam Klich editors, "Cylinder" Library (in Polish). Centrum Mechanizacji Górnictwa „Komag”, Gliwice 2007, p. 99 – 120, figures: 3, bibliographic positions: 6.
 5. Paszota Z.: *Power of energy losses in the hydrostatic drive system elements – definitions, relations, change ranges, energy efficiencies. Part II – Conduits, throttling control assembly, pump*. Chapter in the monograph: "Research, design, manufacturing and operation of hydraulic systems". Andrzej Meder and Adam Klich editors, "Cylinder" Library (in Polish). Centrum Mechanizacji Górnictwa „Komag”, Gliwice 2007, p. 121 – 139, figures: 1, bibliographic positions: 6.

CONTACT WITH THE AUTHOR

Grzegorz Skorek, Ph.D.
Department of Engineering Sciences
Faculty of Marine Engineering,
Gdynia Maritime University
Morska 81/87
81-225 Gdynia, POLAND
e-mail: grzesko@am.gdynia.pl

Assessment of possible application of water-lubricated sintered brass slide bearing for marine propeller shaft

Wojciech Litwin, Ph.D.
Artur Olszewski, Ph.D.
Gdansk University of Technology, Poland

ABSTRACT

Water-lubricated bearings have been applied to support ship screw shafts for over a hundred years. Development of plastic materials has caused that novel sliding polymers appeared available on the market and being approved by classification institutions, possible to be applied in shipbuilding. However in the subject – matter literature there is no reference to application of bearings fitted with metal or ceramic bushes in shipbuilding. Nevertheless they have important merits such as low resistance to motion, long service life or stability of form. But some doubts are evoked by their large value of shape elasticity module which can lead to local stress concentration at the bush edges in the case of non-axiality of bush and shaft axes. Hence this work has been aimed at the testing of a bearing made of bronze-graphite sinter. In the work is presented a comparison of measurement results of resistance to motion, hydrodynamic pressure distributions in lubricating film as well as shaft axis trajectories of the bearing, with those made for a typical elastic polymer bearing. The measurement results have showed high quality of the tested material. In the opinion of these authors it could be applicable to bearing ship propeller shafts.

Keywords: bearing; bearing of ship propeller shafts; tribology; water-lubricated bearings

INTRODUCTION

As a result of becoming screw propulsion on ships widespread it was necessary to elaborate a reliable and durable bearing for ship propulsion shafts. Most of operational problems have been generated by the last section of the shaft on which screw propeller is installed – the so called screw propeller shaft. It results a.o. from a complex loading system in consequence of mass forces and harsh working conditions, especially exposure to salt sea water. From the very beginning of the application of mechanical propulsion to ships till now a slide bearing has been used in the classical propulsion system of floating units. In the past attempts have been made to use rolling bearings, however such solution can be met now rather rarely as it makes repair technology complicated, is less durable as well as cannot be used for large diameter shafts [1, 2].

Since many years ago engineers have faced troubles associated with propeller shaft bearing and in the past many failures of shafts, bearings and sealings, have happened. With the famous ship *Great Eastern* is connected an interesting story dealing with her propeller shaft bearing. This unusual ship propelled by screw propellers and side paddle wheels, of more than 200 m in length, built in 1859, was then several times greater than any other ship. After two cross - Atlantic trips it was revealed that her stern slide bearing fitted with white metal liner was completely worn out. Measurements

of position of the shaft (shaft settling) showed that its wear reached the value of 63 mm. According to suggestion of John Penn, a British engineer, the white metal bearing was replaced by a new one made of guaiac wood (*lignum vitae*) [3]. After completing such modernization the problem of stern bearing did not recur during the entire service period of the ship.

Already at the beginning of 20th century such wooden bearings have been in common use. However they have had some limitations. Among the most important can be numbered the sensitivity to lubrication with a contaminated lubricant e.g. in the conditions of sailing in shallow or inland waters.

Dynamical development of novel tribological materials including plastics has resulted in their successful application as a sliding material to water-lubricated bearings. Today there are a few worldwide companies which produce bearings with a polymer sliding bush approved by ship classification societies for application to ships. The tests performed in the past have demonstrated their high quality, hence they are widely applied today on both small and large ships.

In spite of the common application of polymer bearings, new research projects aimed at elaboration of better and better sliding materials, are still under way. Bronze-graphite sinters of all kinds can serve as an example of a material alternative to plastics. They have many merits, e.g. a high stability of form, higher resistance to elevated temperature and seizing-up.

ORIGIN

For recent years many types of water-lubricated slide bearings have been tested at Gdańsk University of Technology [4÷8]. Among other things, have been performed tests of a water-lubricated bearing fitted with the sliding bush made of BA1032 (CuAl10Fe3Mn2) Al-Fe-Mn bronze and journal of X10CrNi18-8 (AISI 301) stainless steel. The tests showed that such association cannot be lubricated with water, despite its perfect work in the conditions of lubrication with oil or plastic lubricant. The tested bearing has been seized up shortly after its starting (Fig. 1).

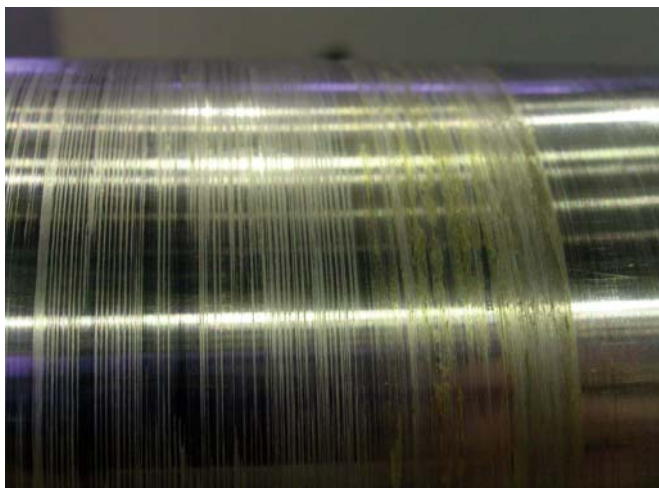


Fig. 1. The damaged shaft made of X10CrNi18-8 stainless steel-fragments of the bronze bush can be observed on its surface

However in recent years novel, special sliding materials made on the basis of bronzes, iron or nickel, capable of operating in water, have appeared. One of such materials is bronze-graphite sinter. Its very good sliding qualities in the case of lubrication with water, advertised by its producer, result from its composite structure. Into bronze-tin matrix a lubricating medium in the form of graphite was inserted. Due to this, even after breaking lubricating film graphite particles effectively lower friction forces and prevent seizing. The material can be applied even in the temperature close to 800°C and is of a high resistance against corrosion. As novel sintered materials are successfully applied to water-lubricated bearings of vertical water turbines it was decided to test a material of the kind in the operational conditions of ship stern tube bearing. It should be stressed that screw propeller shaft which operates in horizontal position, produces much more harsh operational conditions for such bearing in comparison with those for a vertical shaft. It results from greater radial loads due to static and dynamical mass forces occurring in the shaft - screw propeller system.

It was decided that such metal bearing will be compared with a typical, water-lubricated polymer bearing approved by classification institution. Such comparison will make it possible to determine drawbacks and merits of both the solutions.

For the tests was selected a bronze-graphite sinter offered in the form of prefabricated bush elements pressed under high pressure and temperature. The bronze bush was pressed into a steel sleeve and then the internal hole was machined to its final dimensions. For the reason of a relatively high hardness of the implemented bronze (in comparison with that of polymer) the bush of the kind has been intended for interaction with the journal of the hardness of 35HRC at least. Therefore on the shaft made of X10CrNi18-8 steel a hardened-tempered sleeve made of X30Cr13 (AISI 420) steel was bonded by using thermo-

compression method. The sleeve was next grinded and polished to ensure appropriate coaxiality with respect to journals of bearings which supported the shaft during the tests.



Fig. 2. The tested bearing fitted with metal bush: a) the prefabricated sliding bush element made of sintered bronze, b) the complete bearing before its mounting at the test stand, in which the sliding bush and outer steel sleeve with circumferentially placed sockets for pressure transducers, are seen.

PLAN OF THE TESTS

Data of the tested bearings are presented in the tab. 1.

As resulted from measurements, the polymer bearing had a non-ideal form (cylindricity error) as well as a worse state of sliding surface in comparison with that of the bearing made of sinter. It results from difficulty in machining a very elastic polymer and its deformations resulting from absorption of water (soaking).

Many calculations performed in the past, based on hydrodynamic lubrication theory for EHL model [5, 6, 7] have shown that the bearing with rigid bush operated at a larger film thickness in comparison with the same bush but made of polymers. The different thickness of lubricating film in rigid

Tab. 1. Comparison of the tested bearings

Material	Shear modulus [MPa]	Shaft diameter [mm]/Bush length [mm]	Bearing clearance [mm]	Sliding surface roughness R_a [μm]	Shaft journal roughness R_a [μm]
Bronze-graphite sinter	1.1×10^5	100/150	0.15	0.16	0.09
Uniform elastic polymer approved for marine applications	6×10^2		0.17-0.19 (shape errors)	0.35	0.09

bearing and elastic one results from elastic bush deformation under pressure, which changes lubricating gap form [9].

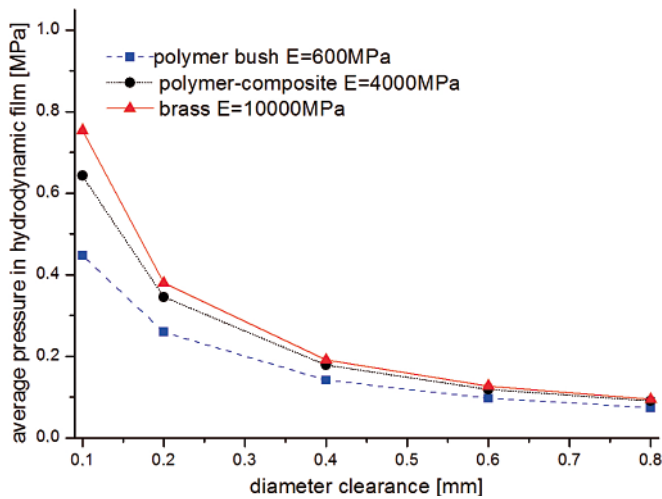


Fig. 3. Influence of shear modulus of bush material on load-carrying capacity of bearing, in function of bearing clearance value; journal diameter of 100 mm, shaft rotational speed of 11 rev/s

One of the main aims of experimental tests was to compare theoretical results with experimental ones as well as to determine drawbacks and merits of the bearings with metal bush.

EXPERIMENTAL TESTS

For the experimental tests was used the test stand already described in the subject-matter literature [6,10]. It has wide research possibilities. During the tests, resistance to motion, pressure in lubricating film as well as shaft axis trajectory was measured.

The tests were performed for working parameters typical for marine application of such bearings. In order to gain as much information about tribological qualities of both the bearings as possible, was planned a set of tests in different conditions realized by changing both load and rotational speed. The load was applied statically by hanging a weight. The tests were performed for three different load values giving the average pressures of 0.2, 0.4 and 0.6 MPa, respectively. Rotational speed was varied in the range from 0 to 11 rev/s. The measurements were taken for the speed values of 1, 2, 3, 5, 7, 9 and 11 rev/s. In the case of determination of resistance to motion also static friction coefficient was measured.

During the tests, water of 15°C temperature was pressed through the bearing. Its flow rate amounting at least to 6 l/min was sufficient to ensure proper lubrication of the bearing. All the measurements was performed for the initially run-in bearings (after 24h working period in the range of low rotational speeds, at mixed friction work).

RESULTS OF THE TESTS

Tests of starting resistance

A very important feature of water-lubricated slide bearings is their capability of starting under load. This is especially important in the case of horizontal ship propeller shafts which exert their weight onto bearings regardless of whether the shaft is in idle or motion state. In slide bearings, in contrast to rolling ones, the problem of appearance of very large values of resistance during start-ups under load, often happens. It results from a large, static friction coefficient which occurs in conditions of lacking hydrodynamical lubrication. In the case of polymer bearings the effect can be heightened by stick-slip

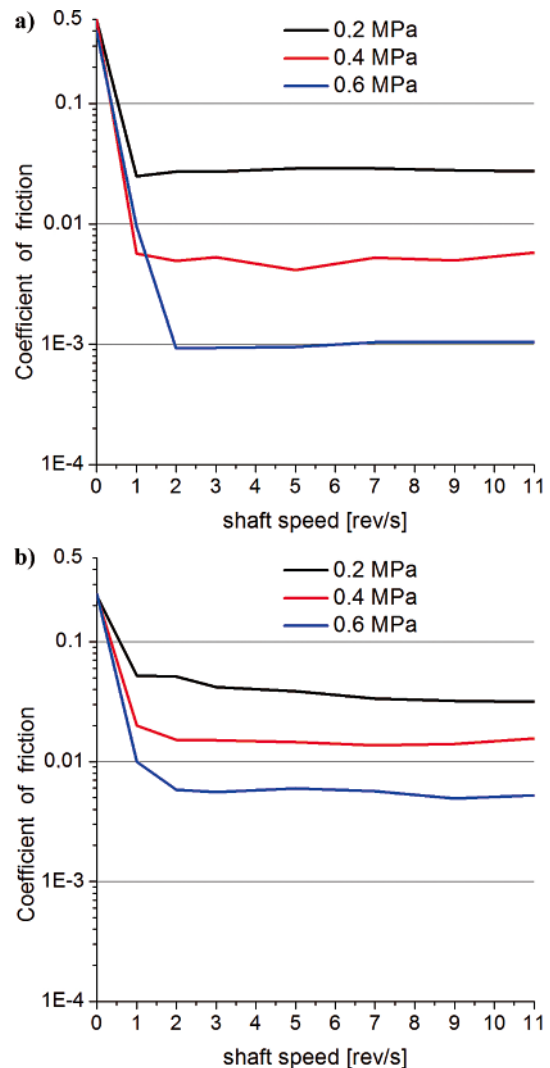


Fig. 4. Measured friction coefficient in: a) bearing with metal bush, b) bearing with polymer bush

phenomena. Usually, after reaching even a low rotational speed (of abt. a few rpm), a partial raise of hydrodynamical pressure occurs and in consequence friction coefficient drops suddenly. In Fig. 4, are presented the diagrams of measured friction coefficients in metal bearing and polymer one in function of rotational speed and average pressure values.

The recorded friction coefficient values indicate that in the bearing of metal bush a larger value of friction coefficient equal to abt. 0.5, occurs. In the same conditions in the polymer bearing the friction coefficient amounts to abt. 0.25. It means that the bearing with metal bush requires at least two times greater starting moment in comparison with the polymer bearing. It is also seen that in the metal bearing dropping resistance to motion is faster because after reaching the rotational speed of 0.5 rev/s the friction coefficient drops to the five times

lower value equal to abt. 0.1. It is undoubtedly connected with forming hydrodynamic lubricating wedge in the rigid bearing faster than in the elastic (polymer) bearing. It should be mentioned that in the bearing with metal bush lower resistance to motion occurs in steady working conditions (regardless of pressure values).

Tests of journal displacement against bush

The trajectory diagrams are presented on the background of experimentally measured clearance circles (Fig. 5 ÷ 10). It makes a better interpretation of the results, possible. Moreover, shape of the clearance circles reflects shape of the bush, hence it makes it possible to assess bush shape errors. The shape error which appears in the bearing of polymer bush is not surprising

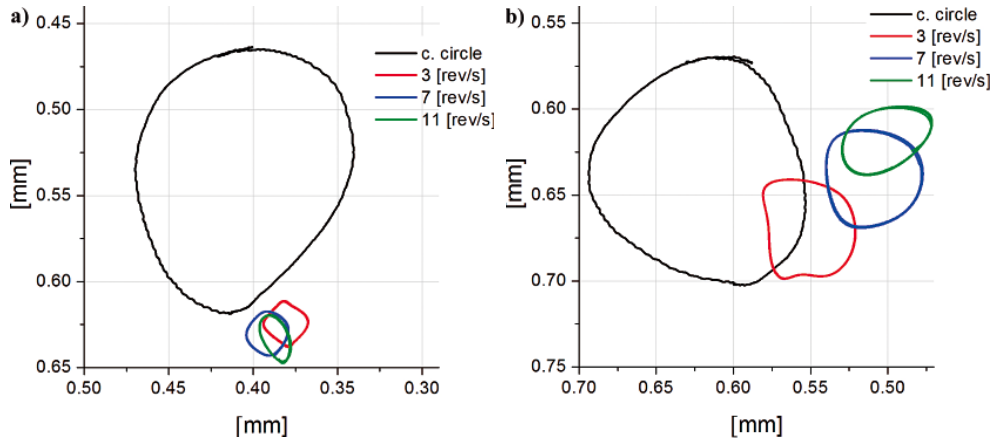


Fig. 5. Shaft orbits measured on both sides of the bearing with metal bush, under load of 0.2 MPa; a) left side of the bush, b) right side of the bearing; orbits for three successive shaft revolutions

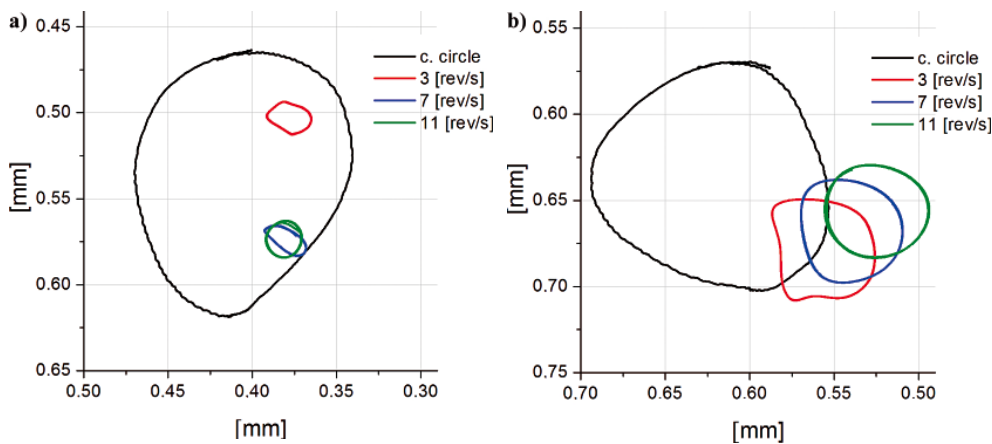


Fig. 6. Shaft orbits measured on both sides of the bearing with metal bush, under load of 0.4 MPa; a) left side of the bush, b) right side of the bearing; orbits for three successive shaft revolutions

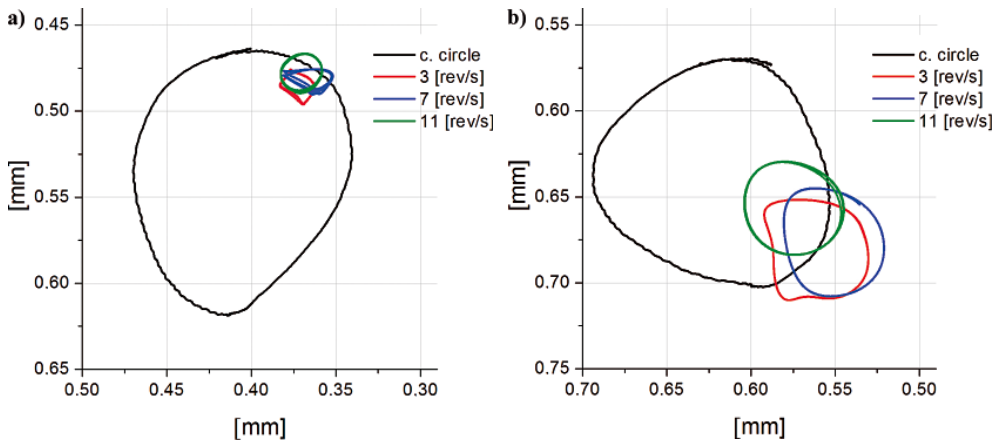


Fig. 7. Shaft orbits measured on both sides of the bearing with metal bush, under load of 0.6 MPa; a) left side of the bush, b) right side of the bearing; orbits for three successive shaft revolutions

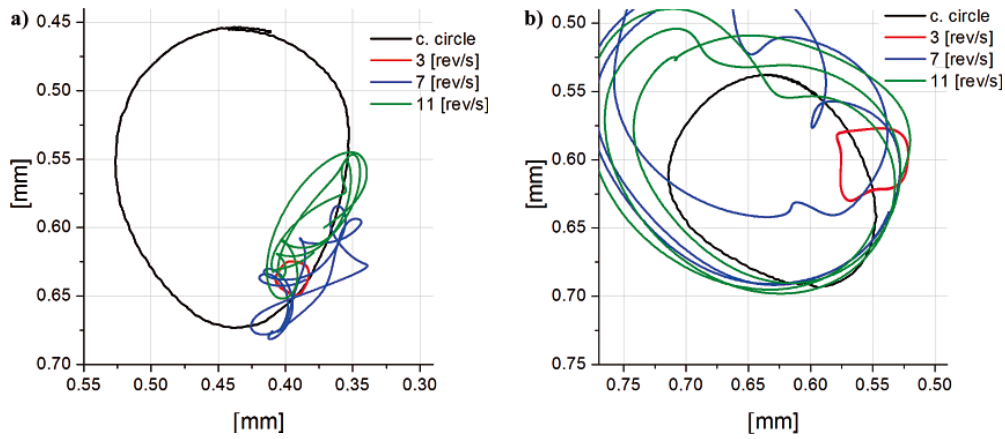


Fig. 8. Shaft orbits measured on both sides of the bearing with polymer bush, under load of 0.2 MPa; **a)** left side of the bush, **b)** right side of the bearing; orbits for three successive shaft revolutions

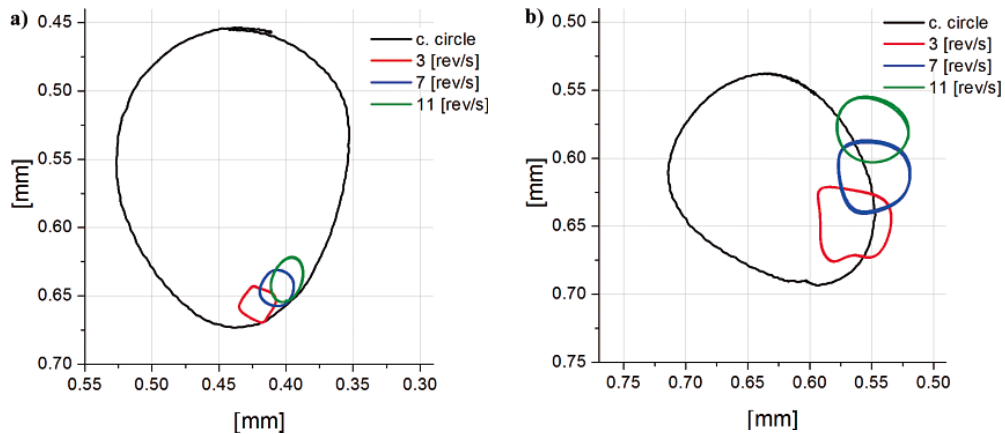


Fig. 9. Shaft orbits measured on both sides of the bearing with polymer bush, under load of 0.4 MPa; **a)** left side of the bush, **b)** right side of the bearing; orbits for three successive shaft revolutions

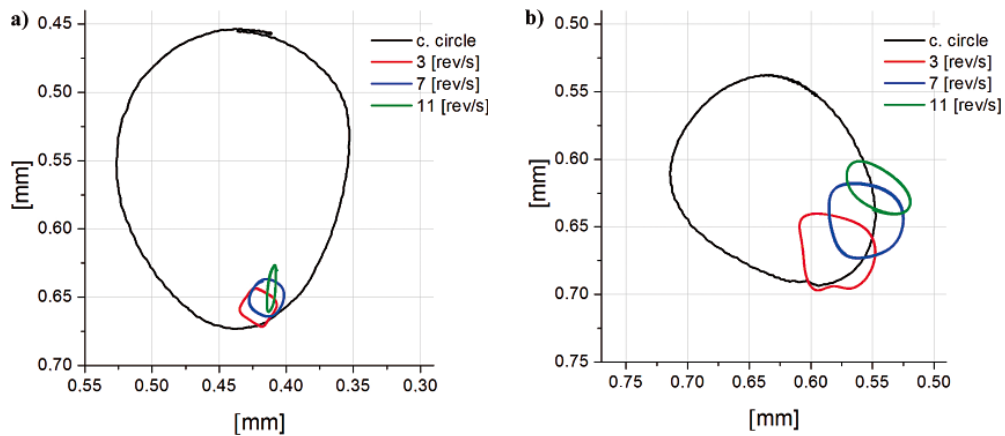


Fig. 10. Shaft orbits measured on both sides of the bearing with polymer bush, under load of 0.6 MPa; **a)** left side of the bush, **b)** right side of the bearing; orbits for three successive shaft revolutions

as it results from machining the elastic water-absorbing polymer. However, is puzzling the shape error of the bearing with metal bush machined to its final form after installation into the metal sleeve. The tests of the bearing made of BA1032 (CuAl10Fe3Mn2) bronze, whose sliding surface was grinded, carried out in the past (as already mentioned), showed that it is possible to obtain its shape almost ideal (Fig. 11). In the discussed case the bush length was as large as 300 mm and in spite of that the high machining precision (H7 tolerance class) was achieved.

As results from the shaft axis trajectory measurements, the bearing operated at a significant non-coaxiality of shaft against bush (Fig. 5 ÷ 10). In spite of that it operated in the range of

fluid friction. In the opinion of these authors it testifies to their high potential and big margin of load-carrying capacity. It should be added that the revealed non-coaxiality does not result from inappropriate assembling work but from free-support of the bearing, hence even a small asymmetry in hydrodynamic pressure distribution produces natural twisting of the bush.

Repeatability of trajectories draws attention. In the diagrams, orbits of three successive revolutions of shaft are presented. In most of the cases the oval orbits smaller than 10 μ m in size cover practically each other. Due to this the bearing practically does not produce vibrations, except of the situations of its unstable work (Fig. 8). Such phenomenon appeared only in the bearing with polymer bush under load of a small value.

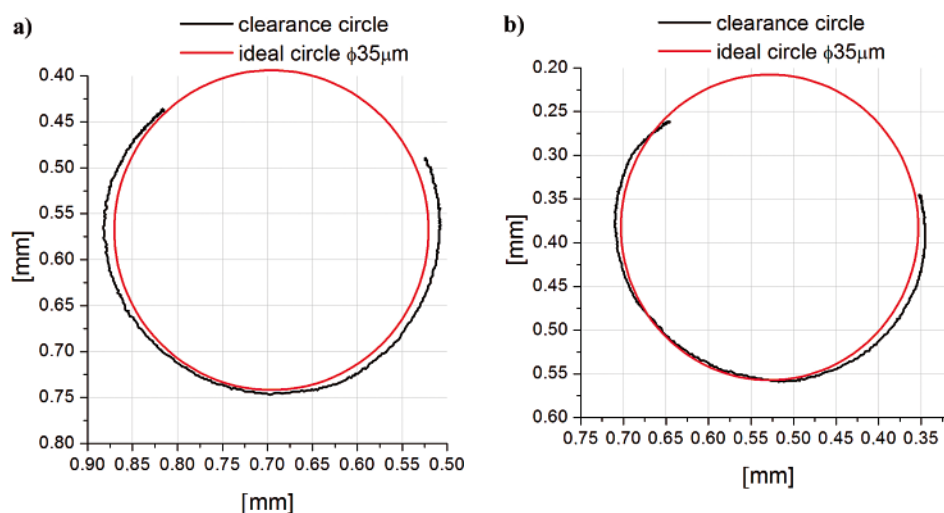


Fig. 11. Experimentally measured clearance circles of BA1032 bronze bearing whose sliding surface was grinded; a) left side of the bush, b) right side of the bearing

Tests of hydrodynamic pressure distribution

Below in Fig. 12 ÷ 14, are presented selected results of experimental tests of hydrodynamic pressure distribution in the metal (rigid) bearing and the polymer (elastic) one. By analyzing the obtained results the significant effect of bush rigidity on pressure distribution form can be observed. In the rigid (metal) bearing much greater maximum pressure which varies in function of values of average pressure and speed, occurs. The averaged values of the results achieved during the tests are given in Tab. 2 below. In the case of the rigid bush the

maximum pressure is up to four times greater than the average nominal one, whereas for the flexible bush the maximum pressure does not exceed twofold value of the average pressure. It results from local change of lubricating gap form in the flexible bush, that leads to dropping maximum pressure at simultaneous increasing lubricating wedge lap angle.

During operation of the bearing in normal conditions pressure pulsations are rather small (Fig. 15a). As expected, the above described unstable work of the bearing (Fig. 8) generates significant pressure pulsations in the lubricating film (Fig. 15b).

Tab.2. Average values of pressure in lubricating film

	Shaft rotational speed [rev/s]	Nominal (average) pressure resulting from load [MPa]	Maximum pressure in lubricating film [MPa]
Rigid (metal) bush	3	0.2	1
	7	0.2	1.2
	11	0.2	0.8
	3	0.4	1.5
	7	0.4	1.7
	11	0.4	1.6
	3	0.6	2.1
	7	0.6	2.1
	11	0.6	2.1
Flexible (polymer) bush	3	0.2	0.38
	7	0.2	0.25
	11	0.2	0.28
	3	0.4	0.58
	7	0.4	0.5
	11	0.4	0.48
	3	0.6	0.75
	7	0.6	0.7
	11	0.6	0.68

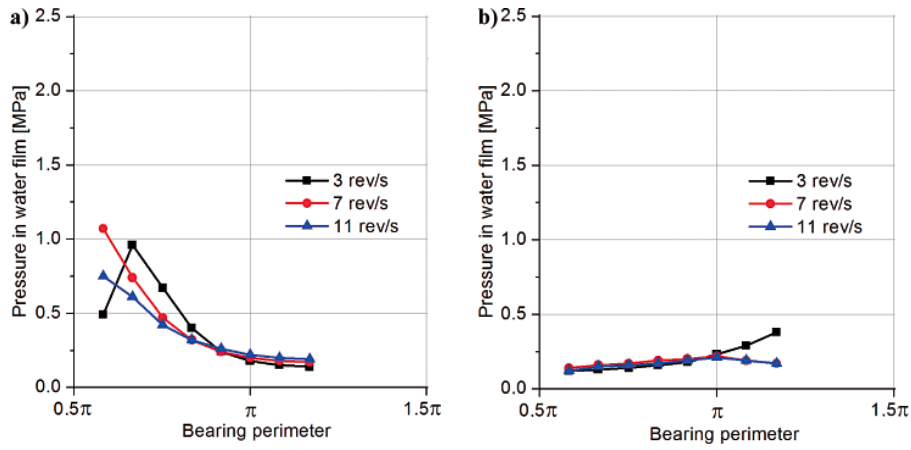


Fig. 12. Measured distributions of pressure in lubricating film in lower half of the bush under load of 0.2 MPa; a) bearing with metal bush, b) bearing with polymer bush

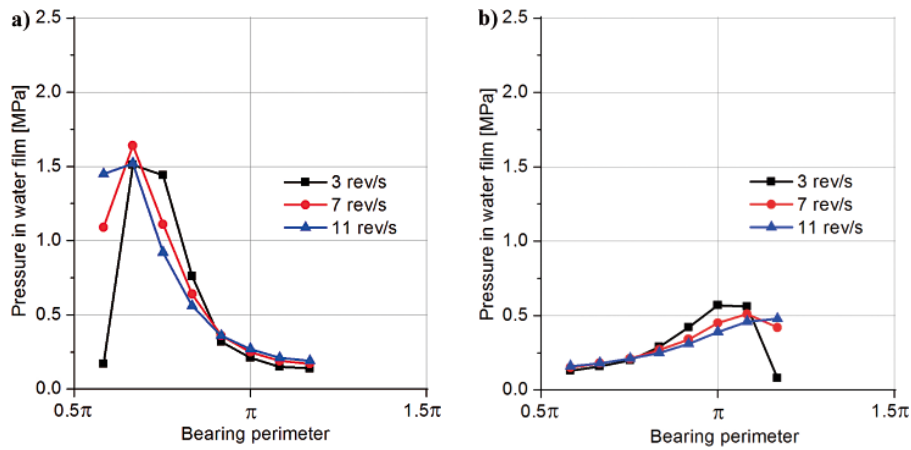


Fig. 13. Measured distributions of pressure in lubricating film in lower half of the bush under load of 0.4 MPa; a) bearing with metal bush, b) bearing with polymer bush

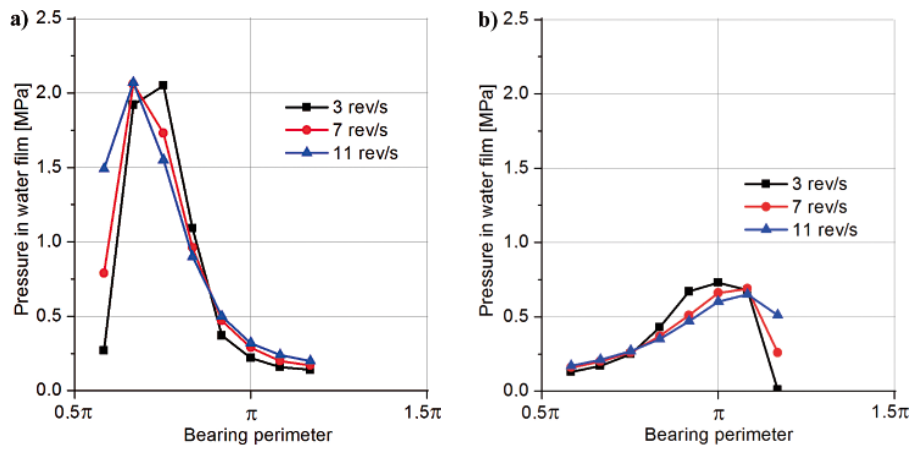


Fig. 14. Measured distributions of pressure in lubricating film in lower half of the bush under load of 0.6 MPa; a) bearing with metal bush, b) bearing with polymer bush

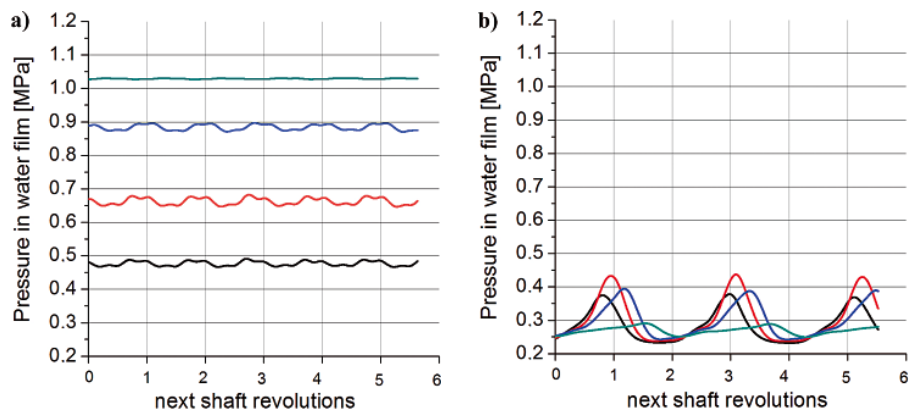


Fig. 15. Comparison of the measured pressure pulsations in lubricating film; a) 0.6 MPa, 11 rev/s, b) 0.2 MPa, 11 rev/s

CONCLUSIONS

- Analyzing the measurement results one can observe distinct difference between behaviour of the rigid (metal) bearing and flexible (polymer) one. Both the bearings generate hydrodynamic pressure distribution of different form. In the rigid bearing the maximum pressure is up to four times greater than the average nominal pressure, and in the flexible bearing – two times greater at the very most. In the metal bearing the starting moment over two times greater than that in the polymer bearing, occurs. Statical friction coefficients amount to 0.5 and 0.25, respectively. Worth adding that in the polymer bearing stick-slip phenomena were observed, that could detrimentally affect its friction coefficient value.
- Hydrodynamic pressure very fast develops and the friction coefficient value recorded during the tests for operation in the fluid friction range, amounted to 0.01, on average. It should be remembered however that due to limitations of the test stand the value is burdened with an error and evidently greatly overstated.
- The water-lubricated bearing with steel bush is of a greater load-carrying capacity in comparison with a typical polymer bearing. It results from lack of deformations of the rigid bush under hydrodynamic pressure as well as a high smoothness of its surface. This way the experimental tests confirmed the calculation results (Fig. 3).
- The bearings with steel bush show a lower sensitivity to contaminations which do not stick in sliding surface. Due to this fact wear occurs mostly on the side of bush, which is favourable from the point of view of repair cost.
- Apparently the necessity of application of hardened stainless steel journals was an obvious disadvantage of the metal bearings, which greatly rises cost of realization of such solution.

RECAPITULATION

The performed tests showed that in the assumed working conditions the water-lubricated bearings with metal bush are of a sufficient load-carrying capacity and can be applied also in the case of ship propeller shafts. Approval of the applied material by ship classification institutions remains to be a formal problem only.

The producer of the material indicates that one of the cardinal merits of such designs is their much greater resistance to wear in the conditions of lubrication with contaminated water since in the metal bearings, in contrast to polymer ones, the contaminations do not stick into bush sliding surface and, consequently, do not scratch the journal. As the referred opinion evokes some doubts, these authors have attempted to prepare tests of bearings of the kind in the conditions of lubrication with contaminated water. However the bearing with metal bush has an important disadvantage. It should be remembered that in the case of ship main propulsion shafts a problem is

their appropriate assembling, and as a rule we then deal with a smaller or greater non-coaxiality between shaft and bush. It may also occur occasionally as a result of deformation of a flexible ship hull at its non-uniform weight distribution of cargo. The effect may also be strengthened due to hull response to waves. Therefore in some cases the so called edging, i.e. concentration of pressure between shaft journal and bush edge, may happen. The phenomenon can generate sudden wear process of the sliding pair. It will not occur in the case of applying elastic polymer because the bush will be deformed elastically, that leads to a greater contact zone.

BIBLIOGRAPHY

1. Cudny K.: *Ship shaft lines* (in Polish). Wydawnictwo Morskie Gdańsk (Gdańsk Maritime Publishers), Gdańsk, 1976
2. Buglacki H., Cicholska M., Cudny K.: *Problems of ship shaft line rolling bearings* (in Polish). Tribologia No.1, 2002, Vol.33
3. Roy L. Orndorff, Jr.: *Water - Lubricated rubber bearings, history and new developments*. Naval Engineers Journal, November 1985
4. Litwin W.: *Marine water lubricated stern tube bearings – design and operations problems*. STLE/ASME International Joint Tribology Conference 07; San Diego, USA
5. Litwin W.: *Water Lubricated Marine Stern Tube Bearings – Attempt At Estimating Hydrodynamic Capacity*. ASME/STLE International Joint Tribology Conference, October 19-21, 2009, Memphis, Tennessee, USA
6. Litwin W.: *Marine water lubricated main shaft bearings, problems, theoretical and experimental research*. Polish Maritime Research No. 4, 2009, Vol. 16
7. Olszewski A., Wodtke M., Hryniewicz M.: *Experimental Investigation of Prototype Water-Lubricated Compliant Foil Bearings*. Key Engineering Materials: Fundamentals of Machine Design, Vol. 490 (2012)
8. Olszewski A.: *Tilting pad journal bearing with ceramic coating*. Automotive and Industrial Lubrication: 15th International Colloquium Tribology: Book of synopses 2006, Stuttgart/Ostfildern, Germany, January 17-19, 2006
9. Litwin W.: *Influence of Bearing Bush Geometry on Properties of Water Lubricated Marine Main Shaft Bearings*. World Tribology Congress 2009, Kyoto, Japan, September 6 – 11, 2009
10. Litwin W.: *Influence of Surface Roughness Topography on Properties of Water-Lubricated Polymer Bearings: Experimental Research*. Tribology Transactions, 05, 2011

CONTACT WITH THE AUTHORS

Wojciech Litwin, Ph. D.
Artur Olszewski, Ph.D.
Faculty of Ocean Engineering
and Ship Technology
Gdansk University of Technology
Narutowicza 11/12
80-233 Gdansk, POLAND
e-mail: wlitwin@pg.gda.pl

Multi-stage magnetic-fluid seals for operating in water – life test procedure, test stand and research results

Part I

Life test procedure, test stand and instrumentation

Leszek Matuszewski, Ph.D.
Gdansk University of Technology, Poland

ABSTRACT



The edge criteria for magnetic-fluid seals durability research are critical for the seal's technological usefulness. The magnetic fluid seal technology in water is much more difficult technological problem in comparison to gas or vacuum environment. There is always problem with immediate contact between magnetic fluid and the environmental uninspected liquids. In the paper are presented ways of experiments definitions carried out with multi-stage rotating magnetic fluid seal operating in permanent contact with utility water. The special test procedures have been elaborated and practically used, with the aim to define main characteristics of magnetic fluid seals. These characteristics were: critical pressure, critical motion velocity and working life of the seal. Some grades of commercial, silicon based magnetic fluids of hydrophobic properties were tested in sealing system. The test stand and its features as well as results of tests are presented in the form of tables, cross section draws and diagrams. In conclusion one can see that multi-stage magnetic-fluid seals could be efficiently used in water for rotating shaft seals in a limited range of motion velocity and work lasting.

Keywords: shaft sealing; utility water; seal durability; critical pressure; critical motion velocity; magnetic fluid

INTRODUCTION

The investigations described in this paper were performed at the test stand designed and built in accordance with the below presented assumptions, especially intended for testing drives used in ocean engineering. The research was financially supported in the frame of research projects of Ministry of Science and Higher Education and NCBR. Many elements of the research methods, measurement data recording and maintenance techniques are entirely original. Therefore it is necessary to describe the applied research process and procedures. Results of testing the single-stage magnetic-fluid (MF) seals have been already published earlier and those dealing with multi-stage ones are given in the second part of this elaboration. The problem in question is below presented on the background of the state of engineering with reference to the most important details given already in the paper [18].

This paper relates results of a continuation of the tests of MF seals in liquid environment, carried out in 2011, this turn with the use of multi-stage sleeves. Worth reminding that the magnetic fluid seals operating in liquid environment are exposed to loss of tightness due to action of factors which occur during direct inter-phase contact of two environments being in the same physical state – magnetic fluid and sealed liquid.

It is hard to compare the problem with the situation where gas environments have to be separated. The basic condition to be fulfilled in designing the seal is to select a magnetic fluid (or environment liquid) of such physical chemical properties that the liquids being in contact to each other do not mix together and on their separation surface a high inter-phase surface tension occurs. In static conditions (i.e. when seal elements do not displace against each other), if only the system is properly designed, satisfaction of the above mentioned conditions usually ensures correct work of the seal. Lack of susceptibility to mixing and high inter-phase surface tension are as a rule insufficient if a MF seal has to be applied in conditions of seal motion or sealed liquid flow in vicinity of the seal. Relative motion of the two liquids generates a surface instability on the boundary of the phases [2, 3], whose intensity greatly increases above certain limiting difference in velocity, that results in washing away the magnetic fluid and loss of tightness of the system along with time. Life time of such seal drops below its profitability.

In the published elaborations [4, 5, 6] are described attempts at determining possible conditions of operation of MF seals in water, depending on pressure and motion speed. In the work [7] are presented investigations on application of MF seal to sealing lubrication oil, and in [8] is given an attempt at design

optimizing the seal intended for the operating also in oil. In the paper [9] its authors present a concept of the „magnetic surface tension” and its impact on MF seal operation in water.

Some years earlier in AGH Laboratory, the tests of MF seals operating in utility water environment were carried out [12, 13, 14] in order to assess their applicability in shipbuilding. Results of the tests conducted in the years 2009÷2010 on the test stand adjusted to operation of the seals in liquids [15] showed that it is possible to apply some commercial magnetic fluids to MF seals operating in direct contact with water in working conditions which occur in many devices met not only in ocean engineering. In the tests of a utility character single-stage MF seals – models of real seals with magnetic fluid - were used; their working conditions were limited only to the assigned technical task, i.e. assessment if performing the tests is purposeful.

In this work are described experimental tests of a magnetic fluid seal of three sealing stages, carried out in its direct contact with water and in ship propulsion conditions as well.

Alike as at the tests of the pack with single-stage sleeve, the tests were performed in variable magnetic field conditions (different number of permanent magnets in magnetic system of the seal), for different set-up values of working pressure and the same magnetic fluid dose delivered to the sealing stages.

In the presented tests a sleeve of three unsymmetrically arranged sealing stages was used. The application of the unsymmetrical (one-sided) arrangement of sealing stages had the practical aim similar to that as in the tests of single-stage seal [18]. In such arrangement the closing of magnetic field is realized by the cylindrical part of the sleeve fitted with a special longitudinal groove, that makes it possible to drain away any leakage and diagnose continuously working state of the seal.

For realisation of the tests was built a test stand, called shortly MFSL-135, composed of a special, purpose-oriented testing head, driving system containing an electric motor and its operation controller, as well as measuring system composed of gauges and transducers for measuring pressure, torque of driving motor and detecting leakage from the tested seal. The test stand is fitted with multi-channel measuring apparatus for measurement, data acquisition, processing and recording.

In the research concept it was assumed to perform short and long - term measurement tests which would make it possible to determine limiting operation features of the MF seals in water, and consequently to predict service life of seals of the type operating in working systems of ocean engineering units. To check influence of both external and structural factors on the seal's operation, it was assumed to perform the tests under different working pressure values of water as well as with switched-on magnetic systems adjusted to generating magnetic field of different intensity within the sealing system.

The design solution of the testing head and measuring system enables also to perform tests of other kinds, e.g. tests of hybrid seals composed of a magnetic-fluid seal and pneumatic shield which prevents the first from direct contact with water. The tests of the MF seal with pneumatic shield performed in the frame of this project were presented in the form of a lecture given during a technical scientific conference [19].

In this paper are presented: the test stand, research concept and assumptions, as well as the criteria necessary for assessing correctness of measurement tests. Also, a programme of the tests, their scope and instrumentation as well as magnetic fluids used for the tests, are described. Moreover, testing procedures, technique of preparation and performance of the tests are highlighted in this part, and the research results are presented in the second part of the article.

RESEARCH CONCEPT

Research hypotheses

Effectiveness of MF seal in the case of direct contact between ferromagnetic fluid and water on the inter-phase surface depends on many external factors as well as physical chemical features of the ferromagnetic fluid used in the seal.

On the basis of the observations and research experiments as well as determination of magnetic fluid features, made during the tests of single-stage MF seals [18], was elaborated the research concept adjusted for conducting the tests of multi-stage MF seals operating in water, and assessing their results.

In the tests in question were used magnetic fluids of physical chemical features determined by their producer, and standardized testing procedures. Elaboration of appropriate procedures and obeying them was a necessary condition for correct assessing influence of external factors on effectiveness of seal operation.

The following basic research hypotheses concerning influence of external factors were advanced:

- **Hypothesis I**
 - Life of MF seal depends on relative speed of its motion in utility water environment.
- **Hypothesis II**
 - In the critical pressure range specific for a given MF seal its life depends on relative value of set-up working pressure in relation to critical pressure.

Relative pressure

Loss of tightness of multi-stage MF seal is a much more complex process than that in the case of single-stage seal. It consists in penetration, resulting from exceedance of critical pressure in successive sealing stages; total penetration pressure of multi-stage seal is a sum of pressure increments causing penetration of successive stages. Worth mentioning that in most cases critical pressure of multi-stage seal is lower than simple multiplicity of critical pressure of single-stage seal of the same geometry and magnetic field parameters [20, 21]. However for purposes of the realized tests was made a simplified assumption that penetration pressure values of successive stages are equal to each other.

As absolute value of working medium pressure greatly affects seal life [18] the original concept of relative pressure was used in the research on magnetic fluids of different critical pressure values. With a view of complexity of the problem the concept in question should be highlighted.

In this research, for each of the tested MF fluid, critical pressure tests were performed with the use of a three-stage seal. The critical pressure of one stage of the seal can be defined as follows:

$$P_{krl} = \frac{1}{3} P_{krlII} \quad (1)$$

On the basis of the assumed critical pressure of one stage of the seal the relative pressure was defined as the ratio of the set-up working pressure of the seal and the critical pressure determined for one sealing stage:

$$P_w = \frac{P_r}{P_{krl}} = 3 \frac{P_r}{P_{krlII}} \quad (2)$$

where:

- P_w – relative pressure,
- P_r – working pressure (set-up for test),
- P_{krl} – critical pressure of one sealing stage,
- P_{krlII} – total critical pressure of a three-stage seal.

RESEARCH ASSUMPTIONS

The following research assumptions were made:

- **Assumption I**
In the tests magnetic fluids of hydrophobic properties, produced by specialized producers (*FerroLabs*) [17], available on the market, will be used.
- **Assumption II**
The tests will be conducted with the use of three-stage seals of 50 mm nominal diameter, already implemented in the previous tests, and 0.1 mm height of the gap filled with magnetic fluid, that should make it possible to compare results of these tests and those performed earlier.
- **Assumption III**
Magnetic field which keeps magnetic fluid in the gap, will be generated by the set of permanent magnets in the form of discs circumferentially and uniformly located between pole shoes of magnetic system. The tests are assumed to be performed for different magnetic fields, that will be realized by changing number of magnets in the magnetic system of the seal.
- **Assumption IV**
The highest motion speed at which, after reaching 1 mln cycles (number of rotations), the tested seal does not yet lose its tightness, will be called the long-term operation speed of a seal in given working conditions.

MEASUREMENTS AND CRITERIA FOR THE DETERMINING OF LIMITING PARAMETERS

Measurements of limiting parameters

The measurements were conducted on the basis of standard measurement tests of three types.

- **The test of total statical critical pressure of the seal.**
The test is realized in statical conditions (motionless shaft). During the test the pressure is continuously increased till occurrence of seal leakage symptoms. The test is aimed at determination of a pressure value which will serve as the basis for the determining of relative pressure values to be applied in the tests.
- **The test of critical speed of the seal**
The measurement of seal critical speed results in continuous increasing rotational speed of the shaft with a constant acceleration, the same for all the tests, till occurrence of seal leakage symptoms. For each relative pressure value used in the research the separate critical speed test is performed. The test is aimed at determination of the highest speed beginning from which the series of measurements of long-term operation of the seal is commenced.
- **The test of long-term operation of the seal**
The test of long-term operation of the seal is composed of the series of measurements conducted for a set-up relative pressure and constant rotational speed of the shaft. Successive measurements are taken at lower and lower rotational speed till reaching the speed at which no leakage of the seal is observed during the period of 1 mln cycles of its operation. On the basis of the obtained results the diagram of seal life versus its motion speed at a given relative pressure, is elaborated.

Criteria and way for the determining of values of limiting parameters

For all the tests lack of leakage was the criterion of correct operation of the seal.

- **The total statical critical pressure of the seal, p_{krIII}**
The total statical critical pressure is such pressure value at which the first leaking drop is observed in the drainage tank or a leakage is recorded by the leakage detector.
- **The statical critical pressure of one seal stage, p_{krI}**
The statical critical pressure of one seal stage was assumed to be equal to one third of the total statical critical pressure of the seal: $p_{krI} = 1/3 p_{krIII}$
- **Critical speed of the seal**
The critical speed of the seal is the lowest value of seal motion speed at which the first drop of leakage is observed in the drainage tank during measurements with continuously increasing speed.
- **Long-term operation speed of the seal**
The long-term operation speed of the seal is equal to the highest rotational speed of the seal, at which no leakage of the seal is observed during the period of 1 mln cycles of its operation.

SCOPE AND PROGRAMME OF THE TESTS

Scope of the work to be performed during the tests in question comprised both short-term and long-term tests. In the tests conventionally called short-term the statical critical pressure and critical speed of the seal was determined, whereas the tests performed in an extended period, conventionally called long-term ones, were aimed at determination of seal life values.

The measure of pressure, used in the tests, was the relative pressure p_r/p_{krI} determined as the ratio of the set-up working pressure and the critical pressure of one seal stage, highlighted and calculated according to the principle given in Ch. 2.2.

In spite of that occurrence of leakage was the main criterion for assessing correct operation of the seal, the following was also measured during the tests: friction moment, seal temperature, shaft rotational speed and pressure. The quantities were used to control run of the tests.

The main tests were performed with the use of magnetic fluids of three kinds applied to the seal of three stages with 0.1 mm magnetic fluid gap height.

In the frame of supplementary research the tests were performed with one kind of magnetic fluid and different numbers of permanent magnets in the seal magnetic system.

Programme of the main tests

The following programme of the tests was prepared:

- Tests of the total statical penetration pressure of the seal.
- Tests of the critical speed of seal operation at the values of the relative pressure p_r/p_{krI} equal to: 0.8; 1.6 and 2.4 multiplicity of the one-seal-stage critical pressure.
- Tests of the seal life at the values of the relative pressure p_r/p_{krI} equal to: 0.8; 1.6 and 2.4 multiplicity of the one-seal-stage critical pressure and different motion speeds beginning from that equal to or near the critical seal speed up to that at which the seal life reaches at least 1 mln cycles.

In the main tests the three selected kinds of magnetic fluid were tested. The performed measurements were later repeated. If the result of the first test differed from the repeated one by more than 10 %, the next, explanatory, test was performed. During running the tests some of them were repeated if necessary.

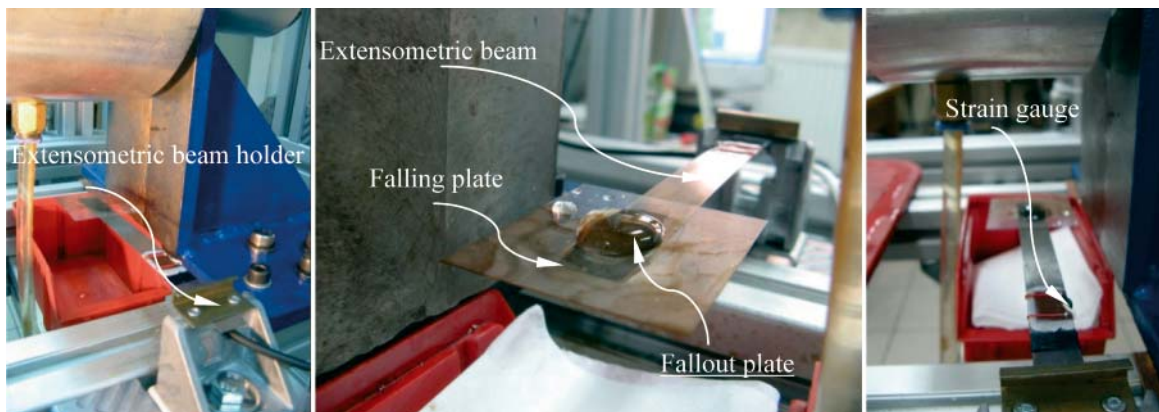


Fig. 1. Extensometric leakage detector at the test stand, in its working state

Programme of the supplementary tests

The supplementary tests were performed with the use of one magnetic fluid (FLA 003.45), selected for these tests on the basis of the results obtained from the main tests. The tests in question were conducted with the number of permanent magnets decreased to 10 pieces and the number of them increased to 18 pieces as compared with the permanent magnets of 14 in number used in the main tests.

In the future is planned realization of the programme of supplementary tests in the same range as that above mentioned for the main tests, as well as determination of minimum intensity of the magnetic field related to N35 standard magnets (of the same volume).

MFSL-135 TEST STAND

The test stand symbolically marked MFSL-135, was designed and built for purposes of this research project. It serves for the testing of magnetic fluid seals operating in contact with water or another non-aggressive liquid, and may be also used for the testing in the environment of air or another non-aggressive gas. Dimensions of the stand's head allow to place in it magnetic fluid seals of up to about 80 mm in diameter. For filling the gaps of sealing stages it is necessary to use only the small amount of magnetic fluid, i.e. of abt. 50-200 μl .

The MFSL 135 test stand makes it possible to determine static seal penetration pressure, limiting seal operation speed and seal life at a given rotational speed in the range up to 100 s^{-1} and pressure up to 0.5 MPa.

Design of MFSL-135 test stand

The multi-functional test stand MFSL-135 intended for the testing of magnetic fluid seals was presented in detail in the previous papers published in this journal, and in the papers [1] and [18]. The full list of its particular units and elements was also given there.

Leakage detector

During the previous tests, necessity of automatic leakage detection was stated in connection with troubles in unambiguous identification of instant of a leakage. Leakage identification during the tests with the use of the MFSL 135 stand was initially based on observation of outflow of water drops from the testing head outflow hole since drop of water pressure or disturbances of torque values during operation of the three-stage seal did not provide an appropriate diagnostic signal. As during the long-

term testing it was not always possible to observe a leakage, an automatic leakage detecting system was designed.

In the photo, Fig. 1, presenting the test stand the leakage detector located in the outflow zone of leaking drops, was shown.

The device is composed of a high-sensitive extensometric beam fastened in a holder, with a glued strain gauge and a falling plate located just under outflow of drops from the casing of MFSL-135G head. The strain gauge was connected to an amplifier and one of the measuring card channels, that ensures recording even single drops flowing out of the testing head casing.

Measuring system of MFSL 135 test stand

In the paper [18] the schematic measurement diagram of the MFSL 135 test stand was shown. The list of particular units and elements of the stand was given in the description of the figure.

Design of particular elements of MFSL 135 test stand

The structural solid model of the test stand was presented in the previous papers published in this journal, e.g. [18].

MFSL-135G testing head

In Fig. 2 is shown the cross-section of the MFSL-135G testing head, where its most important parts are shortly named.

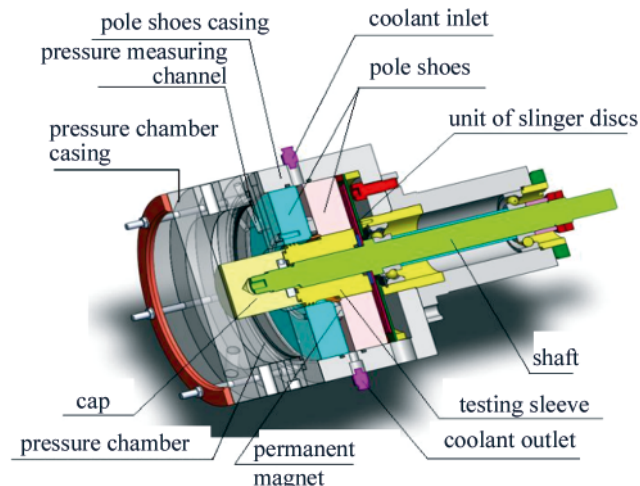


Fig. 2. Model of MFSL-135G testing head, elaborated by using Solid Works software

The shaft made of a non-magnetic steel is rotationally seated in the casing by means of the unit of rolling bearings: radial and angular one. At the end of the shaft is placed a replaceable testing sleeve made of a steel of high magnetic permeability. Axial position of the testing sleeve is fixed by means of the cap fitted with internal threaded hole. The cap, after being screwed on the threaded end of the shaft, presses down the testing sleeve to the unit of slinger discs, and then to the rotary shaft shoulder. The testing sleeve is placed in the hole of the unit of pole shoes made of a material of high magnetic permeability, seated in the casing of a non-magnetic material. Between the pole shoes the unit of permanent magnets is located. The axial position of the pole shoes is fixed by means of the pressure measuring disc and pressure chamber casing which is screwed down to the pole shoes casing by using the unit of bolts and nuts. In the pole shoes casing the inlet and outlet holes are made for the medium which cools the pole shoes during testing.

In Fig.3 the three-stage testing sleeve used in the tests in question, is presented. In the part a) of the figure the cross-section of the sleeve solid model is shown, and in the part b) – the view of the testing sleeve after series of the performed tests.

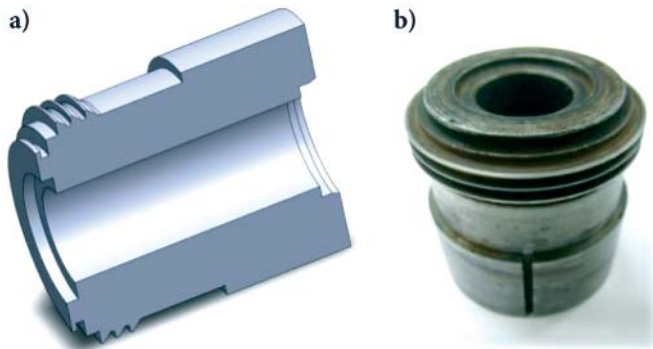


Fig. 3. Three-stage sleeve: a) model; b) real sleeve

In Fig. 4 is presented design structure and operation principle of the tested magnetic-fluid sealing system of three sealing stages. It shows the course of magnetic field lines, location of the sealing stages and cylindrical part with leakage draining groove, as well as location of water zone in the testing chamber. Direction of water flow through the leakage draining groove after loss of tightness by the sleeve, is indicated by the arrow. In the system the rotary slinger disc is placed between the sleeve with stages and the shaft shoulder, and the permanent disc - between the unit of pole shoes and the rear wall of the pole shoes casing.

In the system the rotary slinger disc is placed between the sleeve with stages and the shaft shoulder, and the permanent disc - between the unit of pole shoes and the rear wall of the pole shoes casing.

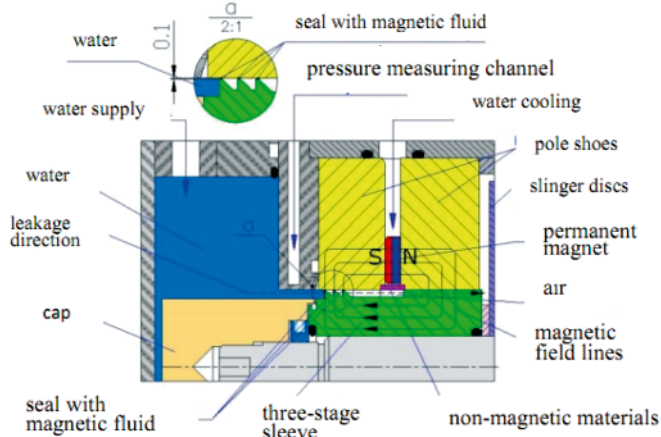


Fig. 4. Design structure of the tested magnetic fluid sealing system with three sealing stages

The rotary disc is aimed at discharging leaking drops onto internal surface of the casing from which they are gravitationally discharged through the leakage outflow hole located in the lower part of the casing, down to the leakage detector plate to trigger recording the leakage instant by LabView software.

In Fig. 5 are shown details of way of bearing the shaft of MFSL-135G testing head as well as of tension control of the angular bearing. From the side of the pole shoes the shaft is seated in the radial bearing whose axial position is fixed by the internal retaining ring. On the shaft, from the side of the drive, is mounted the angular bearing whose tension is controlled by means of the threaded bearing sleeve.

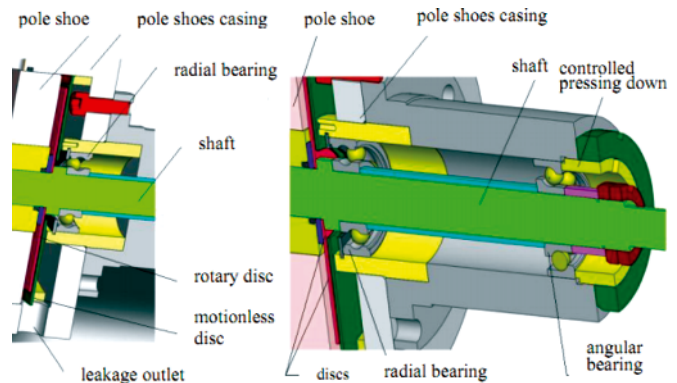


Fig. 5. Slinger discs: motionless and rotary one, mounted in MFSL-135G head

GEOMETRICAL AND STRUCTURAL CHARACTERISTICS OF THE SEAL

In Fig. 6 are shown basic dimensions of the sleeve with sealing stages, arrangement and dimensions of the stages, as well as dimensions of the magnetic system of the seal.

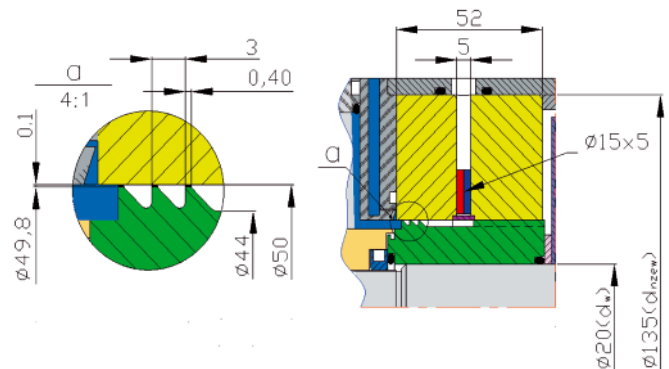


Fig. 6. Basic dimensions of the sleeve with sealing stages and dimensions of the magnetic system of the magnetic fluid seal used in the tests

In Tab. 1 are collected the geometrical and structural parameters of the magnetic fluid seal. The parameters are divided into changeable and constant ones during testing cycle.

MATERIALS AND DEVICES USED DURING THE TESTS

Magnetic fluids

The tests were conducted with the use of three magnetic fluids characterized in Tab. 2. In the table physical features of the tested fluids are compared and their typical technical applications presented.

Tab. 1. Geometrical and structural parameters of the magnetic fluid seal used in MFSL-135G testing head

PARAMETER	Value
Quantities constant during testing	
Shaft diameter, d_w	20 mm
External diameter of pole shoes, $d_{n\ zew}$	135 mm
Breadth of pole shoes unit, d_{nl}	52 mm
Diameter of three-stage sleeve, d_{III}	49,8 mm
Number of stages of testing sleeve, z	3
Nominal gap height, δ	0.1mm
Diameter of permanent magnets, d_m	15 mm
Height of permanent magnets, h	5 mm
Amount of magnetic fluid delivered to each of the stages	100 μ l
Number of permanent magnets fastened in the head casing	10; 14; 18
Working medium	water
Quantities changeable depending on a type of testing	
Rotational speed	1 – 100 rps
Range of set-up values of working pressure	0 – 0.22 MPa
Set-up values of relative pressure, $p_w = p_r/p_{krl}$	$p_r/p_{krl} = 0.8; 1.6; 2.4.$
Cooling intensity	Flow controlled by indications of head temperature transducer
Head starting-up duration time up to instant of reaching the working speed	250 s – for measurements of limiting speed 20 s – for measurements of operation time to leakage

Tab. 2. The most important parameters of the tested ferromagnetic fluids [17]

PARAMETER	Kind of fluid:		
	FLS 040.040	FLA 002.25	FLA 003.45
Kind of suspension vehicle:	Silicone liquid	Siloxane	Siloxane
Saturation magnetization, A/m	40 ÷ 50	25	45
Working temperature, °C	-70 do 150	-70 do 150	-70 do 150
Critical temperature, °C	200	250	200
Freezing temperature, °C	-100	Lack of data	Lack of data
Plastic viscosity in 27°C temperature	0.3-0.8 Pa·s	700-750 mPa·s	400-500 mPa·s
Colour of fluid:	black-brown	black-brown	black-brown
Evaporation index, $g \cdot Sm^{-2}c^{-1}$	Lack of data	$1.0 \cdot 10^{-7}$	$1.0 \cdot 10^{-7}$
Heat conductivity coefficient in 38°C temp., mWt/m·K	Lack of data	150	150
Applications:	Sealing of fermentation tanks, sealing at high motion speeds, for food industry	For speakers of medium and full range as well as sirens	For speakers of low tone and sirens

Permanent magnets

In the tests the permanent magnets in the form of discs of $\varnothing 15 \times 5$ mm dimensions were used. They were purchased from the firm ENES [22]. Their assembling consisted in uniform circumferential location of them in an appropriate number 14; 10; 18 pieces, respectively.

The basic features of the permanent magnets used in the tests are given below:

- magnetic material Neodymium N38
- residual magnetic induction $B_r = 1.23$ T
- coercive force $H_c = 912$ kA/m
- maximum energy density $(BH)_{max} = 294$ kJ/m³
- maximum working temperature 150 °C

Pole shoes and sealing stage sleeves

The pole shoes and sealing stage sleeves were manufactured of a low-carbon steel with the relative magnetic permeability $\mu_r > 2000$.

Magnetic fluid feeder and tool for the assembling/disassembling of sleeves with sealing stages

For dosing the magnetic fluid the laboratory feeder LabMATE LM 100 of HTL firm, was used [23]. The feeder makes it possible to dose the fluid in the amount from 10 to 100 μ l with the filling accuracy error of $\pm 0.8\%$ and repeatability error of $\leq 0.3\%$.

For the filling process the spouts of 200 µl capacity made by UNITIPS® firm were applied.

To apply magnetic fluid to multi-stage seal it was necessary to use a special device as the sleeve with sealing stages was subjected, during its mounting, to action of a very strong magnetic field. The device was aimed at stabilization of the sleeve with sealing stages in a position which could make it possible to deliver magnetic fluid to successive sealing stages.

PROCEDURES FOR CONDUCTING THE TESTS AT THE MFSL 135 TEST STAND

To obtain repeatability of results of measurements aimed at determining critical pressure, critical motion speed and life of magnetic fluid seal it was necessary to elaborate and apply uniform testing procedures. Such procedures applicable to all the tests in question are described below.

Procedure of test stand preparation to conducting the tests

The procedure which makes it possible to conduct the tests consists in mounting the sleeve in an appropriate sequence, ends with application of a magnetic fluid and filling the testing chamber with utility water.

Procedure of determination of critical pressure of the seal

1. After 60 min passing from magnetic fluid application, to activate measurement mode at the control panel and Labview software, open the valve cutting-off compressed air inflow, set-up the flow throttling valve to the pressure increase rate within the range of (0.001÷0.005) MPa/s.
2. To increase the pressure till a leakage from the seal appears and simultaneously observe possible drop of pressure.
3. After ending the test, to deactivate the measurement mode of LabView software.
4. To read, from the Labview records, the maximum pressure value observed during the test (i.e. the pressure at which penetration of the seal occurred).
5. To introduce the measurement data into the testing card.
6. To empty and open the testing chamber.
7. To dismount and clean, by using extraction naphtha, all elements of the seal and testing head.

Procedure of determination of critical motion speed of the seal

1. To activate measurement mode at the control panel and LabView software.
2. To set up frequency converter to the maximum frequency value of 100 s⁻¹ and speed rise time of 250 s.
3. After 45 min passing from magnetic fluid application, to set up water pressure in the chamber in compliance with the relative pressure value $p_r/p_{krt} = 0.8; 1.6; 2.4$, respectively – in line with the testing programme.
4. After 60 min passing from magnetic fluid application, to start up the water cooling circuit of the sealing system (for seal temperature stabilization), and next – start up the drive motor.
5. To monitor increasing rotational speed of the motor and occurring leakage due to lack of tightness of the magnetic fluid seal.

6. After occurrence of lack of tightness to stop the motor and LabView software work.
7. From Labview software records and monitored leakage occurrence instant, to determine the maximum value of rotational motion speed of the seal. The speed at which the leakage occurred is that critical for the seal.
8. To introduce measurement data into the testing card.
9. To empty and open the testing chamber.
10. To dismount and clean, by using extraction naphtha, all elements of the seal and testing head.

Procedure of determination of seal service life

1. To activate measurement mode at the control panel and LabView software.
2. To set up frequency converter to a given rotational speed in line with the testing programme, and speed rise time of 20 s.
3. After 45 min passing from magnetic fluid application, to set up water pressure in the chamber in compliance with the relative pressure value $p_r/p_{krt} = 0.8; 1.6; 2.4$, respectively – in line with the testing programme.
4. After 60 min passing from magnetic fluid application, to start up the water cooling circuit of the sealing system (for seal temperature stabilization), and next – start up the drive motor.
5. To monitor increasing rotational speed of the motor and occurring leakage due to lack of tightness of the magnetic fluid seal.
6. After occurrence of lack of tightness to stop the motor and LabView software work.
7. From Labview software records and monitored leakage occurrence instant, to determine the leakage occurrence time passing from the start-up of the test. The time passing from the start-up of the test to the first leakage instant is the seal service life in the conditions of the test in question.
8. To introduce measurement data into the testing card.
9. To empty and open the testing chamber.
10. To dismount and clean, by using extraction naphtha, all elements of the seal and testing head.

Measurement of pressure in the MFSL-135G testing head

In the MFSL-135G testing head five pressure measuring channels are installed. Channel 1 is intended for the measuring of compressed air pressure. Channels 2 through 5 serve to measure water pressure in the testing chamber. To this end in the measurement disc are made two radial holes of different depth, connected to the testing chamber, that makes it possible to measure pressure values at different distances from shaft rotation axis. The measurements made by using Channel 2 are especially important for the performed tests as the outlet of its measurement hole is located directly in the neighbourhood of sealing stages filled with magnetic fluid. According to the programme realized in the frame of this project the pressure measurements from Channel 1 and 2 were used. Channel 1 serves to control pressure values set up in the phase of preparation of the test stand for carrying out the tests. Channel 2 makes it possible to measure water pressure just at the magnetic fluid seal. In Fig. 7 is shown an example run of the pressure in the testing head during the statical penetration test recorded by the LabView software. The record comes from Channels 2 through 5, in accordance with the pressure measurement points.

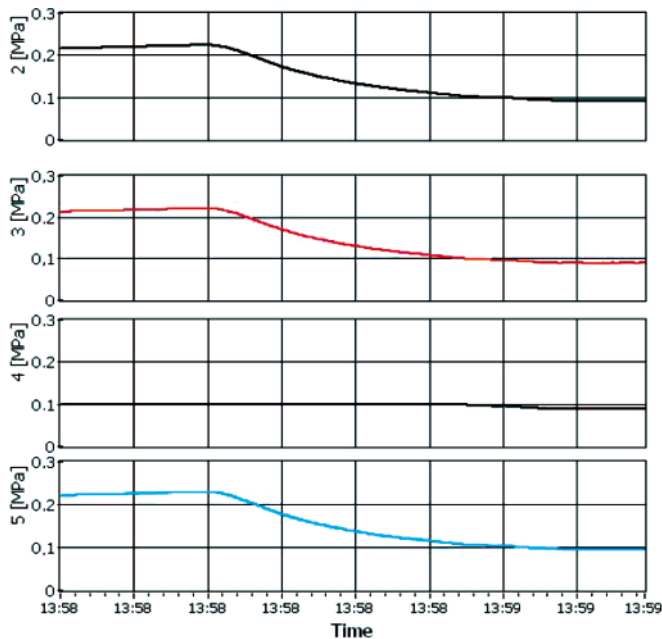


Fig. 7. An example run of the pressure in the testing head during the static critical pressure test. The image taken from the graphical interface of LabView software, for four channels (Channels 2 through 5); the pressure measurement points – as above described

SUMMARY

In compliance with the method of conducting the tests it was assumed to determine, for each of the tested version of the seal, the following:

- statical penetration pressure,
- limiting working speed.

Each of the measurements provides significant information which makes it possible to reach the assigned research aim, i.e.:

- elaboration of a seal life curve and determination of the highest motion speed for which the seal is still capable of reaching, without any failure (lack of leakage), the basic number of cycles (rotations) equal to 1 mln, as assumed in these tests.

A very important factor for the performed tests is the water pressure set-up in the measuring head. The factor was taken into account in the form of the relative pressure defined as the ratio of the set-up pressure and the critical pressure, ($p_w = p_r/p_{krl}$), defined as the seal penetration pressure per one sealing stage, obtained in the statical test.

Due to the assumption of such concept of setting-up testing pressure of water it was possible to simply take into account influence of the factor on seal life for particular tested magnetic fluids, however the assumption also makes comparison of service life of different fluids difficult because of large differences in values of the set-up statical testing pressure for the tested magnetic fluids, which result from very large differences in values of their statical penetration pressure. For instance, the highest long-term operation speed equal to 45 rps was obtained during the tests with the FLA 002.25 magnetic fluid at the set-up pressure of 0.0237 MPa ($p_w = p_r/p_{krl} = 0.8$), resulting from the low penetration pressure of the fluid equal to 0.0297 MPa per one sealing stage. Since the analogous test at the value $p_w = p_r/p_{krl} = 0.8$ for the FLA 003.045 fluid requires to set-up the water pressure value of 0.058 MPa (the penetration pressure per one sealing stage for the fluid is equal to 0.072 MPa) then

the long-term speed for the seal filled with the fluid amounts only to 20 rps. The results indicate a significant influence of pressure on service life of magnetic fluid seal operating in water. Limiting working speed of the seal brings significant research information as it makes it possible to assess the speed value from which elaboration of seal life curve should be commenced, and consequently, determination of seal life for the basic number of cycles equal to 1 mln. However from the utility point of view the parameter is rather not important.

The tests conducted with different numbers of magnets in the sealing system has to show influence of size of magnetic field on limiting speed of magnetic fluids.

The preliminary results of seal life tests for majority of the tested magnetic fluids and seals provide similar picture on the diagrams. At higher rotational speeds short working time to leakage (low number of cycles) is observed. At lower motion speeds the time to leakage appears much longer and clearly tends to a speed value at which seal operation can be considered long-term. The full results of series of the tests will be described in the other part of the article.

BIBLIOGRAPHY

1. Szydło Z., Zachara B., Ochoński W.: *Ferromagnetic fluids and their application in machinery engineering* (in Polish).1st Conference on Automation of Machines, Devices and Processes. Krynica (Poland), 1999
2. Rosensweig R. E.: *Ferrohydrodynamics*. Dover Publications, Inc. Mineola, New York, 1997.
3. Rinaldi C., Chaves A., Elborai S., He X., Zahn M.: *Magnetic fluid rheology and flows*. Current Opinion in Colloid & Interface Science Vol.10, Issue 3-4, October, 2005.
4. Orlov D. B., et al.: *Eksperymentalnoe issledovanie resursa magnitnozdokostnych uplotnenij pri germetizacii zidkich sred* (in Russian). Magnitnaya Gidrodinamika, No. 4, pp.127-130, 1989.
5. Kurfess J., Muller H. K.: *Sealing liquids with magnetic fluids*. Journal of Magnetism and Magnetic Materials, 85, 1990
6. Viherala J., et al.: *Sealing of Liquids with Magnetic Fluid Seals*. Proc. of 6th Nordic Symposium on Tribology, NORDTRIB'94, Uppsala, Sweden, 12-15 June 1994.
7. Kim Y.S., Nakatsuka K., Fujita T., Atarashi T.: *Application of hydrophilic magnetic fluid to oil seal*. Journal of Magnetism and Magnetic Materials 201, 1999, pp.361-363.
8. Liu T., Cheng Y., Yang Z.: *Design optimization of seal structure for sealing liquid by magnetic fluids*. Journal of Magnetism and Magnetic Materials, Vol. 289, March 2005.
9. Guo C., Feng S.: *Sealing mechanism of magnetic fluids*. Journal of Shanghai University (English Edition), 2006, 10(6), pp.522-525.
10. Chorney Alvan F.; Mraz Will.: *Hermetic Sealing with Magnetic Fluids*. Machine Design, May 7, 1992, 64, 9, ProQuest Science Journals p. 79.
11. Mitamura Y., Arioka S., Sakota K., Azegami M.: *Application of a magnetic fluid seal to rotary blood pumps*. J. Phys.: Condens. Matter 20, 2008.
12. Szydło Z., Matuszewski L.: *Experimental research on effectiveness of the magnetic fluid seals for rotary shafts working in water*. Polish Maritime Research No. 4, 2007 vol. 14 pp. 53–58.
13. Szydło Z., Matuszewski L.: *Ring thruster – a preliminary optimisation study of ferrofluid seal and propeller*. Polish Maritime Research, S1 (Special Issue), 2007 pp. 71–74.
14. Szydło Z., Matuszewski L.: *The application of magnetic fluids in sealing nodes designed for operation in difficult conditions and in machines used in sea environment*. Polish Maritime Research, No. 3, 2008, vol. 15, pp. 49–58.
15. *A measuring head for the testing of parameters of ferromagnetic fluid seals* (in Polish). Stanislaw Staszic Academy of Mining and Metallurgy, Cracow. Inventors: Szydło Zbigniew, Ochoński Włodzimierz, Zachara Bolesław. Patent application

- PL 377598 A1, dated: 2005-10-12; published: 2007-04-16, Bulletin of (Polish) Patent Office, 2007, No. 8, p. 22.
16. Bonvouloir J.: *Experimental Study of High Speed Sealing Capability of Single stage Ferrofluidic Seal*. ASME Transactions, Journal of Tribology, Vol.119, July, 1997.
17. Ferrolabs, Inc. Sterling, VA United States, <http://www.ferrolabs.com/> 2010
18. Szydło Z., Matuszewski L.: *Life tests of a rotary single-stage magnetic-fluid seal for shipbuilding applications*. Polish Maritime Research No. 2, 2011, vol. 18, pp. 51–59.
19. Szydło Z.: *High speed magnetic fluid seal operating in water environment*. 17th International Colloquium on Tribology, 19–21 January 2010, book of synopses 2010, ed. Wilfried J. Bartz., Ostfildern, Technische Akademie Esslingen, 2010.
20. Report on realization of the KBN research project No. 7T07B 02412: *Determination of tribological characteristics and limiting working conditions of ferromagnetic fluid seals* (in Polish). Academy of Mining and Metallurgy, Cracow, 2000.
21. Jibin Zou, Jiming Zou, and Jianhui Hu.: *Design and pressure control of high pressure differential magnetic fluid seals*. IEEE Transactions on magnetics, No. 5, Vol. 39, September 2003
22. http://www.magnesy.eu/mw_15_x_5_n38_-_magnes_neodymowy-t-1798.html - product datasheet
23. http://www.htl.com.pl/produkt_53.php - product datasheet

CONTACT WITH THE AUTHOR

Leszek Matuszewski, Ph.D.
Faculty of Ocean Engineering
and Ship Technology
Gdansk University of Technology
Narutowicza 11/12
80-233 Gdansk, POLAND
e-mail: leszekma@pg.gda.pl

The effect of liquid temperature and viscosity on the amplitude-frequency characteristics of a viscotic torsion damper

Wojciech Homik, Ph. D.
Rzeszów University of Technology, Poland

ABSTRACT



The article discusses causes of the appearance of transverse, longitudinal and torsional crankshaft vibrations in multi-cylinder internal combustion engines. Particular attention is paid to the torsional vibration which is the most severe threat to engine crankshafts. Damping methods making use of torsion dampers are presented. With the reference to viscotic dampers, problems with their damping efficiency are discussed in the context of viscosity changes of the damping liquid. The article also presents the amplitude-frequency characteristics of a series of viscotic dampers, which were recorded experimentally on the research rig and on a real object. An idea of vibration damper metric is given.

Key words: torsional vibration; torsional vibration damping; torsional vibration dampers; crankshaft; amplitude-frequency characteristics; liquid viscosity; damper metric

INTRODUCTION

The internal combustion engine. Could the designers of the first internal combustion engines predict that their construction would become the source of progress and development of transport facilities?

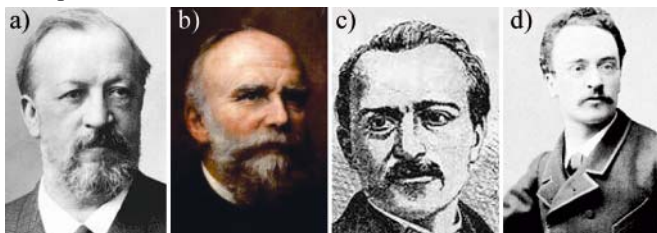


Fig. 1. Designers of piston internal combustion engines [12]: a) Nicolaus-August Otto, b) Eugenem Langenem, c) Étienne Lenoir, d) Rudolf Diesel

Surely, none of them expected that the basic idea of their construction (Fig. 2, 3, 4) [12] which changes the reciprocating linear motion into the rotary motion would remain in a practically unchanged form until now.

The forces acting on the engine crankshaft system include:

- gas pressure forces P_g ,
- inertial forces P_b .

The gas pressure forces P_g and the inertial forces P_b are periodically changing forces. In four-stroke engines the period of the inertial forces is equal to one full revolution of the engine crankshaft, while that of the pressure forces – to two

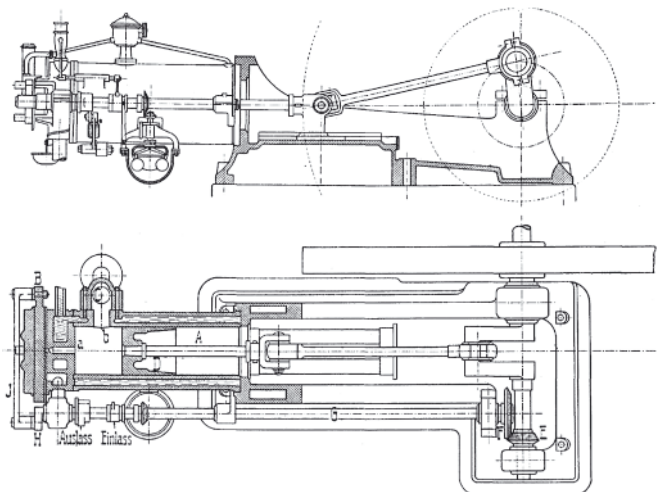


Fig. 2. Design of Otto engine of 1876

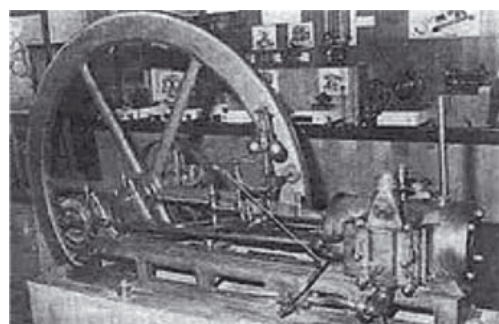


Fig. 3. Construction of Étienne Lenoir engine

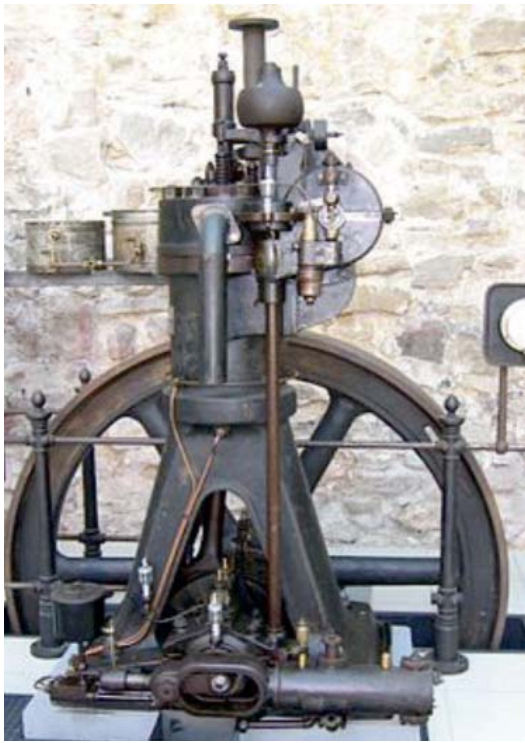


Fig. 4. Construction of Rudolf Diesel engine

revolutions. In two-stroke engines the latter period is also equal to one full crankshaft revolution.

The resultant force of the above forces is their sum [1, 13, 14, 15, 16]

$$P = P_g + P_b \quad (1)$$

The analysis of changes of the resultant force P as a function of the crank angle $\varphi(t)$ reveals that at the final compression phase and the initial expansion phase the inertial forces unload the crankshaft-piston system, while in the remaining time they are the sources of extremely high load, especially during the suction and exhaust strokes.

Since in general, the axis of the connecting rod is not in line with the cylinder axis during engine operation, the resultant force P acting on the piston is not transmitted solely by the connecting rod. It is shifted towards the piston pin axis, in which it is decomposed into two components:

- N component acting on the cylinder surface,
- S component acting along the connecting rod axis.

The magnitude of the force N depends on the coefficient λ , being the ratio of the crank arm length r and the length L of the connecting rod (the larger λ , the larger the force N).

The force S acting along the connecting rod axis acts on the crank, where it is again decomposed into two component forces: the T component which is tangential to the circle described by the crank, and the radial component K acting along the temporary crank arm position.

The above forces are given by the relations:

$$T = S \sin(\varphi + \beta) = \frac{P}{\cos \beta} \sin(\varphi + \beta) \quad (2)$$

$$K = S \cos(\varphi + \beta) = \frac{P}{\cos \beta} \cos(\varphi + \beta) \quad (3)$$

where:

- φ – crank angle,
- β – angle of crankshaft deflection from cylinder axis.

The periodic nature of changes of the gas pressure forces P_g and the inertial forces P_p is the source of the following types of crankshaft vibrations [1, 14, 15]:

- transverse vibration,
- longitudinal vibration,
- torsional vibration.

These vibrations are sort of protection measure, taken by the engine components made of elastic materials, which consists in yielding to the applied load by gradual absorption of the transmitted energy in the form of vibrations. Many engine components, including the abovementioned crankshafts, would be damaged very fast if they did not have the ability to absorb the energy in the form of elastic deformations (Fig. 5).

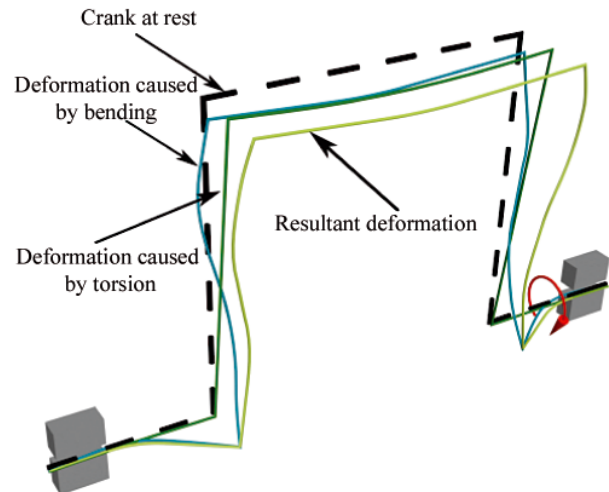


Fig. 5. Sample elastic crank deformations caused by T force

VIBRATIONS

Transverse vibration

The transverse vibration of the crankshaft, also sometimes referred to as the bending vibration, is caused by the action of periodically changing radial forces K on the crank pins. This vibration results in bending the shaft between the bearings (Fig. 6).

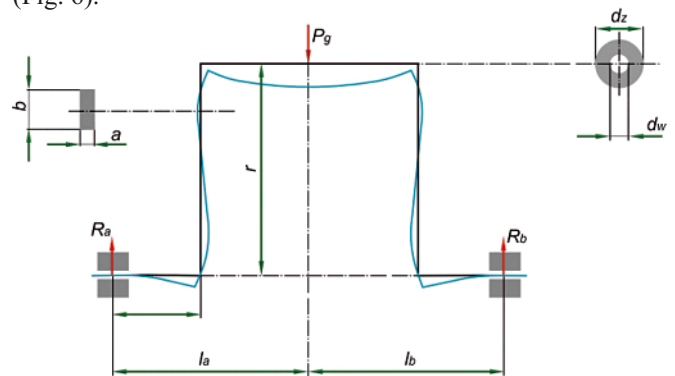


Fig. 6. Shaft deflection between bearings

Longitudinal vibration

The longitudinal vibration of the crankshaft is directly related to its transverse vibration. Any shaft deflection causes its axial shift (Fig. 7).

In most cases this vibration does not disturb the engine operation (especially in motor-car multi-cylinder internal-combustion engines) and is not a severe threat to the durability of the crankshaft, which reveals relatively high rigidity.

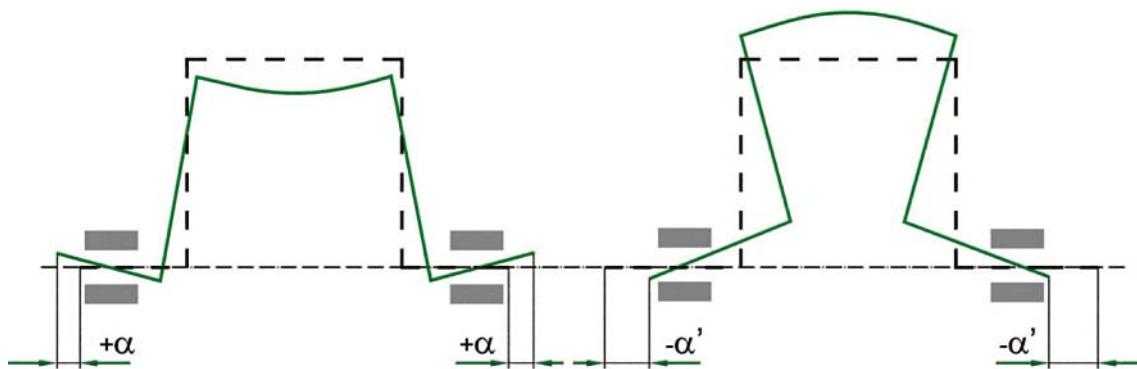


Fig. 7. Longitudinal crankshaft vibration

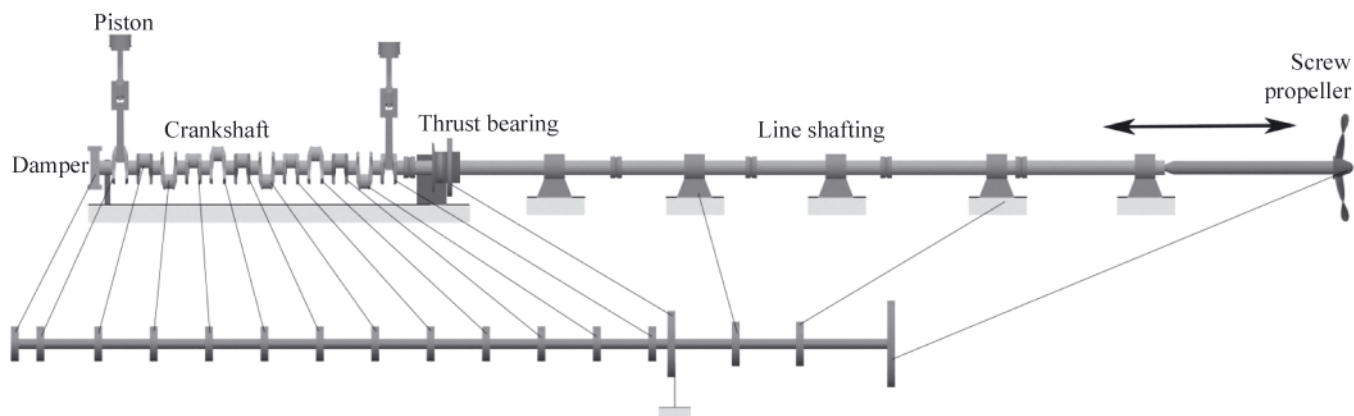


Fig. 8. Real and virtual propulsion system of a watercraft

It should be stressed, however, that this vibration can be a severe problem in marine large-power engines. They make the entire structure (Fig. 8), consisting of the engine crankshaft, the flywheel, the line shafting and the screw propeller, move periodically along its axis. The amplitude of the longitudinal vibration of this structure depends in practice on individual design solutions of the screw propeller, in particular on the number of paddles [14].

Torsional vibration

Among all forces acting on the piston-crankshaft system, the force which makes the crankshaft rotate is the T force tangential to the circle described by the crank.

This force affects the engine torque which is equal to

$$M(\varphi) = T(\varphi) \cdot r = \frac{P}{\cos\beta} r \sin(\varphi + \beta) \quad (4)$$

where:

- $M(\varphi)$ – shaft torque,
- $T(\varphi)$ – tangential force,
- r – crank arm length.

The T force, which is one of two components of the S force acting along the connecting rod axis, is a periodically changing force. Its period is equal to 2π for two-stroke engines and 4π for four-stroke engines. The changing T force is a source of accelerations in the rotational motion of the engine crankshaft, and torsional vibrations, as a further consequence (Fig. 9), which change with the changed rotational speed of the shaft [15].

Among all vibrations, the torsional vibration creates the biggest threat to the crankshaft.

It is noteworthy that the crankshaft deflection is only limited by the torsional stiffness of the shaft, and the amplitude of the

torsional vibration can exceed the permissible values. In case of total lack of damping, the curve according to which the vibration changes tends to infinity for any speed generating a resonance harmonic.

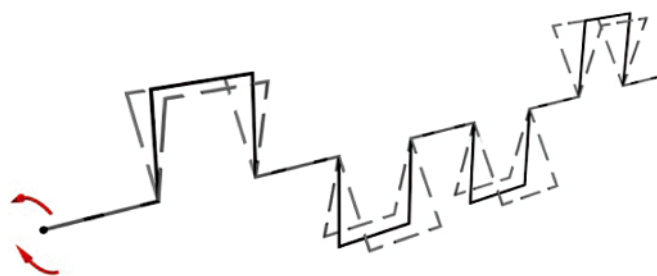


Fig. 9. Torsional crankshaft vibration

Torsion break of the shaft takes place when the permissible value of the amplitude φ_{dop} (permissible torsion angle) is exceeded

$$\varphi_{tz} > \varphi_{dop} \quad (5)$$

The permissible value of the torsion angle φ_{dop} depends on the conditions of engine operation and is determined by general tolerance of geometrical parameters. A term which is frequently used for its easy comparison is the elementary torsion angle [2, 3]:

$$\varphi' = \frac{\varphi}{l} = \frac{M_s}{GI_0} \left[\frac{\text{rad}}{\text{m}} \right] \quad (6)$$

where:

- M_s – torque,
- G – torsional modulus,
- I_0 – polar moment of inertia

For steel propeller shafts and fluctuating loads:

$$\varphi'_{\text{dop}} = 0.004 \left[\frac{\text{rad}}{\text{m}} \right] \quad (6a)$$

while for alternating loads:

$$\varphi'_{\text{dop}} = 0.0025 \left[\frac{\text{rad}}{\text{m}} \right] \quad (6b)$$

The permissible values of the torsion angle are most frequently within the limits:

$$\varphi'_{\text{dop}} = (0.002 \div 0.01) \left[\frac{\text{rad}}{\text{m}} \right] \quad (6c)$$

For the shaft revealing changing torsional stiffness (profiled crankshaft) the basic condition (6) takes the form:

$$\varphi' = \frac{M_s}{G} \sum_{i=1}^n \frac{1}{I_{0i}} \leq \varphi'_{\text{dop}} \quad (7)$$

TYPES OF TORSION DAMPERS

Detecting the torsional vibration of the engine crankshaft is more difficult than in case of other vibration types. Its presence can be sometimes testified by, for instance, non-uniform engine operation, the timing gear of which is driven by the torsionally vibrating crankshaft via a mechanical transmission (for instance belt, chain, or gear transmission).

The variety of vibration forms and the existence of different harmonics of the tangential force T are the reasons why the crankshaft can work in the zone of resonance at different rotational speeds of the engine.

The engine operation in critical (resonance) conditions is most frequently avoided by the use of vibration dampers (Fig. 10).



Fig. 10. Torsion dampers

Their task is to decrease the amplitude of the resonant torsional vibrations of the engine crankshaft. A properly designed (selected, “tuned”) torsion damper provides opportunities for decreasing the amplitude of torsion vibration resonance by even as much as ten times. But we should keep in mind that each damper consumes part of the effective power of the engine.

In the past, the threat coming from torsional vibrations of watercraft power transmission systems was minimised using the following types of dampers:

- frictional dampers,
- rubber dampers,
- viscotic dampers,
- spring dampers.

The above named dampers are typical dynamic resonant vibration dampers in which the vibration is damped using the inertia force [4, 5]. Despite a common name, the dynamic dampers differ between each other not only by constructional designs but, what is more important, also by operating characteristics [10]. It is also noteworthy that these dampers work effectively only within a certain range of rotational speed.

Among all the above mentioned dampers, it is the viscotic dampers which have found the widest application in watercraft power transmission systems. This most likely results from their simple structure, operating reliability, relatively simple manufacturing technology and low production costs, as compared to other solutions.

Nowadays the viscotic torsion dampers are filled with stabilised silicone oils of AK type produced by Bayer and Wacker (Fig. 11). A basic parameter characterising the oil (like any other real liquid) is its viscosity, defined as the internal resistance which appears during displacement of a liquid layer. In this sense the viscosity is decisive about fluid friction: the higher viscosity, the larger the internal friction of the liquid.

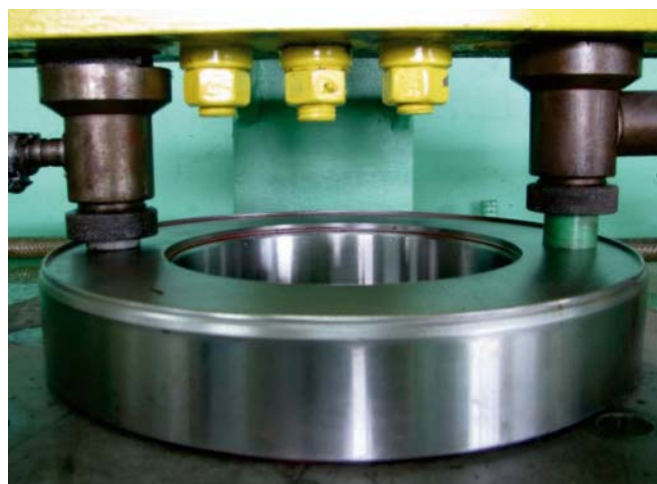


Fig. 11. Process of filling the viscotic torsion damper [8]

The silicone AK oils are watery clear liquids, the viscosity of which changes with shear velocity changes (Fig. 12).

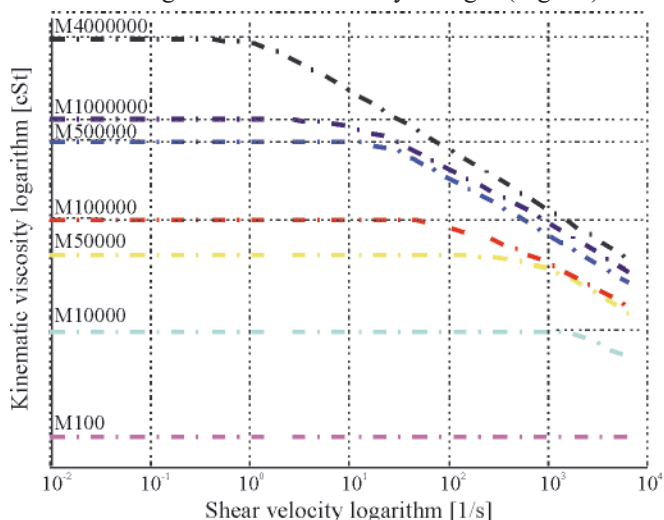


Fig. 12. Kinematic viscosity logarithm vs. shear velocity logarithm [20]

Changes of liquid viscosity are caused not only by the increase of its shear velocity but also by changes of the operating temperature and oil ageing processes [6, 7]. Cases are well-known in which improper use of the damper has resulted

in remarkable increase of the oil viscosity and change of the oil aggregation state (Fig. 13) [9, 10]

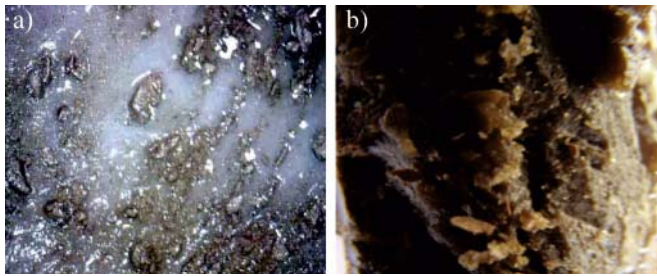


Fig. 13. Samples of oils – magnified 200 times: a) oil with particles of damper parts, b) oil having the consistence of a solid body

Oil viscosity changes cannot be neglected at the stage of selection (designing) of the viscotic damper for a certain power transmission unit [11]. When selecting the damper, calculations are performed to determine an optimal liquid viscosity, i.e. the viscosity for which the value of the energy dissipated by the damper in given operating conditions reaches the maximum.

As a rule, the damper calculations take into account the nonlinearity of the liquid. Among other publications, this issue was discussed in detail in the work entitled “Optimisation of the viscotic torsion damper” [4]. In that work, in order to define the effect of liquid nonlinearity of the efficiency of the viscotic torsion damper, the damping coefficient α which, as mentioned above, depends on the liquid viscosity, was described using the following functions:

$$\alpha = \alpha_N (1 - c |\dot{\phi}_o - \dot{\phi}_p|), \quad \alpha_N \in <0, \infty) \quad (8)$$

$$\alpha = \alpha_N \exp(1 - c |\dot{\phi}_o - \dot{\phi}_p|), \quad c \geq 0 \quad (9)$$

$$\alpha = \alpha_N \dot{\gamma}^{(n-1)} \quad (10)$$

where:

α_N – damping coefficient of a damper with Newtonian liquid,

$\dot{\phi}_o - \dot{\phi}_p$ – relative speed of the casing with respect to the ring,

c – coefficient taking into account the effect of the shear velocity on viscosity.

Sample results of calculations are shown in Figs. 14 - 18.

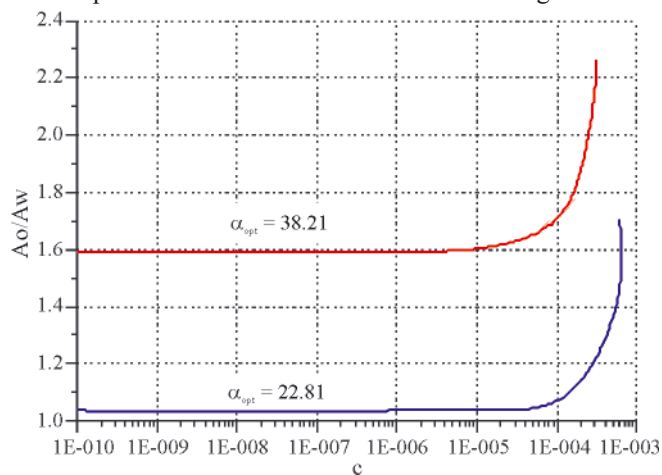


Fig. 14. Casing vibration amplitude vs. logarithm c

At present, for technological reasons the viscotic torsion dampers make use of oils the viscosity of which does not exceed 300000 [cSt] at temperature of 20°C. In those cases, when modelling the viscotic torsion dampers we can assume that the analysed liquid is the linear liquid.

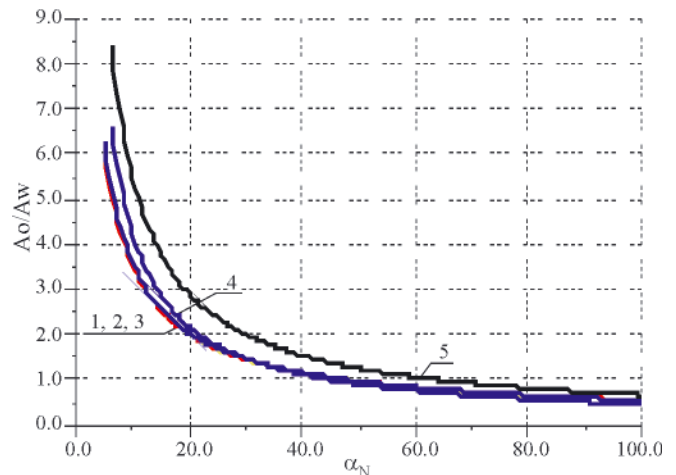


Fig. 15. Casing vibration amplitude as a function of α_N . 1: $c = 0$; 2: $c = 10^{-6}$; 3: $c = 10^{-5}$; 4: $c = 10^{-4}$; 5: $c = 10^{-3}$

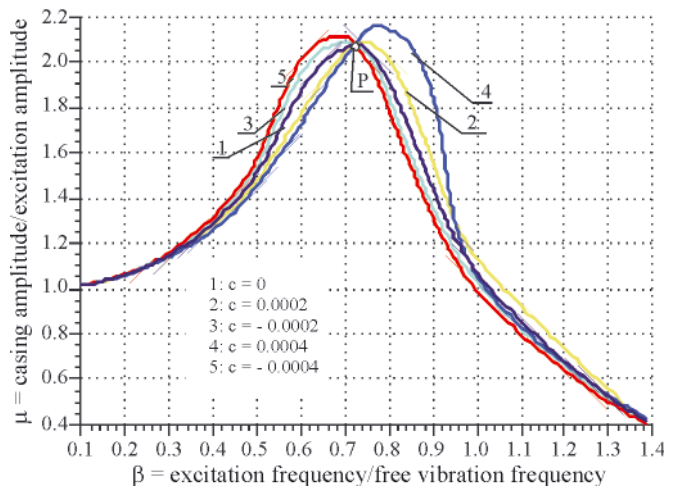


Fig. 16. Amplitude-frequency characteristics for different c values

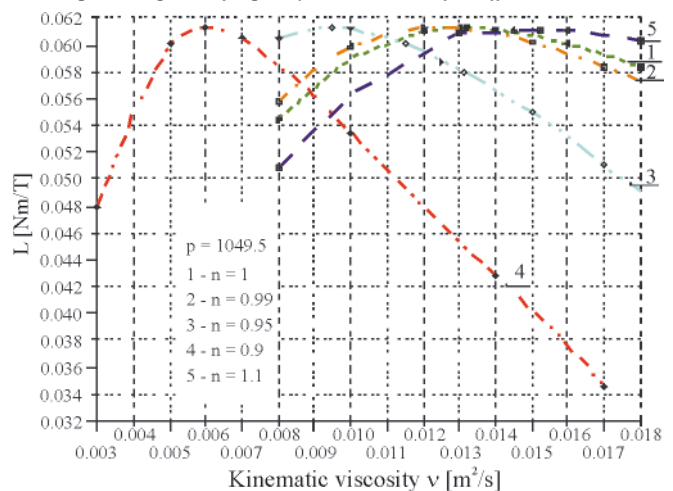


Fig. 17. Work L vs. kinematic viscosity

Before the damper is finally allowed to be used in a given power transmission unit, each respected producer of dampers looks for confirmation of his theoretical analyses in experimental tests, also those performed on a real object, if possible. The results of these tests provide opportunities for final verification of the already performed theoretical analyses of vibration dampers.

The tests are oriented on determining the amplitude-frequency characteristics of the examined dampers. These characteristics, complemented by such damper parameters as:

- I_p – mass moment of inertia of the ring in the damper,
- I_{ow} – mass moment of inertia of the casing,

- η - viscosity of the silicone oil, compose the “metric” of the damper, which should be made available by each producer of vibration dampers.

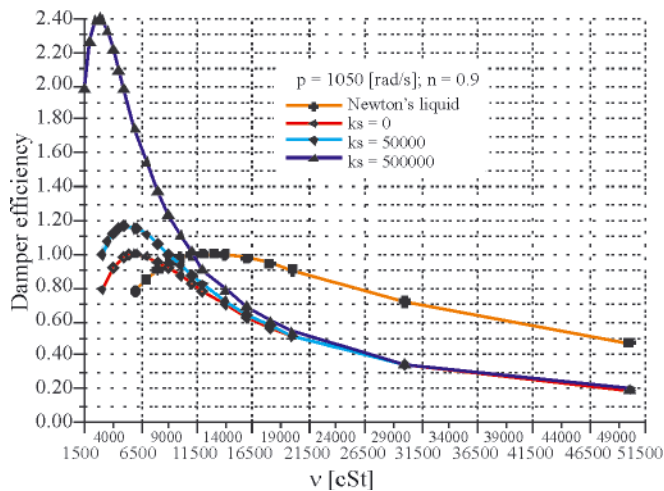


Fig. 18. Damper efficiency as a function of kinematic viscosity v for liquid with $n = 0.9$

Damper tests which make it possible to work out their amplitude-frequency characteristics are most frequently done in temperatures close to those in which the damper is expected to work most often (different operating conditions are expected for a damper used in watercraft power transmission systems or electric current generation units, and different for that working in power transmission systems in vehicles).

In order to illustrate the differences in amplitude-frequency characteristics between different dampers, a series of viscotic dampers:

- TW 30 – viscotic damper with damping liquid of viscosity of 30000 [cSt],
- TW 60 – viscotic damper with damping liquid of viscosity of 60000 [cSt],
- TW 100 – viscotic damper with damping liquid of viscosity of 100000 [cSt],
- TW 130 – viscotic damper with damping liquid of viscosity of 130000 [cSt],
- TW 160 – viscotic damper with damping liquid of viscosity of 160000 [cSt],
- TW 200 – viscotic damper with damping liquid of viscosity of 200000 [cSt],
- TW seized,

having the same geometric parameters were tested at three different operating temperatures:

- ambient temperature 25°C,
- mean operating temperature 45°C,
- saturation temperature 80°C,

within the range of the exciting frequencies changing between 25 and 300 [Hz]. These frequencies were introduced to the shaft of the research rig using the motor TYP FD. The parameter which was measured in the tests was the torsional vibration of the damper hub which was directly connected to the vibrating shaft.

A brief analysis of the presented results reveals that for each damper at a given temperature there is an optimal viscosity value for which the shaft torsion angle reaches its minimum. It is noteworthy that within the range of lower exciting frequencies, between 25 and 100 [Hz], the viscosity of the damping liquid does not affect remarkably the efficiency of the damper, irrespective of the temperature.

The viscosity of the liquid is decisive for the efficiency of the damper within higher excitation frequency ranges, between 200 and 300 [Hz].

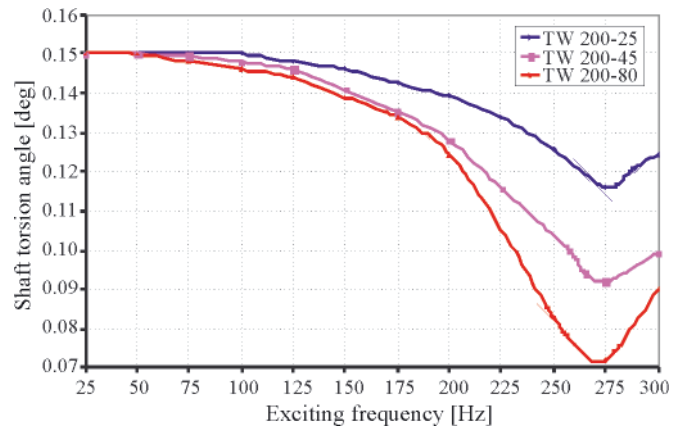


Fig. 19. Comparing amplitude-frequency characteristics of the TW200 damper in temperatures 25°, 45°, 80° [C]

The amplitude-frequency characteristics provide good opportunities for final selection of optimal viscosity of the liquid in a damper which damps torsional crankshaft vibrations in an electric current generator unit which most often works with constant rotational speed (and practically constant excitation frequency). It is much more difficult to select the optimal liquid viscosity for a damper used for damping torsional crankshaft vibrations in a marine engine and, perhaps most of all, a motor-car engine in which the excitation frequency changes with rotational speed changes. In those cases the practically optimal viscosity is calculated for most dangerous excitation frequency (resonance).

The optimal damping is calculated using the formula:

$$\alpha_{\text{opt}} = I_p \omega_o \quad (7.4)$$

where:

- ω_o – real frequency at which hub vibration is the smallest,
- I_p – mass moment of inertia of the inertial ring.

For instance, the optimal viscotic damping α_{opt} for the damper TW130 at temperature of 45°C is:

$$\alpha_{\text{optTW130}}(45) = 0.006750877 \cdot 1650 = 11.195 \text{ [Nms]}$$

CONCLUSIONS

- In order to confirm the theoretical analyses and the result obtained in the experiments done on a model research rig, investigations were performed on a real object, which was a car VW Passat with the engine cubic capacity of 3.6 l and power of 290 [KM]. A parameter which was recorded during the tests performed in the engine test house was the amplitude of the torsional vibration of the free shaft end, within the engine rotational speed ranging between 700 and 6100 [rev/min].
- The harmonic analysis of the signal recorded during the tests has revealed, most of all, that the examined dynamic system cannot safely work without a torsional vibration damper, especially when the rotational speed exceeds 3500 [rev/min], and that the biggest threats for the system are the 3-rd and 6-th harmonics.
- Moreover, the tests performed on the real object have confirmed the conclusions resulting from the theoretical analyses and research rig tests about the existence of optimal values of liquid viscosity [4] for which the maximal resonance amplitudes of the engine crankshaft reach their minimum (Fig. 20, 21).

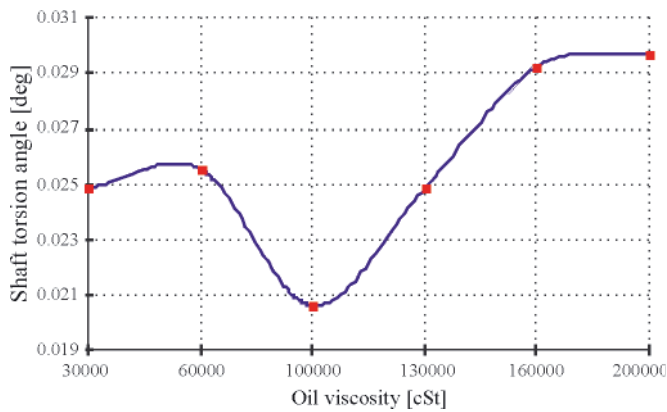


Fig. 20. Shaft torsion angle changes vs. oil viscosity

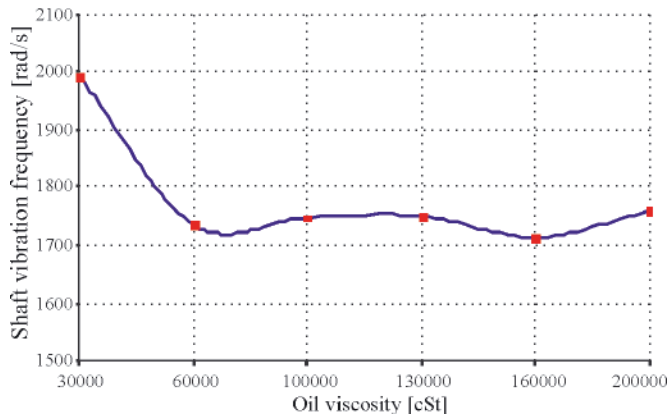


Fig. 21. Shaft vibration frequency changes vs. oil viscosity

- The analysis of the characteristics shown in Figs. 20 and 21 clearly confirms the opinion that the classical viscotic vibration dampers are the optimal dampers only in a very narrow range of frequency excitations, which is caused by the fact that during the operation of the dynamic system we cannot change physical parameters in a viscotic damper (its physical characteristics are constant in practice and cannot be adapted to changing working conditions – changing excitations). That narrow band of efficient operation of these dampers is undoubtedly their disadvantage, but their simple structure and relatively low production costs are the reasons why they are commonly used for damping torsional crankshaft vibrations in power transmission systems.

Notice

The article was financed by the National Science Centre within the framework of the Research Project no. N N509 547440

BIBLIOGRAPHY

1. Brun R.: *High-speed Diesel engines*, (in Polish) WKiL 1973
2. Dąbrowski Z. Maksymiuk M.: *Shafts and axles*, (in Polish) PWN 1984,
3. Dąbrowski Z.: *Machine shafts*, (in Polish) PWN 1999
4. Homik W.: Ph.D. thesis: *Optimisation of the viscotic torsion damper* (in Polish), Rzeszow 1997
5. Homik W.: *Design of viscotic torsion dampers* (in Polish). Przegląd Mechaniczny 10' 07
6. Homik W.: *Torsional vibration of the engine crankshaft without damper and with a viscotic vibration damper* (in Polish), Przegląd Mechaniczny No. 9' 2008 r.
7. Homik W.: *Liquid viscosity changes during the operation of a viscotic vibration damper* (in Polish), Przegląd Mechaniczny No. 3' 2009 r.
8. Homik W., Szlachta A.: *Technology of machining and assembly of viscotic dampers* (in Polish), International Scientific Conference, Pro-Tech-Ma 2009
9. Homik W.: *Criteria of characteristics evaluation – "quality factor" of the viscotic torsion damper for an internal-combustion engine crankshaft* (in Polish), Western Scientific Centre of Ukrainian Transport Academy - Transportna Akademia Ukraini. Praci Zachodnowo Naukowo Centrum No. 19. 2009,
10. Homik W.: *Diagnostics, maintenance and regeneration of torsional vibration dampers for crankshafts of ship diesel engines*, Polish Maritime Research, No 1/2010
11. Homik W.: *Damping of torsional vibration of ship engine crankshafts – general selection methods of viscous vibration damper*. Polish Maritime Research, No 3/2011
12. <http://www.google.pl/search?q=tw%C3%B3rcy+silnik%C3%B3w+spalinowych>
13. Jędrzejowski J.: *Mechanics of motor-car engine crankshaft assemblies* (in Polish)
14. Niewiarowski K.: *Piston internal-combustion engines* (in Polish), WKiL 1973
15. Wajand J. A., Wajand J. T.: *Medium- and high-speed piston internal-combustion engines* (in Polish), PWN 1984
16. Wajand J.A.: *Diesel engines* (in Polish), WKiL 1973

CONTACT WITH THE AUTHOR

Wojciech Homik, Ph. D.
 Rzeszów University of Technology
 The Faculty of Mechanical Engineering and Aeronautics
 Al. Powstańców Warszawy 8,
 35-959 Rzeszów, POLAND
 tel.: +48 17 865 11 00 w. 1637, +48 17 865 16 37
 e-mail: whomik@prz.edu.pl
 e-mail: whomik@interia.pl

Data fusion in a navigational decision support system on a sea-going vessel

Piotr Borkowski, Ph.D.
Maritime University of Szczecin, Poland

ABSTRACT



The problem of data fusion in a navigational decision support system on a sea-going vessel has been analyzed. The computing algorithm herein applied for solving the formulated problem is based on a multi-sensor Kalman filter. On the practical side, results of the tests done in real conditions are shown. The tests conducted onboard m/s Navigator XXI, have been aimed at the verification of the proposed computing algorithm implemented in a prototype navigational decision support system.

Key words: data fusion; navigational decision support system; multi-sensor Kalman filter

INTRODUCTION

In the literature on the problems of information processing the terms data integration and data fusion are very often used as synonyms [9]. This author assumes that the term data integration is understood as a process in which data from various, generally physically separate sources are combined into a consistent and readable whole in a manner allowing to obtain new, more comprehensive information that would be impossible to get from each individual source. Data fusion, on the other hand, is understood as a process of merging data from various sources, however, describing the same quantity. Therefore, this process results in obtaining more reliable and more accurate information.

Data fusion algorithms are naturally applied when input data needed to solve a specific problem are simultaneously obtained from many redundant measurement devices. For further overall processing these data have to be transformed into one signal, which will take account for the information from all sensors. Thus obtained data should be more precise than those derived individually from one source. Besides, this approach increases the level of safety of system which may be affected by a possible lack of input data. Even if one source (device) fails the others guarantee effective operation. This observation is of particular importance in real time systems.

Methods and algorithms of data fusion find applications in many problems across various scientific disciplines, e.g. in medicine [7], land transport [14], processes of knowledge retrieval from data bases [17], problems of mobile agents [18], satellite image integration [11]. In this article data fusion is used for solving problems of dynamic object (vessel) positioning in marine navigation.

Chapter V, paragraph 19 of the SOLAS (Safety Of Life At Sea) Convention [5] deals with mandatory fitting of sea-going ships with navigational systems and equipment. Which equipment items a ship should carry depends on the date the ship's building commenced (laying the keel) and on its gross tonnage. According to the above mentioned document, ships with a tonnage above 500 GT (majority of sea-going vessels) whose construction started after 01 July 2002 should be equipped with, but not limited to:

- Global Navigation Satellite System (GNSS) receiver, determining ship's position (latitude and longitude) automatically,
- AIS system (Universal Shipborne Automatic Identification System), providing, *inter alia*, information on own ship's position (latitude and longitude).

Practice has shown that most sea-going vessels comply with the above requirements as they have redundant equipment. This is an effect of continually reduced costs of GNSS receivers due to growing demand for satellite navigation systems in land transport.

No wonder, modern ships have several different devices with sensors measuring their own position (latitude and longitude). The navigator, having differing data on his ship's position, may face difficulties in making the right decision. On the other hand, relying exclusively on measurements from one device is a risky solution as the information source may fail. Therefore, it seems purposeful to apply the process of navigational data fusion. One of the methods to solve this problem is application of a multi-sensor Kalman filter [1, 15,16].

ALGORITHM OF NAVIGATIONAL DATA FUSION WITHIN THE KALMAN FILTER

To meet the demands of the herein considered algorithm of navigational data fusion, we introduce the following mathematical model of discrete stochastic system with l sensors [2,3,4]:

$$\begin{aligned} \mathbf{x}(t+1) &= \Phi \cdot \mathbf{x}(t) + \mathbf{w}(t) \\ \mathbf{y}_i(t) &= \mathbf{H}_i \cdot \mathbf{x}(t) + \mathbf{v}_i(t) \quad i = 1, 2, \dots, l \end{aligned} \quad (1)$$

where:

$$\mathbf{x}(t) = \begin{bmatrix} x(t) \\ y(t) \\ v_x(t) \\ v_y(t) \end{bmatrix} \in \mathbb{R}^4 \text{ -- state vector at instant } t,$$

$(x(t), y(t))$ -- Cartesian coordinates of vessel position at instant t ,

$(v_x(t), v_y(t))$

-- vector of vessel velocity in the reference system at instant t ,

$y_i(t) \in \mathbb{R}^2$

-- measurement vector of i -th sensor (Cartesian coordinates of vessel position from a GNSS receiver, vessel velocity vector from a Doppler log) at instant t ,

$$\Phi = \begin{bmatrix} 1 & 0 & 1 & 0 \\ 0 & 1 & 0 & 1 \\ 0 & 0 & 1 & 0 \\ 0 & 0 & 0 & 1 \end{bmatrix}$$

-- constant system matrix,

\mathbf{H}_i

-- constant matrix of i -th sensor (GNSS receiver: $\begin{bmatrix} 1 & 0 & 0 & 0 \\ 0 & 1 & 0 & 0 \end{bmatrix}$, Doppler log: $\begin{bmatrix} 0 & 0 & 1 & 0 \\ 0 & 0 & 0 & 1 \end{bmatrix}$),

$\mathbf{w}(t), \mathbf{v}_i(t)$

-- vectors of disturbances with characteristics of white Gaussian noise with zero expected values and covariance matrices \mathbf{Q} and \mathbf{R}_i , respectively, at instant t .

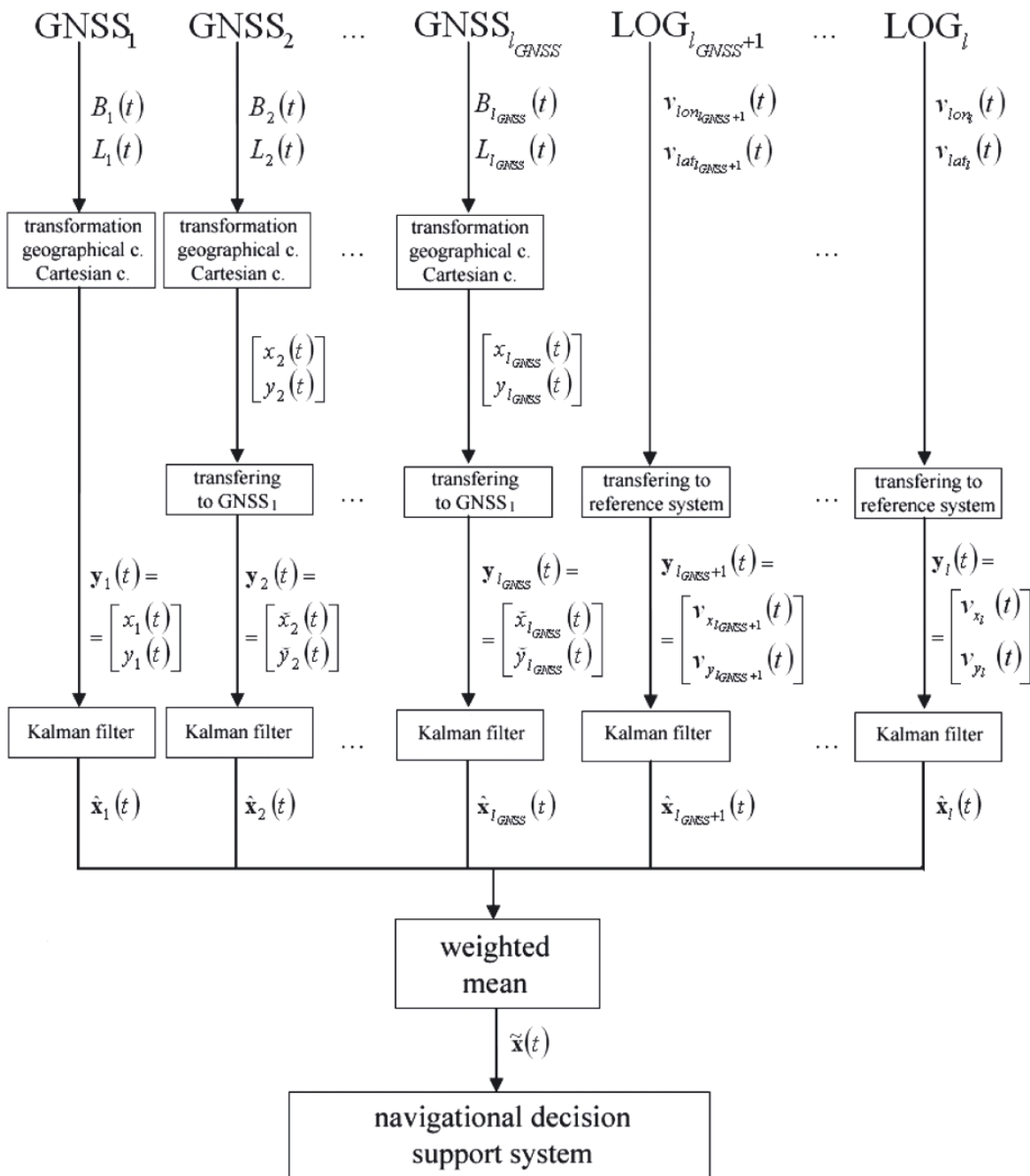


Fig. 1. A general diagram of the proposed navigational data fusion algorithm

A general diagram of navigational data fusion algorithm within the Kalman filter is shown in Fig. 1.

Denotations of the quantities included in Fig. 1:

- l_{GNSS} – number of GNSS receivers ($1 \leq l_{GNSS} \leq l$),
- $B_i(t), L_i(t)$ – latitude and longitude of the vessel obtained by i -th GNSS receiver at instant t ($1 \leq i \leq l_{GNSS}$) [$^\circ$],
- $v_{lon_i}(t), v_{lat_i}(t)$ – longitudinal and transverse velocities of the vessel obtained by i -th Doppler log at instant t ($l_{GNSS} + 1 \leq i \leq l$) [m/s],
- $(\tilde{x}_i(t), \tilde{y}_i(t))$ – results of measurement of the Cartesian coordinates of the vessel, obtained by i -th GNSS receiver at instant t and transferred to the position of the first GNSS receiver ($2 \leq i \leq l_{GNSS}$) [m],
- $v_{x_i}(t), v_{y_i}(t)$ – results of measurement of vessel velocity vector obtained by i -th Doppler log at instant t ($l_{GNSS} + 1 \leq i \leq l$) [m/s],
- $\hat{x}_i(t)$ – estimates of state vector obtained through Kalman filtration for i -th subsystem,
- $\tilde{x}(t)$ – vector of state estimates fusion.

The following navigational systems and equipment are sources of input data for the algorithm, where they undergo the fusion process:

- satellite navigation system receivers and the AIS system which carry out measurements of own vessel's position (latitude and longitude), represented as GNSS receivers in Fig. 1,
- Doppler logs, which provide measurements of longitudinal and transverse velocity components of own vessel.

For the effective operating of the algorithm the vessel must carry at least two of the mentioned devices. Additionally, a gyrocompass allowing to measure own vessel's heading needed in the process of internal data transformations, is required.

The circulation of signals in the proposed algorithm (Fig. 1) will be further described in detail.

Transformation of geographical coordinates into Cartesian coordinates

Results of measurements of own vessel position delivered by GNSS receivers have a form of geographical coordinates (Fig. 2), so that they cannot be directly used in the model (1). To transform them into the Cartesian coordinates the Gauss-Krüger projection was applied [6]. Then the relevant transformation formulas obtain the following form:

$$\begin{aligned}
 x(t) = & N(t) \cdot \cos(B(t)) \cdot \Delta L(t) + \\
 & + \frac{1}{6} \cdot N(t) \cdot \cos^3(B(t)) \cdot (1 - T^2(t) + \eta^2(t)) \cdot (\Delta L(t))^3 + \\
 & + \frac{1}{120} \cdot N(t) \cdot \cos^5(B(t)) \cdot (5 - 18 \cdot T^2(t) + T^4(t) + 14 \cdot \eta^2(t) - 58 \cdot T^2(t) \cdot \eta^2(t)) \cdot (\Delta L(t))^5 + \\
 & + \frac{1}{5040} \cdot N(t) \cdot \cos^7(B(t)) \cdot (61 - 479 \cdot T^2(t) + 179 \cdot T^4(t) - T^6(t)) \cdot (\Delta L(t))^7 \\
 y(t) = & S(t) + \frac{1}{2} \cdot N(t) \cdot \cos^2(B(t)) \cdot (\Delta L(t))^2 + \\
 & + \frac{T(t)}{24} \cdot N(t) \cdot \cos^4(B(t)) \cdot (5 - T^2(t) + 9 \cdot \eta^2(t) + 4 \cdot \eta^4(t)) \cdot (\Delta L(t))^4 + \\
 & + \frac{T(t)}{720} \cdot N(t) \cdot \cos^6(B(t)) \cdot (61 - 58 \cdot T^2(t) + T^4(t) + 270 \cdot \eta^2(t) - 330 \cdot T^2(t) \cdot \eta^2(t)) \cdot (\Delta L(t))^6 + \\
 & + \frac{T(t)}{40320} \cdot N(t) \cdot \cos^8(B(t)) \cdot (1385 - 3111 \cdot T^2(t) + 543 \cdot T^4(t) - T^6(t)) \cdot (\Delta L(t))^8
 \end{aligned} \tag{2}$$

where:

$$N(t) = \frac{a^2}{b \cdot \sqrt{1 + \eta^2(t)}} \quad \begin{array}{l} \text{-- radius of the first vertical curvature (for WGS 84 ellipsoid we can assume: } a = 6378137 \text{ [m],} \\ \text{ } b = 6356752.3141 \text{ [m])}, \end{array}$$

$$\eta^2(t) = \frac{a^2 - b^2}{b^2} \cdot \cos^2(B(t)) \quad \text{-- non-dimensional auxiliary variable,}$$

$$\Delta L(t) = L(t) - L_0 \quad \text{-- difference between measurement results of a given longitude and the longitude of the axial meridian of the examined area (for the Szczecin area we can assume } L_0 = 0.2618 \text{ [rad])},$$

$$T(t) = \text{tg}(B(t)) \quad \text{-- non-dimensional auxiliary variable,}$$

$$S(t) \quad \text{-- length of meridian arc } B(t) \text{ [m].}$$

```

12:38:23 $GPRMC,103817,A,53.58,580,N,01423.174,E,010.2,249.4,030909,002.1,E*72
12:38:24 $GPRMC,103818,A,53.58,579,N,01423.169,E,010.2,249.6,030909,002.1,E*75
12:38:25 $GPRMC,103819,A,53.58,578,N,01423.165,E,010.2,249.6,030909,002.1,E*79
12:38:26 $GPRMC,103820,A,53.58,577,N,01423.160,E,010.2,249.6,030909,002.1,E*79
12:38:27 $GPRMC,103821,A,53.58,576,N,01423.156,E,010.2,249.4,030909,002.1,E*7E
12:38:28 $GPRMC,103822,A,53.58,575,N,01423.151,E,010.2,249.5,030909,002.1,E*78
12:38:29 $GPRMC,103823,A,53.58,574,N,01423.147,E,010.3,249.4,030909,002.1,E*7F
12:38:30 $GPRMC,103824,A,53.58,573,N,01423.142,E,010.3,249.3,030909,002.1,E*7D
12:38:31 $GPRMC,103825,A,53.58,572,N,01423.138,E,010.2,249.4,030909,002.1,E*76
12:38:32 $GPRMC,103826,A,53.58,571,N,01423.133,E,010.2,249.5,030909,002.1,E*7C
12:38:33 $GPRMC,103827,A,53.58,570,N,01423.129,E,010.2,249.7,030909,002.1,E*75

```

Fig. 2. Data from a GNSS receiver

The meridian arc length $B(t)$ is found from the following formula:

$$\begin{aligned} S(t) = & 6367449 \cdot B(t) + \\ & - 16038.50874 \cdot \sin(2 \cdot B(t)) + \\ & + \sin(4 \cdot B(t)) - 0.022198 \cdot \sin(6 \cdot B(t)) + \\ & + 0.00003 \cdot \sin(8 \cdot B(t)) \end{aligned} \quad (3)$$

The proposed transformation reproduces accurately only measurements close to the axial meridian. The difference in the transformed length grows when it is further from the axial meridian, reaching a maximum at the edge of the zone (for a six-degree zone it equals 67 cm per 1 km of length). The area subject to navigational situation analysis to which the data from the fusion process will apply, should not exceed a circle with the radius of 10 nautical miles. If we take this into account and the fact that the selected axial meridian has to cross the analyzed area we can assume that transformation errors are minor and will not affect the quality of the fusion.

Transferring the measurement results from GNSS receivers to one common point

Aerials of GNSS receivers installed on board a ship are generally mounted in different places. As the aerials are some distance apart, the obtained measurement results should be brought, after passing through the block of transformation from geographical coordinates to Cartesian coordinates, to one common place to be subjected to the fusion process. This is due to the fact that in the model (1) the vessel position is understood as a specific material point. Most often it is interpreted as the hull centre of gravity. Unfortunately, it rarely happens that any of the aerials is placed exactly at such point, and the process of bringing the measurement results to a specific point is always burdened with an error (this is due to the need of using, in the process, the gyrocompass heading which is a measured quantity burdened this way with an error). Therefore, it is decided that in the proposed algorithm the place to which all measurement results are transferred is the position of one GNSS receiver aerial, preferably that of the most accurate receiver (if there is such). In this approach measurement results from one GNSS receiver (GNSS₁) will be free from additional deformations caused by the geometrical transformation. This transformation consists in combining the rotation by the angle (course) and the translation by the vector according to the following equations:

$$\begin{aligned} \tilde{x}(t) = & x(t) + w_x \cos(\psi(t)) - w_y \sin(\psi(t)) \\ \tilde{y}(t) = & y(t) + w_y \cos(\psi(t)) + w_x \sin(\psi(t)) \end{aligned} \quad (4)$$

where:

$\mathbf{w} = [w_x, w_y]$ – vector which specifies the position of a GNSS aerial relative to the GNSS₁ receiver aerial (Fig. 3) [m],

ψ – gyrocompass heading [rad].

Shifting the measurement results obtained from GNSS receivers will increase the measurement error by the value:

$$2\sqrt{w_x^2 + w_y^2} \cdot \sin\left(\frac{e_{\text{gyro}}}{2}\right) \quad (5)$$

where:

e_{gyro} – gyrocompass error [rad].

As the gyrocompass error should not exceed 0.009 rad, while the distance between the GNSS aerials should not

exceed 15 m, we can assume that errors caused by bringing the measurement results to one common location are negligibly small and will not affect the fusion quality.

Transferring the velocity measurement results to the reference system

In parallel with position measurement transformations, similar operations concerning velocity (over ground) measurements should be performed by using Doppler logs. Measurements of longitudinal and transverse velocity components of a vessel should be related to the introduced reference system through a rotation by the gyrocompass heading in accordance with the following equations:

$$\begin{aligned} v_x(t) = & v_{\text{lon}} \cos(\psi(t)) - v_{\text{lat}} \sin(\psi(t)) \\ v_y(t) = & v_{\text{lat}} \cos(\psi(t)) + v_{\text{lon}} \sin(\psi(t)) \end{aligned} \quad (6)$$

The transformation will increase the measurement error by the value:

$$2\sqrt{v_{\text{lon}}^2 + v_{\text{lat}}^2} \cdot \sin\left(\frac{e_{\text{gyro}}}{2}\right) \quad (7)$$

Since the gyrocompass error should not exceed 0.009 rad and the vessel speed should not be higher than 15 m/s, we can assume that errors caused by bringing velocity measurements to the reference system are also negligibly small and will not affect the fusion quality.

The Kalman filter

Estimates of the state vector $\hat{\mathbf{x}}_i(t)$ for i -th subsystem (relating to a sensor) are obtained by using a Kalman filter [8] for the model (1):

$$\begin{aligned} \hat{\mathbf{x}}_i(t|t-1) = & \Phi \cdot \hat{\mathbf{x}}_i(t-1|t-1) \\ \mathbf{E}_i(t) = & \mathbf{y}_i(t) - \mathbf{H}_i \cdot \hat{\mathbf{x}}_i(t|t-1) \\ \mathbf{P}_i(t|t-1) = & \Phi \cdot \mathbf{P}_i(t-1|t-1) \cdot \Phi^T + \mathbf{Q} \\ \mathbf{K}_i(t) = & \mathbf{P}_i(t|t-1) \cdot \mathbf{H}_i^T \cdot [\mathbf{H}_i \cdot \mathbf{P}_i(t|t-1) \cdot \mathbf{H}_i^T + \mathbf{R}_i]^{-1} \\ \mathbf{P}_i(t|t) = & \mathbf{P}_i(t|t-1) - \mathbf{K}_i(t) \cdot \mathbf{H}_i \cdot \mathbf{P}_i(t|t-1) \\ \hat{\mathbf{x}}_i(t|t) = & \hat{\mathbf{x}}_i(t|t-1) + \mathbf{K}_i(t) \cdot \mathbf{E}_i(t) \end{aligned} \quad (8)$$

where:

$\mathbf{E}_i(t)$ – vector of innovation at instant t ,

$\mathbf{K}_i(t)$ – filter gain matrix at instant t ,

$\mathbf{P}_i(t|t-1)$ – filtration errors covariance matrix determined without the knowledge of filter gain at instant t ,

$\mathbf{P}_i(t|t)$ – updated filtration errors covariance matrix,

$\hat{\mathbf{x}}_i(t|t-1)$ – estimate of the state vector determined without the knowledge of measurements at instant t ,

$\hat{\mathbf{x}}_i(t|t)$ – updated estimate of the state vector.

Data fusion

The fusion of a set of data obtained from l sensors is expressed as a weighted mean:

$$\tilde{\mathbf{x}}(t) = \mathbf{A}_1(t) \cdot \hat{\mathbf{x}}_1(t) + \mathbf{A}_2(t) \cdot \hat{\mathbf{x}}_2(t) + \mathbf{K} + \mathbf{A}_l(t) \cdot \hat{\mathbf{x}}_l(t) \quad (9)$$

where:

$\mathbf{A}_i(t)$ – weight matrices.

The weight matrices are derived from the formula:

$$\mathbf{A}_i(t) = \left[\sum_{j=1}^l \mathbf{P}_{jj}^{-1}(t) \right]^{-1} \cdot \mathbf{P}_{ii}^{-1}(t) \quad (10)$$

where:

$\mathbf{P}_{ij}(t)$ – matrix of cross covariance of error filtration between i-th and j-th subsystem of model (1).

Matrices of the cross covariance of filtration errors are determined from the following formula:

$$\mathbf{P}_{ij}(t) = [\mathbf{I}_4 - \mathbf{K}_i(t) \cdot \mathbf{H}_i] \cdot [\Phi \cdot \mathbf{P}_{ij}(t-1) \cdot \Phi^T + \mathbf{Q}] \cdot [\mathbf{I}_4 - \mathbf{K}_j(t) \cdot \mathbf{H}_j]^T \quad (11)$$

where:

\mathbf{I}_4 – 4 x 4 unit matrix.

The proposed approach is optimal as it minimizes the trace of error variance matrix of the fusion estimator [15, 16].

It should be emphasized that due to the used model (1), the algorithm of navigational data fusion is a positioning algorithm for rectilinear movement. That is why the fusion process cannot be continued when the vessel starts turning.

DATA FUSION IN THE NAVIGATIONAL DECISION SUPPORT SYSTEM

Rapid advancements in information technologies we have been witnessing in recent years, significantly affect the organization and execution of maritime transport processes. More attention is being paid to the construction of intelligent systems which utilize a wide range of telecommunication, computer, automation and measurement technologies, in order to protect traffic participants, increase effectiveness of the maritime transport system and protect natural environment resources. Intelligent transport systems (ITS) [12] are advanced applications with a capability of safer and better coordinated use of transport networks. One example of such applications is the Vessel Traffic Monitoring and Information System (VTMIS) presently being developed within the EU. The VTMIS consists of several components: the Vessel Traffic Service (VTS), Automatic Identification System (AIS), Ship Reporting System (SRS), Maritime Assistance Services (MAS), Long Range Identification and Tracking System (LRITS), computer-aided system of information exchange (SafeSeaNet).

In December 2005 the International Maritime Organization (IMO) started working on developing and implementing a new navigational strategy - e-navigation [10]. E-navigation is understood as gathering, integration, transmission, management and presentation of navigational information by means of electronic formats for the navigational support of port-to-port operations. The concept of e-navigation goes in line with the concept of maritime intelligent transport systems.

The development of navigational equipment and systems installed on sea-going ships created a demand for data integration and devising methods of navigational data presentation which would facilitate the navigator in decision making. Another stage consists in building specialized information systems assisting decision processes on the ship, such as pilotage and docking systems. Their development proceeds towards decision support systems which in turn have such functions as current situation analysis and generation of proposed solutions to dangerous (i.e. collision) situations.

The research team at the Institute of Marine Navigation, Maritime University of Szczecin, has developed a prototype navigation decision support in open sea areas, thus making a contribution toward the global work on intelligent systems and meeting today's demands of the maritime industry [13]. The computer-based system (hardware and software) can be easily

installed on board a ship and work in real time. The prototype has the following functions:

- recording and decoding navigational data,
- navigational data integration,
- navigational data fusion,
- identification of a navigational situation,
- analysis and assessment of a navigational situation,
- generating anti-collision manoeuvre,
- prediction of a navigational situation,
- presentation of the processed information.

One of the functions is the process of navigational data fusion. In the prototype system this process is based on the implemented algorithm such as that presented in the previous chapter. The use of the computing algorithm ensures a number of advantages:

- increased reliability of the system,
- reduction of measurement errors,
- continuity of the system operation,
- data acquisition at greater frequency.

THE RESULTS OF FIELD TESTS

The algorithm of navigational data fusion implemented in the navigational decision support system was verified in real conditions on board the m/s *Navigator XXI*. The field tests were carried out in the area of the Szczecin-Świnoujście fairway at the southwest Baltic Sea. During the tests the ship had the following navigational equipment and systems essential for the algorithm verification:

- AIS system - Nauticast X-Pack DS,
- GNSS receiver - CSI MiniMax,
- GNSS receiver - Koden KGP-913D,
- GNSS receiver - Trimble NT 200D,
- gyrocompass - Gyro STD22 Anschutz.

For technical reasons the input data for the tested algorithm were signals from two GNSS receivers (MiniMax, Koden) and the gyrocompass. The MiniMax was chosen as the primary GNSS receiver (GNSS₁) due to its higher accuracy.

The disturbance covariance matrix was assumed as:

$$\mathbf{Q} = \begin{bmatrix} 0 & 0 & 0 & 0 \\ 0 & 0 & 0 & 0 \\ 0 & 0 & 0 & 0 \\ 0 & 0 & 0 & 0 \end{bmatrix} \quad (12)$$

while the sensor-related data (accounting for the characteristics of measuring devices) were assumed as:

$$\mathbf{R}_1 = \begin{bmatrix} 0.25 & 0 \\ 0 & 0.25 \end{bmatrix}, \quad \mathbf{w}_1 = \begin{bmatrix} 0 & 0 \end{bmatrix} \\ \mathbf{R}_2 = \begin{bmatrix} 2.25 & 0 \\ 0 & 2.25 \end{bmatrix}, \quad \mathbf{w}_2 = \begin{bmatrix} 0.56 & -1.04 \end{bmatrix} \quad (13)$$

These are the initial matrices of filtration error covariance and matrices of cross covariance of filtration errors (applied after each filter cancellation – subsequent start-up of the algorithm):

$$\mathbf{P} = \begin{bmatrix} 1 & 0 & 0 & 0 \\ 0 & 1 & 0 & 0 \\ 0 & 0 & 0.0625 & 0 \\ 0 & 0 & 0 & 0.0625 \end{bmatrix} \quad (14)$$

First measurements from each device were assumed as the remaining initial values.

Fig. 4 and 5 present example records of ship positions measured when the ship proceeded along a straight track section. It can be seen that the measurements from the two GNSS receivers do not form a straight line, while the fusion of these measurements approximately makes up a straight line. This proves that the tested algorithm incorporating the signals from GNSS₁ and GNSS₂ receivers, performs correctly.

Fig. 6, in turn, illustrates a situation when measurement data from the GNSS₁ receiver (more accurate) form a straight line, but there occurs a period when the signal fades away. The fusion signal, however, is maintained thanks to signals from the other, GNSS₂ receiver. This is important from the viewpoint of the navigational decision support system, as fading may destabilize the system.

Fig. 7 presents a situation when the ship was not moving, lying at anchor. Also in this case for the navigational decision

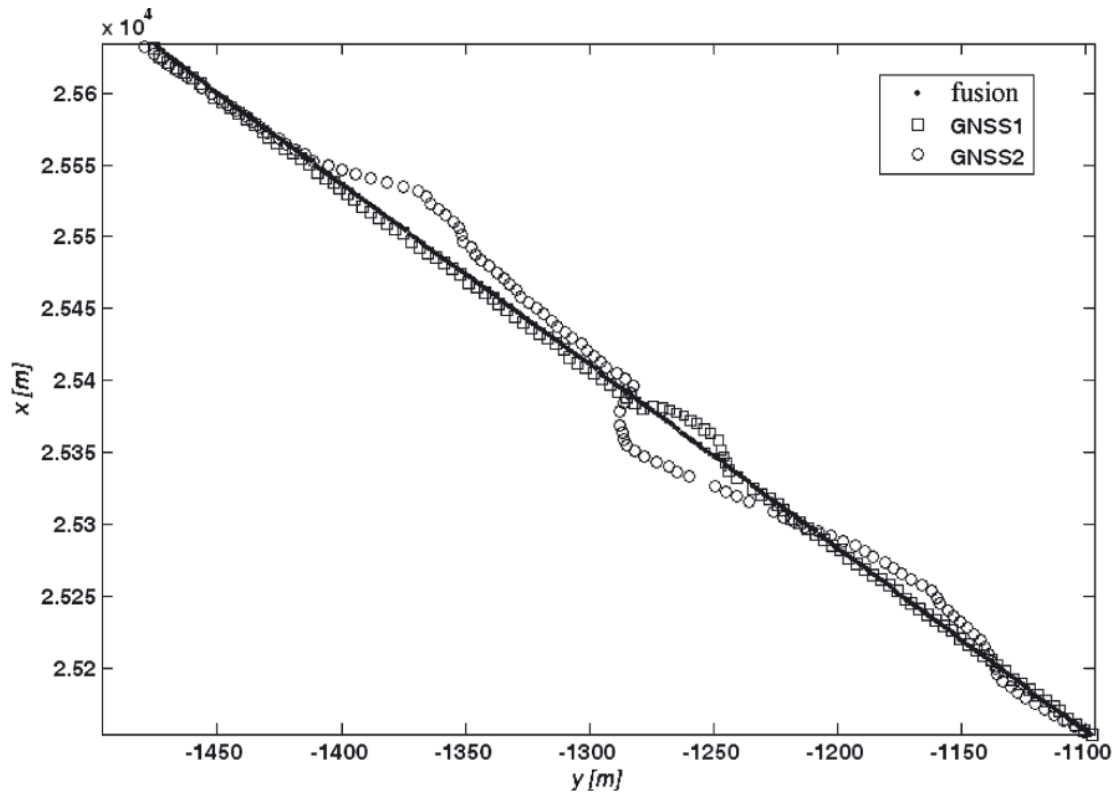


Fig. 4. Ship's positions measured by GNSS₁ and GNSS₂ receivers and the measurement fusion – situation 1

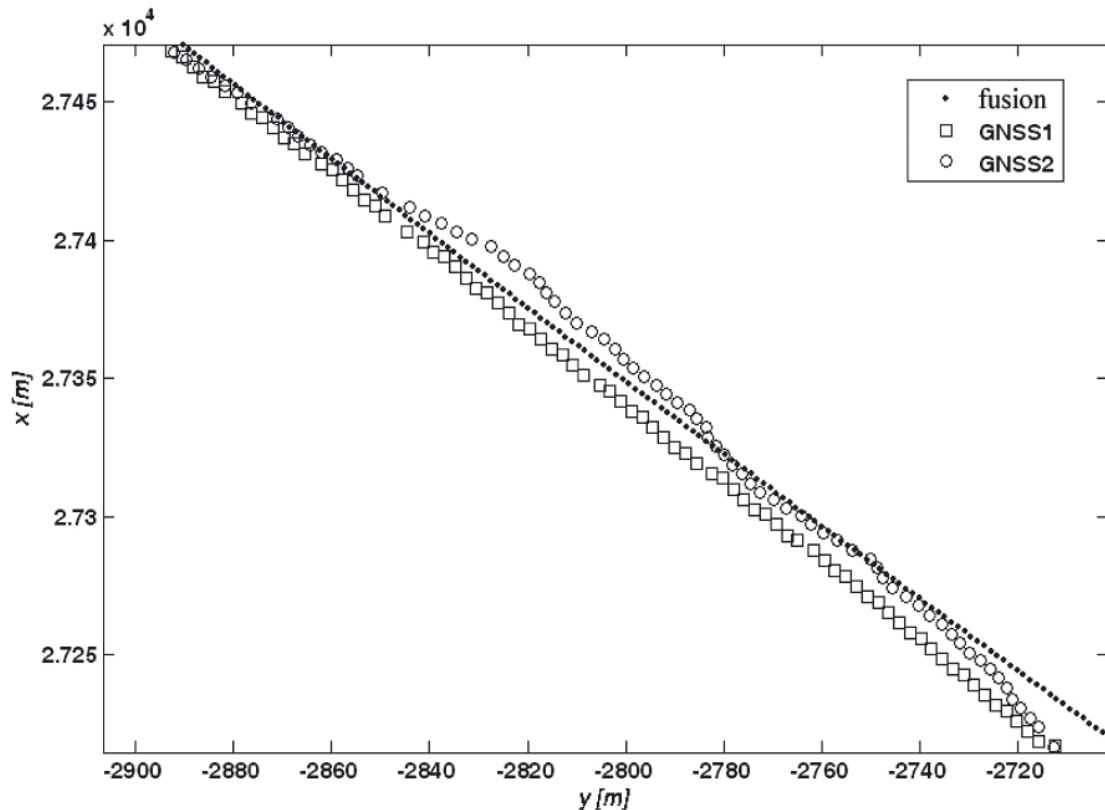


Fig. 5. Ship's positions measured by GNSS₁ and GNSS₂ receivers and the measurement fusion – situation 2

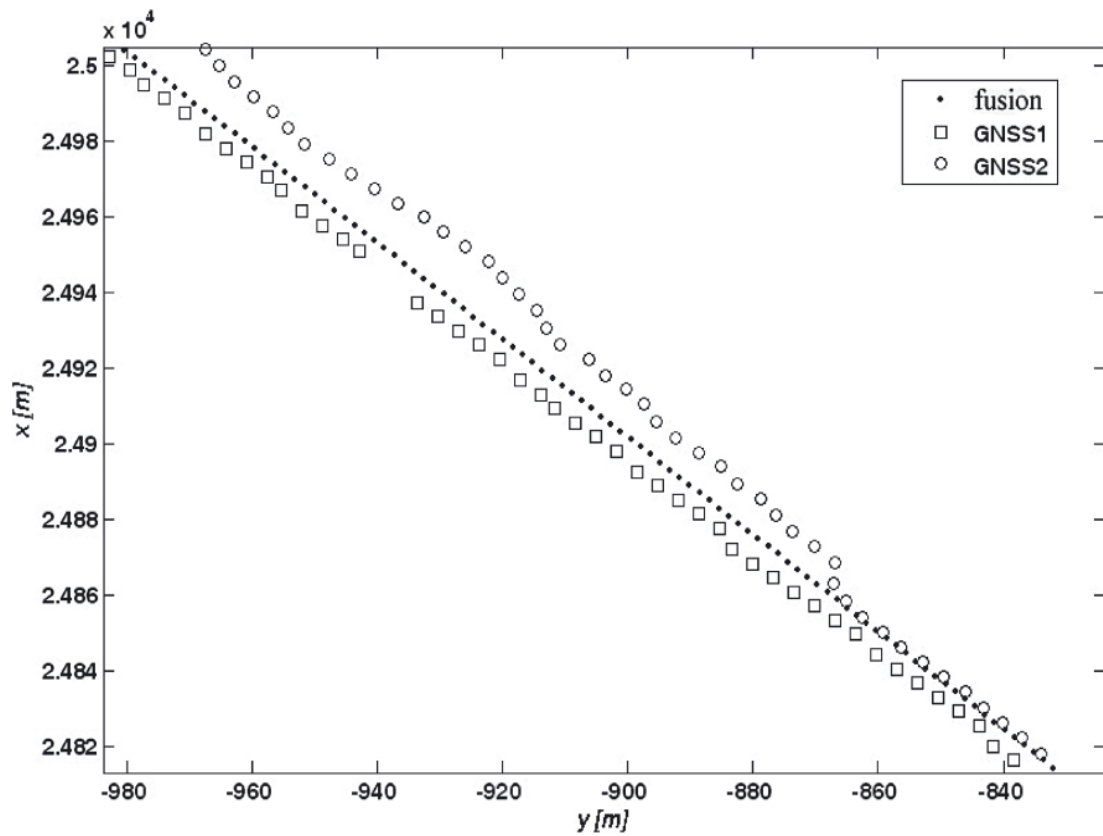


Fig. 6. Ship's positions measured by GNSS₁ and GNSS₂ receivers and the measurement fusion – situation 3

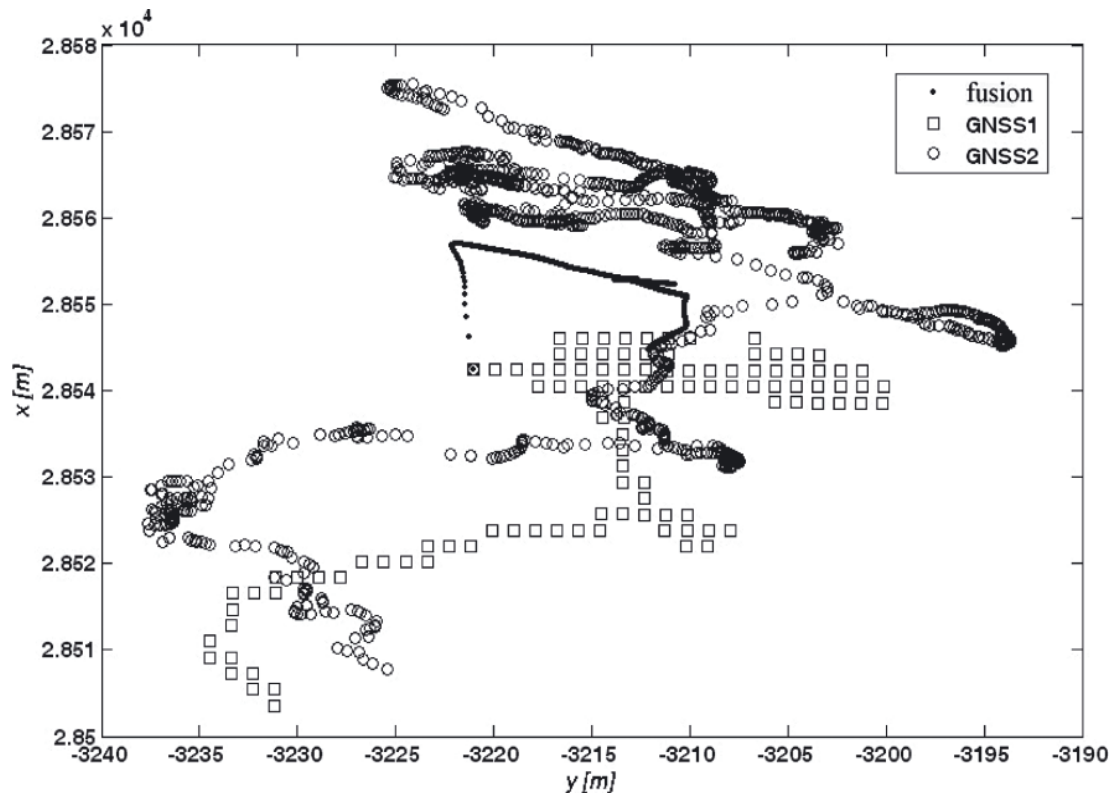


Fig. 7. Ship's positions measured by GNSS₁ and GNSS₂ receivers and the measurement fusion – situation 4

support system the measurement data fusion is the most proper, i.e. most stabilized.

The presented situations are typical for the overall test results. No case was observed when the fusion of measurement data from a rectilinear track section would be 'worse' than autonomous signals received from GNSS receivers.

SUMMARY

In this article the problem of navigational data fusion was analyzed. The discussed computing algorithm is based on a multi-sensor Kalman filter. The algorithm combines navigational data measurements received from single autonomous receivers.

Implemented in the navigational decision support system, it was verified on the m/s *Navigator XXI*. The field tests have indicated that the used algorithm improves the accuracy and reliability of measurements of navigational parameters. This confirms the effectiveness of algorithm operation in real conditions.

It should be emphasized that the presented method can be also used in other systems, e.g. automatic control systems.

BIBLIOGRAPHY

1. Bar-Shalom Y., Willett P., Tian X.: *Tracking and data fusion*. YBS Publishing, Storrs 2011
2. Borkowski P.: *Algorithm of multi-sensor navigational data fusion – testing of estimation quality*. Polish Journal of Environmental Studies, Vol. 17, No. 3B, 2008 (43-47)
3. Borkowski P., Pietrzykowski Z., Magaj J. Mąka M.: *Fusion of data from GPS receivers based on a multi-sensor Kalman filter*. Transport Problems, Vol. 3, No. 4, 2008 (5-11)
4. Borkowski P., Stateczny A.: *An algorithm of navigational data integration*. Maintenance Problems No. 68, 2008 (181-188)
5. IMO: *Carriage requirements for shipborne navigational systems and equipment*, SOLAS, London 2005
6. Hofmann-Wellenhof B., Lichtenegger H., Collins J.: *Global Positioning System*. Springer, Wien 2001
7. Jannin P., Grova C., Gibaud B.: *Medical applications of NDT data fusion*. Applications of NDT data fusion, Kluwer Academic Publishers, Boston 2001 (227-267)
8. Kaczorek T.: *Linear control systems*. John Wiley and Sons Ltd., New York 1992
9. Liggins M., Hall D., Llinas J.: *Handbook of multisensory data fusion*. CRC Press, Boca Raton 2008
10. Patraiko D., Wake P., Weintrit A.: *E-navigation and the human element*. Marine navigation and safety of sea transportation, CRC Press, London 2009 (29-34)
11. Phol C., Ganderen J.: *Multi-sensor image fusion in remote sensing: concept, methods and applications*. International Journal of Remote Sensing, Vol. 19, No. 5, 1998 (823-854)
12. Pietrzykowski Z.: *Maritime intelligent transport systems*. Communications in Computer and Information Science, series No. 104, Springer, Berlin 2011 (455-462)
13. Pietrzykowski Z., Borkowski P., Wolejsza P.: *Marine integrated navigational decision support system*. Communications in Computer and Information Science, series No. 329, Springer, Berlin 2012 (284-292)
14. Sroka R.: *Data fusion methods in measurements of road traffic parameters* (in Polish). AGH University of Science and Technology, Cracow 2008
15. Sun S.: *Multi-sensor optimal information fusion Kalman filters with application*. Aerospace Science and Technology, Vol. 8, No. 1, 2004 (57-62)
16. Sun S., Deng Z.: *Multi-sensor optimal information fusion Kalman filter*. Automatica, Vol. 40, 2004 (1017-1023)
17. Torra V.: *Information fusion in data mining*. Springer, Heidelberg 2003
18. Xu Y., Qi H.: *Distributed computing paradigms for multi-sensor data fusion in sensor networks*. Journal of Parallel and Distributed Computing, Vol. 64, No. 8, 2004 (945-959)

CONTACT WITH THE AUTHOR

Piotr Borkowski, Ph.D.
Institute of Marine Technologies
Faculty of Navigation
Maritime University of Szczecin
Wały Chrobrego 1-2,
70-500 Szczecin, POLAND
e-mail: p.borkowski@am.szczecin.pl



The Ship Handling Research and Training Centre at Ilawa is owned by the Foundation for Safety of Navigation and Environment Protection, which is a joint venture between the Gdynia Maritime University, the Gdansk University of Technology and the City of Ilawa.

Two main fields of activity of the Foundation are:

- Training on ship handling. Since 1980 more than 2500 ship masters and pilots from 35 countries were trained at Ilawa Centre. The Foundation for Safety of Navigation and Environment Protection, being non-profit organisation is reinvesting all spare funds in new facilities and each year to the existing facilities new models and new training areas were added. Existing training models each year are also modernised, that's why at present the Centre represents a modern facility perfectly capable to perform training on ship handling of shipmasters, pilots and tug masters.
- Research on ship's manoeuvrability. Many experimental and theoretical research programmes covering different problems of manoeuvrability (including human effect, harbour and waterway design) are successfully realised at the Centre.

The Foundation possesses ISO 9001 quality certificate.

Why training on ship handling?

The safe handling of ships depends on many factors - on ship's manoeuvring characteristics, human factor (operator experience and skill, his behaviour in stressed situation, etc.), actual environmental conditions, and degree of water area restriction.

Results of analysis of CRG (collisions, rammings and groundings) casualties show that in one third of all the human error is involved, and the same amount of CRG casualties is attributed to the poor controllability of ships. Training on ship handling is largely recommended by IMO as one of the most effective method for improving the safety at sea. The goal of the above training is to gain theoretical and practical knowledge on ship handling in a wide number of different situations met in practice at sea.

For further information please contact:

The Foundation for Safety of Navigation and Environment Protection

Head office:
36, Chrzanowskiego Street
80-278 GDAŃSK, POLAND
tel./fax: +48 (0) 58 341 59 19

Ship Handling Centre:
14-200 ILAWA-KAMIONKA, POLAND
tel./fax: +48 (0) 89 648 74 90
e-mail: office@ilawashiphandling.com.pl
e-mail: office@portilawa.com